TRANSITING SYSTEMS

CHARACTERIZING THE EXOPLANETS AND THEIR HOST STARS

Dissertation
zur Erlangung des Doktorgrades
des Fachbereichs Physik

der Universität Hamburg

vorgelegt von

Carolina von Essen

aus Ciudad Autónoma de Buenos Aires, Argentina

Hamburg
2013

Gutachter der Dissertation:	Prof. Dr. J. H. M. M. Schmitt Prof. Dr. S. Dreizler
Gutachter der Disputation:	Prof. Dr. P. Hauschildt Dr. F. V. Hessman
Datum der Disputation	28.10.2013
Vorsitzender des Prüfungsausschusses	Dr. R. Baade
Vorsitzender des Promotionsauschusses	Prof. Dr. P. Hauschildt
Dekan der Physik Falkultät	Prof. Dr. H. Graener

To my dad, for reading me Carl Sagan when I was only a baby child.
To my mom, for providing the magic that made all the rest come true.
<3.

Abstract

Only when a planetary orbit is favorably aligned, we can indirectly observe an extrasolar planet crossing its parent star disk. When these events occur, the observed brightness of the star drops a small amount. By analyzing this periodic variations we can estimate the planetary size in terms of the size of its host. This is the foundation of the transit method. In this context, the hot Jupiter HD 209458b represents a milestone in extrasolar planet research, because it was the first transiting system ever found. Since then, the transit method has been responsible for one third of the extrasolar planetary discoveries, following the radial velocity technique in efficiency. In contrast to the planets of our Solar System, which can be studied *in situ* and individually, the large distances to extrasolar planets imply that they can usually be only observed together with their host stars. A proper characterization of an exoplanet requires, in consequence, a thorough understanding of many aspects of stellar astrophysics. Therefore, my thesis focuses on the characterization of transiting exoplanets as well as their host stars.

From the first discovery of an exoplanet almost 20 years ago, the observing techniques along with the instruments developed to detect exoplanets have been rapidly improving. Therefore, the rate of detection and our knowledge about extrasolar planets has been increasing as well. In the beginning, and due to their simplicity, the radial velocity and the primary transit methods were mainly used. Nowadays we can extend our studies about extrasolar planet characterization by means of new techniques.

As starting point I focus on WASP-33 which defines, certainly, a system that is one of a kind. The host is a δ Scuti star that shows pronounced pulsations with periods on the order of one hour and amplitudes in the milli-magnitude regime. The exoplanet, that has been detected through its transit, is the hottest one known to date. Showing an unusually large radius, WASP-33b belongs to the class of anomalously inflated exoplanets. Since the host star pulsations completely deform the primary transit feature, by means of an extensive photometric data set I characterize the pulsation spectrum of WASP-33A, identifying eight significant pulsation frequencies, which are likely to be associated with low-order p-modes. Afterward, I use the knowledge of the pulsations to clean the primary transit light curves, carrying out an improved transit modeling by means of pulsation-free primary transits. The main goal is to analyze to which extent do the stellar pulsations affects the exoplanet characterization.

The polarimetric detection of the reflected stellar light that is scattered by an exoplanet opens new opportunities to learn about the conditions in their atmospheres. Therefore, a part of my work involves the study of the WASP-33 system but, in this opportunity, with respect to its polarization signal. Since extremely accurate measurements collecting large amounts of stellar photons are required to separate the bright unpolarized stellar light from the faint light that has been polarized by the exoplanetary atmosphere, I develop a new method capable to collect stellar light efficiently, in order to achieve the high signal-to-noise required to disentangle the exoplanetary polarized signal from the noise.

Despite the improvements in technology, the transit method is mainly restricted to the detection of relatively large planets in close orbits around their parent stars. Although it might sound that the ability of the method is narrowed down to large planets, this is not the complete picture. By the variations in the timings of gas giants one can infer the presence of smaller planets. Therefore, a further part of my work involves the study of primary transit light curves with the main goal to extend the exoplanetary quest. To accomplish this I observe Qatar-1, a hot Jupiter presenting deep primary transit features easily to detect. Initially, there were indications for possible long-term transit timing variations, which could be reproduced by considering different dynamical scenarios. However, further primary transit observations could not replicate the same results.

All together, the studies produced in this work demonstrate the power of photometric data, showing how deep can we look into an extrasolar system by analyzing them.

Resumen

Si la geometría lo permite y la órbita planetaria está favorablemente alineada respecto a un observador, podemos observar indirectamente un exoplaneta cuando está cruzando el disco estelar. Cuando este evento sucede, el flujo estelar observado decrece en una pequeña cantidad. Es mediante el análisis de estas variaciones periódicas que podemos estimar el tamaño del exoplaneta con respecto al tamaño de la estrella huésped. Éstas son las bases del método de tránsito primario. En este contexto, el "hot-Jupiter" HD 209458 b representa un hito en lo que respecta a la búsqueda exoplanetaria, ya que fue el primer exoplaneta encontrado mediante el método de tránsito primario. A partir del mencionado descubrimiento, este método ha sido el responsable de un tercio de los exoplanetas descubiertos hasta hoy día, siguiendo al método de velocidades radiales en eficiencia. En contraste a los planetas de nuestro sistema solar, los cuales pueden ser estudiados en sitio e individualmente, las grandes distancias involucradas entre nosotros y los planetas extrasolares implican que estos sistemas pueden ser, mayormente, solamente observados en conjunto con su estrella huésped. Una adecuada caracterización de un exoplaneta requiere, en consecuencia, un profundo entendimiento de varios aspectos relacionados con astrofísica estelar. Por lo tanto, mi tesis se focaliza en la caracterización del planeta y la estrella huésped, particularmente cuando conforman un sistema que transita.

Como punto inicial me concentré en WASP-33 el cual define, ciertamente, un sistema que es único en su clase. La estrella huésped es una variable tipo δ Scuti que presenta pulsaciones pronunciadas con períodos del orden de una hora, y amplitudes en el régimen de mili-magnitud. El exoplaneta, el cual ha sido detectado mediante el método de tránsito primario, es el más caliente conocido hasta hoy. Presentando un radio inusualmente grande, WASP-33 b está clasificado como exoplaneta anormalmente inflado. Como las pulsaciones de la estrella huésped deforman completamente el tránsito primario, a través de un extenso set de datos fotométricos caractericé el espectro de pulsación de WASP-33 A. Identifiqué ocho pulsaciones significativas, las cuales están más probablemente asociadas con modos de tipo p de bajo orden. Luego, utilicé el conocimiento adquirido de las pulsaciones para limpiar las curvas de luz durante tránsito primario y produje un análisis de las resultantes curvas de luz, libres de pulsaciones. Mi meta principal es analizar hasta qué punto están los determinados parámetros orbitales del sistema afectados por las pulsaciones de la estrella huésped. Desde el primer descubrimiento hace ya casi 20 años, las técnicas observacionales tal como los instrumentos desarrollados para detectar exoplanetas han sido mejorados significativamente. Por lo tanto, la tasa de detección y nuestro conocimiento respecto de los planetas extrasolares han crecido también. En los comienzos, y debido a su alta simplicidad, el método de velocidades radiales y el de tránsitos primarios eran las técnicas más utilizadas. Hoy en día podemos extender nuestros estudios y conocimientos acerca de la caracterización de exoplanetas por medio de técnicas nuevas. Primeramente, la detección de luz estelar que ha sido polarizada por la atmósfera planetaria abre nuevas oportunidades para aprender acerca de las condiciones presentes en las atmósferas planetarias. Por lo tanto, una parte de mi trabajo involucra el estudio de WASP-33 pero respecto a su señal de polarización. Como medidas altamente precisas son requeridas para separar lo que es el flujo estelar no polarizado de la pequeña cantidad de luz estelar que ha sido polarizada por la atmósfera planetaria, creé un método capaz de colectar luz estelar eficientemente, de forma tal de poder obtener una alta relación señal-ruido y, de esta forma, apartar la señal de polarización. En segundo lugar, a pesar de las mejoras en tecnología que ocurrieron en estos últimos años, la técnica se utiliza mayormente en exoplanetas que son relativamente grandes y que orbitan muy próximos a la estrella huésped. Sin embargo, midiendo variaciones en los instantes de mínimo, consecuentes exoplanetas cuyos tamaños pueden asemejarse a nuestra propia Tierra pueden ser indirectamente detectados. Por lo tanto, una subsecuente parte de mi trabajo involucra el estudio de tránsitos primarios con la principal meta de extender la búsqueda exoplanetaria.

En conjunto, los estudios producidos en este trabajo demuestran el poder que yace en las curvas de luz fotométricas, mostrando cuán profundo puede llegar a ser el análisis de estos sistemas extrasolares a través del análisis de las curvas de luz.

Zusammenfassung

Wenn die Orientierung der Planetenbahn günstig ist, können wir den Durchgang eines extrasolaren Planeten vor seinem Zentralstern indirekt beobachten. Bei diesem Ereignis verringert sich die beobachtete Helligkeit des Sterns um einen kleinen Betrag. Durch die Analyse dieser periodischen Helligkeitsveränderungen können wir die Planetengrösse in Einheiten der Sterngrösse abschätzen. Auf diesem Prinzip basiert die Transitmethode. Der Exoplanet HD 209458b, ein sogenannter Hot-Jupiter, stellt einen Meilenstein der Exoplanetenforschung dar, weil es der erste Exoplanet war, dessen Transit beobachtet werden konnte. Seitdem war die Transitmethode verantwortlich für ein Drittel aller Entdeckungen extrasolarer Planeten, der Radialgeschwindigkeitsmethode in Effizienz folgend. Im Gegensatz zu den Planeten unseres Sonnensystems, welche in situ und einzeln untersucht werden können, können extrasolare Planeten aufgrund ihrer Entfernung nur zusammen mit ihren Zentralsternen beobachtet werden. Eine exakte Charakterisierung eines Exoplaneten setzt daher ein genaues Verständnis vieler Aspekte der stellaren Astrophysik voraus. Meine Arbeit konzentriert sich daher auf die Charakterisierung Transit zeigender Planeten sowie ihrer Zentralsterne.

Von der ersten Entdeckung eines Exoplaneten vor fast zwanzig Jahren an haben sich die Beobachtungsmethoden zusammen mit den zur Entdeckung extrasolarer Planeten entwickelten Instrumenten rapide verbessert. Deshalb haben sich die Entdeckungsrate und unser Wissen über extrasolare Planeten ebenfalls gesteigert. Am Anfang wurden aufgrund ihrer Einfachheit hauptsächlich die Radialgeschwindigkeits- und die Primärtransitmethode verwendet. Heutzutage können wir unsere Studien extrasolarer Planeten durch neue Techniken erweitern.

Als Ausgangspunkt konzentriere ich mich auf WASP-33, welches sicherlich ein einzigartiges System darstellt. Der Zentralstern ist ein δ Scuti-Stern, der ausgeprägte Pulsationen mit Perioden von etwa einer Stunde und Amplituden im Millimagnituden-Bereich zeigt. Der Exoplanet, welcher über seinen Transit entdeckt wurde, ist der heisseste bislang bekannte Exoplanet. Aufgrund der Tatsache, dass die Pulsationen des Zentralsterns zu einer vollständigen Deformierung des Primärtransits führen, charakterisiere ich mit Hilfe eines umfangreichen photometrischen Datensatzes das Pulsationsspektrum des WASP-33A und identifiziere acht signifikante Pulsationsfrequenzen, welche wahrscheinlich mit p-Wellen niedriger Ordnung verbunden sind. Anschliessend wende ich die Erkenntnisse über die Pulsationen an, um die Primärtransitlichtkurven zu bereinigen und führe eine verbesserte Transitmodellierung mit den pulsationsfreien Primärtransits durch. Das Hauptziel dabei ist, zu analysieren in welchem Ausmass die stellaren Pulsationen die Charakterisierung von Exoplaneten beeinflussen.

Die polarimetrische Detektion des durch einen Exoplaneten gestreuten Sternlichts eröffnet neue Möglichkeiten, etwas über die Bedingungen in seiner Atmosphäre zu lernen. Ein Teil meiner Arbeit beinhaltet daher die Untersuchung des WASP-33-Systems im Hinblick auf sein Polarisationssignal. Da extrem genaue Messungen, die grosse Mengen stellarer Photonen sammeln, notwendig sind um das helle unpolarisierte Sternlicht von dem schwachen Licht zu unterscheiden, das von der Atmosphäre des Exoplaneten polarisiert wurde, entwickle ich eine neue Methode, die es ermöglicht das Sternlicht effizient zu sammeln, um das hohe Signal-Rausch-Verhältnis zu erreichen, welches benötigt wird um das polarisierte exoplanetare Signal von dem Rauschen zu trennen.

Ungeachtet der technischen Verbesserungen ist die Transitmethode beschränkt auf die Detektion relativ grosser Planeten in engen Umlaufbahnen um ihre Zentralsterne. Obwohl es sich so anhören mag, dass die Anwendbarkeit der Methode auf grosse Planeten beschränkt ist, ergeben sich weitere Möglichkeiten: Von den Verschiebungen in den Zeitpunkten der Transits der Gasriesen kann man auf die Anwesenheit kleinerer Planeten schliessen. Aufgrund dessen beschäftigt sich ein weiterer Teil meiner Arbeit mit der Untersuchung von Primärtransitlichtkurven mit dem Ziel die Untersuchung von Exoplaneten zu erweitern. Um dieses zu erreichen, beobachte ich Qatar-1, einen Hot-Jupiter, der einfach zu detektierende tiefe Transitstrukturen zeigt. Anfänglich zeigten sich Anhaltspunkte fÃ¼r mögliche Langzeitvariationen der Transitzeitpunkte, die mit verschiedenen dynamischen Szenarios reproduziert

werden konnten. Weiterführende Primärtransitbeobachtungen konnten diese Ergebnisse jedoch nicht bestätigen.

Die Untersuchungen in dieser Arbeit veranschaulichen insgesamt das Potential photometrischer Daten, indem sie zeigen wie tief wir durch ihre Analyse in extrasolare Systeme blicken können.

Contents

Part I

Preface

Chapter 1

Motivation and Outline of the Thesis

The first exoplanet detection happened in 1995 using the radial velocity method. Unexpectedly, 51 Pegasi b was a gas giant orbiting a main-sequence star each four days only. Since then, the number of detected planets has raised up to almost one thousand. Repetitive discoveries of extra solar planets whose characteristics were similar to Jupiter, but experiencing elevated surface temperatures due to their proximity to the parent star instead, build up a classification of its own: the so–called "hot Jupiters". Although most efforts are invested towards the discovery of a planet that can sustain life, it was not until 2004 and 2011 that the first "hot Neptune" and "super Earth" were found. Scientist should wait even further to find, in December 2011, the first super-Earth in the habitable zone. Clearly, our understandings of the nature and characteristics of the vast exoplanetary sample lies in the observing capabilities. "Hot Jupiters" are the easiest ones to detect via the radial velocity technique, for instance, because the oscillations they induce in the parent stars motion are large enough to be measured even using middle-class telescopes. On the contrary, "super Earths" require larger telescopes and more refined techniques.

The number of exoplanets known to date, and the velocity at which these planets are being found, requires the combined efforts of many. However, it is essential to keep in mind that we will be able to throw some light into the formation and evolution of such intriguing systems only by means of a proper characterization of the already detected exoplanets.

Although the radial velocity technique is leading the discovery efficiency, there are several other techniques that present their own advantages. My work focuses on the exoplanets that are named after a detection method: the transiting systems.

WASP-33 as a pulsating star

Tides are familiar to us. We can see the response of Earth's oceans to the gravitational pull of the Sun and the Moon. Another clear example of tidal effects is seen within the Jupiter-Io system. Io's volcanic activity is caused by the force of Jupiter's gravity, coupled with the gravitational pull of Europa, Callisto, and Ganymede. As a result of opposite tidal forces, the surface of the moon rises and falls by about 100 meters; the ocean tides on Earth are as high as 18 meters. This ongoing friction generates heat, causing molten material and gases to rise through fractures in the crust and to erupt onto the surface.

Similar effects will arise between *any* orbiting bodies. If an exoplanet orbits close to its parent star, the result of the tidal interactions are the alteration of the size of the orbit (i.e., the semi-major axis) and the shape of the orbit (i.e., the eccentricity). In general, both parameters will decrease in time. In addition, close-in planets will raise tidal bulges on the stellar surface and *vice versa*. If the orbital period is shorter than the stellar rotational period, which is likely to happen since the orbital periods of hot Jupiters are extremely short, a redistribution of mass will occur. This, in turn, will cause a torque that drains angular momentum from the planetary orbit. This drain should cause measurable changes in the orbital periods of the exoplanets. All together, it is clear that the study of tidal star-planet interactions can help us to understand the formation, evolution, and migration of hot Jupiters.

Although theoretically tidal star-planet interactions (TSPI) seem to be straight forward to detect, the large distances to the exoplanets in combination with the intrinsically small expected variations, make the detection of TSPI a real challenge. Therefore, to maximize the chances of detecting such effects, one has to look into systems that offer the most advantageous conditions. That is how WASP-33 came into picture. It is the only transiting system that has a δ Scuti as host. This means, that the star presents pronounced pulsations with periods of the order of hours and amplitudes in the milli-magnitude regime, easily to detect using middle class telescopes. The exoplanet is a hot Jupiter, orbiting the star each ~1.22 days. Taking into account the system configuration, the question came naturally: could the pulsations of the host star be induced by the exoplanet via tidal interactions? What I had to do was straight forward: I had to carry out a photometric follow-up of the system in order to study if the observed pulsations were integer multiples of the orbital period of WASP-33b.

To test these hypothesis, due to the intrinsic brightness of the host star (V~ 8.3) I carried out a photometric follow-up of the system using Hamburger Sternwarte's facilities. Along two years I collected ~30 observing nights, mostly acquired in bluer bands, where the pulsations of the host are expected to be larger in amplitude. It was, indeed, due to the brightness of the host star and the large aperture of the Oskar Lühning Telescope (OLT), that I could reach milli-magnitude precision. This was required to resolve the low-amplitude pulsations of the δ Scuti star. Under a collaboration between German, Spanish, and United States institutes, we collected ~450 hours of in- and out- of transit observations of the star. With the observations and a proper analysis, we could characterize the pulsation spectrum of the host as never before. We found eight clear frequencies, which were present in all data sets. Although we found no clear evidences of TSPI, with the pulsations and a pulsation model, we cleaned up the primary transit light curves and improved, by means of pulsation-free transiting light curves, the orbital parameters of the system. An introduction to asteroseismology and an explanation to the work I performed on the data is given in Chapter 2.

WASP-33 in polarized light

The question that humanity has been asking itself for hundreds of years is: "are we alone?". In scientific language, this would be rephrased as: "is the Earth unique?" To answer this fundamental question by means of ongoing observations, we have to be able to recognize exoplanetary atmospheres that resemble our own: with water vapor, oxygen, ozone, and carbon monoxide. These strong absorbers would produce features in the spectrum that we could eventually resolve. Unfortunately, we are technologically immature to carry out such observations. Therefore, we can prepare ourselves by learning from hot Jupiter and hot Neptune atmospheres, that can be observed in transiting systems during primary and secondary eclipses.

Another way to look into the exoplanet atmosphere is via polarization. When the light of a star, which is mainly unpolarized, reaches the planetary atmosphere, it is scattered by the different layers and reflected back. Some part of that scattered light will go towards Earth. Using adequate telescopes and instruments this signal, which carries the properties and composition of the atmosphere that has scattered it, can be detected. For the case of resolved Solar System planets this measurements are easy to obtain. However, in the case of hot Jupiters we can not disentangle the planet from the star. In consequence, it is hard to differentiate the large amounts of unpolarized stellar flux from the small fraction of polarized light. To distinguish such small signature from the "noise", many photons have to be collected. With the main goal to strengthen an observing technique that could be powerful to characterize exoplanets (it provides independent measurements of orbital inclination and composition of the atmosphere of the exoplanet) I developed an observing technique, practiced in Calar Alto observatory, that efficiently collects stellar photons carrying polarization information. Furthermore, since the polarization signal from an exoplanet atmosphere is small in nature (the polarization degree is expected to be ~0.01 - 0.1%) and strongly depends on the orbital and physical parameters of the system, not every planetary system will be adequate to perform such observations. This is how, one more time, WASP-33 came into the picture. Firstly, the spectral type of the host star is A5. Therefore, most of the stellar photons are emitted in the blue. Assuming that Rayleigh scattering is the main engine of polarized light, this type of stars would make the scattering as efficient as it can be, only due to the nature of the radiation. Secondly, the proximity between planet and star, and the intrinsically large size of the exoplanet, makes the scattering surface (i.e., the exoplanet atmosphere) to appear large. All combined produces one of the best-case scenarios for polarimetric detection. Chapter 3 shows my ongoing work on the topic and some initial results.

Transit timing variations

There are, basically, two theories that explain how hot Jupiters are formed. One theory predicts the presence of nearby companion planets, and the other one does not. Which theory is more adequate can be pin pointed by looking at Kepler light curves for example, analyzing whether hot Jupiters are found together with other types of planets or not. The model that is empirically taking the lead favors loner hot Jupiters. Supporting theories propose that gas giants initially had elliptical orbits and circularized over time. As they migrate inward, their gravitational pull would scatter the planetesimals. This reasoning could explain why hot Jupiters are found to be alone.

In the ongoing quest for Earth-like exoplanets, several methods have been developed. One of them is the transit timing variation technique (TTV). By observing variations in the timing of transiting planets such as gas giants, the presence of additional exoplanets can be inferred. The method is extremely sensitive, capable of detecting planets with sizes potentially as small as the Earth.

In order to make a small contribution in the understandings of the planet formation and evolution, I used the OLT and the Planet Transit Studies Telescope (PTST) to follow-up a transiting system, Qatar-1, fully described in Chapter 4. My main goal was to study TTVs. Particularly located at high declinations (δ ~65), Sternwarte's latitude allowed almost continuous monitoring of the target. Combining both telescopes, I acquired up to 42 primary transit light curves. Since the observations were performed quite frequently and over more than 2 years, the collected data were optimal to study the truthfulness of TTVs in the system. In addition, I dedicate part of my time to study TTVs on the KOI-676 system, an active star with two planets in mean-motion resonances observed by the Kepler space telescope.

The power of the TTV method has been claimed to be that small-sized telescopes can be used to carry out the observations required to develop this technique. Motivated by our results, I produce synthetic primary transit light curves affected by the macro effects that non-photometric conditions produce over photometric data, to study if ground-based facilities can succeed in the detection of exoplanets by means of the TTV technique. What we found is in complete agreement with what we see in our photometric data: in order to detect Earth-sized planets using the TTV technique, the photometric light curves need to fulfill certain requirements of quality.

Exoplanet oblateness

Fascinated by the proximity between planets and stars, one of the ongoing questions astrophysics tries to answer is how, and to which extent, do the planet and the star interact with each other. Due to their mutual proximity, planets are affected by stellar gravity. Identically as the Jupiter-Io system, hot Jupiters are expected to be tidally elongated. Motivated by the fact that most of the Solar System planets are oblate, caused either by tidal interaction or by large rotation rates (e.g., Saturn), I produce a simple primary transit model that includes the exoplanet oblateness as extra parameter (Chapter 5). If the oblateness of an exoplanet is known, the rotation rate of the exoplanet can be estimated and, with it, the evolutionary tracks of the system. Once the model was produced, I studied under which conditions could the oblateness be retrieved by means of light curve fitting procedures.

Stellar activity and exoplanets

It was with the advent of highly-precise space-based light curves that stellar activity studies closely related to planetary science really began. Only then, it was clear how much could activity influence the transit light curves and, in consequence, the parameters of the system. In order to produce a proper characterization of the exoplanets orbiting active stars, stellar activity needs to be taken into account. Motivated by this, our group studied in detail the CoRoT-2 transiting system, conformed by the most active star known to date that hosts an exoplanet and a hot Jupiter, CoRoT-2b. In Chapter 6 I show the efforts invested by studying transit observations of CoRoT-2, to demonstrate the power of the Rossiter-McLaughlin effect for the exploration of the stellar atmosphere.

Part II

Scientific contributions

Chapter 2

WASP-33: A pulsating, planet-bearing star

Γεωμετρία υπάρχει στο άσμα των χορδών.
Μουσική στα διαστήματα των σφαιρών.
There is geometry in the humming of the strings.
There is music in the spacings of the spheres.

Pythagoras

2.1 Asteroseismology

It is widely known how much does oil impacts our global economy. Thus, many resources have been invested in the pursuit of the so–called "black gold". Geologists use the propagation of seismic waves through the Earth interiors not only to learn about the structure of our planet, but also to reveal possible crude oil and natural gas formations. The technique records sound waves as they echo within the Earth. By studying the echoes, the depth and the structure of geologic formations can be inferred.

Equivalently, but in a less-lucrative scale, asteroseismology studies the stellar interiors via the oscillations caused by sound waves within the stars. By means of photometric and spectroscopic astronomical data the frequencies, the amplitudes, and the phases of the acoustic waves at the stellar surface can be determined. By matching observations with mathematical models of how stars *should* pulsate, we can infer the temperature and chemical composition of the stellar interiors, impossible to obtain in other ways.

Since stars are three–dimensional objects, the displacements caused by the oscillations are represented as a function of the distance to the center, r, the co–latitude, θ, and the longitude, ϕ. The nodes of a given pulsation (points along the medium that appear to be standing still) are then concentric shells at constant r, cones of constant θ, and planes of constant ϕ. Except for the case of rapidly oscillating Ap stars, in most pulsating stars the pulsation axis coincides with the rotation axis (Aerts et al. 2010).

The oscillation modes of a pulsating star are described by three quantum numbers: n, the *overtone of the mode*, is related to the number of radial nodes; ℓ, the *degree of the mode*, specifies the number of surface nodes that are present; m, the *azimuthal order of the mode*, describes how many surface nodes are lines of longitude. Since the values of m range from $-\ell$ to ℓ, there are $2\ell + 1$ modes for each degree ℓ. The higher the ℓ value, the more divisions will undergo the stellar surface (see Figure 2.3). Despite theoretical predictions, asteroseismological measurements are not precise enough to resolve the exact position of the nodal lines from photometric or spectroscopic data, because the measurements reveal only either surface–averaged brightness or radial velocity.

Helioseismology is the study of the propagation of wave oscillations in the Sun. For the case of our most nearby star, the seismic information from the observed solar wave field has unprecedented accuracy and spatial resolution. Figure 2.1 shows surface oscillations in the Sun with periods near five minutes (Kosovichev et al. 1998; Larson & Schou 2008). Each ridge corresponds to a given value of the radial order n. Only waves with specific combinations of period and wavelength resonate within the Sun. This is closely related to the Sun's interior structure, composition, and dynamics. The $\ell - \nu$ (period versus wavelength) diagram was obtained from 2 months of the SOHO/MDI (Michelson Doppler Imager) Medium$-\ell$ program in 1996. The instrument provided continuous observations of oscillation modes of angular degree ℓ, from 0 to ~300 (Scherrer et al. 1995). To better comprehend how accurate these measurements are, the width of the ridges equates to 1000σ error bars.

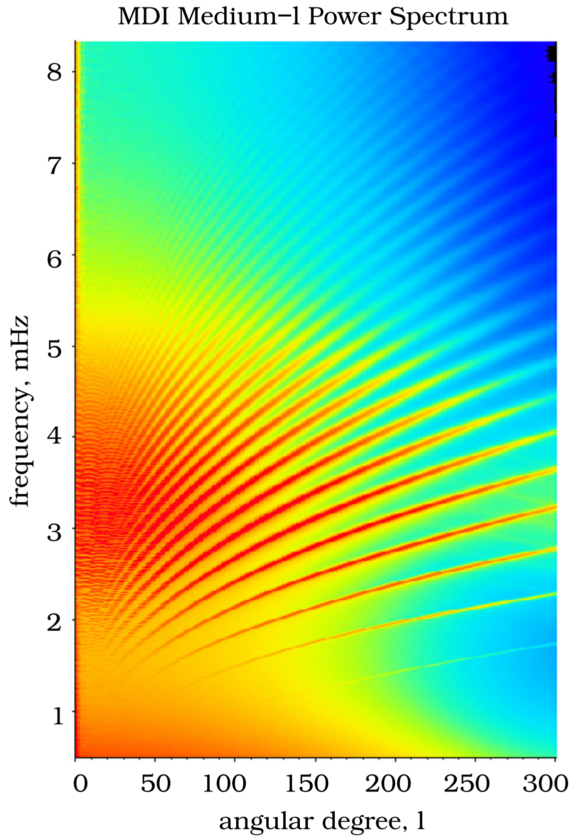

Source: SOHO/MDI.

Figure 2.1: m–averaged oscillation power spectrum, revealing the Sun's internal structure and rotation. Courtesy of SOHO/MDI consortium. SOHO is a project of international cooperation between ESA and NASA.

Although it is unfair to compare seismological observations between our completely resolved Sun and far away stars, there are, however, certain aspects of stellar oscillations that can be accurately measured, such as the nature of the modes or the mechanism that triggers the pulsations.

2.1.1 Radial and non–radial pulsators

Two classes of largely studied *radial* pulsators are RR Lyrae and δ Cepheid variables. They are intrinsically bright and, thus, often used as "standard candles" (i.e., distance estimators). This type of stars reveal pulsation periods that are closely related to their absolute luminosities.

Generally, the radial oscillations of a pulsating star are the result of sound waves resonating in the stellar interiors. Layers of gas in constant expansion and contraction are the mechanisms powering these standing waves. For the fundamental radial mode, a rough approximation of the pulsation period can be obtained, considering how long does it takes to a sound wave to cross the stellar diameter, i.e.,

$$\Pi \sim \frac{R}{< v_s >} \,, \tag{2.1}$$

where $< v_s >$ is a suitable average of the sound speed. Generally, the speed of sound v_s in an ideal gas is given by the Newton-Laplace equation:

$$v_s = \sqrt{\frac{\gamma P}{\rho}} \,, \tag{2.2}$$

where P is the pressure, γ is the adiabatic index (the ratio of specific heats of a gas at a constant–pressure to a gas at a constant–volume, C_P/C_V), and ρ the mean density. Approximating the density by the mean density and using the equation of hydrostatic support we have the following estimates:

$$\begin{aligned} \rho &\sim \frac{M}{R^3} \,, \\ P &\sim \frac{GM^2}{R^4} \,. \end{aligned} \tag{2.3}$$

where G is the universal gravitational constant, M the stellar mass, and R the radius of the star. Using Eq. 2.3 to estimate $< v_s >$ (Eq. 2.2) yields

$$\Pi \sim \left(\frac{R^3}{GM}\right)^{1/2} \tag{2.4}$$

Thus, $\Pi \propto (G\rho)^{-1/2} \propto \left(\frac{M}{R^3}\right)^{-1/2}$.

Cepheid and RR Lyrae are found in a narrow and almost vertical strip in the HR diagram (see Fig. 2.5, Section 2.2.1). The effective temperatures are, therefore, quite similar and weakly dependent on luminosity. The distance estimation via the "period–luminosity" relation can be calibrated with great precision (see e.g., Leavitt & Pickering 1912, for the discovery article). For these stars, $L = 4\pi R^2 \sigma T_{eff}^4$ and $T_{eff} \sim$ constant. Hence, $L \propto R^2$. Eliminating the stellar radius R, the "period–luminosity" relation reveals:

$$\Pi \propto L^{3/4} M^{-1/2} , \tag{2.5}$$

which is similar to the empirical relation $\Pi \propto L^{0.87 \pm 0.06}$ (e.g., Anderson et al. 2013; Ngeow et al. 2012; Benedict & McArthur 2012). The importance of radial oscillators for the determination of astronomical distances is, thus, out of the question.

But how do the radial modes look like? The simplest radial mode is the fundamental mode. The star is in continuous expansion and contraction, heating and cooling, always spherically–symmetrically. For the fundamental radial mode the core behaves as a node and the surface as a displacement antinode (Figure 2.2, a)). The first overtone radial mode (Fig. 2.2, b)), has a shell between the core and the stellar surface working as a node. The motions below and above the node move in antiphase. Stars such as Cepheid, RR Lyrae, and δ Scuti stars can pulsate in the first and second fundamental radial modes (Breger et al. 2005).

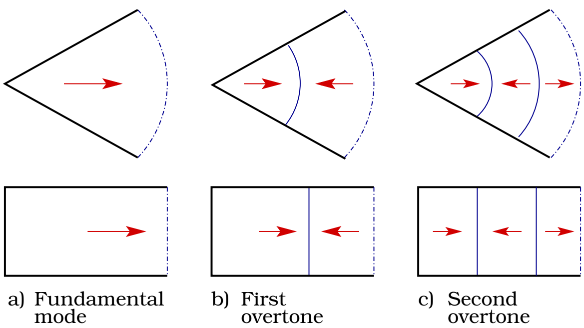

Source: C. von Essen.

Figure 2.2: Analogy between the first three one–dimensional oscillation modes for an organ pipe, in comparison to the three–dimensional oscillations in a radial pulsating star.

The *non–radial* mode picture is slightly more complicated. A non–radial pulsation only means that some parts of the stellar surface will move inwards, while others will move outwards *at the same time*. Thus, it is important to keep in mind that non–radial modes *do have* a radial component. Non–radial modes occur only for $n \geq 1$. Thus, there is at least one radial mode within the star when non–radial modes are excited. Modes with $\ell = 1$ (the so–called dipole mode) are common in rapidly oscillating Ap stars (Kurtz et al. 1994, 1997; Handler et al. 2006). Modes with $\ell = 2$ (two surface nodes) are called quadrupole modes. Octupole modes are the ones with $\ell = 3$, and so on and so forth. Figure 2.3 shows a sketch of the radial component of various non–radial modes, as seen by an observer under an inclination angle of 50°. Although the sketch of the non–radial modes seem to be simple in nature, as stated before it is not possible to resolve the exact positions of the nodal lines. The higher the ℓ–value, the more divided will be the stellar surface. Since we can only measure integrated quantities, *partial cancellation*, a consequence of the total number of nodal lines in the stellar surface, is expected to occur. Thus, the larger the degree of a non–radial mode, the more difficult it will be to identify it.

But how are the modes excited in δ Scuti stars? For instance, turbulent motions in stellar convection zones generate acoustic energy (Belkacem et al. 2008), part of which is then supplied to normal modes of the star. Also, the tidal action of a companion can in principle be an effective way to trigger oscillations in binary components (Cowling 1941).

2.1.2 Pressure and gravity modes

The observed patterns on the surface of a star are caused by sound waves that are propagating through the whole stellar structure. Stellar waves can be divided into two main categories, depending on the mechanism that keeps them ongoing: p–modes and g–modes.

p–modes are acoustic waves that have pressure as equilibrium–restoring force. These modes are more sensitive to conditions in the outer part of the star. They are trapped between the stellar surface and a turning point, $r = r_t$, where the waves undergo total internal refraction.

As two waves propagate into the star (continuous and dashed lines of Figure 2.4, as an illustrative example), the deeper waves experience a higher sound speed and, consequently, move faster. As a result, the direction of propagation is bent away from the radial direction. After the turning point, the wave moves out again until it reaches the surface. At the surface, the acoustic waves are re-

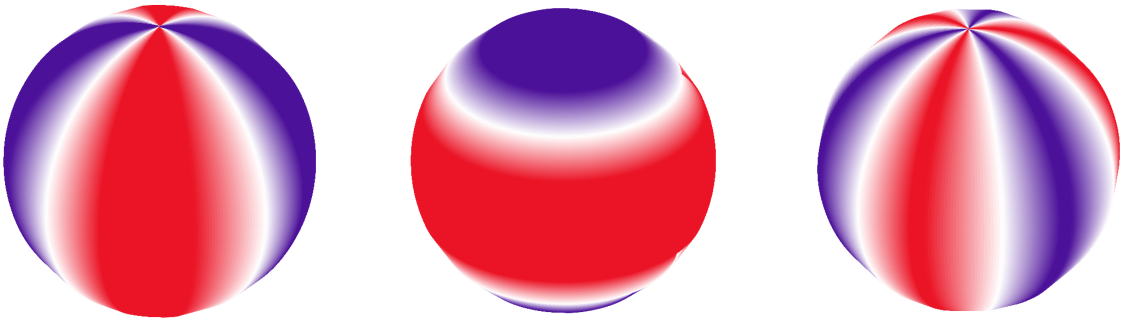

Source: C. von Essen.

Figure 2.3: Snapshot of the radial component of some modes as seen by an observer under an inclination of 55°. The red and the blue represent the sections of the star that are moving in (red) and out (blue). The white bands represent the positions of the surface nodes. From left to right: $(\ell, m) = (2,2)$, $(\ell, m) = (2,0)$, and $(\ell, m) = (3,3)$.

flected by the rapid decrease in density.

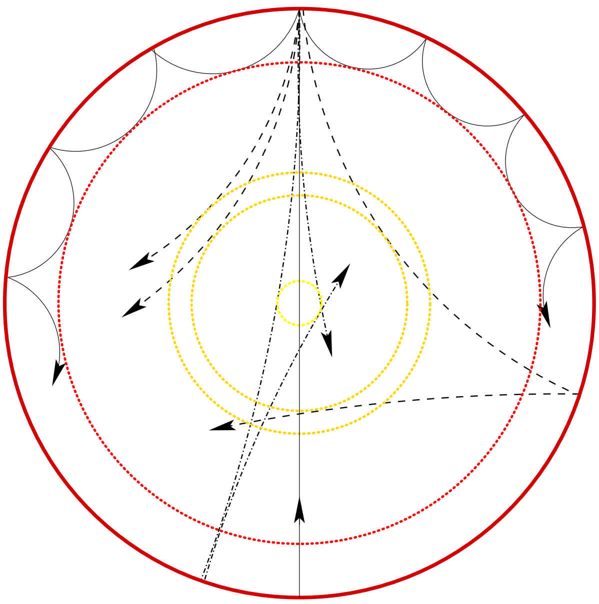

Source: C. von Essen.

Figure 2.4: Propagation of p–type waves in a stellar cross–section. The waves are bend with the increase of sound speed as a function of depth, until they reach the inner turning point, where they undergo total internal refraction.

Generally, the natural frequencies of a structure, S_ℓ, are the frequencies at which the structure naturally tends to vibrate if it is subjected to a disturbance. Its definition is given by (Aerts et al. 2010):

$$S_\ell^2 = \frac{\ell(\ell+1)c^2}{r^2} . \tag{2.6}$$

The inner turning point is located where $S_\ell = \omega$, being ω the pulsation frequency. In this case, $r_t = r_t(\ell, \omega)$ and

$$\frac{c^2(r_t)}{r_t^2} = \frac{\omega^2}{\ell(\ell+1)} . \tag{2.7}$$

Therefore, a larger degree ℓ will correspond to a less penetrating wave. The sound speed in the stellar interior can then be traced by identifying the ℓ's of the observed pulsations. In the case of the resolved Sun, for $\ell \geq 40$ the modes are completely trapped inside the convection zone, which has a depth of about $0.28R$.

Gravity, acting on the density perturbation, provides the dominant restoring force for *g-modes*. For these modes, the turning point positions are determined by the condition $N = \omega$. N is called the "buoyancy frequency", the angular frequency at which a vertically displaced element will oscillate within a statically stable environment. These modes are, thus, confined into the stellar core. Known g–mode pulsators are the Slowly Pulsating B–type stars and the γ–Dor stars. Theoretical three-dimensional simulations show that g–mode oscillations might be induced by the convection coupled to the rotation in, for instance, early A–type stars (Browning et al. 2004). The pulsation frequencies are expected to be of the order of or less than two times the rotation frequency of the star.

2.2 Relevant aspects on pulsating stars

2.2.1 The Hertzsprung-Russell diagram

Pulsating stars are found almost all over the Hertzsprung–Russell (HR) diagram. Thus, pulsations happen in stars at different temperatures, luminosities and evolutionary stages. Figure 2.5 shows two theoretical HR diagrams (Handler 2013). The plot on the left contains the regions occupied by the pulsating stars that were known 40 years ago, while the plot on the right shows an up–to–date HR diagram. What basically differentiates the individual classes is the pulsation mode that excites them, the stellar mass, and the evolutionary state (i.e., the temperature and the luminosity).

The majority of pulsating stars occupy regions on the HR diagram called "instability strips" (IS). Stars turn variable when they enter this strip. The instability occurs as main sequence stars transition to and along the giant and supergiant branches of the HR diagram. These stars intersect the main sequence in the region of spectral types from A to F stars (1–2 $M_{\odot}$) and extends to G and early K bright supergiants. Generally, massive stars cross the IS from the main–sequence to the giant branch, burning Helium. These stars will become part of the Cepheid variables. "Lighter" stars enter the IS when they fall down from the giant branch after the Helium flash occurred, turning into RR Lyrae and W Virginis later on.

There are three regions in the HR diagram where p–mode and g–mode pulsators of similar stellar structure coexist: on the upper main sequence, the β Cep and Slowly Pulsating B stars; for the δ Sct (mostly p–mode) and γ Dor stars on the middle of the main sequence; in the central part of the HR diagram, for the sdBVr and sdBVs stars. p–mode pulsators are indicated in Fig. 2.5 with blue regions, while g–mode's in red. "Asteroseismically" speaking, stars such as δ Sct's, pulsating in both p– and g–modes, are the best candidates to study the stellar interiors.

2.2.2 How do stars pulsate

To understand how stars pulsate, their relevant time scales need to be considered. Quantities such as the stellar radius, the internal energy, and the nuclear energy of the star, will dictate the stellar fate.

To start, the *nuclear time scale*,

$$\tau_{nuc} = \frac{\epsilon q M c^2}{L} , \tag{2.8}$$

expresses how long can the star shine, when nuclear fusion is the energy source. In this case, q is a small fraction of the stellar mass that can take part in the nuclear burning, ϵ is the fraction of that mass that is converted into energy in the nuclear reactions, M is the stellar mass and L its luminosity. In the solar case, $\tau_{nuc} \sim 1 \times 10^{10}$ years.

The internal structure of a star is determined by the existent equilibrium between different physical processes. Due to hydrostatic equilibrium

$$\rho g = -\frac{dP}{dr} , \tag{2.9}$$

the outward force due to the pressure gradient within the star is exactly balanced by the inward force due to gravity and, hence, small perturbations go unnoticed. Pressure and gravity are self–compensating to keep the stellar structure in equilibrium. When, however, a small contraction does take place, the temperature around the perturbation will increase, which will induce the outward pressure to rise. The layer will then expand, until equilibrium is recovered. The *dynamical time scale* is, then, nothing more than the time needed to recover from such a small contraction,

$$\tau_{dyn} = \sqrt{\frac{R^3}{G\rho}} , \tag{2.10}$$

where ρ is the mean stellar density and R the stellar radius. For the Sun, τ_{dyn} ~20 minutes, while for a white dwarf it can go down to a few seconds.

The last relevant time scale is the *thermal time scale*,

$$\tau_{th} = \frac{GM^2}{RL} , \tag{2.11}$$

which expresses the time that a star can shine with gravitational potential energy as its only energy source. For the Sun, τ_{th} is to be tens of million of years.

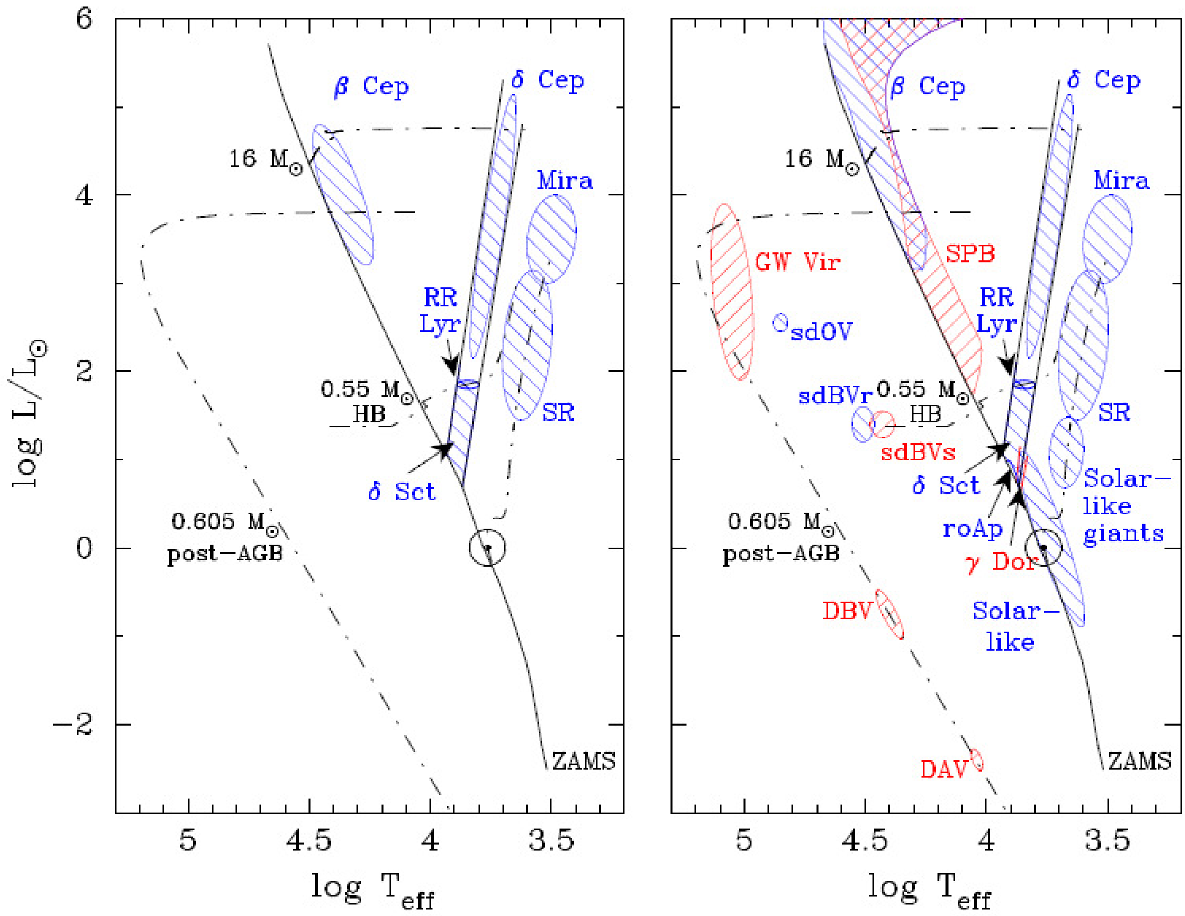

Source: *Handler (2013)*.

Figure 2.5: Theoretical HR diagrams showing where are pulsating stars located. Left: 40 years ago; right: up–dated classes of pulsators. The classification names are usually given after a prototypical star. The "classical instability strip" is indicated with almost vertical parallel continuous lines, containing primarily the δ Cep, RR Lyr, roAp and δ Sct stars.

2.2.3 Why do stars pulsate: excitation mechanisms

A proper answer to "Do all stars pulsate?" mainly relies on the precision of astronomical data. If we consider a photometric precision of 10^{-5} (e.g., Borucki et al. 2010), and ~1 m/sec in radial velocity (e.g., Quirrenbach et al. 2010), we can state that not all stars pulsate.

Nuclear reactions produce heat at the center of a star, which is dumped out in the form of luminosity. The pulsations "disturb" this balance in three main ways: modulating the radiative luminosity (κ–mechanism, γ–mechanism), and modulating the nuclear reaction rate in the core (ϵ mechanism).

κ–mechanism: Within the pulsation cycle, a radial layer of stellar material loses support against the star's gravity, falling inwards. The layer is then compressed, heats up and becomes more opaque to radiation. As a result, radiation cannot diffuse as fast as before, so the layers beneath heat up. The pressure rises below the compressed layer, pushing it outwards. During the expansion phase, the layer cools down and becomes more transparent to radiation. Thus, energy can escape easily again, dropping the pressure beneath. The layer falls inwards and the cycle repeats. One cycle's requirement is that the opacity of a layer should increase with compression. This easily occurs when hydrogen and helium are available. The κ–mechanism is responsible for the pulsations existing in stars

within the classical IS. A sketch of the mechanism is seen in Figure 2.6.

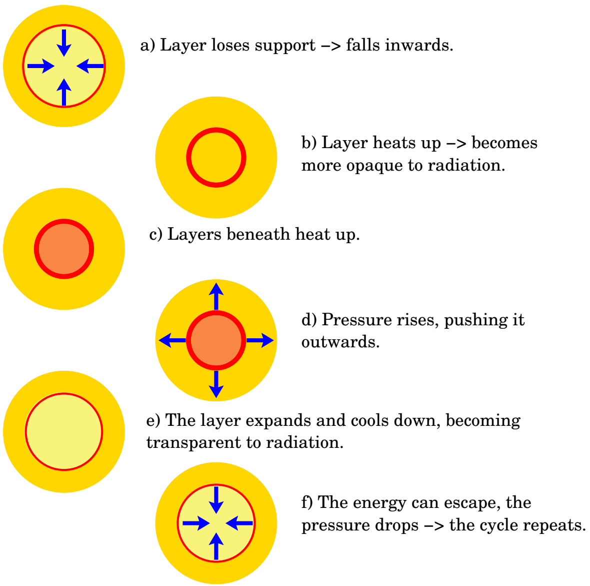

Source: C. von Essen.

Figure 2.6: Schematic diagram of the κ–mechanism.

γ–mechanism: The temperature gradient that exists between the partial ionized zone close to the compressed layer and the adjacent layers induces more heat to flow towards the compressed zone, producing further ionization. Thus, the κ–mechanism is reinforced by the γ–mechanism in driving the pulsation instability.

ϵ mechanism: In nuclear–burning regions of very massive and evolved stars, when a radial layer is compressed, the temperature and thus, the nuclear energy generation rate, are higher than in equilibrium. Under this conditions, the matter gains thermal energy and expands. After the expansion, the nuclear energy generation rate is lower than in equilibrium, and hence the matter loses its thermal energy and compresses. There are no known pulsating stars that are thought to be driven by the ϵ–mechanism alone.

2.3 Mode identification

Once photometric or spectroscopic asteroseismological data are collected and the frequencies within the data are identified, the next natural step would be to understand what pulsation mode gives rise to each frequency. This study is called *mode identification*.

The empirical mode identification requires a detailed confrontation between observational characteristics of the pulsations (such as the observed phases and amplitudes) and oscillation theories (e.g., Aerts 1996; Balona & Evers 1999; Dupret et al. 2003; Zima 2006). In this way, the numbers that describe non–radial pulsations, n, ℓ, and m, are assigned to each frequency.

A proper mode identification requires either high–resolution spectroscopy (typically with a resolution above 40 000) in combination with a high signal–to–noise ratio above 200 (Mathias et al. 1997), and/or photometric data (Heynderickx et al. 1994; Matthews et al. 2004), both obtained on time scales longer than the pulsation periods that are being studied. Although the mode identification via spectroscopic data can give a more detailed picture of the pulsation pattern in variable stars[1], this kind of observations require large–aperture telescopes and sophisticated instrumentation. Photometric data can, in turn, be obtained with smaller and "cheaper" telescopes.

2.3.1 Mode identification via multicolor photometry

As a result of the pulsations, a pulsating star changes in temperature and in shape. Thus, a variation in its bolometric luminosity occurs. Photometric and spectroscopic observations do not provide bolometric (or monochromatic) fluxes. Stellar observations are principally sensitive to filter transmission curves, CCD quantum efficiencies, and atmospheric transmission, all wavelength–dependent.

The variation of the stellar brightness due to pulsation depends, primarily, on the overall temperature change in the star. This variation is typically sinusoidal in shape, and correlated with the pulsation period (De Ridder et al. 2002*b*,*a*). To illustrate how the amplitude of the pulsation depends on the wavelength (i.e., the filter used to perform the observations), I simulated a simplified sinusoidal temperature variation as a function of time, rang-

[1] Spectroscopic mode identification does not rely on oscillation theories in the outer atmosphere of stars, but only in the velocity field of the pulsations.

ing between 7300 and 7500 K. After the convolution of each black body with a CCD quantum efficiency and the transmission function of standard filters (Johnson-Cousins BVR, Strömgren vby), I calculated the measured flux, and converted it to magnitudes. Figure 2.7 shows the resulting light curves. It is clearly seen that the bluer the filter, the larger the amplitude of the pulsation. The intensity change is larger in the blue than in the red, just because of the shape of the black body curves.

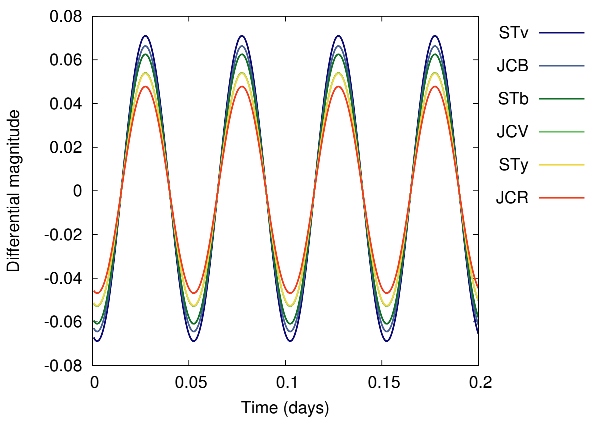

Figure 2.7: Simulated noise-free magnitude variation as a function of time, as recorded for different filters.

In addition to this effect, the intensity variation also depends on the geometry of the variations of the temperature, and on the change in the geometrical cross section. This will give rise to measurable changes in the amplitude and the phase of the pulsations as a function of wavelength, which will in turn be the basis for mode identification.

The photometric mode–identification was first proposed by Stamford & Watson (1981). More recent works like Garrido et al. (1990) includes limb–darkening effects; Balona & Evers (1999) specializes in the mode identification for δ Scuti stars; and main sequence stars are treated in Dupret et al. (2003), as some examples.

The theoretical expressions for the amplitude and the phase of a given pulsation as a function of wavelength (or, equivalently, the photometric filter) mainly depend on the geometrical configuration of the nodal lines with respect to the observer. Thus, an estimate of (ℓ,m,i), where i is the inclination angle between the symmetry axis of the oscillation and the line–of–sight, is required for mode identification.

The identification is produced by computing the theoretical amplitude ratios and phase differences of the previously identified pulsations between different filter bands. The theoretical quantities strongly depend on the metallicity, the surface gravity, and the stellar effective temperature. Thus, the errors on the stellar parameters have to be taken into account. As an example, Figure 2.8 shows observations of amplitude ratios in the uvy Strömgren filters, from the β Cephei ν Eridani pulsating star (De Ridder et al. 2004).

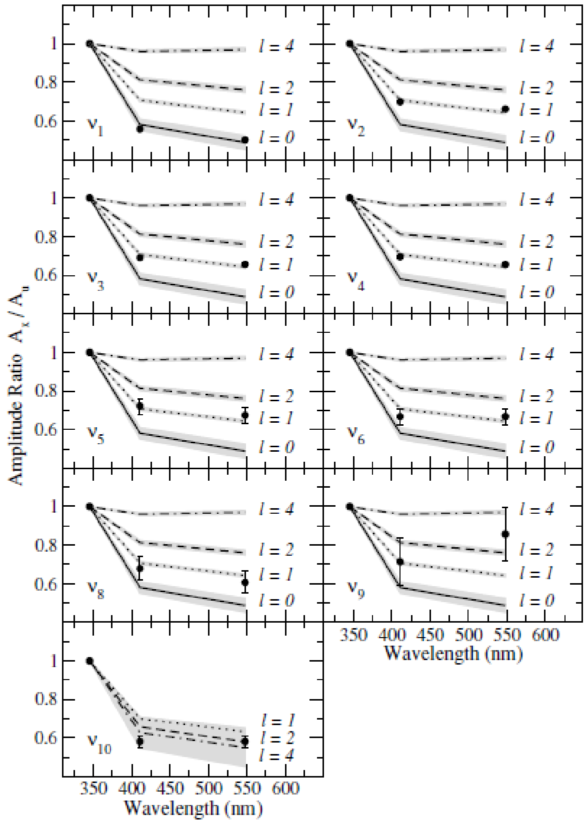

Source: De Ridder et al. (2004).

Figure 2.8: Mode identification of the β Cephei ν Eridani pulsating star via amplitude ratios. The dots correspond to observations carried out in the Strömgren uvy filters, while the continuous and dashed lines correspond to the theoretical amplitude ratios. The gray bands take into account the uncertainty of the stellar parameters.

2.4 WASP-33

The WASP-33 system is conformed by an A5 star, which – to date – remains the only known pulsating, planet-host star (Herrero et al. 2011), and a hot Jovian planet transiting the parent star every 1.22 d in a retrograde orbit (Christian et al. 2006). The planet has been detected through its transits in the frame of the WASP campaign (Pollacco et al. 2006). A spectral time series analyzed by Collier Cameron et al. (2010) clearly confirms the presence of a planet, whose "shadow" is visible as a deformation in the spectral line profiles, where it has been used to trace the planet's retrograde orbital motion (see Figure 2.10).

In a photometric study of WASP-33A's pulsations, Herrero et al. (2011) find that the star is of δ Scuti type showing pulsations with periods of about one hour and visual-band amplitudes of ≈ 2 mmag. Furthermore, the authors provide tentative evidence for star-planet interactions; in particular, they have identified a potential commensurability between the period of their highest-amplitude pulsation component and the orbital period with a factor of 26.

Smith et al. (2011) observe thermal emission from WASP-33b during secondary eclipse. In line with the intense illumination of the planet (Collier Cameron et al. 2010), the authors derive a high dayside temperature of 3620^{+200}_{-250} K and conclude that the day-night-side energy redistribution in WASP-33b is inefficient. As pointed out by Smith et al. (2011) and Collier Cameron et al. (2010), the pulsating nature of WASP-33A interferes both with accurate radial-velocity measurements and photometric transit modeling. Consequently, only a lower mass limit of $M\ \sin(i) < 4.59\ \mathrm{M}_J$ is known for this transiting planet and no tangible estimate for the orbital eccentricity could be derived, although Smith et al. (2011) favor a value of zero.

In the frame of an international collaboration, between August 2010 and October 2012, we obtained 457 hours of photometry of WASP-33 distributed across 56 nights using six telescopes: one in Germany (the Oskar Lühning telescope, OLT, located in Hamburger Sternwarte) and five in Spain. From the 56 nights, 29 were obtained using the OLT (see Figure 2.9 for an image of WASP-33's field of view at the site). Particularly, our out-of-transit data provide ~3 times more temporal coverage than the Kovács et al. (2013) data set, which is the most extensive one available in the bibliography. In addition, our data set is the only one that comprises dedicated out-of-transit photometric coverage to study the stellar pulsations in detail, and multi-color and simultaneous observations to study the nature of the modes. The pulsation frequency analysis is performed using PERIOD04, a package that has been specialized for variable stars (Lenz & Breger 2005).

Figure 2.9: OLT's field of view of WASP-33. North is oriented up, while East left. The brightest star of the field is WASP-33. The differential photometry was obtained between WASP-33 and the second brightest star North-West from WASP-33, BD+36 488, which is one magnitude fainter.

A deep study over the pulsation spectrum of WASP-33 reveals, for the first time, eight significant frequencies. Along with the associated amplitudes and phases, we construct a pulsation model which we use to correct the primary transit light curves, with the main goal to re-determine the orbital parameters by means of pulsation-clean data.

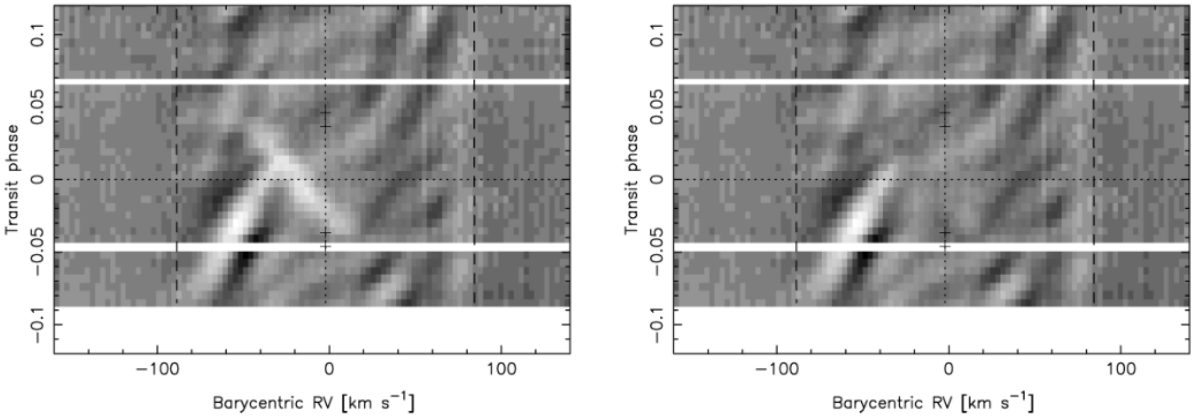

Source: Collier Cameron et al. (2010).

Figure 2.10: Time series of the residual average spectral line profile of WASP-33 during one primary transit. Wavelength or radial velocity increases from left to right, while time from bottom to top. The four contact times of the transit are indicated by "+" symbols. The planet signal is the bright feature that moves from right to left (retrograde orbit), coincident with the duration of the photometric transit. In the right panel, the model planet signature has been subtracted from the data, leaving only the pattern of non-radial pulsations.

Pulsation analysis and its impact on the primary transit modeling in WASP-33

C. von Essen, S. Czesla, U. Wolter, M. Breger, E. Herrero, M. Mallonn, I. Ribas, K. G. Strassmeier & J. C. Morales
Submitted to A&A, August 2013
Recommended for publication after minor revision

Astronomy & Astrophysics ESO 2013
September 4, 2013

Pulsation analysis and its impact on the primary transit modeling in WASP-33

C. von Essen[1], S. Czesla[1], U. Wolter[1], M. Breger[2,6], E. Herrero[3], M. Mallonn[4], I. Ribas[3], K. G. Strassmeier[4] and J. C. Morales[3,5]

[1]Hamburger Sternwarte, University of Hamburg, Gojenbergsweg 112, 21029 Hamburg, Germany
[2]Department of Astronomy, University of Texas, Austin, TX 78712, USA
[3]Institut de Ciències de lEspai (CSIC-IEEC), Campus UAB, Facultat de Ciències, Torre C5 parell, 2a pl, 08193 Bellaterra, Spain
[4]Leibniz-Institut für Astrophysik Potsdam, An der Sternwarte 16, 14482, Potsdam, Germany
[5]Dept. dAstronomia i Meteorologia, Institut de Ciències del Cosmos (ICC), Universitat de Barcelona (IEEC-UB), Martí Franquès 1, E08028 Barcelona, Spain
[6]Institut für Astronphysik der Universität Wien, Türkenschanzstr. 17, A1180, Wien, Austria
e-mail: `cessen@hs.uni-hamburg.de`

Received ; accepted

ABSTRACT

Aims. To date, WASP-33 is the only δ Scuti star known to be orbited by a hot Jupiter. The pronounced stellar pulsations, showing periods comparable to the primary transit duration, interfere with the transit modeling. Therefore, our main goal is to study the pulsation spectrum of the host star to re-determine the orbital parameters of the system by means of pulsation-cleaned primary transit light curves.
Methods. Between August 2010 and October 2012 we obtained 457 hours of photometry of WASP-33, using telescopes located mostly in Spain and in Germany. Our observations comprise the wavelength range between the blue and the red, and provide full phase coverage of the planetary orbit. After a careful detrend, we focus our pulsation studies in the high frequency regime, where the pulsations that mostly deform the primary transit exist.
Results. The data allow us to identify, for the first time in the system, eight significant pulsation frequencies. The pulsations are likely associated with low-order p-modes. Further, we find that pulsation phases evolve in time. We use our knowledge of the pulsations to clean the primary transit light-curves and carry out an improved transit modeling. We find that taking into account the pulsations in the modeling has little influence in the derived orbital parameters. However, the uncertainties in the best-fit parameters are significantly reduced in comparison to the ones reported by other authors. Additionally, we find indications for a possible dependence between wavelength and transit depth, but only with marginal significance. A clear pulsation solution, in combination with an accurate orbital period, allows us to extend our studies and search for star-planet interactions (SPI). Although we find no conclusive evidence of SPI, we believe that the pulsation nature of the host star and the proximity between members, makes WASP-33 a promising system for further SPI studies.

Key words. stars: planetary systems – stars: individual: WASP-33 – methods: observational

1. Introduction

Among the extensive classification of variable stars that we can count with nowadays, the δ Scutis have been among us for more than hundred years. The first observation of a δ Scuti star was obtained in 1900 (Campbell & Wright 1900). However, it was not until 1956 that Eggen (1956) pointed out the need to define the δ Scuti classification. With time, and the increase of photometric precision, this particular class started to be populated. Nowadays, the Kepler telescope alone provides highly precise light-curves of several hundred of δ Scuti stars (e.g., Uytterhoeven et al. 2011).

In the Hertzsprung-Russell diagram, the δ Scuti stars are located in an instability strip covering spectral types between A and F (Baglin et al. 1973; Breger & Stockenhuber 1983). Most δ Scuti stars belong to Population I (Breger 1979) with typical masses of 2 $M_\odot$ (Milligan & Carson 1992). Due to both radial and non-radial pulsations, δ Scuti stars show brightness variations from milli-magnitudes up to almost one magnitude in blue bands. In δ Scuti stars, pulsations are driven by opacity variations. There are two distinct types of pulsation modes that might occur (e.g., Breger et al. 2012): short-period p-modes (pressure modes, for which pressure serves as the restoring force), and long-period g-modes (gravity modes, with buoyancy as restoring force). A typical δ Scuti pulsation spectrum shows dozens of periods (Breger et al. 1999a,b), with cycle durations ranging from a couple of hours to the minute regime.

WASP-33 (HD 15082) is a bright ($V \sim 8.3$), rapidly rotating ($v \sin(i) \sim 90$ km/s) [1] δ Scuti star; in fact, it is both the hottest and only δ Scuti star known to date to host a hot Jupiter (Christian et al. 2006). The planet, WASP-33b, has been detected through its transits in the frame of the WASP campaign (Pollacco et al. 2006). It circles its host star every 1.22 d in a retrograde orbit. With a brightness temperature of 3620 K, WASP-33b is the hottest exoplanet known to date (Smith et al. 2011). Showing an unusually large radius, WASP-33b belongs to the class of anomalously inflated exoplanets (Collier Cameron et al. 2010). For its mass and, hence,

Send offprint requests to: cessen@hs.uni-hamburg.de

[1] i corresponds to the inclination of the stellar rotation axis.

density, only an upper limit of $M\sin(i) < 4.59\ M_J$ [2] has been determined.

The host star, WASP-33A, shows pronounced pulsations with periods on the order of one hour. Collier Cameron et al. (2010) note that the presence of these pulsations offers "the intriguing possibility that tides raised by the close-in planet may excite or amplify the pulsations in such stars". The discovery of WASP-33's pulsations within photometric data have first been reported by Herrero et al. (2011), who suggest a possible commensurability between a pulsation period and the planetary orbital period with a factor of 26, indicative of star-planet-interaction.

We study the pulsations and primary transits using a total of 56 light curves of WASP-33, observed during two years and providing complete orbital phase coverage.

2. Observations and Data Reduction

Between Aug. 2010 and Oct. 2012, we obtained 457 hours of photometry of WASP-33 distributed across 56 nights using six telescopes: one in Germany and five in Spain. Figure 1 shows the temporal coverage provided by the individual telescopes; the details of the observations are given in Tables 1 and 2 and the technical characteristics of the telescopes are summarized in Table 3.

Throughout the analysis, the barycentric dynamical time system is used (BJD_{TDB}). Conversions between different time reference systems have been carried out using the web-tool made available by Eastman et al. (2010)[3].

WASP-33 is located in a sparse stellar field. Therefore, the defocusing technique did not produce any undesired effect, such as overlapping of the stellar point spread functions. However, either after defocusing or considering the natural seeing of the sites, the optical companion identified by Moya et al. (2011) is contained, in most of the cases, inside the selected aperture radius. A discussion on third light contribution will be addressed in Section 4.

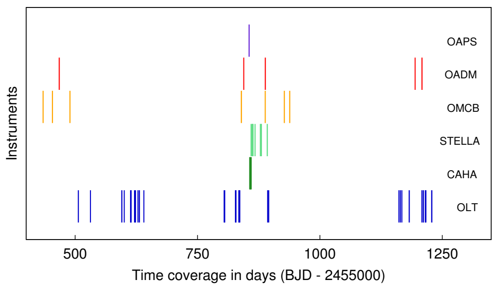

Fig. 1: Sampling of our observations.

Table 1: Overview of observation nights for OLT and STELLA.

Date	Duration (h)	F[a]	NoP[b]	Airmass
	OLT			
2010 November 6	5.9	R	803	1.0→1.2
2010 December 1	1.4	B	60	1.5→2.1
2011 February 3	5.2	R	869	1.0→1.4
2011 February 8	4.0	R	89	1.0→1.2
2011 February 21	5.9	R	1277	1.0→2.3
2011 February 22	5.3	R	769	1.0→2.3
2011 March 1	4.0	B	83	1.0→1.6
2011 March 3	3.6	B	176	1.0→1.6
2011 March 8	2.5	B	186	1.2→2.3
2011 March 11	4.6	B	296	1.1→2.4
2011 March 20	3.3	B	277	1.2→2.1
2011 August 31	5.5	B	541	1.0→2.4
2011 September 1st	5.2	B	906	1.0→2.5
2011 September 23	4.1	B	632	1.0→2.9
2011 September 24	4.3	B	632	1.0→1.2
2011 September 30	5.8	B	754	1.1→2.0
2011 October 1	3.2	B	443	1.4→3.1
2011 October 2	3.5	B	439	1.5→2.2
2011 November 28	7.1	B	650	1.0→1.4
2011 November 30	7.6	B	1174	1.0→2.4
2012 August 23	5.2	B	545	1.0→2.3
2012 August 25	6.5	B	242	1.0→1.8
2012 August 28	3.9	B	243	1.3→2.8
2012 September 12	7.3	B	621	1.0→2.1
2012 October 8	6.6	B	758	1.0→2.4
2012 October 11	8.6	B	1160	1.0→2.0
2012 October 15	2.9	B	241	1.3→2.1
2012 October 16	4.9	B	667	1.0→1.5
2012 October 28	11.8	B	736	1.0→2.6
	STELLA			
2011 October 25	11	v	78	1.0→2.9
	11	b	81	
2011 October 27	10.4	v	301	1.0→2.6
	10.4	b	144	
2011 October 28	10.1	v	322	1.0→2.5
	10.1	b	318	
2011 October 29	6.7	v	254	1.0→2.6
	5.4	b	194	
2011 November 2	8.5	v	326	1.0→2.2
	8.5	b	320	
2011 November 13	4.4	v	123	1.0→1.9
	4.4	b	116	
2011 November 14	10.4	v	357	1.0→2.7
	10.4	b	358	
2011 November 15	6.4	v	236	1.0→1.8
	4.7	b	203	
2011 November 26	4.8	v	175	1.0→1.5
	4.8	b	187	
2011 November 27	8.6	v	311	1.0→1.7
	8.6	b	313	

Notes. [a] Filter (F), [b] Number of photometric data points (NoP)

2.1. Hamburger Sternwarte

The Oscar Lühning Telescope[4] (OLT) is located at the Hamburger Sternwarte, Germany. It is equipped with an Apogee Alta U9000 CCD camera with guiding system.

Between Nov. 2010 and Oct. 2012, we observed WASP-33 for 29 nights using the Johnson-Cousins B and R filters (see Table 1 for details). The exposure time was between 10 to 40 s, mainly depending on the night quality. The airmass ranged from principally 1 to 3, only when photometric nights allowed such observations. The typical seeing at the Hamburger Sternwarte is 2.5-3 arcsec. Therefore, saturation has not been an issue. During a total time of ~ 150 h, we obtained 18 090 photometric data points providing both in- and out-of-transit coverage.

[2] i corresponds to the inclination of the planetary orbit.
[3] http://astroutils.astronomy.ohio-state.edu/time/
[4] http:www.hs.uni-hamburg.de/

Table 2: Overview of observation nights for CAHA, OADM, OMNP, and OMCB.

Date	Duration (h)	F[a]	NoP[b]	Airmass
CAHA				
2011 October 22	4.1	v, b, y	130	1.0→1.9
2011 October 23	3.2	v, b, y, d	178	1.3→2.2
2011 October 24	3.4	v, b, y	157	1.0→1.9
2011 October 25	11.9	v, b, y	462	1.0→2.2
OADM				
2010 September 28	3.7	R	279	1.0→1.3
2011 October 10	3.5	V	344	1.0→1.5
2011 November 23	4	V	320	1.0→1.1
2012 September 24	4.2	V	630	1.0→1.0
2012 October 8	4	V	588	1.0→1.1
OMNP				
2011 October 21	4.6	V	439	1.0→1.5
OMCB				
2010 August 26	6.4	R	162	1.0→2.2
2010 September 14	5.3	R	125	1.0→1.2
2010 October 20	5.6	R	138	1.0→1.7
2011 October 5	7.6	R	195	1.0→1.4
2011 November 23	5.1	R	127	1.0→1.3
2012 January 1	4.5	V	112	1.0→1.2
2012 January 12	5.2	V	130	1.0→1.4

Notes. [a] Filter (F), [b] Number of photometric data points (NoP)

Table 3: Technical telescope data: primary mirror diameter, Ø, field of view (FOV), plate scale, and observatory location.

Name	Ø (m)	FOV[a]	Scale ("/pix)	Location[b]
OLT	1.2	$9' \times 9'$	0.158	G
CAHA	2.2	$18' \times 18'$	0.135	S
STELLA	1.2	$22' \times 22'$	0.322	CI
OADM	0.8	$12' \times 12'$	0.36	S
OMNP	0.4	$21' \times 21'$	1.24	S
OMCB	0.3	$16' \times 11'$	0.62	S

Notes. [a] Full field of views are listed. [b] Germany (G), continental Spain (S), Canary Islands (CI).

Additionally, calibration frames were obtained for each individual night.

For bias subtraction and flat fielding, we used the *ccdproc* package in IRAF, and aperture photometry was carried out using IRAF's *apphot*. To obtain differential photometry, we measured unweighted fluxes in WASP-33 and two reference stars using various aperture radii. The final light curve was produced using the aperture that minimizes the scatter of the differential light curve. It is based on the brighter of the two reference stars, BD+36 488, which is, however, still one magnitude fainter than WASP-33. The remaining reference star was used to obtain control light curves to ensure that the photometry is based on a proper reference.

2.1.1. Calar Alto observatory

The German-Spanish Astronomical Center at Calar Alto (CAHA) is located close to Almería, Spain. It is a collaboration between the Max-Planck-Institut für Astronomie (MPIA) in Heidelberg, Germany, and the Instituto de Astrofísica de Andalucía (CSIC) in Granada, Spain.

We used the BUSCA[5] instrument, mounted at the 2.2 m telescope. BUSCA allows simultaneous measurements in four different spectral bands. To reduce read-out time, we exposed only the half-central part of the CCD. We observed WASP-33 using the Strömgren v, b, and y filters and a filter labeled d, centered at 753 nm with a FWHM of 30 nm. As BUSCA requires simultaneous read-out of all CCDs, we used an exposure time of 4 s, which provides adequate signal-to-noise ratios in the Strömgren bands and avoids saturation of the source. The photometry obtained by means of the d-filter was discarded due to low signal-to-noise. During our observations, the seeing ranged between 1 and 1.5 arcsec. In the visible, the extinction was between 0.15 and 0.2 mag/airmass. Observing for ∼ 23 h, we obtained 927 photometric data points per filter. The data reduction has been carried out as described in Sect. 2.1.

2.2. Observatorio del Teide

STELLA[6] consists of two fully robotic 1.2 m telescopes, one dedicated to photometry and the other to spectroscopy (Strassmeier et al. 2010). The photometer is a wide field imager called WiFSIP. It is equipped with a 4092^2 15-μm pixel back-illuminated CCD.

We observed WASP-33 using STELLA for one month starting at the end of Oct., 2011. STELLA's optical setup offers a field of view of $22' \times 22'$. However, for the purposes of these observations and with the main goal of reducing readout times, we used only a $15' \times 15'$ sub-frame. To obtain quasi-simultaneous multiband photometry, we alternated between the Strömgren v and b filters. In this way, we obtained 2483 photometric measurements with the v and 2234 with the b filter, which equates to ∼75 hours per spectral range. Accounting for read-out time, the typical temporal cadence was of 90 s. The optics had to be defocused to avoid saturation of the target.

We carried out the data reduction using ESO-MIDAS. Bias frames were obtained every night, evening, and morning and combined into a master bias on a daily basis. Twilight flat-field frames for both the Strömgren b and v filters were obtained approximately every 10 d. Bias subtraction and flat-fielding were performed as usual. We carried out aperture photometry using SExtractor's MAG AUTO option. Here, SExtractor computes an elliptical aperture for every detected object in the field, following its light distribution in x and y, and scales the aperture width with the SExtractor parameter k, which we set to 2.6. As a flux calibrator, we used the summed, unweighted flux of three reference stars, viz., BD+36 493, BD+36 487, and BD+36 488. The background, estimated locally for each object, was generally low.

2.3. Primary transit observations

To increase our sample of primary transit light-curves, we used three telescopes with apertures between 0.3 and 0.8 m. To carry out the observations we defocused the telescopes. In the particular case of bright sources such as WASP-33, long exposures after defocusing can reduce scintillation noise and flat-fielding errors (e.g., Southworth et al. 2009; Gillon et al. 2009). In this way, we reached milli-magnitude precision in all of the primary transit light curves obtained using small-aperture telescopes.

The Telescopi Joan Oró is a fully robotic telescope located at the Observatori Astronòmic del Montsec[7] (OADM). It is

[5] http://www.caha.es/CAHA/Instruments/BUSCA/intro.html
[6] http://www.aip.de/stella/
[7] http://www.oadm.cat/en/

equipped with an FLI Proline 4240 CCD and standard Johnson-Cousins filters. Observing for five nights distributed over two years, we collected 19.4 h of data at a temporal cadence of ~ 45 sec.

The Observatori Montcabrer[8] (OMCB) is located in Cabrils, Spain. We used its remotely operated 0.3 m telescope, which is equipped with an SBIG ST-8 CCD and standard Johnson-Cousins filters for 7 nights distributed over 1.5 yr. In total, we collected ~ 40 h of data with typical exposure times of ~ 120 s. Although the observatory is located in a light polluted area, a photometric precision of about 1 mmag could be reached.

The Observatori Món Natura Pirineus[9] (OMNP) contributed an 0.4 m telescope equipped with an SBIG STL-1001E CCD. With this telescope we observed one primary transit using the Johnson-Cousins V filter.

The data of all the telescopes were corrected for bias, dark current, and flat-fielded using MaximDL and new calibration images for every night. The light curves were produced using Fotodif[10]. In all cases, the aperture radius has been selected such that the scatter in the out-of-transit sections of each light curve is minimized.

3. WASP-33 as a δ Scuti star

The primary transit light curves of WASP-33 are deformed by the host star's pulsations. This interferes with transit modeling and, therefore, the determination of the orbital and physical parameters of the system. As the removal of an inappropriate primary transit model could introduce a spurious signal in the pulsation spectrum of the star, associated with the planetary orbital period rather than intrinsic stellar variability, we use only off-transit data points to determine WASP-33A's pulsation spectrum.

The pulsation frequency analysis is performed using PERIOD04, a package intended for the statistical analysis of large astronomical data sets containing gaps, with single-frequency and multiple-frequency techniques (Lenz & Breger 2005). The package utilizes both Fourier and multiple-least-squares algorithms, which do not rely on sequential prewhitening or assumptions of white noise.

3.1. Light curve normalization

To avoid variations apart from the periodicity that we want to characterize, the light curves need to be first detrended. Thus, to study the pulsation spectrum in the high-frequency regime, we normalize each individual light curve. In this way, we eliminate the low-frequency signals that might be associated with systematic effects, such as residual fluctuations due to atmospheric extinction, unrelated to intrinsic stellar variations.

Our procedure is the following: first, we bin the light curves using time-bins with a duration of ~1.3 hours, to "hide" the high-frequency pulsations inside them. Second, we calculate the mean value of time and flux in the bins and fit a low-order polynomial to the binned light curves. The degree of the polynomial depends on the number of available data points, and therefore, on the duration of the observing night. Finally, we subtract the fitted polynomial from the unbinned light curve and convert magnitudes into flux. To ensure a proper normalization, we visually inspected the results of our procedure. Figure 2 shows a representative example.

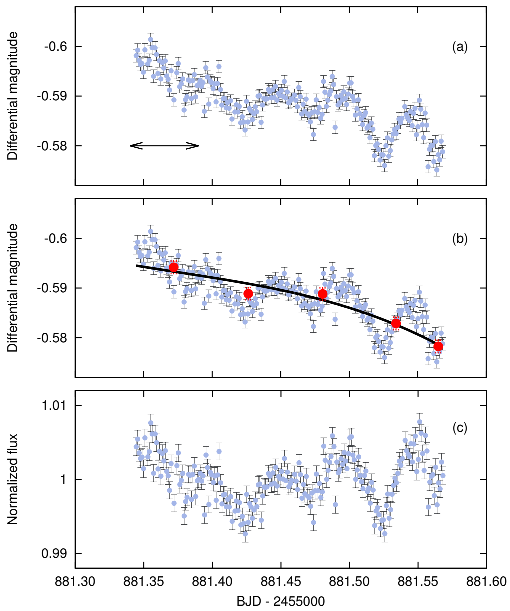

Fig. 2: Our normalization procedure: (a) Differential light curve in magnitudes, obtained using the STELLA telescope and the Strömgren v filter. The length of the arrow indicates the width of the time-bins. (b) Thick red points: the binned time, flux, and photometric error. Continuous black line: third degree polynomial fitted to the binned data points. (c) Normalized light curve in flux units.

3.2. Light curve normalization and its relevance for periodogram analysis

To study the impact of the normalization on the high-frequency domain, we applied an alternative normalization subtracting only the mean value of the light curves. We then compared the periodograms obtained for each data set based on the two normalizations. Figure 3 shows the resulting power spectra for our STELLA data obtained with the Strömgren b-filter as an example. The vertical dashed line in the figure indicates the frequency corresponding to the average length of our observing nights. The difference between the periodograms shows how the normalization process affects the power spectrum. The discrepancy is strongest for frequencies corresponding to periods longer than the average night length. Beyond that limit, the effect of the normalization becomes weak. Figure 3 shows close-ups of the periodograms around $\nu \sim 20$ c/d and $\nu \sim 10$ c/d. While the amplitudes of individual peaks change, the structure of the periodogram and the position of the peaks remain stable.

To verify the stability of the peak positions, we searched both periodograms for strong peaks and compared their frequency.

[8] http://cometas.sytes.net/
[9] http://monnaturapirineus.com/en/content/observatory
[10] http://www.astrosurf.com/orodeno/fotodif/index.htm

To determine the peak positions, we used a Gaussian fit. Based on 66 peak pairs in the > 10 c/d regime, we derive a shift of -0.003 ± 0.0025 c/d. At lower frequencies the uncertainty becomes larger, which is in agreement with the behavior observed in Figure 3. Thus, we conclude that the normalization does not seriously impede the analysis in the high-frequency regime.

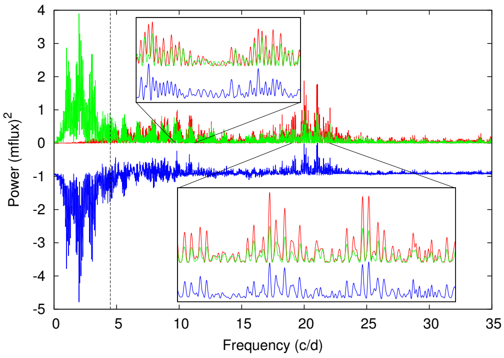

Fig. 3: Periodogram for STELLA *b* data for the polynomial normalization in red, the alternative normalization with a constant in green, and their difference in blue (arbitrarily shifted). The vertical dashed line indicates the mean duration of the observing nights.

3.3. Determination of WASP-33's frequency spectrum

Our frequency analysis is based on the STELLA, CAHA, and OLT data. The latter provide a total temporal coverage of approximately two years, essentially concentrated, however, in three observing seasons. Each OLT season was considered separately in our frequency search. We were left with five data sets obtained in four different spectral filters. Although the photometric amplitudes of δ Scuti stars depend on wavelength, it is possible to combine multi-filter data to determine the frequencies via Fourier methods. Consequently, we combine the data obtained with the v, B, and b filters, for which we found the difference in amplitude values to be statistically insignificant.

We identified the frequencies of the dominating pulsations by analyzing the combined data set, which provides the cleanest spectral window and the highest precision in the determined frequencies.

To estimate the signal-to-noise level of a given pulsation with amplitude A_o, we computed the average amplitude, σ_{res}, over a frequency interval with a width of 2 c/d from a periodogram obtained from the final residuals (see Fig. 4), and estimated the amplitude signal-to-noise ratio (ASNR) of each pulsation as A_o/σ_{res}. Following Breger et al. (1993), we consider a pulsation to be significant when the estimated ASNR of the periodogram peak is larger than 4.

The residual power spectrum indicates strong departures from white noise arising from a potentially highly complex pulsation spectrum and/or aliasing problems. Nonetheless, all remaining peaks remain below our significance curve.

Since we have made annual solutions, the phase and amplitude shifts from year to year have been taken care of. However, if small and systematic changes occur from year to year, there will exist smaller changes within each observing season. Such changes are not taken care by PERIOD04, and will lead to close side-lobes in the periodogram. However, since the solution presented in this work does not contain very close frequencies, these side-lobes will not affect the solution.

Strong aliasing represents an unavoidable difficulty, leading to 1 c/d ambiguities and a large number of strong peaks at the 30% level (relative to the main peak). This aliasing, combined with a large number of frequencies, sets the limits of our multi-frequency analysis. To minimize the effect of aliasing and the window function on our frequency selection, we checked that the significant peaks are present in all subsamples, where we, however, tolerated lower ASNR levels. As the subsamples comprise only a fraction of the data, the frequencies cannot be determined with the same accuracy as in the combined sample. We obtained estimates of the frequency and the uncertainty (see Sect. 3.4) from the subsamples and verified that the results are consistent with the values obtained using the combined data set. Only if this was the case, we, finally, accepted a frequency. One frequency near 7.3 c/d, detected in the combined data set, could not be found in all individual data sets and is, consequently, not included in our analysis.

Altogether, eight frequencies were extracted from the data. Table 4 shows the frequencies, amplitudes, phases, and the associated ASNRs. Additionally, we provide the mean frequency and error obtained from the subsamples. Figure 5 shows our pulsation model, plotted over some of the available off-transit light curves. The displayed pulsation model is obtained after fitting the phases to each individual night only. A clear motivation to this procedure will be given in Section 3.5.

3.3.1. Analysis of fit quality

To quantify the improvement in the description provided by our pulsation model, we calculate the resulting χ^2 values for the pulsation model and a constant, $\chi^2_{\mathbb{C}}$ and χ^2_{mod}, and carry out an F-test. In particular, we calculate the F-statistics using

$$F = \frac{(\chi^2_{mod} - \chi^2_{\mathbb{C}})/(\nu_{mod} - \nu_{\mathbb{C}})}{\chi^2_{\mathbb{C}}/\nu_{\mathbb{C}}}\,, \qquad (1)$$

where ν corresponds to the degrees of freedom; $\nu_{mod} = 14701$ and $\nu_{\mathbb{C}} = 14725$. Formally, we obtain a p-value of $1{\times}10^{-16}$, indicating that the pulsation model accounts for a substantial fraction of the light curve variations.

Although our model reproduces the overall stellar pulsation pattern, the bottom panels of Fig. 5 show flux residuals that do not behave as random-uncorrelated noise. Such residuals may be produced by non-sinusoidal pulsations, low-amplitude pulsations not accounted for in the model, or local changes in the atmospheric conditions, not entirely removed by the differential photometry. At any rate, the remaining scatter in the data defines the limiting accuracy achievable in cleaning the primary transits.

3.4. Error treatment

Preliminary error estimates for the frequencies listed in the second column of Table 4 were obtained in two ways. First, we followed the analytical expressions of Breger et al. (1999a). Second, we fitted a Gaussian function to the peaks and used the standard deviation as our error estimate. To be conservative, we used the larger of these as frequency-error estimate. As the residuals show correlated noise, the true uncertainties in our frequen-

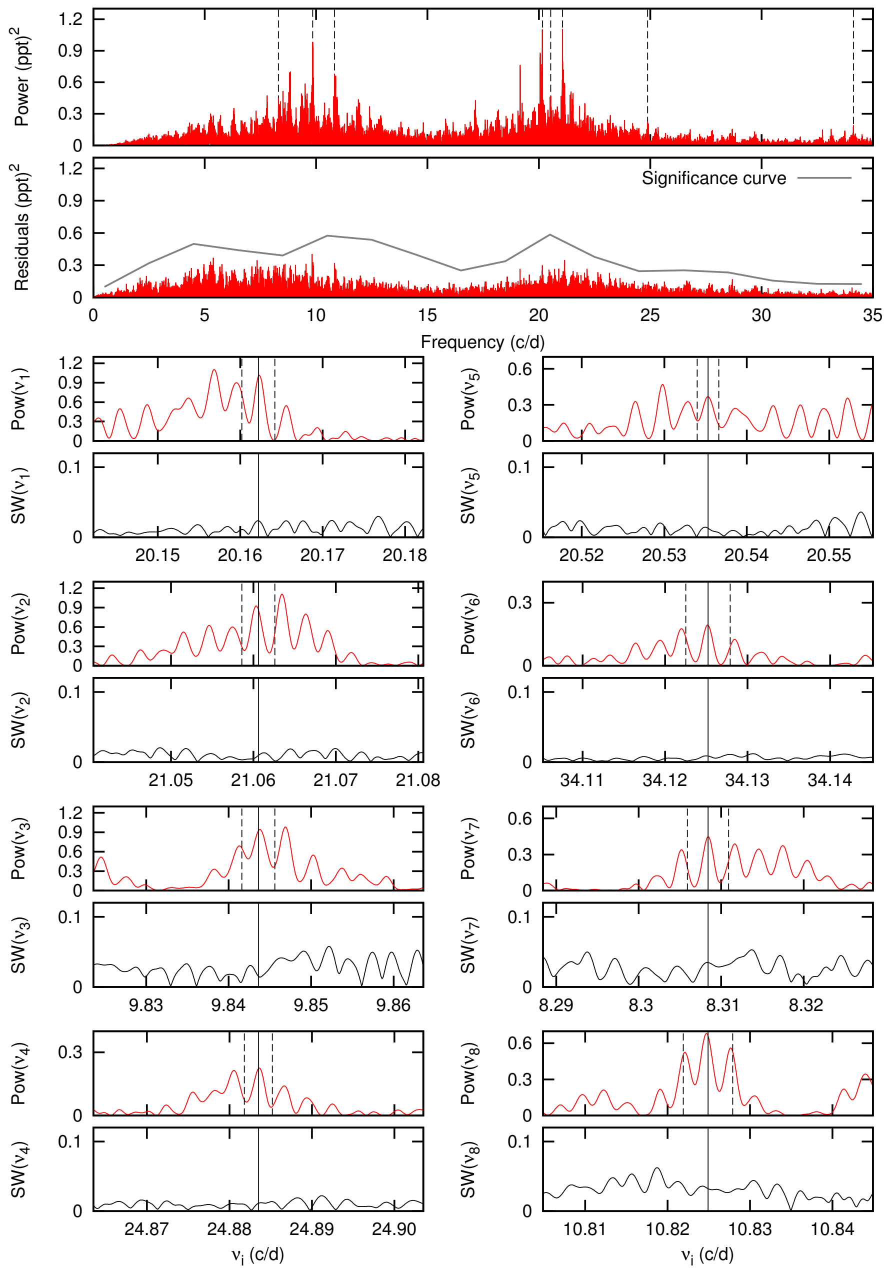

Fig. 4: Top panels: Periodogram of the combined data set and the final residuals in part-per-thousand (ppt). The solid line indicates the significance curve. Bottom panels: A closer look at the periodogram around the detected frequencies and the spectral window, SW. Dashed vertical lines around the peaks indicate our error estimates as listed in Table 4.

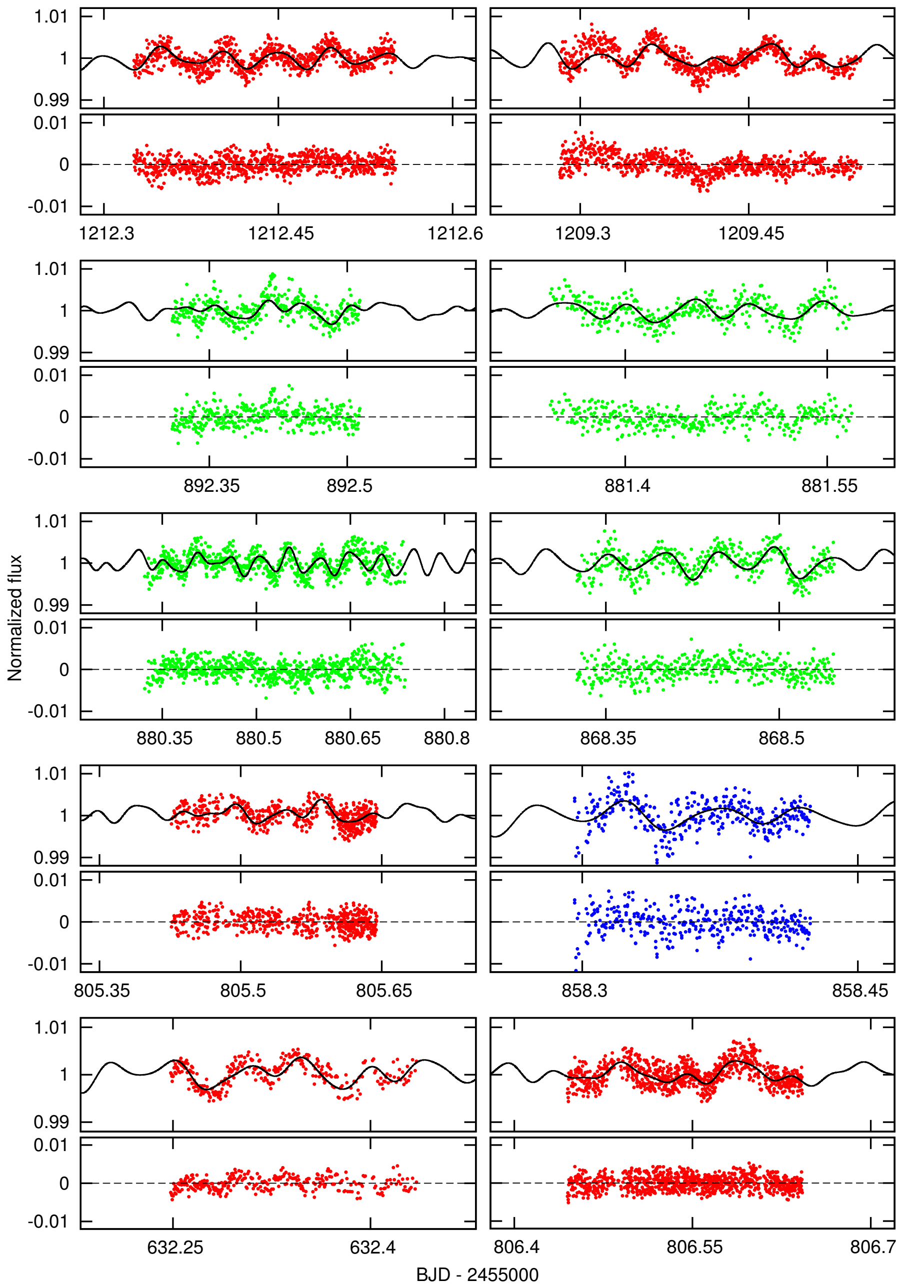

Fig. 5: Exemplary off-transit light curves color-coded in red for OLT, green for STELLA and blue for CAHA, overplotted with the pulsation model in black continuous line. Top panels: normalized flux. Bottom panels: residuals after the pulsation model has been subtracted.

Table 4: Parameters of the pulsations with 1-σ errors. FR: frequency ratios of the pulsations and the orbit (see Sect. 5.3).

	Combined data				Subsample analysis	FR
PN	$\nu \pm \sigma_\nu$ (c/d)	$A \pm \sigma_A$ (10^{-3})	$\phi \pm \sigma_\phi$ (2π)	ASNR	$\nu \pm \sigma_\nu$ (c/d)	
$Puls_1$	20.16214 ± 0.00063	0.95 ± 0.03	0.5718 ± 0.0049	7.8	20.1621 ± 0.0023	24.595
$Puls_2$	21.06057 ± 0.00058	0.93 ± 0.03	0.3594 ± 0.0050	7.6	21.0606 ± 0.0023	25.691
$Puls_3$	9.84361 ± 0.00066	0.79 ± 0.03	0.4804 ± 0.0058	6.3	9.8436 ± 0.0023	12.008
$Puls_4$	24.88351 ± 0.00056	0.42 ± 0.03	0.3009 ± 0.0110	4.3	24.8835 ± 0.0017	30.355
$Puls_5$	20.53534 ± 0.00057	0.71 ± 0.03	0.5207 ± 0.0065	5.9	20.5353 ± 0.0013	25.050
$Puls_6$	34.12521 ± 0.00054	0.49 ± 0.03	0.5738 ± 0.0096	8.0	34.1252 ± 0.0027	41.628
$Puls_7$	8.30842 ± 0.00054	0.63 ± 0.03	0.5173 ± 0.0074	4.2	8.3084 ± 0.0025	10.135
$Puls_8$	10.82492 ± 0.00058	0.64 ± 0.03	0.9969 ± 0.0072	5.8	10.8249 ± 0.0030	13.205

cies could be considerably larger. A deeper discussion of errors is given below.

3.4.1. Correlated noise and unevenly spaced data for periodogram analysis

Montgomery & O'Donoghue (1999) present analytical results of the effect that random, uncorrelated noise has on a least-squares fit of a sinusoidal, evenly-sampled signal. They provide the following expressions for the uncertainties:

$$\sigma_\nu = \frac{\sqrt{6}\,\sigma_N}{\pi\sqrt{N}AT} \tag{2}$$

$$\sigma_A = \sqrt{\frac{2}{N}}\sigma_N \tag{3}$$

$$\sigma_\phi = \frac{\sigma_N}{\pi\sqrt{2N}A}\ , \tag{4}$$

where σ_ν, σ_A, and σ_ϕ are the standard deviations for a sinusoidal signal with frequency ν, amplitude A, and phase ϕ. The remaining parameters are N for the total number of data points, T for the total duration of the observing campaign, and σ_N for the average measurement error of the data points. If the time-series are unevenly sampled and show correlated noise, as is often the case, for instance, due to atmospheric extinction, Montgomery & O'Donoghue (1999) suggest to estimate errors according to

$$\sigma^2(\omega) = \sigma_o^2(\omega)\cdot A(\omega, D) \tag{5}$$

$$A(\omega, D) = D\frac{\sqrt{\pi}}{2}e^{-(\frac{D\Delta t\omega}{4})^2}\ , \tag{6}$$

where σ_o^2 is the variance of the parameter for uncorrelated data sets, given by Eqs. 2, 3, and 4. Further, Δt is the mean exposure time of the data set, D is an estimate of the number of consecutive correlated data points, and $\omega = 2\pi\nu$ is the angular frequency of the pulsation.

An upper limit for the error can be obtained by maximizing Eq. 6. This occurs when the correlation time is on the order of the signal period. In this case, we obtain $A = A_{max} \sim 0.24P/\Delta t$. Table 5 shows the upper-limit uncertainty estimates for our pulsation model parameters, obtained by means of Eq. 5. Here, we used the last column of Table 4 as an estimate for the "uncorrelated" errors. The estimated upper error limits remain satisfactory to characterize the pulsations photometrically.

Table 5: Upper limits for the errors of the pulsation-associated parameters.

	$<\sigma_\nu>$	$<\sigma_A>$	$<\sigma_\phi>$
$Puls_1$	0.009	0.18	0.031
$Puls_2$	0.008	0.18	0.031
$Puls_3$	0.021	0.38	0.078
$Puls_4$	0.007	0.15	0.058
$Puls_5$	0.008	0.18	0.041
$Puls_6$	0.004	0.11	0.036
$Puls_7$	0.020	0.49	0.116
$Puls_8$	0.016	0.35	0.087

3.4.2. Photometric errors

The photometric reduction tasks used in this work neglect systematic effects and provide statistical measurement errors, which are rather lower limits to the true uncertainties. We study the impact of the measurement errors on our frequencies analysis, based on the OLT, STELLA, and CAHA data (Johnson-Cousins B filter for OLT and Strömgren v for STELLA and CAHA).

In particular, we randomly increase the photometric errors by a factor of up to two and recalculate the position of the leading peaks and their respective ASNR. After having repeated this procedure 10^4 times, we analyzed the resulting statistics of peak positions and ASNR. We find that the observed change in frequency is contained within the previously derived error. The ASNR decreases, but remains higher than ~4 in all cases. Therefore, we conclude that our frequency analysis is robust against a moderate increase of up to 100% in the photometric error.

3.5. *Phase-shift analysis*

Photometry provided by the *Kepler* satellite has widely been used to study the pulsation spectrum and its evolution in δ Scuti stars (e.g., Balona et al. 2012b; Southworth et al. 2011; Balona et al. 2012a; Murphy et al. 2012). Most of the analyzed δ Scuti stars pulsate in several modes. For example, Breger et al. (2012) identify 349 frequencies in the rapidly rotating Sct/Dor star KIC 8054146, for which the authors even find variations in amplitude and phase.

Following the method of Breger (2005) to identify amplitude variations and phase shifts, we divided our off-transit data sets into four sub-sets: from BJD~2455596 to BJD~2455641 (~ 1.5 months), from BJD~2455805 to BJD~2455837 (~ 1 month), from BJD~2455858 to BJD~2455896 (~ 1 month), and from BJD~2456162 to BJD~2456217 (~ 2 months). This particular choice avoids including data gaps due to seasonal effects in the subsamples and, therefore, limits the impact of aliasing. As the amplitude of WASP-33's pulsations is too low to identify am-

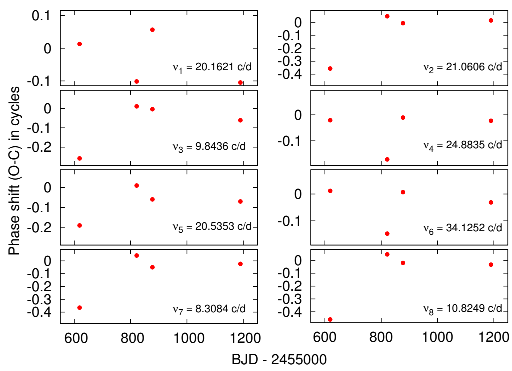

Fig. 6: Temporal phase evolution of the pulsation frequencies.

plitude variations by means of our photometric data, we focus on phase shifts. In particular, we fit the phases in each subsample, fixing the amplitudes and frequencies to the values listed in Table 4. Figure 6 shows our results. Error bars are on the order of ~0.005 and, therefore, rather negligible in the plot.

For all eight detected pulsations, we find a change in phase. There are striking similarities between the O-C diagrams of ν_2, ν_3, ν_5, ν_7, and ν_8, as well as between ν_4 and ν_6. The largest observed gradient is about 2×10^{-3} d^{-1} assuming a linear evolution. Clearly, such shifts must be taken into account in the construction of a pulsation model to clean the transits.

3.6. Mode identification

A particularly interesting question related to the observed frequencies is their association to specific pulsation modes, i.e., the radial order, n, degree, ℓ, and azimuthal number, m, of the underlying spherical harmonic, $Y^m_{n,\ell}$. While the most reliable method for pulsation mode identification is to analyze the line-profile variation using high-resolution spectroscopy (Mathias et al. 1997), our analysis remains limited to photometric data. Nonetheless, we apply three methods of mode identification based on photometry.

3.6.1. Mode identification based on the pulsation constant Q

The pulsation constant, Q, takes unique value for any given pulsation frequency and can be used for mode identification (Breger & Bregman 1975). It is defined by $Q = P\sqrt{\bar{\rho}/\bar{\rho_\odot}}$ with P being the pulsation period and $\bar{\rho}$ and $\bar{\rho_\odot}$ the mean densities of the star and the Sun. Two important Q-values are 0.033 d and 0.026 d – they correspond to the fundamental and first radial overtone expected in δ Scuti stars. Expressing the densities as a function of the radius and eliminating the radius via the luminosity, the expression for Q can be recast (Breger 1990):

$$\log\left(\frac{Q}{P}\right) = 0.5\log(g) + 0.1\ M_{bol} + \log(T_{eff}) - 6.456\ . \quad (7)$$

Taking into account the uncertainties in the stellar parameters, Breger (1990) estimate the uncertainty in the Q-value to be 18%. For WASP-33A, we adopted $\log(g) = 4.3 \pm 0.2$, d = 116 ± 16 pc, and $T_{eff} = 7430 \pm 100$ K (Collier Cameron et al. 2010). We derived the absolute bolometric brightness $M_{bol} = 2.85 \pm 0.07$ using the expression $M_{bol} = 42.36 - 5\log(R/R_\odot) - 10\log(T_{eff})$ (Allen 1973). For the eight pulsation frequencies in our pulsation model, we derive the Q-values listed in Table 6; errors have been estimated by error propagation.

Table 6: Q-values and errors for the eight frequencies found in our data.

ν (c/d)	Q (d)
ν_1 = 20.1621 ± 0.0023	Q_1 = 0.035 ± 0.008
ν_2 = 21.0606 ± 0.0023	Q_2 = 0.033 ± 0.007
ν_3 = 9.8436 ± 0.0023	Q_3 = 0.071 ± 0.016
ν_4 = 24.8835 ± 0.0017	Q_4 = 0.028 ± 0.006
ν_5 = 20.5353 ± 0.0013	Q_5 = 0.034 ± 0.007
ν_6 = 34.1252 ± 0.0027	Q_6 = 0.021 ± 0.005
ν_7 = 8.3084 ± 0.0025	Q_7 = 0.085 ± 0.019
ν_8 = 10.8249 ± 0.0030	Q_8 = 0.065 ± 0.015

Comparing the Q-values to the ones expected in δ Scuti stars (Breger 1998, and references therein), we find that ν_1, ν_2, ν_4, ν_5, and ν_6 are within the range of radial oscillations. Any further mode identification is not possible via Q-values.

To illustrate the difficulty of assigning modes accurately only by means of the pulsation constant, Q, we compare our most accurate Q_6 value with the ones theoretically predicted by Fitch (1981). The model that best matches the WASP-33A parameters is labeled "1.5M21". Within errors, the following modes correspond to Q_6: first, second, and third harmonic (Table 2A, radial modes); p_2 and p_3 (Table 2B, $\ell = 1$ modes); p_1, p_2, and p_3 (Table 2C, $\ell = 2$ modes); and p_1, p_2, and p_3 (Table 2D, $\ell = 3$ modes). Therefore, the only conclusive result is that Q_6 corresponds to a p-mode, which is expected for a high-frequency pulsation.

3.6.2. The empirical period-luminosity-color relation

Empirical period-luminosity-color (P-L-C) relations have been studied, e.g., by Petersen & Hog (1998), López de Coca et al. (1990), and King (1991), among many others.

Stellingwerf (1979) derive a theoretical P-L-C relation

$$\log P = -0.29 M_{bol} - 3.23\log(T_{eff}) + \mathbb{C}\ , \quad (8)$$

where P is the period in days and $\mathbb{C}$ is a constant equal to 11.96, 11.85, and 11.76 for the fundamental and first and second harmonics. Substituting our values for M_{bol} and T_{eff}, yields $\nu_{0,S}$ = 23.43 c/d, $\nu_{1,S}$ = 30.18 c/d, and $\nu_{2,S}$ = 37.13 c/d, i.e., periods that have not been identified within our data.

In an observational study, Gupta (1978) finds that a separate P-L-C relation for each pulsation mode provides a better agreement with the observations than a general one. The author derived the following empirical P-L-C relations for the fundamental mode, F (Eq. 9), and the first, $H1$ (Eq. 10), and second harmonic, $H2$ (Eq. 11):

$$M_{bol\pm0.20} = -2.83\log(P_o) - 11.07\log(T_{eff}) + 41.61 \quad (9)$$
$$M_{bol\pm0.14} = -3.57\log(P_1) - 10.21\log(T_{eff}) + 37.13 \quad (10)$$
$$M_{bol\pm0.24} = -2.45\log(P_2) - 10.22\log(T_{eff}) + 38.35\ . \quad (11)$$

These relations predicts $\nu_{0,G}$ = 27.91 c/d, $\nu_{1,G}$ = 29.41 c/d, and $\nu_{2,G}$ = 45.47 c/d, again not observed within our data. At least for WASP-33A's stellar parameters, the theoretical and observational relation seem to be mutually inconsistent.

3.6.3. Multi-color photometry

In δ Scuti stars, the photometric amplitude and phase of pulsations depend on the spectral band. The amplitude and phase of a given pulsation are determined by the local effective temperature and cross-section changes, which is defined by the pulsation mode. Therefore, different modes lead to distinguishable modulations in flux. This allows to carry out mode identification by means of multi-color photometry (Balona & Evers 1999; Daszyńska-Daszkiewicz et al. 2003; Dupret et al. 2003).

FAMIAS (Frequency Analysis and Mode Identification for AsteroSeismology) is a collection of software tools for the analysis of photometric and spectroscopic time series data (Zima 2008). The photometry module uses the method of amplitude ratios and phase differences in different photometric passbands to identify the modes (Balona & Stobie 1979; Watson 1988). The determination of the l-degrees is based on static plane-parallel models of stellar atmospheres and on linear non-adiabatic computations of stellar pulsations. To compute the theoretical photometric amplitudes and phases, FAMIAS applies the approach proposed by Daszyńska-Daszkiewicz et al. (2002).

FAMIAS requires the stellar parameters effective temperature, T_{eff}, surface gravity, $\log g$, and metallicity, [Fe/H], which we obtained from Collier Cameron et al. (2010). As additional input to FAMIAS, we obtained the pulsation frequency, the amplitude, and the phase for the Strömgren v and b bands using our STELLA and CAHA data; amplitude ratios and phase differences were obtained using PERIOD04. Figure 7 shows our results for the case of ν_2, ν_4, and ν_5. The pulsations seem to correspond to lower-order modes: $\ell = 0{,}1$ for ν_5 and ν_4, and $\ell = 2{,}3$ for ν_2. A more detailed characterization of these modes remains impossible in our analysis. For the remaining five frequencies in our model, no reliable information on the associated modes could be derived.

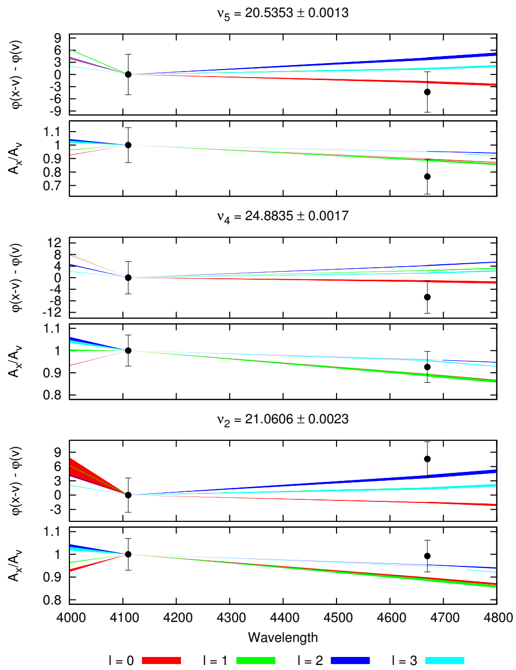

Fig. 7: Amplitude ratios and phase differences in degrees relative to the Strömgren v filter for WASP-33, resulting from the three available nights obtained at Calar Alto. The filled curves indicate the uncertainty of the theoretical prediction due to observational errors in T_{eff} and $log\ g$.

3.6.4. The effect of rotation

Any asteroseismological study of main-sequence δ Scuti stars is not completely fulfilled until stellar rotation is considered (Goupil et al. 2000, and references therein). The effects of rotation over the pulsation spectrum has been theoretically studied (e.g., Deupree 2011; Deupree et al. 2012), as well as observed (e.g., Breger et al. 1999b, 2005a, 2012). The main effect of rotation is the splitting of the non-radial mode frequencies. If such splitting is observed, then the rotation rate of a star can be determined (Christensen-Dalsgaard & Berthomieu 1991).

From a purely geometrical argument, stellar rotation affects the observed frequencies. In an inertial frame, an observer finds that a frequency is split uniformly according to the azimuthal order m:

$$\nu_m = \nu_o + \Omega\, m\ , \qquad (12)$$

where Ω is the angular velocity of the star, ν_o is the frequency of the pulsation in the frame rotating with the star, and m the azimuthal mode. Using this simplified version of mode splitting (see e.g., Cowling & Newing 1949, for the contribution of Coriolis forces to the frequency splitting), we produced the following analysis: from the eight frequencies that conform our pulsation model we assume that one of them, $\nu_{j,m}$, is the product of mode splitting. Therefore, knowing the azimuthal order m associated to $\nu_{j,m}$ and the rotational period of the star, we can determine ν_o. With ν_o, we can further calculate the values of the remaining $\nu_{j,m}$'s for a given ℓ degree ($|m| < \ell$), and compare them with our remaining model frequencies.

Although this approach might sound straight forward, there is no knowledge of the rotational period of WASP-33A. Therefore, we assumed that WASP-33A's $v \sin(i)$ is coincident with the equatorial velocity. Furthermore, our attempt to identify the nature of the observed frequencies did not produce any substantial results. In consequence, for our most accurately identified ν_2 frequency ($\ell = 2{,}3$) we assumed all possible m values and found, through this reasoning, that the remaining observed frequencies were not the product of mode splitting.

Any further study would require, for instance, a complete mode identification and the knowledge of the rotational period of the star. The complexity around mode identification clearly indicates that Q values, P-L-C relations, rough period ratios, and even poor mode identification via multicolor photometry can not be used for mode identification without further evidence.

4. Primary transit analysis

Our data comprise 19 primary transit observations. Table 7 lists, among others, the date and site of observation, the filter, and a code indicating the transit coverage of the observation. To determine the orbital parameters, we focus on the eight primary-transit light-curves providing complete temporal coverage (TC = OIBEO in Table 7).

Moya et al. (2011) report on the detection of an optical companion about ∼ 2" from WASP-33, which could affect our observations through third light contamination. Based on the color information (J_c, H_c, K_c, and FII filters), the authors speculate that it might be a physical companion of WASP-33, for which they estimate an effective temperature of $T_{eff} = 3050 \pm 250$ K. As the third light contribution provided by such an object is $\lesssim 4 \times 10^{-4}$ in all used filters, it can be neglected in our analysis.

Orbiting a fast rotator in a quasi polar orbit (projected spin-orbit misalignment $\lambda \sim 255°$, Collier Cameron et al. (2010)), the transits light-curves may be affected by gravity darkening, which manifests in a latitudinal dependence of the stellar effective temperature (von Zeipel 1924). As the rotational period of WASP-33 is unknown, we estimate it using $v\sin(i) \sim 90$ km s^{-1} and the stellar radius $R_s \sim 1.444\,R_\odot$ (Collier Cameron et al. 2010). Close to the system geometry, we estimate the polar to equatorial temperature ratio. Using a gravity-darkening exponent of $\beta = 0.18$ (Claret 1998), for g the magnitude of the local effective surface gravity, and β the gravity-darkening exponent, following Maeder (2009):

$$T = T_{pole}\frac{g^{\beta}}{g^{\beta}_{pole}}\,, \tag{13}$$

we estimate that the polar temperature of WASP-33 is ≈ 2.2% higher than the equatorial temperature, too small to reproduce the observed transit depth wavelength-dependent variation. Further, using the primary transit code of Barnes (2009), adequate for fast rotators, we determine that the differences in the transit shape observed in the blue and red bands caused by gravity darkening are on the order of 0.06% and, therefore, negligible in our analysis. Therefore, the *occultquad* routine provided by Mandel & Agol (2002) is adequate for our transit modeling.

4.1. Photometric noise

Often, the scatter in the light curve is used as a noise estimate. If, however, correlated noise is present, this method may considerably underestimate the impact of the scatter on the parameter estimates. The effect of correlated noise on transit modeling has been studied by several authors, e.g., Carter & Winn (2009); Pont et al. (2006).

While we have identified the significant pulsations in Sect. 3, our analysis has also shown that there is an unknown number of weak pulsations, we cannot account for in our modeling. The unaccounted pulsations will manifest in time-correlated noise in the transit analysis. Therefore, a treatment of time-correlated noise is important in the transit modeling.

To quantify the amplitude of time-correlated noise in our data, we applied the "time averaging method" proposed by Pont et al. (2006), which is based on the comparison of the variance of binned and unbinned residuals. To obtain the residuals, we normalized the transit light-curves fitting a polynomial to the out-of-transit data and subtracted a preliminary transit model. We verified that the results do only slightly depend on the details of the normalization and transit model.

Subsequently, the residual light curves were divided into M bins of equal duration. Each bin contains N data points. As our data are not always equally spaced, we applied a mean value for the number of data points per bin. In the absence of red noise, the expectation value of the variance of the unbinned residuals, σ_1, is related to the variance of the binned residuals, σ_N, according to (cf., Carter & Winn 2009, Eq. 36)

$$\sigma_N = \sigma_1\sqrt{\frac{M}{N(M-1)}}\,. \tag{14}$$

This may now be compared with a variance estimate, σ'_N, derived from the binned residuals

$$\sigma'_N = \sqrt{\frac{1}{M}\sum_{i=1}^{M}(\overline{\mu}-\mu_i)^2} \quad \text{with} \quad \overline{\mu} = \frac{1}{M}\sum_{j=1}^{M}\mu_j\,. \tag{15}$$

If correlated noise is present, then σ'_N will differ from σ_N by a factor β_N, which estimates the strength of correlated noise. A proper estimator, β, may be found by averaging β_N over a range Δn corresponding to the most relevant timescale. To account for the correlated noise in a conventional white-noise analysis, the individual photometric errors are enlarged by a factor of β. If there is no prior information, this leaves the parameter estimates unaffected and enlarges the errors by a factor β.

In the case of our transit analysis, the relevant timescale is the duration of ingress or egress, which is ∼ 16 minutes for WASP-33. In Table 7 we show the resulting β factors. In a first step, we deliberately ignored our results derived in Sect. 3 and treated the light curves as if we had no knowledge on the pulsations. In the thus derived β_1 values, all pulsations show up as correlated noise. In a second step, we subtracted the pulsation model derived in Sect. 3 and determined the β_2 values. Taking into account the pulsation model always yields a better, i.e., smaller β factor, indicating that a substantial fraction of the time-correlation is accounted for by it.

Table 7: Summary of our primary transit observations and modeling parameters.

F[a]	Date	Obs.	TC[b]	β_1	β_2	D[c]
B	2011 Sept 24	OLT	- IBEO	2.61	2.15	0
	2012 Aug 23	OLT	OIB - -	3.14	2.47	1
	2012 Oct 11	OLT	OIBE -	4.55	4.15	1
	2012 Oct 16	OLT	OIBEO	4.41	3.87	1
V	2011 Oct 10	OADM	- IBE -	3.57	2.61	0
	2011 Oct 21	OAPS	- IBEO	1.97	1.33	0
	2012 Jan 1	RNAV	OIBEO	2.24	2.07	0
	2012 Jan 12	RNAV	OIBEO	1.93	1.42	1
	2012 Sept 24	OADM	- - BEO	4.53	3.84	2
R	2010 Aug 26	RNAV	OIBEO	1.67	1.07	0
	2010 Oct 20	RNAV	OIBEO	1.23	1.15	1
	2010 Nov 6	OLT	OIBEO	3.24	2.85	2
	2011 Oct 5	RNAV	OIBEO	2.05	1.63	0
	2011 Nov 23	RNAV	OIBEO	1.95	1.52	0
v	2011 Oct 22	CAHA	- IBEO	1.41	1.18	0
	2011 Nov 2	STELLA	OIBE -	2.36	1.95	0
b	2011 Oct 22	CAHA	- IBEO	1.49	1.37	0
	2011 Nov 2	STELLA	OIBE -	2.48	2.27	0
y	2011 Oct 22	CAHA	- IBEO	1.52	1.06	0

Notes. [a] The Filter B, V, and R for Johnson-Cousins and v, b, and y for Strömgren filters. [b] The letter code that specifies the transit coverage goes as follows: O for "out of transit before ingress", I for "ingress", B for "bottom", E for "egress", and O for "out of transit, after egress". [c] Degree of the polynomial used for light curve normalization.

4.2. Polynomial order of transit light-curve normalization

In the transit modeling, the normalization of the light curves is crucial. To normalize the transit light-curves, we fit polynomials with an order between zero and four to the out-of-transit data and determine the order, k, that minimizes the Bayesian information criterion, BIC = χ^2 + k ln N.

The order of the resulting optimal polynomial is listed in Table 7. According to our modeling, a constant or linear model is sufficient to normalize the transit in all but two cases, where a quadratic normalization is required. Finally, we visually inspected the resulting light curves to ensure a proper normalization.

4.3. Transit modeling

Collier Cameron et al. (2010) detect the planetary "shadow" of WASP-33b in the line profile of WASP-33A during transit. Their spectroscopic time series analysis reveals that the planet traverses the stellar disk at an inclination angle incompatible with 90°. As the inclination is less affected by parameter correlations in the spectroscopic analysis, we impose a Gaussian prior on the inclination. In particular, we use the value of $i = 87.67 \pm 1.8$ deg obtained by Collier Cameron et al. (2010) in their combined photometric and spectroscopic analysis.

In our analysis, we fixed the linear and quadratic limb-darkening coefficients, u_1 and u_2, to the values listed in Table 8, which we obtained from Claret & Bloemen (2011) considering the stellar parameters $\log(g) = 4.5$, $T_{eff} = 7500$, and $[Fe/H] = 0.1$. Therefore, we are left with the following free parameters: the mid-transit time, T_o, the orbital period, Per, the semi-major axis in stellar radii, a/R_s, the orbital inclination, i, and the planet-to-star radius ratio, $p = R_p/R_s$.

Table 8: Linear (u_1) and quadratic (u_2) limb-darkening coefficients.

Filter	u_1	u_2
J-C B	0.3561	0.3625
J-C V	0.2725	0.3535
J-C R	0.1954	0.3511
Str v	0.3828	0.3678
Str b	0.3612	0.3512
Str y	0.2795	0.3533

To obtain the parameter estimates, their errors, and mutual dependence, we sample from the posterior probability distribution using an MCMC approach. For the parameters a, p, Per, and T_o, we defined uniform priors covering a reasonable range. Errors are given as 68.3% highest probability density (HPD) credibility intervals. To carry out MCMC sampling, we used Python routines of `PyAstronomy`[11], which provide a convenient interface to fit and sample algorithms implemented in the PyMC (Patil et al. 2010) and SciPy (Jones et al. 2001) packages.

In a first attempt to fit the transits, we ignore the pulsations and fit only the transit light-curve. In our approach, all transit light-curves are fitted simultaneously using the model of Mandel & Agol (2002). Note that we also fitted the coefficients of the normalizing polynomial, whose degree remains, however, fixed to that listed in Table 7. Our best-fit solutions, obtained after 5×10^5 iterations, is given in Table 9.

In a second attempt, we combine the primary transit model with the pulsation model with frequencies and amplitudes fixed to the values listed in Table 4. In Sect. 3.5, we demonstrate that there is a temporal evolution in the phases. Therefore, the phases have been considered free parameters in our modeling. However, we did not allow them to take arbitrary values, but restricted the allowed range to the limiting cases derived in Sect. 3.5. For instance, the phase of the first frequency, ν_1, could not deviate by more than 0.1 cycle from the mean value (cf., Fig. 6).

The results are shown in the lower part of Table 9; in Fig. 8 we show the 19 primary transit light-curves and the best-fit model. Interestingly, the parameters derived using this more elaborate approach are consistent with those obtained ignoring the pulsations. Taking into account the pulsation model, does, however, improve the uncertainty in the parameter estimates.

The values derived in our analysis are broadly consistent with those derived previously by Collier Cameron et al. (2010) and Kovács et al. (2013). While we find a slightly smaller semi-major axis than Collier Cameron et al. (2010), the planet-to-star radius ratio and the inclination are compatible. Kovács et al. (2013) find an 8 − 10% larger radius ratio and a slightly lower inclination.

Table 9: Parameters obtained by Collier Cameron et al. (2010) and Kovács et al. (2013), our best-fit result obtained from primary transit modeling, first, without and, second, with taking into account the pulsations.

Parameter	Value
Collier Cameron et al. (2010)	
a (R_s)	3.79 ± 0.02
i (°)	87.67 ± 1.81
p (R_p/R_s)	0.1066 ± 0.0009
Per (days)	1.2198669 $\pm 1.2 \times 10^{-6}$
Kovács et al. (2013)	
a (R_s)	3.69 ± 0.01
i (°)	86.2 ± 0.2
p (R_p/R_s)	0.1143 ± 0.0002
Transit fit ignoring pulsations	
a (R_s)	3.69± 0.04
i (°)	88.17 ± 1.53
p (R_p/R_s)	0.1052 ± 0.0008
Per (days)	1.2198667 $\pm 1.5 \times 10^{-6}$
T_o (BJD_{TDB})	2455507.5225 ± 0.0004
Transit fit accounting for pulsations	
a (R_s)	3.68 ± 0.03
i (°)	87.90 ± 0.93
p (R_p/R_s)	0.1046 ± 0.0006
Per (days)	1.2198675 $\pm 1.1 \times 10^{-6}$
T_o (BJD_{TDB})	2455507.5222 ± 0.0003

4.3.1. Impact of the pulsations on the transit fits

To better understand the effect of the pulsations on the transit fits, we fit the primary transits individually and study the behavior of a, i, and p. One more time, we carry out the fit, first, ignoring the pulsations and, second, taking them into account via our pulsation model. During the fit, the ephemeris were fixed to the corresponding values in Table 9. The outcomes are based on 5×10^5 iterations of the MCMC sampler; they are given in Table 10.

To study the impact of the pulsation model on the individual parameters, we scrutinized the ratio of the derived values. In particular, we focused on the eight complete transits, for which the parameters can be determined most reliably. For the ratios of values determined with pulsations considered in the model

[11] http://www.hs.uni-hamburg.de/DE/Ins/Per/Czesla/PyA/PyA/index.html

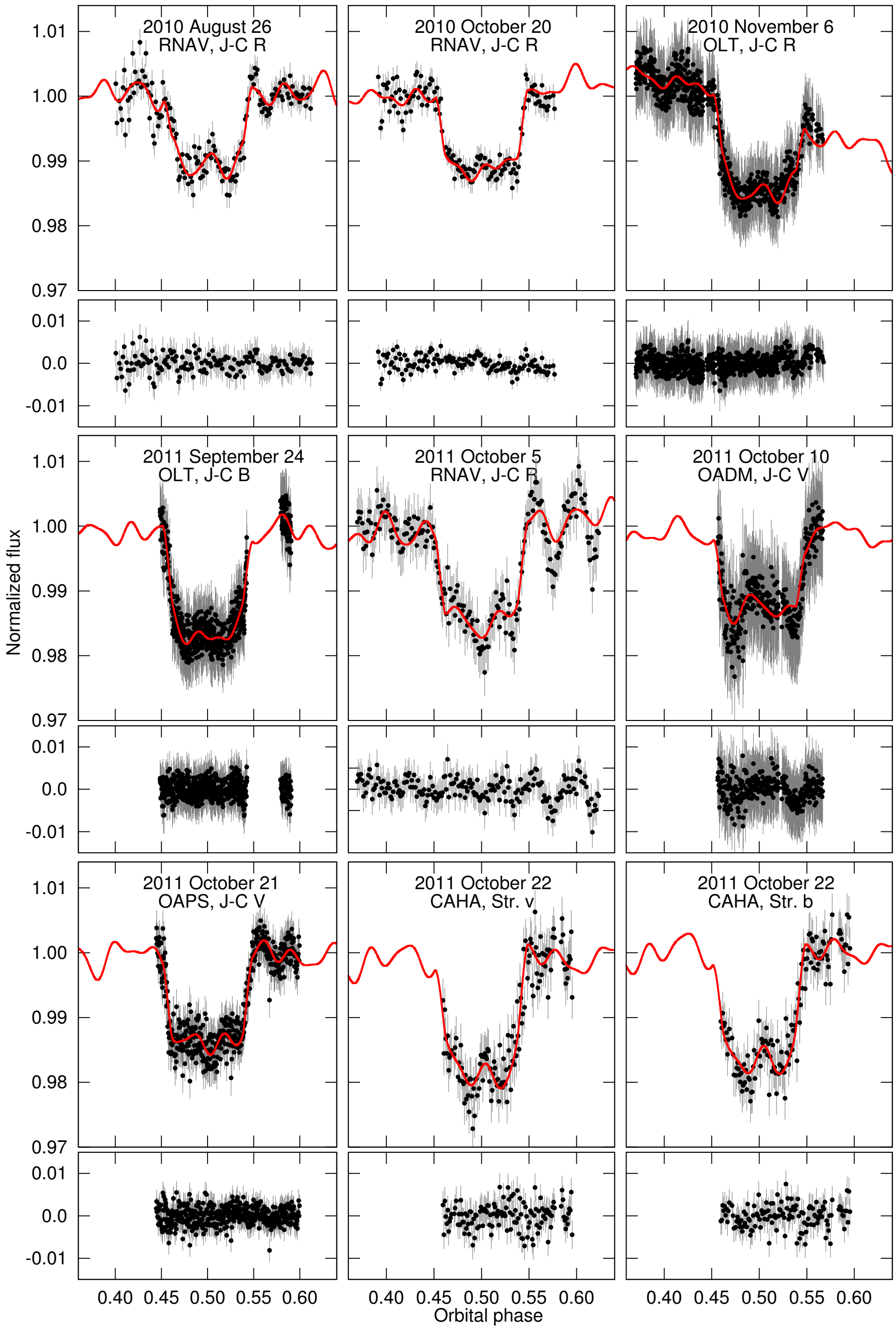

Fig. 8: Top panels: The 19 primary transits in black points along with the photometric error bars accounting for correlated noise cf. Sec. 4.1. Overplotted in continuous red line is the best fitted primary transit model modulated by the host star pulsations and the low-order normalization polynomial. Bottom panels: residuals.

C. von Essen et al.: Pulsations on WASP-33b

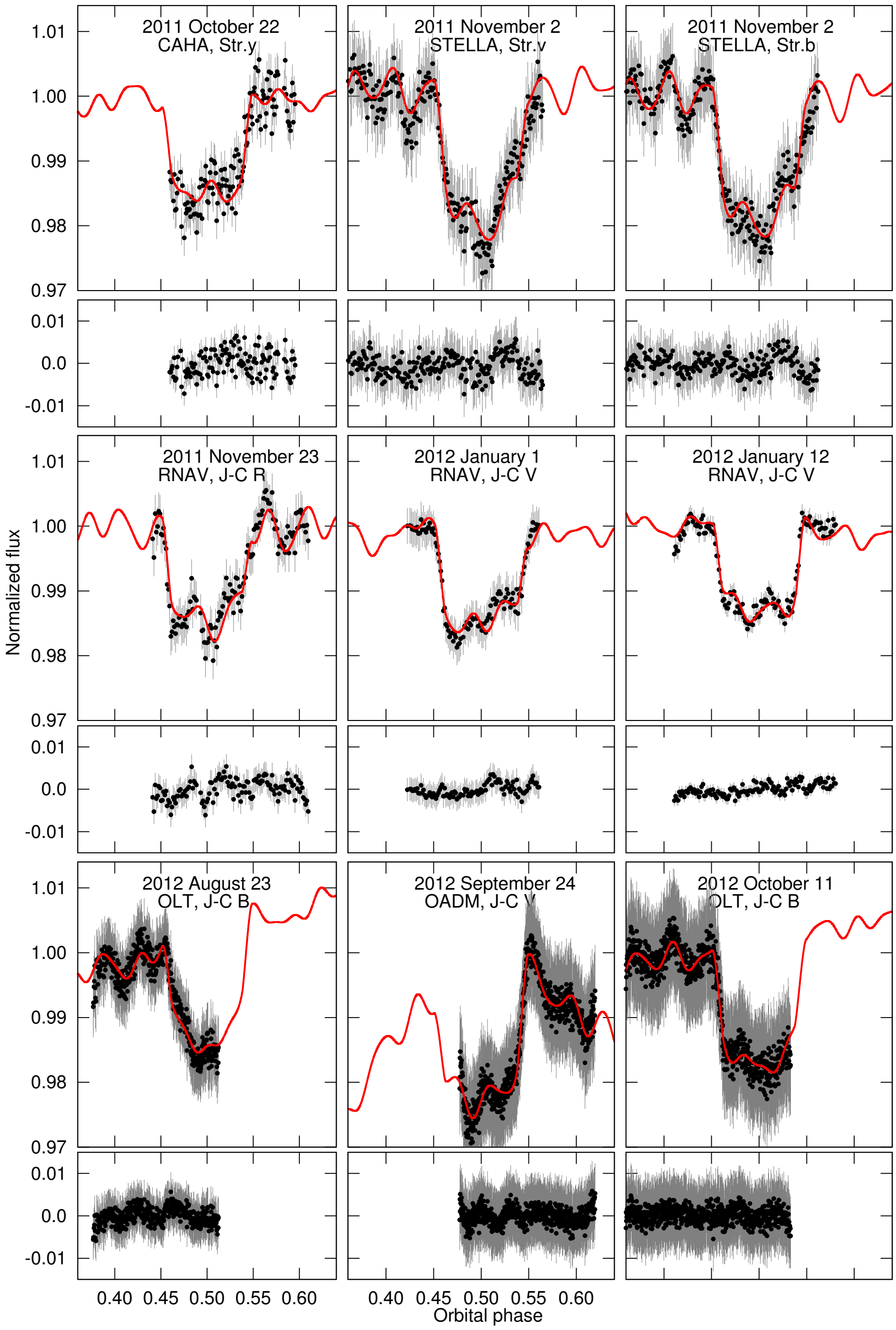

Fig. 8: See Figure 8

C. von Essen et al.: Pulsations on WASP-33b

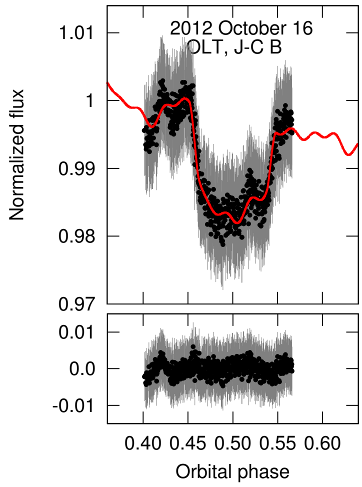

Fig. 8: See Figure 8

Table 10: Results of individual transit fits.

Date	F	a (R_s)	i (°)	p	$\hat{p}$
Pulsations ignored					
2010 Aug. 26	R	3.88 ± 0.12	87.74 ± 1.77	0.0999 ± 0.0026	0.0988 ± 0.0027
2010 Oct. 20	R	3.72 ± 0.06	88.05 ± 1.60	0.1006 ± 0.0016	0.1004 ± 0.0016
2010 Nov. 6	R	3.69 ± 0.08	87.62 ± 1.78	0.1095 ± 0.0019	0.1071 ± 0.0023
2011 Sept. 24	B	3.63 ± 0.06	88.07 ± 1.62	0.1239 ± 0.0021	0.1231 ± 0.0019
2011 Oct. 5	R	3.50 ± 0.10	87.73 ± 1.76	0.1145 ± 0.0033	0.1131 ± 0.0032
2011 Oct. 21	V	3.48 ± 0.06	87.94 ± 1.69	0.1111 ± 0.0018	0.1101 ± 0.0017
2011 Oct. 22	v	3.68 ± 0.10	87.72 ± 1.79	0.1241 ± 0.0028	0.1238 ± 0.0027
2011 Oct. 22	b	3.56 ± 0.10	87.61 ± 1.82	0.1223 ± 0.0026	0.1217 ± 0.0025
2011 Oct. 22	y	3.61 ± 0.11	87.74 ± 1.75	0.1137 ± 0.0033	0.1134 ± 0.0031
2011 Nov. 2	v	3.92 ± 0.17	87.36 ± 1.87	0.1311 ± 0.0032	0.1287 ± 0.0032
2011 Nov. 2	b	3.92 ± 0.21	87.34 ± 1.92	0.1271 ± 0.0035	0.1248 ± 0.0036
2011 Nov. 23	R	3.56 ± 0.09	87.64 ± 1.80	0.1101 ± 0.0030	0.1088 ± 0.0030
2012 Jan. 1st	V	3.43 ± 0.09	87.73 ± 1.77	0.1113 ± 0.0033	0.1093 ± 0.0035
2012 Jan. 12	V	3.70 ± 0.07	87.93 ± 1.69	0.1058 ± 0.0018	0.1061 ± 0.0017
2012 Aug. 23	B	4.21 ± 0.18	86.94 ± 2.07	0.1174 ± 0.0024	0.1093 ± 0.0026
2012 Oct. 11	B	3.48 ± 0.12	87.69 ± 1.79	0.1115 ± 0.0032	0.1131 ± 0.0032
2012 Oct. 16	B	3.63 ± 0.10	87.71 ± 1.76	0.1098 ± 0.0031	0.1097 ± 0.0031
Pulsations taken into account					
2010 Aug. 26	R	3.74 ± 0.07	87.80 ± 1.71	0.1011 ± 0.0015	0.1008 ± 0.0015
2010 Oct. 20	R	3.73 ± 0.06	88.11 ± 1.59	0.1046 ± 0.0014	0.1046 ± 0.0014
2010 Nov. 6	R	3.61 ± 0.07	87.83 ± 1.69	0.1050 ± 0.0016	0.1050 ± 0.0016
2011 Sept. 24	B	3.64 ± 0.06	88.20 ± 1.57	0.1194 ± 0.0024	0.1186 ± 0.0020
2011 Oct. 5	R	3.49 ± 0.09	87.62 ± 1.73	0.1143 ± 0.0024	0.1112 ± 0.0024
2011 Oct. 21	V	3.54 ± 0.06	87.79 ± 1.75	0.1103 ± 0.0013	0.1098 ± 0.0012
2011 Oct. 22	v	3.49 ± 0.13	87.57 ± 1.84	0.1236 ± 0.0008	0.1229 ± 0.0025
2011 Oct. 22	b	3.33 ± 0.10	87.56 ± 1.83	0.1235 ± 0.0024	0.1216 ± 0.0024
2011 Oct. 22	y	3.52 ± 0.13	87.65 ± 1.77	0.1143 ± 0.0023	0.1136 ± 0.0022
2011 Nov. 2	v	3.79 ± 0.17	87.03 ± 1.00	0.1212 ± 0.0016	0.1296 ± 0.0025
2011 Nov. 2	b	3.90 ± 0.25	87.14 ± 1.96	0.1277 ± 0.0034	0.1249 ± 0.0032
2011 Nov. 23	R	3.53 ± 0.08	87.64 ± 1.83	0.1126 ± 0.0023	0.1093 ± 0.0022
2012 Jan. 1st	V	3.54 ± 0.09	87.76 ± 1.75	0.1082 ± 0.0026	0.1077 ± 0.0026
2012 Jan. 12	V	3.73 ± 0.07	87.80 ± 1.69	0.1034 ± 0.0012	0.1031 ± 0.0011
2012 Aug. 23	B	4.00 ± 0.12	87.29 ± 1.87	0.1157 ± 0.0019	0.1135 ± 0.0019
2012 Oct. 11	B	3.27 ± 0.09	87.42 ± 1.85	0.1245 ± 0.0023	0.1256 ± 0.0023
2012 Oct. 16	B	3.64 ± 0.10	87.79 ± 1.71	0.1054 ± 0.0027	0.1075 ± 0.0030

(wp) and neglected pulsations (pn), we obtained a_{wp}/a_{pn} = 1.0 ± 0.02, $i_{wp}/i_{pn} = 1.000 \pm 0.001$, and $p_{wp}/p_{pn} = 0.99 \pm 0.03$. These numbers indicate that, on average, the parameter estimates remain unaffected by taking into account the stellar pulsations. Regarding individual fits, the expected deviation amount to 0.08 R_s in the semi-major axis, 0.1° in the inclination, and 3×10^{-3} in p. Clearly, the relative uncertainty is largest in the semi-major axis and the radius ratio, p. Taking into account also the transits with incomplete observational coverage, we obtain comparable numbers, however, with larger uncertainties.

4.4. Wavelength dependence of the planet-to-star radius ratio

Our data comprise transit observations from the blue to the red filter. To check whether a dependence of the planet-to-star radius ratio on the wavelength can be identified, we fixed all parameters but the radius ratio to the values listed in Table 9 and fitted only the radius ratio, $\hat{p}$, for each individual transit. The resulting $\hat{p}$-values, based on the pulsation-corrected light curves, are listed in the last column of Table 9. We verified that we obtain comparable results, if the pulsations are not considered.

Figure 9 shows $\hat{p}$ as a function of wavelength. The red points mark the transits with full observational coverage, while the black points were derived from transits with incomplete temporal coverage (see Table 7). In the fit, we used the central wavelength of the filters, which are indicated by vertical, dashed lines in the plot. To produce a less crowded figure, the data points are artificially shifted from the central wavelength.

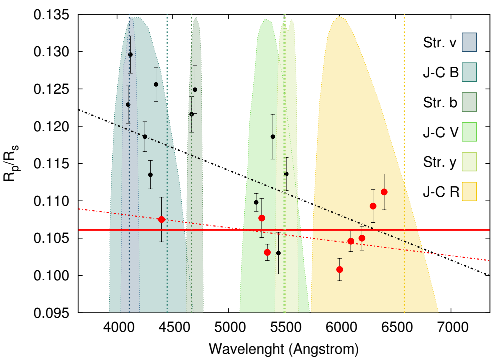

Fig. 9: Planet to star ratio $\hat{p} = R_p/R_s$ obtained from complete light curves (red points) and incomplete ones (black points), when the pulsations have been accounted in the model fitting. Vertical color-dashed lines indicate the central wavelength of each filter. The dashed/dotted black line shows the best-fitting linear model to the 19 Rp/Rs data points. In red and considering complete primary transits only, the dashed/dotted line shows the low-significant wavelength-dependent trend, while the continuous line accounts for the mean radius ratio.

The values for $\hat{p}$, derived from the complete transits, show a wavelength-dependent trend, but only with marginal significance. These values are also consistent with a constant radius ratio of R_P/R_S =0.1061 ± 0.0031, in concordance with the mean value and the standard deviation of the 8 data points. Both the linear and constant models produce comparable χ^2_{red} values of 1.9 and 1.8, respectively. Hence, it is unclear which model best fits the data.

If all transit observations are taken into account, the data indicate a decrease of 0.65%/1000Å in the planet-to-star radius ratio with wavelength. Formally, the correlation coefficient between radius-ratio and wavelengths amounts to $r \sim 0.7$. We caution, however, that the observed trend may be feigned by an inappropriate transit normalization, because many transits lack full observational coverage.

Kovács et al. (2013) also notice a substantial difference in the transit depth derived from an observation in Hα and a simultaneously obtained J-band light curve (their Fig. 9). In particular, the J-band transit is shallower, which would be consistent with the wavelength trend. However, the signature observed through the Hα-line may significantly differ from those observed in broad-band filters, because the Hα-line is affected by strong chromospheric contributions.

5. Discussion

5.1. The stellar pulsation spectrum

The pulsation spectrum of WASP-33 has been studied by several authors, who report a wealth of frequencies, see Table 11. All studies find pulsations with amplitudes on the order of 1 mmag, which is compatible with our results.

Deming et al. (2012) observed WASP-33 during two secondary transits in the K_s band using the 2.1 m telescope at Kitt Peak National Observatory and for another two nights using the Spitzer telescope. All observations were performed during secondary transits. Their frequency analysis has been carried out for individual nights. Their first three frequencies (21.1, 20.2, and 9.8 c/d) are compatible with our ν_1, ν_2, and ν_3 (see Table 4). Also de Mooij et al. (2013) observed secondary transits of WASP-33b in the K_s-band for two nights each lasting ~ 5 h. Although the frequencies they report are within the range of values we find, the values are numerically inconsistent with our results.

Herrero et al. (2011) observed for nine nights mainly during primary transit using Johnson-Cousins R filter. They report pulsation frequencies, which might correspond to our ν_1. Smith et al. (2011) carried out observations during one secondary transit using an S[III] narrow-band filter centered at 9077 Å. The observations were performed for almost 9 hours during a single night lacking photometric conditions. Among the pulsation frequencies they find, 21.6 ± 0.6 c/d and 34.3 ± 0.4 c/d likely correspond to our ν_2 and ν_6.

The most extensive pulsation analysis is carried out by Kovács et al. (2013). It is based on four photometric datasets including that of Herrero et al. (2011). Kovács et al. (2013) report two frequencies that are compatible with our ν_1 and ν_2. The ~ 15.2 c/s frequency does not show up in our analysis.

Among the different data sets, pulsations with frequencies around ~21 c/d and ~20 c/d that correspond to our most pronounced frequencies ν_1 and ν_2 consistently occur. Other pulsation frequencies are only found in some cases. We note, however, that the data have been acquired in different spectral bands, mostly in the infrared, where pulsations are expected to be lower in amplitude. The residuals after subtracting our pulsation model clearly indicate the presence of further low-amplitude pulsations, which might correspond to those found in previous studies. Additionally, our phase shift analysis in Sect. 3.5 has shown that the pulsation spectrum might be intrinsically variable. The amplitudes of the pulsations found by the various studies are all on the order of 1 mmag, which is compatible with our results. As the amplitudes are intrinsically small and, furthermore, wavelength dependent, we refrain from a detailed comparison of the derived numbers.

Table 11: From top to bottom, the evolution on the reported frequencies and amplitudes for WASP-33's pulsation spectrum.

Frequency (c/d)	Amplitude (mmag)
Herrero et al. (2011)	
21.004 ± 0.004	0.98 ± 0.05
21.311 ± 0.004	~0.86
Smith et al. (2011)	
26.9 ± 0.4	1.479 ± 0.069
18.8 ± 0.6	0.567 ± 0.134
34.3 ± 0.4	0.766 ± 0.115
21.6 ± 0.6	0.605 ± 0.105
Deming et al. (2012)	
~21.1	~1.3
~20.2	~2.3
~9.8	~1.6
~26.6	~2.1
~11.4	~2.1
de Mooij et al. (2013)[a]	
22.5 ± 0.1	0.95 ± 0.04^{N1}
33.3^{N1}	0.41 ± 0.04
27.3 ± 0.2	0.56 ± 0.06^{N2}
33.2^{N2}	0.17 ± 0.05
22.0^{N1}	0.11 ± 0.06
17.1^{N1}	0.13 ± 0.06
Kovács et al. (2013)[b]	
15.21643 ± 0.00004	0.758 ± 0.085^{HN}
20.16229 ± 0.00004	0.733 ± 0.080^{HN}
21.06339 ± 0.00004	0.719 ± 0.078^{HN}
15.21517 ± 0.00001	$0.477 \pm 0.054^{H+F}$
20.16230 ± 0.00001	$0.739 \pm 0.053^{H+F}$
21.06346 ± 0.00001	$0.728 \pm 0.049^{H+F}$
This work	
20.1621 ± 0.0023	1.03 ± 0.03
21.0606 ± 0.0023	1.01 ± 0.03
9.8436 ± 0.0023	0.86 ± 0.03
24.8835 ± 0.0017	0.45 ± 0.03
20.5353 ± 0.0013	0.77 ± 0.03
34.1252 ± 0.0027	0.53 ± 0.03
8.3084 ± 0.0025	0.68 ± 0.03
10.8249 ± 0.0030	0.69 ± 0.03

Notes. [a] Following the nomenclature of de Mooij et al. (2013), the superscripts $N1$ and $N2$ refer to "Night I" and "Night II". [b] The superscript HN stands for "HATNet" and $H + F$ for "HATNet+FUP".

In our analysis, we identify eight significant pulsation frequencies. Although the pulsation spectrum is probably much more complex than that, the amplitudes of the pulsations are intrinsically low and more data is required to characterize the components in further detail. We show that the pulsation phases vary in time with a gradient, dp, of up to $|dp| \lesssim 2 \times 10^{-3}$ d^{-1} assuming a linear evolution. This suggests that also the amplitudes and frequencies show temporal variability. However, our data do not allow to verify this.

We find that most of the detected frequencies are likely associated with low-order p-modes. We attempt to further identify the modes using Q-values, empirical period-luminosity- color relations, as well as amplitudes and phases of multi-color photometry. However, we find the detected frequencies to be largely incompatible with all these relations. We argue that this is not uncommon, (cf. e.g. Breger et al. 2005b).

5.2. Transit modeling

In their analysis of photometric follow-up data, Kovács et al. (2013) find a persistent "hump" in the residuals obtained after subtracting the transit model shortly after mid-transit time. While our residuals do clearly show unaccounted pulsations, we do not see any such hump, recurrently occurring at the same phase. Therefore, we find no evidence for a persistent structure on the stellar surface like, e.g., a spot belt as suggested by Kovács et al. (2013).

Although our transit modeling is consistent with a constant star-to-planet radius ratio with respect to wavelength, there may be a slight trend indicating a decrease in the radius ratio as the wavelength increases. Although this would be compatible with the results of Kovács et al. (2013), who find that the radius ratio in the J-band is smaller than that observed in Hα, we caution that the formation of the Hα-line may be different from that observed in broad-band filters – a caveat already mentioned by Kovács et al. (2013). Based on the currently available data, we conclude that a constant planet-to-star radius ratio seems most likely.

5.3. Star-planet interaction

Collier Cameron et al. (2010) report on a non-radial pulsation at a frequency of ~ 4 c/d, which might be tidally induced by the planet. Unfortunately, this frequency lies outside the sensitivity range of our analysis.

In close binary systems, tidal interaction affects stellar oscillations (e.g., Cowling 1941; Savonije & Witte 2002; Willems 2003). Particularly, Hambleton et al. (2013) studied a short-period binary system that presents δ Scuti pulsations and tidally excited modes. In addition to the already known commensurability between the pulsation frequencies and the orbital period of the system, the authors found that the spacing between the detected p-modes was an integer multiple of the system's orbital frequency. Although it is clear that the nature of WASP-33 does not resemble a short-period eccentric binary system, in order to analyze star-planet interaction we search for commensurability of the detected pulsation frequencies with the planetary orbital period, and investigated the spacings between them.

As the exact rotation period of the host star WASP-33A remains unknown, it is not entirely clear how exactly the planet affects the stellar surface in the frame of the star; in particular, the period at which the planet affects the same surface element is unknown for the larger fraction of the stellar surface. However, as the planet orbits in a highly tilted, nearly polar orbit, the stellar poles experience a periodic force with a period identical to once and twice the planetary orbital period. When the planet crosses a pole, the effective gravity on both poles is lowered due to the planetary gravity and orbital motion; the effect is, however, not the same on both poles.

Using our best fit orbital period of 1.2198675 d, we express the pulsation frequencies in terms of the orbital frequency of the planet. The result is presented in the last column of Table 4, where the ratios of the pulsations and the orbit are displayed. We expect the error in the pulsation frequencies to be considerably larger than those in the orbital period. The closest commensurability is found for the 9.8436 c/d, which corresponds to 12.008 times the orbital frequency.

To assess the significance of such a result, we carry out a Monte-Carlo simulation. In particular, we randomly generate eight frequencies between 8 and 34, i.e. in the approximate range of our detected pulsations. We then calculate the associated ratio based on the orbital frequency, and, finally, search for the best match. After 50 000 runs, we find that the cumulative probability distribution for the minimum distance from an integer frequency ratio is given by

$$F(d_{min}) = 1 - e^{-\frac{d_{min}}{0.060934}} \; . \tag{16}$$

Using this relation, we find that the probability of finding at least one of the ratios as close or closer than 0.008 c/d to an integer ratio to be 12%. Although the ratio may, indeed, be integer considering the error in the frequency determination (see Sect. 3), we note that our phase-shift analysis also revealed variability in the frequency spectrum, which we find hard to reconcile with a simple picture of tidally excited pulsations.

Additionally, we found that the spacing between the frequencies can not be described by harmonics of the orbital period of the system. In fact, the best case scenario is given by ν_5 and ν_7. Considering our best-fit orbital period, the departure from an integer number is 10 times their estimated error.

Therefore, we conclude that there is no evidence for a direct relation between any of our pulsation frequencies and the planetary orbital period.

6. Conclusions

In this work, we obtained and analyzed an extensive set of photometric data of the hottest known star hosting a hot Jupiter, WASP-33. The data cover both in- and out-of-transit phases and are used to study the pulsation spectrum and the primary transits.

Particularly, our out-of-transit data provide ~3 times more temporal coverage than the (Kovács et al. 2013) data set, which is the most extensive among those listed in Table 11. In addition, our data set is the only one that comprises dedicated out-of-transit photometric coverage to study the stellar pulsations in detail, and multi-color and simultaneous observations to study the nature of the modes.

A deep study over the pulsation spectrum of WASP-33 reveals, for the first time, eight significant frequencies. Additionally, some of the found frequencies seem to be consistent with previous reports. Along with the associated amplitudes and phases, we construct a pulsation model which we use to correct the primary transit light curves, with the main goal to re-determine the orbital parameters by means of pulsation-clean data.

In our transit modeling, we find system parameters consistent with those reported by Collier Cameron et al. (2010) and Kovács et al. (2013). Interestingly, the derived parameter values are hardly affected by taking into account the pulsations in the modeling, albeit, the errors decrease. One possible explanation could be that the amplitudes of WASP-33, at least in the high frequency range where our studies focus, are found to be small in nature. Our extense primary transit observations, obtained in different filter bands, allows us to notice a decrease in the planet-to-star radius ratio with wavelength, also observed by other authors. Simultaneous multi-band photometry of primary transits of WASP-33 will help to better constrain this dependency.

Considering that our work has been produced using fully ground-based observations, we were able to provide an extense study of the pulsation spectrum of this unique δ Scuti host star. This, in turn, has helped to better comprehend how much do the pulsations affect the determination of the system parameters.

Acknowledgements. C. von Essen acknowledges funding by the DFG in the framework of RTG 1351, and Dr. Andres Moya and Prof. Rafael Garrido for discussing issues on δ Scuti stars. E. H. and I. R. acknowledge financial support from the Spanish Ministry of Economy and Competitiveness (MINECO) and the "Fondo Europeo de Desarrollo Regional" (FEDER) through grant AYA2012-39612-C03-01. The Joan Oró Telescope (TJO) of the Montsec Astronomical Observatory (OAdM) is owned by the Generalitat de Catalunya and operated by the Institute for Space Studies of Catalonia (IEEC). We further thank Ramon Naves for operating the 0.3 m telescope at Observatori Montcabrer, and Thomas Granzer for his support on STELLA observations and data reduction.

References

Allen, C. W. 1973, Astrophysical quantities
Baglin, A., Breger, M., Chevalier, C., et al. 1973, A&A, 23, 221
Balona, L. A., Breger, M., Catanzaro, G., et al. 2012a, MNRAS, 424, 1187
Balona, L. A. & Evers, E. A. 1999, Delta Scuti Star Newsletter, 13, 26
Balona, L. A., Lenz, P., Antoci, V., et al. 2012b, MNRAS, 419, 3028
Balona, L. A. & Stobie, R. S. 1979, MNRAS, 189, 649
Barnes, J. W. 2009, ApJ, 705, 683
Breger, M. 1979, PASP, 91, 5
Breger, M. 1990, Delta Scuti Star Newsletter, 2, 13
Breger, M. 1998, in Astronomical Society of the Pacific Conference Series, Vol. 135, A Half Century of Stellar Pulsation Interpretation, ed. P. A. Bradley & J. A. Guzik, 460
Breger, M. 2005, in Astronomical Society of the Pacific Conference Series, Vol. 335, The Light-Time Effect in Astrophysics: Causes and cures of the O-C diagram, ed. C. Sterken, 85
Breger, M. & Bregman, J. N. 1975, ApJ, 200, 343
Breger, M., Fossati, L., Balona, L., et al. 2012, ApJ, 759, 62
Breger, M., Handler, G., Garrido, R., et al. 1999a, A&A, 349, 225
Breger, M., Lenz, P., Antoci, V., et al. 2005a, A&A, 435, 955
Breger, M., Lenz, P., Antoci, V., et al. 2005b, A&A, 435, 955
Breger, M., Pamyatnykh, A. A., Pikall, H., & Garrido, R. 1999b, A&A, 341, 151
Breger, M., Stich, J., Garrido, R., et al. 1993, A&A, 271, 482
Breger, M. & Stockenhuber, H. 1983, Hvar Observatory Bulletin, 7, 283
Campbell, W. W. & Wright, W. H. 1900, ApJ, 12, 254
Carter, J. A. & Winn, J. N. 2009, ApJ, 704, 51
Christensen-Dalsgaard, J. & Berthomieu, G. 1991, Theory of solar oscillations, ed. A. N. Cox, W. C. Livingston, & M. S. Matthews, 401–478
Christian, D. J., Pollacco, D. L., Skillen, I., et al. 2006, MNRAS, 372, 1117
Claret, A. 1998, A&AS, 131, 395
Claret, A. & Bloemen, S. 2011, A&A, 529, A75
Collier Cameron, A., Guenther, E., Smalley, B., et al. 2010, MNRAS, 407, 507
Cowling, T. G. 1941, MNRAS, 101, 367
Cowling, T. G. & Newing, R. A. 1949, ApJ, 109, 149
Daszyńska-Daszkiewicz, J., Dziembowski, W. A., & Pamyatnykh, A. A. 2003, A&A, 407, 999
Daszyńska-Daszkiewicz, J., Dziembowski, W. A., Pamyatnykh, A. A., & Goupil, M.-J. 2002, A&A, 392, 151
de Mooij, E. J. W., Brogi, M., de Kok, R. J., et al. 2013, A&A, 550, A54
Deming, D., Fraine, J. D., Sada, P. V., et al. 2012, ApJ, 754, 106
Deupree, R. G. 2011, ApJ, 742, 9
Deupree, R. G., Castañeda, D., Peña, F., & Short, C. I. 2012, ApJ, 753, 20
Dupret, M.-A., De Ridder, J., De Cat, P., et al. 2003, A&A, 398, 677
Eastman, J., Siverd, R., & Gaudi, B. S. 2010, PASP, 122, 935
Eggen, O. J. 1956, PASP, 68, 238
Fitch, W. S. 1981, ApJ, 249, 218
Gillon, M., Smalley, B., Hebb, L., et al. 2009, A&A, 496, 259
Goupil, M.-J., Dziembowski, W. A., Pamyatnykh, A. A., & Talon, S. 2000, in Astronomical Society of the Pacific Conference Series, Vol. 210, Delta Scuti and Related Stars, ed. M. Breger & M. Montgomery, 267
Gupta, S. K. 1978, Ap&SS, 59, 85
Hambleton, K. M., Kurtz, D. W., Prša, A., et al. 2013, MNRAS, 434, 925
Herrero, E., Morales, J. C., Ribas, I., & Naves, R. 2011, A&A, 526, L10
Jones, E., Oliphant, T., Peterson, P., et al. 2001, SciPy: Open source scientific tools for Python, http://www.scipy.org
King, J. R. 1991, Information Bulletin on Variable Stars, 3562, 1
Kovács, G., Kovács, T., Hartman, J. D., et al. 2013, A&A, 553, A44
Lenz, P. & Breger, M. 2005, Communications in Asteroseismology, 146, 53
López de Coca, P., Rolland, A., Garrido, R., & Rodriguez, E. 1990, Ap&SS, 169, 211
Maeder, A. 2009, Physics, Formation and Evolution of Rotating Stars
Mandel, K. & Agol, E. 2002, ApJ, 580, L171

Mathias, P., Gillet, D., Aerts, C., & Breitfellner, M. G. 1997, A&A, 327, 1077
Milligan, H. & Carson, T. R. 1992, Ap&SS, 189, 181
Montgomery, M. H. & O'Donoghue, D. 1999, Delta Scuti Star Newsletter, 13, 28
Moya, A., Bouy, H., Marchis, F., Vicente, B., & Barrado, D. 2011, A&A, 535, A110
Murphy, S. J., Grigahcène, A., Niemczura, E., Kurtz, D. W., & Uytterhoeven, K. 2012, MNRAS, 427, 1418
Patil, A., Huard, D., & Fonnesbeck, C. J. 2010, Journal of Statistical Software, 35, 1
Petersen, J. O. & Hog, E. 1998, A&A, 331, 989
Pollacco, D. L., Skillen, I., Collier Cameron, A., et al. 2006, PASP, 118, 1407
Pont, F., Zucker, S., & Queloz, D. 2006, MNRAS, 373, 231
Savonije, G. J. & Witte, M. G. 2002, A&A, 386, 211
Smith, A. M. S., Anderson, D. R., Skillen, I., Collier Cameron, A., & Smalley, B. 2011, MNRAS, 416, 2096
Southworth, J., Hinse, T. C., Jørgensen, U. G., et al. 2009, MNRAS, 396, 1023
Southworth, J., Zima, W., Aerts, C., et al. 2011, MNRAS, 414, 2413
Stellingwerf, R. F. 1979, ApJ, 227, 935
Strassmeier, K. G., Granzer, T., Weber, M., et al. 2010, Advances in Astronomy, 2010
Uytterhoeven, K., Moya, A., Grigahcène, A., et al. 2011, A&A, 534, A125
von Zeipel, H. 1924, MNRAS, 84, 665
Watson, R. D. 1988, Ap&SS, 140, 255
Willems, B. 2003, MNRAS, 346, 968
Zima, W. 2008, Communications in Asteroseismology, 157, 387

Chapter 3

Polarized stellar light by an exoplanet atmosphere: the case of WASP-33

3.1 Astronomical polarization

In 1852, George G. Stokes introduced a parametrization for the polarization state of electromagnetic radiation today known as "Stokes parameters". The four Stokes parameters I, Q, U, and V describe the polarization state of light: I is the total intensity, Q and U characterize linear polarization, and V denotes circular polarization. Stokes' ideas were taken up by Chandrasekhar almost a hundred years later (e.g., Chandrasekhar 1946). Chandrasekhar demonstrated that the radiation emerging from the limb of early type stars, in comparison with the radiation emerging from the center of the disk, should be considerably polarized due to electron scattering[1] (~11%). In systems such as eclipsing binaries, where the radial symmetry is broken when the late–type companion masks the disk of the early–type star, Chandrasekhar also predicted a modulation of polarization as a function of the orbital phase.

At the same time Öhman (1946), in his work called "On the Possibility of Tracing Polarization Effects in the Rotational Profiles of Early-Type Stars", studied how the line profiles of stars with high values of $v\sin(i)$ are affected by polarized light. He expected the wings of the lines to be produced by radiation emerging from the equatorial limb, and the core of the lines by stellar light from the center of the stellar disk, this in combination producing a variation in the line profiles related to polarization. Although 60 years ago the resolution of the instruments was too low to detect such effects, nowadays they are widely observed (e.g., Landi Degl'Innocenti & Landolfi 2004; Stenflo et al. 1980, 2000).

In an attempt to substantiate Chandrasekhar's prediction about the polarization of electron-scattered light in early-type stars' atmospheres, Hall (1949) and Hiltner (1949*a*) discovered, "by accident", the polarizing properties of the interstellar medium. Particularly, the description of how interstellar polarization became established is stated in Hiltner (1949*b*). His observations of the binary system CQ Cep revealed a polarization of ~10%, which was *independent of the stellar phase*. This fact made the author conclude that the observed polarization was not associated with the stars, but introduced to the stellar radiation in its passage through the interstellar space. Furthermore, he stated that if the polarization was a consequence of scattering by interstellar particles, the particles must be asymmetrical, elongated some how, and subject to some alignment force, coming most probably from magnetic fields. This statement is the exact foundation of interstellar medium polarization. Some decades later, Mathewson & Ford (1970) produced Figure 3.1, an outstanding work on polarization over nearly 7000 stars in both the Northern and Southern hemispheres.

Although Hiltner and Hall saw no wavelength dependence (most probably related to instrumental precision), broadband spectropolarimetry finally gained a leading role in stellar polarization studies. Behr (1959) and Gehrels (1960) were pioneers

[1]Electron scattering is the process whereby an electron is deflected from its original trajectory. Electrons can be scattered by other charged particles as well as deflected by magnetic fields. Common electron scattering processes include Compton scattering, Bremsstrahlung, and Synchrotron emission.

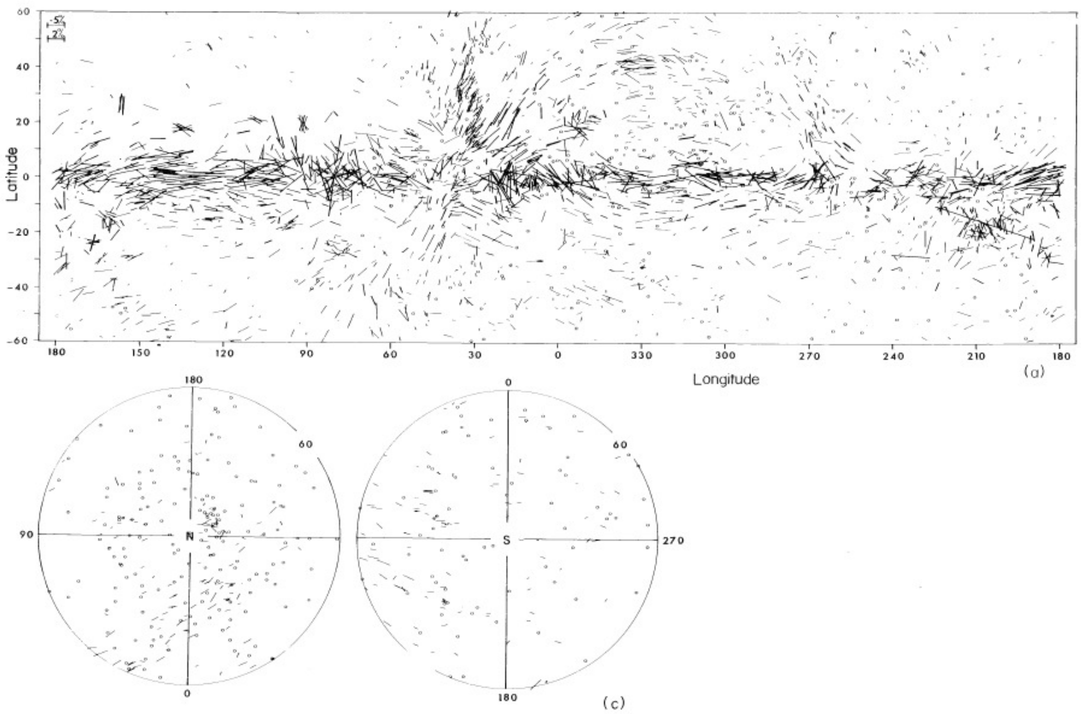

Source: Mathewson & Ford (1970).

Figure 3.1: Polarization vectors of stars on a Galactic map. (a) Stars along the Galactic equator with Galactic latitudes -60° $\leq \beta \leq$ 60°. (b,c) Galactic poles.

in the study of the wavelength dependence of interstellar polarization. But it wasn't until 1970 that Serkowski (1973), after normalizing both the polarization measurements and the wavelength points of the observations, found a unique curve, independent of the Galactic position, known today as Serkowski's law (Coyne et al. 1974; Serkowski et al. 1975; Codina-Landaberry & Magalhaes 1976). The law (purely empirical) describes the polarization degree as a function of wavelength:

$$P(\lambda) = P_{max} \exp[-\kappa\, ln^2(\lambda_{max}/\lambda)] \,, \tag{3.1}$$

where λ_{max} is the wavelength of the maximum polarization P_{max}, and κ, also called *width parameter*, is linearly correlated with λ_{max} ($\kappa \sim 1.66\lambda_{max} + 0.01$) (Wilking et al. 1980, 1982; Whittet et al. 1992). The general shape of the polarization curve is nowadays well established. It rises in the IR, peaks generally in the visual, and decreases toward the UV (see Figure 3.2). This implies that the non–spherical grains, aligned with magnetic fields, are typically sub–micron in size.

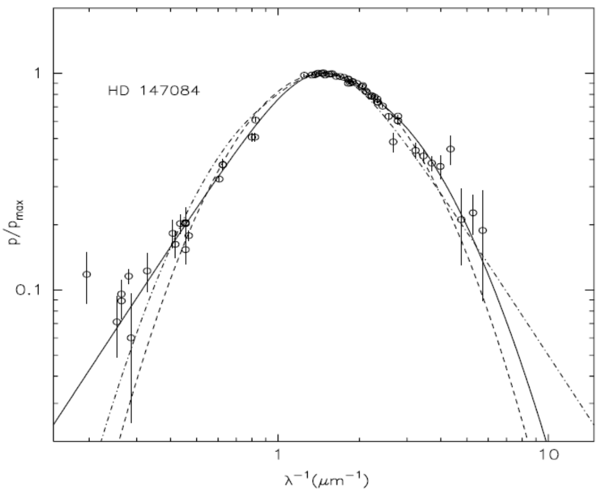

Source: (Martin et al. 1999).

Figure 3.2: One of the many examples of interstellar polarization as a function of wavelength, observed towards the variable star HD 147084. The dashed line shows the Serkowski relation.

Today, polarimetry has evolved into a powerful astronomical technique. Polarized light from radio to X-ray wavelengths has been used to study, among others, young stars (e.g., Feigelson et al. 1998), the structure and interstellar medium of galaxies (e.g., Fendt et al. 1998), and active galactic nuclei (e.g., Villforth et al. 2009).

3.1.1 Polarization of light

The light can get polarized either due to the interaction with the medium through which it propagates, or due to the mechanism of emission itself.

Polarization at the source occurs when the radiation is constrained in their degrees of freedom. A classical example is synchrotron radiation, which is caused because magnetic fields constrain the motion of the radiating charges. In the case of astronomical masers, the observed polarization results from the presence of magnetic fields producing Zeeman splitting of the magnetic quantum levels.

The polarization due to the propagating medium is caused because some media are anisotropic in nature (for example, elongated dust particles, which are aligned by the ambient magnetic fields) so they absorb one component of light in preference to others. This dust grains are capable of introducing polarization into the incident unpolarized light, as much as to change the state of polarization if the incident light results to be already polarized.

Most astrophysical situations involve polarization produced by scattering. Scattering is a physical process where the radiation is forced to deviate from its original trajectory by non-uniformities in the medium through which it passes. It can occur in two basic forms: single (the radiation is deviated in one direction) and multiple (the randomness of the interaction tends to be averaged out by the large number of scattering events). Most particularly, Rayleigh scattering is the scattering of radiation by particles *much smaller than the wavelength of the radiation*. It is the result from the electric polarizability of the particles: when the oscillating electric field reaches the particles, it causes them to move at the same frequency. The particle therefore becomes a small radiating dipole whose radiation we see as scattered light. A typical Rayleigh scattering + single scattering is observed in Figure 3.3.

Source: `http://cg.ibds.kit.edu/170.php`.

Figure 3.3: Rayleigh scattering and single scattering events, daily seen on Earth. The sky is blue because the molecular composition of our atmosphere scatters short-wavelength light more than longer wavelengths.

3.2 Polarization in exoplanets

The mainly unpolarized light that is emitted by the central star becomes partially polarized when it is scattered off circumstellar material such as disks and, particularly of our interest, exoplanets (Seager et al. 2000; Baba & Murakami 2003; Stam et al. 2004).

In 2008, Berdyugina et al. (2008) reported the first polarimetric detection of an extrasolar planet. Their analysis is based on B-band observations carried out with the "Double Image POLarimeter" (DIPOL) mounted at the 60 cm "Kungliga Vetenskaplika Academy" (KVA) telescope. From 2006 to 2007, Berdyugina et al. (2008) observed the exoplanet system HD 189733 – an active K4 dwarf with a transiting hot Jovian planet. They found two maximum values with an amplitude of $\approx 2 \times 10^{-4}$ in the polarization degree near planetary elongation (see Figure 3.4). Berdyugina et al. (2008) concluded that the planet's scattering radius exceeds the opaque body by 30% and that the orbit is nearly aligned with the North–South direction.

The detection reported on by Berdyugina et al. (2008) has been challenged by the results of Wiktorowicz (2009), who did not find any significant orbital variability in the polarization degree of the HD 189733 system using the POLISH instrument (POLarimeter for Inclination Studies of High mass x-ray binaries/hot Jupiters), mounted at the

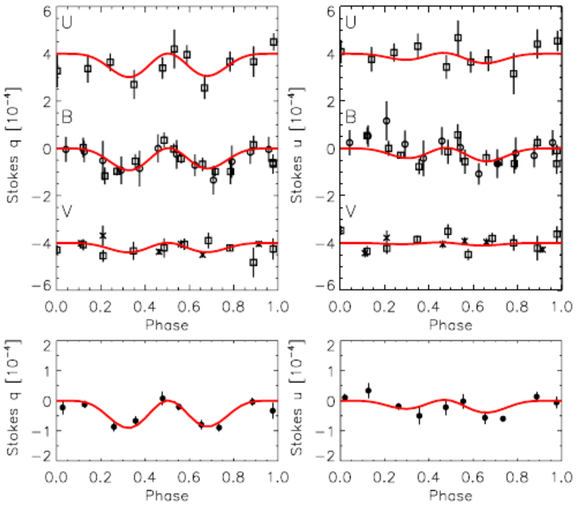

Source: Berdyugina et al. (2008).

Figure 3.4: First detection of polarized light from the exoplanet HD 189733. The observations were obtained in three filter bands: Johnson-Cousins U, B, and V. 1σ errors are plotted. The lower panels show the complete data sets binned together. Curves are the best–fit solutions for the Rayleigh–Lambert atmosphere. The modulation of the polarization signal will be explained along this text.

5-m telescope in Palomar Observatory, California; in particular, the author determined an upper limit of 7.9×10^{-5} for the variability in the polarization degree at the 99% confidence level. Subsequently, however, Berdyugina et al. extended their observations using the "Turku UBVRI Photopolarimeter" (TurPol) at the 2.5 m Nordic Optical Telescope (Berdyugina et al. 2011). They substantiated their previously reported detection, viz., a polarization degree maximum with an amplitude of 10^{-4} in the B– and U–band. Simultaneously, they found that the signal in the V–band is "at least a factor of two" lower than in the B–band; consequently, Berdyugina et al. (2011) argued that their results were compatible with that of Wiktorowicz (2009) taking into account the broader band used in their study. Furthermore, Berdyugina et al. (2011) concluded that the polarized light most likely originates in the planetary atmosphere where Rayleigh scattering dominates at optical wavelengths beyond 4000 Å.

3.3 Polarized light by exoplanet atmospheres

3.3.1 The polarization model

Large efforts are being invested in measuring the excessively small polarization signal produced by exoplanet atmospheres. The main motivation relies in the potential to determine the orbital inclination and, with it, true masses for exoplanets instead of upper limits, given by the radial velocity technique.

Polarization of exoplanets arises by scattering of incident starlight by gas molecules, aerosols, and dust grains in the atmosphere of the exoplanet (Seager et al. 2000). In the case of face–on and circular orbits, the exoplanet is always seen with half of its disk illuminated by the stellar light. Therefore, if the exoplanet atmosphere is featureless, the intensity of light that is scattered by the exoplanet is constant in nature at every orbital phase. In turn, the position angle of polarization rotates 360° each orbit, because the scattering plane rotates as the exoplanet moves in its orbit.

Figure 3.5 shows the basic geometry that involves polarization measurements when the exoplanet is seen nearly edge–on. The Stokes plane (Q,U) is indicated with continuous and dashed black lines. +Q is pointing at the celestial North, and -Q at East. For this system configuration, a periodic variability in the degree of polarization appears. In this case, the position angle of the polarization direction does not vary significantly throughout the orbit, because the scattering plane is nearly coplanar with the orbital plane.

The most simplified case of the modulation of polarization is given for a Lambertian phase function and Rayleigh scattering. For a Lambertian sphere, the surface's luminosity is isotropic. Therefore, the apparent brightness is the same, regardless the observer's angle of view. In such cases, the polarization degree is given by:

$$P(\phi) = \epsilon F(\phi) P_o(\phi) \ . \qquad (3.2)$$

ϕ represents the orbital phase. $\phi = 0$ corresponds to the superior conjunction of the exoplanet. $\epsilon = p(R_P/a)^2$ is the fraction of the stellar flux scattered by an exoplanet with radius R_P and semi–major axis a. p represents the geometric albedo, which is nothing more than the fraction of the ex-

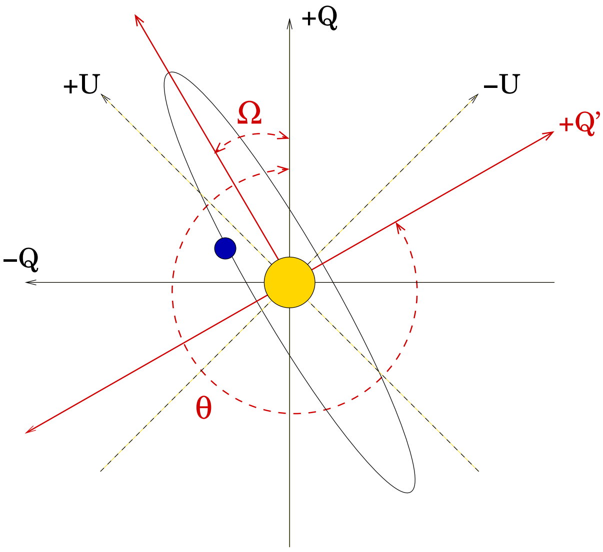

Source: C. von Essen.

Figure 3.5: Basic geometry of polarization measurements when the exoplanet orbit is seen nearly edge–on. $\theta = 270° + \Omega$.

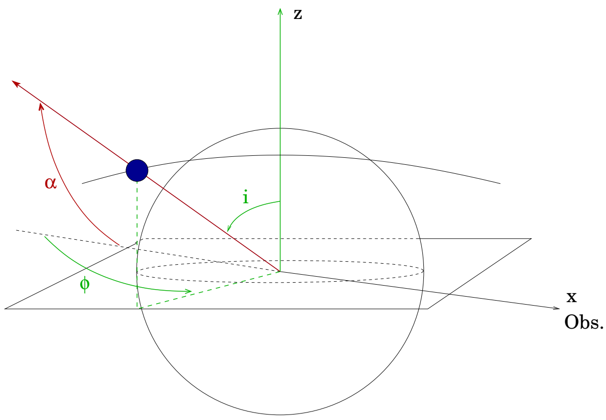

Source: C. von Essen.

Figure 3.6: The phase angle α is in the plane formed by the observer–star center and star center–planet vectors. On the contrary, ϕ is located in the stellar equatorial plane. The inclination i is the angle between the z-axis and the plane of the orbit.

oplanetary scattered flux in comparison to the flux scattered by a Lambertian disk. $F(\phi)$ is the fraction of intercepted flux scattered toward the observer (also called the phase function), and $P_o(\phi)$ is the polarization of the scattered flux.

The phase function is usually given in terms of the phase angle α (i.e., the angle between the continuation of the line from the observer to the star, and the line from the star to the planet). For a Lambertian sphere, it has the following expression (Russell 1916):

$$F(\alpha) = \frac{\sin(\alpha) + (\pi - \alpha)\cos(\alpha)}{\pi} \; . \tag{3.3}$$

The relation between α and the orbital inclination i is $a\cos(\alpha) = a\sin(i)\sin(\phi)$. The basic geometry is sketched in Figure 3.6. Thus, $F(\phi)$ can be determined, specially for transiting systems where all the parameters are known.

Shakhovskoi (1965) studied the behavior of polarized light from 17 eclipsing binaries. In their work, the authors presented expressions for the Stokes parameters (Q',U'), measured *in the orbital frame*, as a function of the orbital angles i and ϕ. In this system, +Q is defined to be in the direction of the orbital angular momentum vector.

$$\begin{aligned} Q'(\phi) &= \epsilon F(\phi)(\sin^2(\phi) - \cos^2(\phi)\cos^2(i)) \\ U'(\phi) &= \epsilon F(\phi)\sin(2\phi)\cos(\phi) \; . \end{aligned} \tag{3.4}$$

Furthermore, to convert polarization vectors from the orbital frame into the celestial coordinate system, the ascending node Ω has to be known (Figure 3.5). In the celestial frame:

$$\begin{aligned} Q(\phi) &= Q'(\phi)\cos(2\theta) - U'(\phi)\sin(2\theta) \\ U(\phi) &= Q'(\phi)\sin(2\theta) + U'(\phi)\cos(2\theta) \\ P(\phi) &= \sqrt{Q(\phi)^2 + U(\phi)^2} \; . \end{aligned} \tag{3.5}$$

The polarization degree clearly depends on the chemical composition of the reflecting area. In the case of rocky planets and satellites, their solid scattering surfaces make the polarization degree be dependent on the albedo (Figure 3.7).

On the contrary, in hot Jupiters multiple scattering occurs and, as a result, the polarization degree reduces (Seager et al. 2000; Stam et al. 2004, see e.g.,). Lucas et al. (2009) studied how the expected polarization degree (%P) would look like in systems hosting hot Jupiters. The authors assume that the star has a finite angular size, with a limb-darkened edge. Furthermore, the eccentricity of the planetary orbit is set to zero. All photons hit the

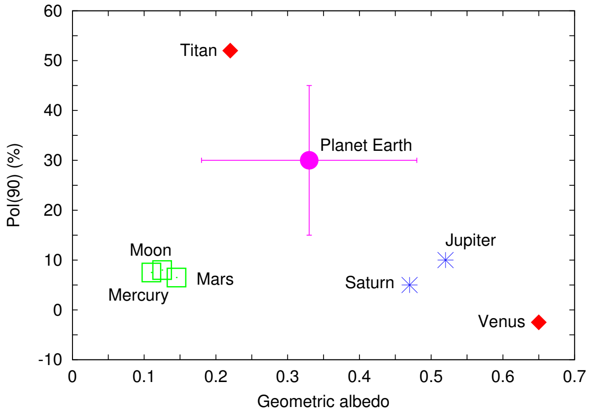

Figure 3.7: References: Mercury (Dollfus & Auriere 1974); Venus (Dollfus & Coffeen 1970); Moon (Coyne & Pellicori 1970); Mars (Dollfus et al. 1983); Titan (Tomasko & Smith 1982); Jupiter (Smith & Tomasko 1984); Saturn (Tomasko et al. 1984); Earth (Wolstencroft & Breon 2005).

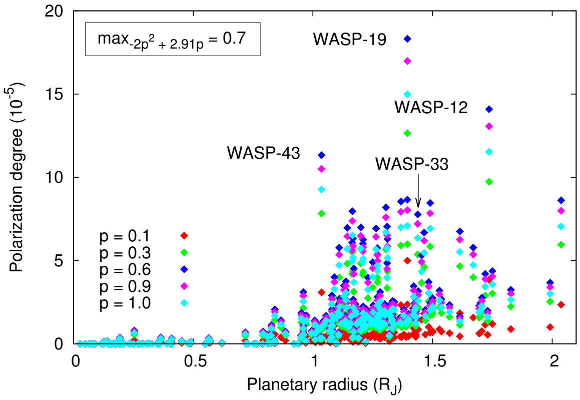

Figure 3.8: Polarization degree plotted as a function of the planetary radius, for different values of albedos.

star-facing side of the planetary disk in random locations. The polarization is dominated by Rayleigh or Mie scattering, while they do not include molecular or atomic absorption. Finally, the authors assume a uniform, locally plane parallel semi-infinite atmosphere with no variation of density with depth. All together, using Monte Carlo simulations, Lucas et al. (2009) find that %P can be described as a function of the orbital parameters:

$$\begin{aligned} \Delta P_{i=90^\circ} &= (-2.10p^2 + 2.91p) \times \left(\frac{a}{0.05AU}\right)^{-2} \times \\ &\left(\frac{R_P}{1.2R_J}\right)^2 \times 10^{-5} \\ \Delta P_i &= 1.43 \Delta P_{i=90^\circ} . \end{aligned} \tag{3.6}$$

Figure 3.8 shows the polarization degree obtained via Eq. 3.6. The exoplanets with the highest %P have been identified. WASP-33, on which I carried out polarimetric measurements, is also indicated.

3.3.2 The model: dependency on the nature of Rayleigh scattering and phase function

The shape of the polarization signal is quite particular but also easy to comprehend. Firstly, it is widely known that Rayleigh scattering is wavelength dependent, such that $R_{scatt} \propto \lambda^{-4}$. This means that, in order to observe polarization of stellar light scattered by an exoplanet atmosphere, it is more adequate to observe in bluer bands. Secondly, Rayleigh scattering also depends on θ, which is the angle between the direction of incidence of light, and the direction in which the light is scattered once the reflecting surface is reached (see Figure 3.9). In this case, $R_{scatt} \propto \frac{sin^2(\theta)}{1.+cos^2(\theta)}$. The maximum value is reached for rays which are scattered perpendicularly to incidence ($\theta = \pm\pi$).

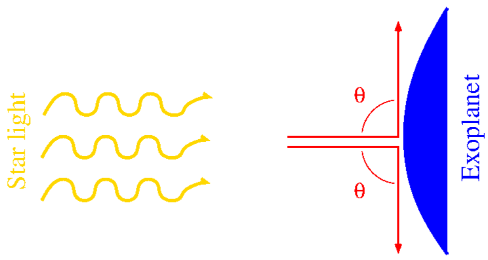

Source: C. von Essen.

Figure 3.9: The angle between the direction of light's incidence and the direction in which the light is scattered is θ. This will modulate the shape of the polarization signal.

Secondly, the polarization properties also depend on the shape and composition of the scattering surface. As mentioned before, the simplest model involves a Lambertian sphere with a given phase function (see previous sections). The amount of reflected light given by the phase function reaches its maximum value at opposition.

It is *the combination* of Rayleigh scattering and the phase function that gives the polarization modulation. Figure 3.10 shows how the polarization degree changes as a function of the orbital position of the exoplanet.

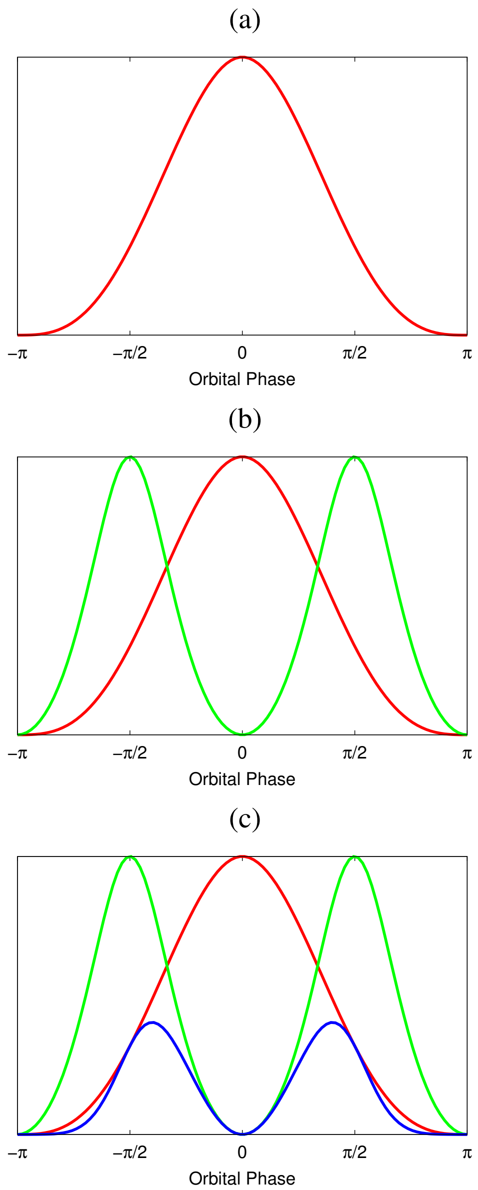

Figure 3.10: From top to bottom: (a) The Lambertian phase function in red. (b) The Rayleigh scattering angle–dependency is over plotted in green. (c) The final polarization modulation, product from the combination of the Lambertian phase function and Rayleigh scattering, is over plotted in blue. Orbital phase $\phi = 0$ coincides with the planet at opposition.

3.3.3 The model: dependency on the orbital parameters

Now that the global shape of the polarization degree is known, it is worth to understand how does it further change as a function of the orbital parameters.

Figure 3.11 shows how the polarization modulation changes, as a function of the orbital inclination i. Fig. 3.11 (a) shows how %P varies when the orbital inclination is 90°. This configuration is usual in transiting systems. Although the polarization degree is small, in this case the changes of %P with respect to the exoplanet orbital position are the largest. Fig. 3.11 (b) shows intermediate values of inclination and, finally, Fig. 3.11 (c) also includes $i = 0°$. In this case the orbit is seen face–on, so the amount of illuminated surface, as seen by a far observer, is always the same (constant phase function). In other words, the planet is always seen under the same phase angle α. Therefore, the polarization degree shows a constant behavior.

The modulation of the polarization also depends on the ascending node Ω. This modulation is more evident in the Stokes Q and U parameters. The position angle of the ascending node rotates during the orbit around the line–of–sight (see Fig. 3.5). This would be analogous as rotating the reference frame for polarization. In such cases, the degree of polarization does not change, but the plane of linear polarization rotates. If Ω is increased from 0, then the shape of Stokes Q changes from being symmetric to antisymmetric (Figure 3.12 (c)). The opposite is true for Stokes U. At $\Omega = 90°$ both curves reach the same shape as for $\Omega = 0°$, but with opposite signs. Stokes Q and U do not change under a rotation plane of polarization by 180°. Therefore, the polarization curves remain unaltered when shifting Ω by 180°.

3.4 A novel high S/N observing technique

We carried out observations of the WASP-33 exoplanet system using the "Calar Alto Faint Object Spectrograph" (CAFOS), mounted at the 2.2 m telescope (CAHA). The close-in orbit of WASP-33b and the high apparent brightness of its host star make the WASP-33 system an ideal target to study

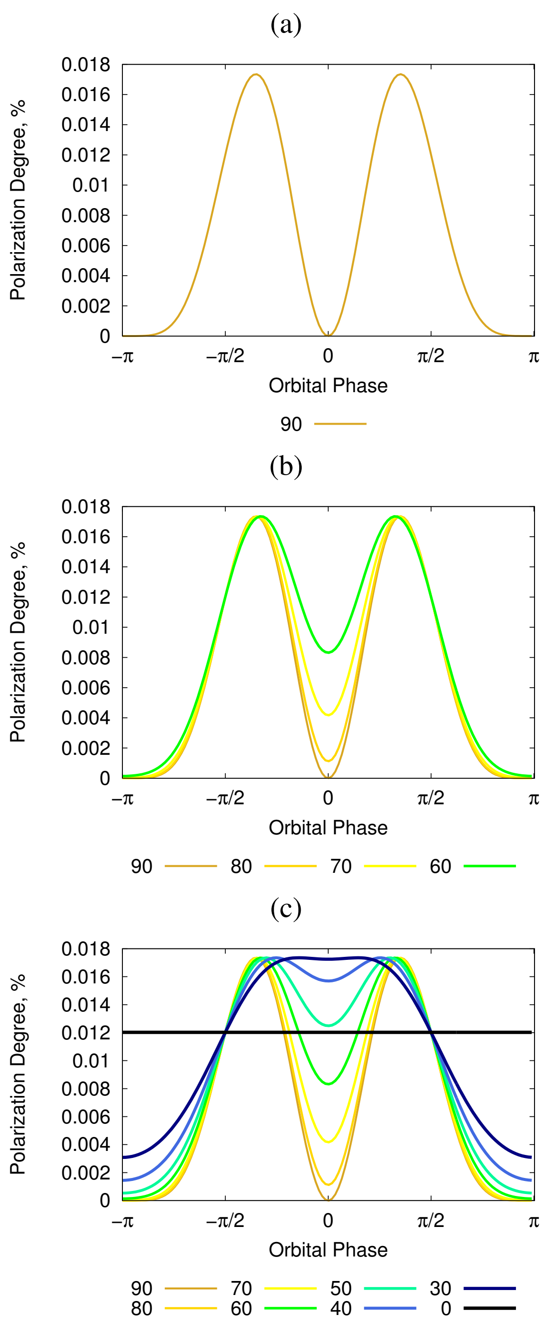

Figure 3.11: Changes in the polarization modulation and degree as a function of the orbital inclination. Semi–major axis a, planetary radius R_P, and inclination i are fixed to the values of WASP-33 system. $\Omega = 90°$.

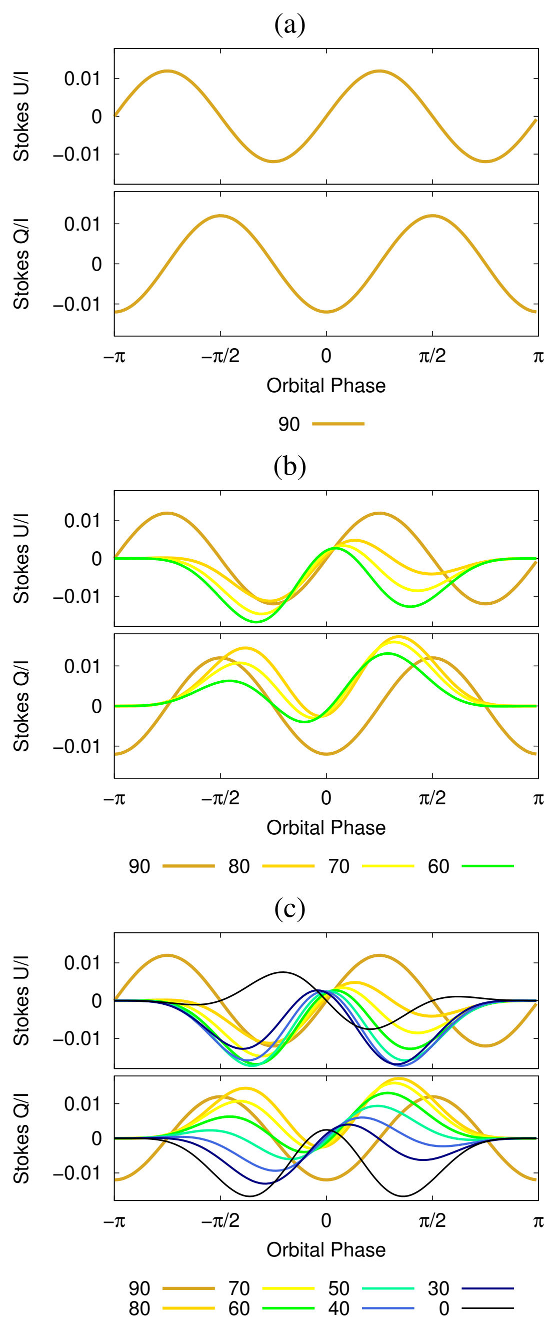

Figure 3.12: Changes in the Stokes parameters Q and U as a function of the ascending node. Semi–major axis a, planetary radius R_P, and inclination i are fixed to the values of WASP-33 system.

polarization.

For hot Jovian planets, the typical polarization signal has been found to be around 10^{-4} in the B- and U-band (Berdyugina et al. 2008, 2011). Therefore, a signal-to-noise (S/N) ratio higher than 10^4 is needed to disentangle the polarimetric signature from photon noise. This, in turn, requires 10^8 source photons to be collected, which is hardly possible in a single exposure with current detectors. Consequently, stacking is necessary.

A major source of overhead in obtaining polarimetric data points at short cadence is the read-out time of the detector. To minimize the time lost due to read-out, we developed a new observing technique, which is based on obtaining multiple data points during a single exposure.

The CCD at CAFOS has a size of 2k×2k pixels, of which only the central 1k×1k pixels were used in our observations to avoid vignetting in the outer parts. We subdivided the 1k×1k section into 14 stripes, of which each was further subdivided into two stripes for the ordinary and extraordinary beam. Additionally, we rotated the entire instrument to place a reference star on the same stripe, located there for further polarimetric and photometric studies.

Figure 3.13 (a) shows one "original" polarimetric image on top. In Figure 3.13 (b) a composed and zoomed-in polarimetric image is depicted. Here, the bright source at the top is WASP-33 and the one at the bottom is a reference star. The images on the right are convolved with the ordinary and extraordinary masks.

We proceeded by calculating displacements in right ascension and declination. The application of these displacements enabled us to locate the target and reference star consecutively on each of the 14 available stripes starting from the leftmost one. Only after all stripes had been exposed, we triggered CCD read-out. In this way, we obtained 14 times the stellar fluxes in a row and converted $13 \times 90\ \mathrm{s} = 19.5$ min of read-out time into usable exposure time. Once we completed a polarimetric point, viz., 16 rotations of the half-wave retarder plate (HWP), we stacked the 14 flux sources to increase the S/N ratio. Including a reference star within the field, in combination with the fast production of one high signal-to-noise polarimetric point, reduces the effects of temporal variability in the instrumental calibration and sky conditions, which are potential sources of systematic errors.

(a)

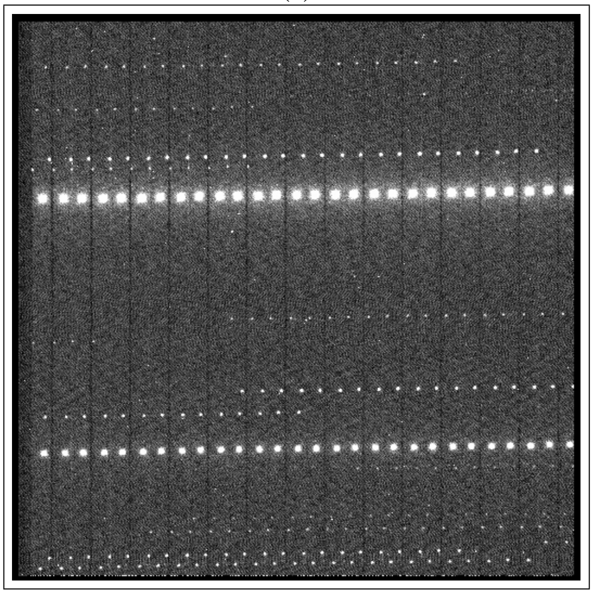

(b)

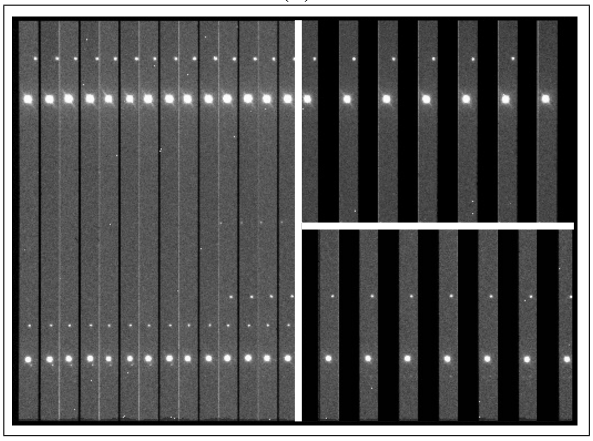

Figure 3.13: (a) Photo polarimetric image obtained with CAFOS. The image is complete. Therefore, the 28 repetitions of the same star (14 for the ordinary and 14 for the extraordinary ray) are seen. The bright, upper source is WASP-33 and the fainter one at the bottom is the reference star. (b) Left: "zoom-in" of the image showing ordinary and extraordinary beams. Upper right: Excerpt of the image showing only the stripes illuminated by the ordinary beam. Lower right: As upper right panel but for the extraordinary beam.

3.5 Observations and data reduction

We carried out our observations using the 2.2 m telescope at Calar Alto Observatory in Spain during two seasons in 2012: the first observing campaign was from January 22 to 31, and the second one from September 12 to 15. We observed WASP-33, HD 204827 and HD 25443 as standard polarized stars, and HD 21447 and HD 212311 as unpolarized standard stars. To perform the observations we used CAFOS[2]. CAFOS is a dual-beam polarimeter composed of a HWP followed by a Wollaston prism that produces two beams with orthogonal

[2]http://www.caha.es/CAHA/Instruments/CAFOS/

planes of polarization, which are called the ordinary and the extraordinary beam (Figure 3.14). The Stokes parameters are derived from the intensities in both beams at given set of the HWP angles (Patat & Taubenberger 2011).

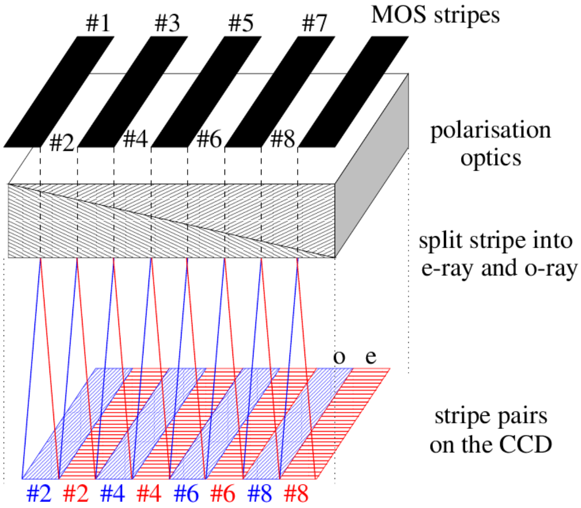

Source: `http:www.caha.es`.

Figure 3.14: The orthogonal beams (i.e., the ordinary and extraordinary rays) do not suffer from overlapping. This is achieved using a mask that blocks half of the field of view (the so–called “stripes”).

During the first campaign, the weather conditions allowed us to observe for three complete nights and five partial nights. The photometric conditions of the second campaign were remarkable, some times even with a seeing below 1". Table 3.1 summarizes the details of the observed targets and the polarimetric cycles obtained per night, along with the mean value of the full-width at half-maximum (FWHM). The standard stars were selected from the sample of Schmidt et al. (1992), convenient to the location of the observatory and the season.

We reduced the data using the `apphot` package of IRAF. Since the images of the stars are distributed across the chip and no guiding system was used, flat-fielding was necessary to correct for the pixel-to-pixel and large-scale sensitivity inhomogeneities of the detector. In taking sky flats at dawn, we took into account that the Earth’s atmosphere introduces a polarization signature. To minimize the effect of changing sky illumination and polarization, we selected 3 to 6 sky flats per night,

Table 3.1: Summary of the observations, first campaign. C/n denotes cycles per night, and HWP$_\alpha$ amount of the angles in which the HWP was rotated.

First campaign				
22/01	WASP-33		2	16
23/01	WASP-33		3	16
	HD 21447	UPS	1	16
24/01	WASP-33		3	16
	HD 21447		2	16
	HD 25443	PS	1	8
25/01	WASP-33		3	16
	HD 21447		1	16
26/01	HD25443		1	8
29/01	WASP-33		1	16
30/01	WASP-33		3	16
	HD 21447		1	16
31/01	WASP-33		2	16
	HD 21447		1, 1	16, 8
	HD 204827	PS	1	8
Second campaign				
12/09	WASP-33		2	16
	HD 212311	UPS	1	16
13/09	WASP-33		4	16
	HD 212311		1, 1	16, 8
14/09	WASP-33		4	16
	HD 212311		1	16
15/09	WASP-33		4	16
	HD 212311		1	16
	HD 25443		1	8

which show the same sky conditions, in particular, the same solar elevation. After applying bias and flat-field corrections, we carried out aperture photometry. In our analysis, we considered aperture radii between 2 and 15 arcsec (plate scale P = 53"/pix) and produced growth curves, which we used to identify the optimal aperture radius, i.e., the one maximizing the S/N ratio. Due to the weather conditions, the optimal aperture radius shows considerable night-to-night variability.

3.6 Polarimetric measurements

Our observations yield the normalized Stokes parameters Q/I and U/I and, therefore, the fraction of linearly polarized light.

3.6.1 Measuring linear polarization

To measure Q/I and U/I, we followed the prescription given by Patat & Romaniello (2006). From our measurements, we calculated the normalized flux differences F_i:

$$F_i = \frac{f_{O,i} - f_{E,i}}{f_{O,i} + f_{E,i}} \,, \tag{3.7}$$

where $f_{O,i} + f_{E,i}$ is the total flux, and $f_{O,i}$ and $f_{E,i}$ are the fluxes measured inside the chosen apertures for the ordinary and extraordinary beam. The index $i = 1, ..., N$ denotes the different positions of the HWP.

Based on the normalized flux differences, F_i, we calculated the Stokes parameters of WASP-33 and the standard stars as follows:

$$\hat{Q} = Q/I = \frac{2}{N}\sum_{i=1}^{N} F_i \cos\left(\frac{\pi}{8}i\right)$$

$$\hat{U} = U/I = \frac{2}{N}\sum_{i=1}^{N} F_i \sin\left(\frac{\pi}{8}i\right) \,. \tag{3.8}$$

Errors for $\hat{Q}$ and $\hat{U}$ were estimated by propagating the photometric errors, which, in turn, were derived using Poisson statistics.

3.7 First results

In order to measure such small polarization values, we first have to measure the polarization degree of the instrument.

During the first campaign we observed the unpolarized star HD 21447 during five nights using the technique outlined in Sect. 3.5. In particular, we obtained 6 cycles each with 16 HWP angles or, equivalently, 84 polarimetric points. By averaging the polarimetric data points, we obtained an estimate of the instrumental polarization. Figure 3.15 shows our first results.

As the reference star – simultaneously observed – is about 30 times fainter the the polarimetric standard in this case, we neglected it in the analysis.

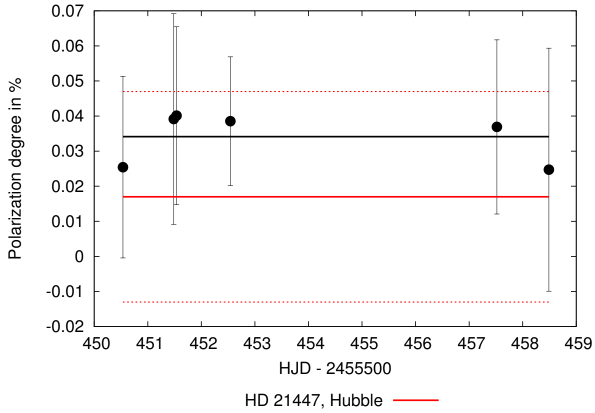

Figure 3.15: Polarization degree for an unpolarized standard star that was observed to calibrate Hubble Space telescope. Our measurements (black dots) are in agreement with previously reported values, indicated with red horizontal lines.

Chapter 4

Transit timing variations

4.1 Brief history

The meticulous observation of celestial bodies and the description of their movements started with the Greeks. Ptolemy (~300 BC) invented the epicycles system, a geometrical model used to explain the variations in direction and velocity of the Moon, the Sun, and the planets. In such an intricate system, the celestial bodies moved along small circles called *epicycles*. In turn, they moved along a larger circle called *deferent*, orbiting around a spatial point located between the Earth and the *equant* (see Figure 4.1). Although the first model not including epicycles was a Spanish product of the 12^{th} century, the Ptolemaic system was not ruled out until Johannes Kepler developed his theories.

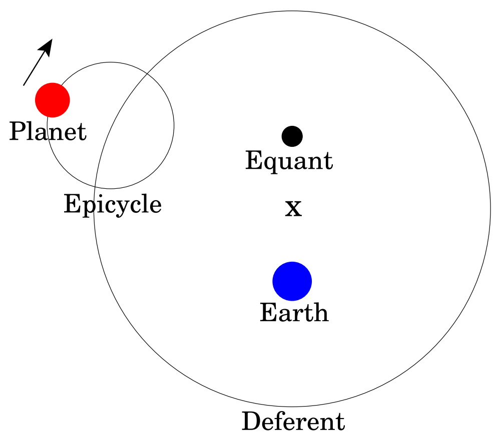

Source: C. von Essen.

Figure 4.1: Basic geometry of Ptolemy's epicycles system.

Nowadays it is widely known that the dominant influence on any planetary orbit is the mass of the star (Newton 1999, *"Principia")*. In the simplified case where a system is formed by a central body (the star) and one orbiting planet, the planet moves in a Keplerian orbit. If the planet transits the star, the transit events will occur exactly periodically. If, however, further bodies are present in the system, the orbits are no longer Keplerian and the time between transits varies (Holman & Murray 2005; Agol et al. 2005). Therefore, once an exoplanet is detected via the transit method, further exoplanets in the system can be indirectly detected using variations of the mid-transit time measurements of primary transit events. How large the timing variations are, depends on the masses of the involved bodies and the geometry of their orbits.

4.2 Orbital elements

Johannes Kepler was a German mathematician, astronomer, and astrologer. He published his three laws of motion during the 20 first years of the 17^{th} century. He found the first two laws in 1609, analyzing the astronomical observations of Tycho Brahe. For the Solar System, the three laws of Kepler are the following:

- Each planet moves, relative to the Sun, in an elliptical orbit. The Sun lies at one of the two foci of the ellipse.
- The rate of motion in the elliptical orbit is such that the vector pointing to the position of the planet relative to the Sun, spans equal areas of the orbital plane in equal times.
- The square of the orbital period P is proportional to the cube of the semi-major axis a of the orbital ellipse.

The orbital elements are six parameters, commonly used in astrophysics, required to uniquely identify a specific orbit. In celestial mechanics these elements are generally considered in classical two-body systems, where a Kepler orbit is used. Figure 4.2 shows a sketch of the three parameters that describe the shape of the orbit. In principle, only the semi-major axis a and semi minor axis b are required. Both parameters define the eccentricity $e = (a^2 - b^2)/a^2$, which is an indicator of how much does the orbit differ from a circular one. On an elliptical orbit, the closest point to the central body is called pericenter and the farthest one apocenter. It is easier and also of common use, to denote the position of a body using an orthogonal system with the origin at the focus of the ellipse (q_1, q_2). Alternatively, also polar coordinates (r, ν) can be used. From Fig. 4.2, the following relationships sustain:

$$\begin{cases} q_1 &= a(\cos E - e) \\ q_2 &= a\sqrt{1-e^2}\sin E \end{cases} \tag{4.1}$$

$$\begin{cases} r &= a(1 - e\cos E) \\ \cos\nu &= \frac{\cos E - e}{1 - e\cos E} \end{cases} \tag{4.2}$$

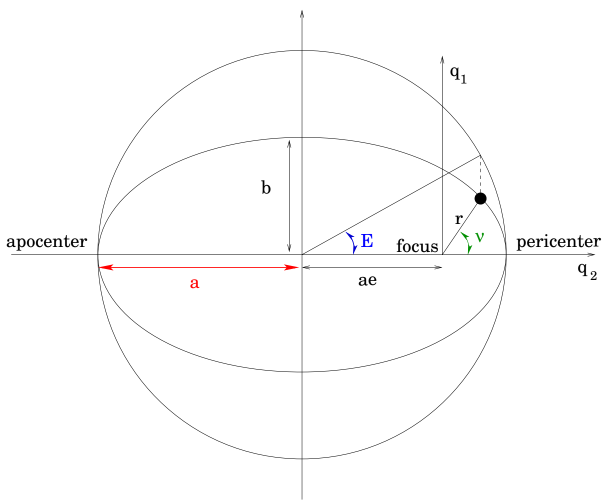

Source: C. von Essen.

Figure 4.2: Definition of a, e, ν, and E for a Keplerian orbit.

The true anomaly ν is the angle between the position of the orbiting body and the direction from the focus to the pericenter, measured counter clockwise. The eccentric anomaly E is the angle subtended at the center of the ellipse by the projection of the position of the body on the circle with radius equal to the semi-major axis. One only requires a, e and E to describe the position of a body in its orbit.

The Kepler equation relates the eccentric anomaly with time:

$$E - e\sin E = n(t - t_o) \,, \tag{4.3}$$

where

$$n = \sqrt{G(m_{cen} + m_{body})}a^{-3/2} \,, \tag{4.4}$$

is the orbital frequency or mean motion of the body. The mean anomaly M is then defined as an orbital element that defines the position of the body in its orbit and changes linearly with time.

Further, we need to characterize the orientation of the orbit in space. To do so, we use of an orthogonal reference frame (x,y,z) which center coincides with the position of the central body. Figure 4.3 shows a sketch of the required orbital parameters.

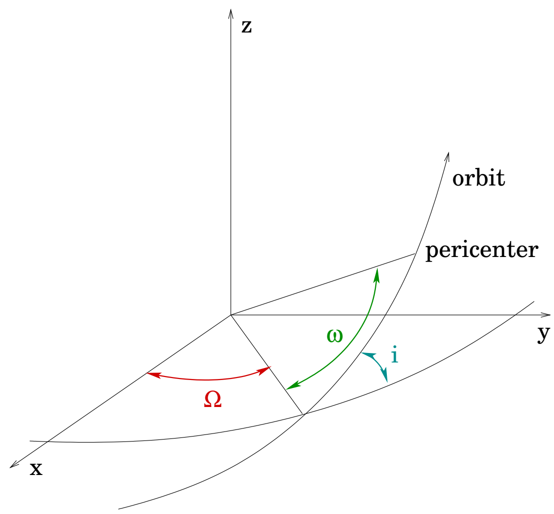

Source: C. von Essen.

Figure 4.3: Definition of i, ω and Ω for Keplerian motion.

The inclination i is the angle of the orbital plane, with respect to the reference plane (x, y). In astrophysics the reference plane is usually the plane of the sky. If the orbit has a non-zero inclination, then it intersects the reference plane in two points, distinguished as the ascending node when the orbiting body passes from the negative to positive z and the descending node in the other case. The orientation of the orbital plane in space is determined by the longitude of the node Ω, which is the angle between the ascending node and the reference direction indicated by the x-axis. For example, when the equatorial coordinate system is used, the reference direction is usually pointing at the vernal equinox γ. Finally, the argument of pericenter ω describes the orientation of the ellipse in the plane of the orbit. It is measured in the orbital plane relative to the line connecting the central body to the ascending node. The orbital elements a, e, i, ω, Ω and M give a complete picture of the position and velocity of the secondary body with respect to the central one.

4.3 The shapes of the orbits in the context of hot Jupiters

The detection of an Earth-size planet in the habitable zone has been the main goal of exoplanetary studies. Since these planets are very challenging to detect, it is helpful to model the known exoplanetary systems to establish whether such planets could exist (Jones et al. 2006). To understand the whole picture, certain effects need to be taken into consideration.

4.3.1 The Roche lobe and the Hill radius

The tidal force, or the "differential gravitational force" arises because different parts of a body experiences different gravitational forces. As a result, the body is deformed and sometimes, when conditions allow it, even disrupted. For the study of multiple planetary systems it is important to estimate the minimum distance at which two objects can orbit, without being disrupted. The Roche limit R_L is the distance within which a celestial body, held only by its own gravity, will disintegrate due to the tidal forces caused by the presence of a second body. This is a simplified view, because the limiting distance depends of other factors like the rigidity of the involved bodies. For example, a solid body will maintain its shape until the tidal forces break it apart, while a fluid body will gradually be deformed in an elongated way.

To determine the Roche limit, the mass of the planet m_P with a radius r_P and a "test mass" m_t in the surface of the planet have to be considered.

Assuming that the planet is orbiting around a massive star, the mass m_t will suffer the pull towards the planet and the pull towards the star. Then, the gravitational pull F_G on the mass m_t towards the planet can be expressed as

$$F_G = \frac{Gm_P m_t}{r_P^2} . \tag{4.5}$$

If the centers of the two bodies are separated by the distance d, the tidal force F_T on the mass m_t towards the star with mass M and radius R, can be expressed as:

$$\begin{aligned} F_T &= \frac{GMm_t}{(d-r_P)^2} - \frac{GMm_t}{d^2} \\ &= GMm_t \frac{d^2-(d-r_P)^2}{d^2(d-r_P)^2} \\ &= GMm_t \frac{2dr_P - r_P^2}{d^4 - 2d^3 r_P + r_P^2 d^2} . \end{aligned} \tag{4.6}$$

If we consider that $r_P << R$ and $R < d$, then

$$\begin{aligned} F_T &= GMm_t \frac{2dr_P}{d^4} \\ &= \frac{2GMm_t r_P}{d^3} . \end{aligned} \tag{4.7}$$

The Roche limit is reached when the gravitational force and the tidal force balance each other, $F_G = F_T$.

$$\frac{Gmm_t}{r_P^2} = \frac{2GMm_t r_P}{d^3} . \tag{4.8}$$

Therefore,

$$R_L = d = r_P \left(2\frac{M}{m_P}\right)^{1/3} . \tag{4.9}$$

Furthermore, Jones et al. (2006) defined a critical distance from a giant planet within which an Earth-mass planet would be ejected from its orbit. Using numerical simulations, the authors found this distance to be three times the Hill radius R_H. The Hill sphere is defined as the volume of space around a planet where the planet, rather than the star, dominates the gravitational attraction. A derivation of R_H can be obtained by equating the orbital angular speed of the orbiter around the planet, and the orbital angular speed of the planet around the host star. This would be the radius at which the gravitational influence of the star equals that of the planet.

$$\begin{aligned} \Omega_P &= \Omega_* \\ \sqrt{\frac{Gm_P}{R_H^3}} &= \sqrt{\frac{GM_*}{a^3}} \\ \frac{m_P}{R_H^3} &= \frac{M_*}{a^3} . \end{aligned} \tag{4.10}$$

Therefore,

$$R_H = \left(\frac{m_P}{M_*}\right)^{1/3} . \tag{4.11}$$

The critical distance given by $3 \times R_H$ depends on the orbital eccentricity (assumed to be zero in this simple deduction). Furthermore, the distance is being reduced towards the star, because the gravitational influence of the star is stronger there.

4.3.2 Circularization

Exoplanetary orbits are altered via tidal friction. When an exoplanet orbits close to the parent star, the tidal interaction between members can alter the orbit of the exoplanet. Generally, both semi-major axis and eccentricity are reduced, going to the minimum energy requirements, given by circular orbits. This process is called circularization. The circularization timescale for an orbit is defined as the ratio between the eccentricity and the rate of change of eccentricity with time:

$$\tau_{circ} = \frac{e}{|\dot{e}|} . \tag{4.12}$$

If the system is formed by a single planet orbiting a star, a more detailed mathematical treatment of tides shows that:

$$\tau_{circ} = \frac{3\omega^{-1}a^5}{18s + 7p} , \tag{4.13}$$

where ω is the mean orbital angular speed of the planet, a is the semi-major axis, and s and p two parameters that depend on the response of the bodies to the tides. The above formula shows that the circularization timescale strongly depends on the semi-major axis. Therefore, the timescales depend strongly on the size of the orbits. $\tau_{circ} \propto a^{13/2}$. As an example, if the orbit of an exoplanet is 10 times larger than that of another exoplanet with the same parameters, the circularization timescales will differ $10^{13/2} \sim 3 \times 10^6$ years. The smaller the orbit, the faster it will be circularized.

4.3.3 Eccentricity and exoplanetary orbits

The mean eccentricity of the known exoplanets increases with the increase in semi-major axis and period (see Figure 4.4). The short period exoplanets are in circular orbits because their circularization timescales are quite short. However, there are some close-in planets that still have significant orbital eccentricities. Either the planets are young, or some mechanism increases their eccentricity, such as resonant interactions between planets, close encounters between planets, or even interactions with a companion star in the system. The latter would imply that some exoplanetary systems have stellar companions that are still undetected.

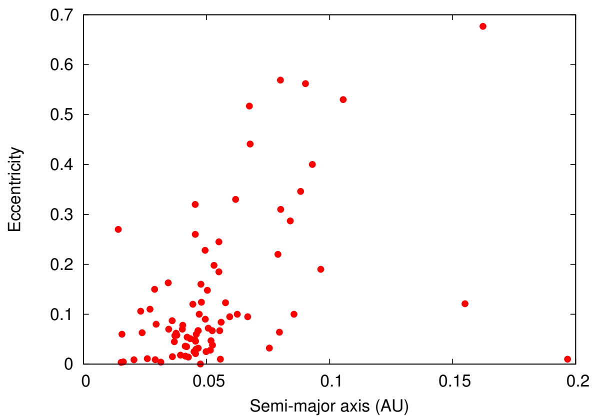

Source: http://www.exoplanet.eu.

Figure 4.4: Semi-major axis in astronomical units versus the eccentricity for the transiting systems known to date.

A *mean motion orbital resonance* happens when the orbital periods of two bodies share an integer ratio. The resonances can stabilize and also destabilize the systems. The stabilization happens when the two bodies never approach. This is the case of Pluto and Neptune: for every 2 orbits of Pluto, Neptune completes 3 around the Sun, but the 2 bodies never come close. Destabilization orbits are also found within our Solar System: considering Jupiter and the asteroid belt, there is a lack of asteroids at orbital period resonances of 3:1, 5:2, 7:3, and 2:1 with the orbital period of Jupiter. Similarly, within the rings of Saturn there is a gap, which corresponds to a 2:1 resonance with the orbital period of Saturn's moon Mimas (the gap is 4800 km wide, and is called "Cassini Division", Figure 4.5).

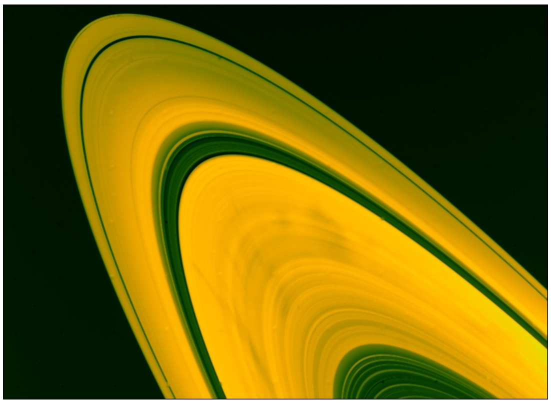

Source: http://zebu.uoregon.edu/~imamura/121/lecture-13/rings.html.

Figure 4.5: Large gap separating the main rings A and B, known as the Cassini Division. A particle moving in the Cassini Division has an orbital period 1/2 that of a moon Mimas.

Furthermore, for a *secular resonance*, eccentric orbits may precess, or change their orientation with time. Typically, the longitude of the pericenter or the longitude of the ascending node precess, changing the orientation of the orbit. In turn, during a *Kozai resonance*, the eccentricity and the inclination of an orbit oscillate with time. Regularly, the eccentricity increase while the inclination decreases, and *vice versa*.

4.4 Perturbation theory in the context of transit timing variations

About 25% of the known planetary systems form multiple planet systems (146 from 727 systems, September 2013, www.exoplanet.eu). Most multiple systems are formed by two planets. In addition, about one-third of the multiple systems appear to be in mean motion resonant orbits. Table 4.1 shows the basic orbital and physical parameters of one multiple system, Kepler-11.

Observations seem to prove that multiple systems are not rare. For transiting exoplanets it is, therefore, natural to study if the mid-transit times are affected by the presence of other bodies in the system. Depending on the orbital configuration, the perturbation will have a certain amplitude and period. Many efforts have been invested already to model such effects (e.g., Nesvorný & Morbidelli 2008; Agol et al. 2005).

To perform our transit timing variation analysis on Qatar-1, we used an N-body code (Agol et al. 2005), capable of producing timing variations caused by the presence of a third body in the system. The input parameters for the code are the stellar mass, the semi-major axis, the period, the inclination, the eccentricity, the longitude of ascending node, and the longitude of periastron for the two involved planets. The simplified case involves co-planar orbits. Using a MCMC approach for fast convergence, the program returns the best-fit orbital parameters by minimizing the residuals between the mid-transit times residuals of the transiting exoplanet and the model. The most relevant cases that Agol et al. (2005) considers are briefly explained below.

4.4.1 Inner perturber in a circular orbit

If both planets are in circular orbits, we can treat the system as consisting of an "inner binary" comprising the star and the perturber orbiting around the common barycenter, and an "outer binary" consisting of the inner binary and the transiting exoplanet (Figure 4.6). The transits of the outer planet will occur when it lines up with the star, as seen from a far observer. Since the inner binary orbits around its barycenter, the star will move with respect to the observer. Thus, the transit timing variations are caused because the star is displaced by the perturber.

4.4.2 Outer perturber

In the case in which the transiting exoplanet (labelled 1) is in a short inner circular orbit, and the perturber (labelled 2) is exterior to it and in an eccentric orbit, the presence of this planet causes an increase in the period of the orbit of the transiting planet by an amount that depends on the distance from the outer planet to the star (see Figure 4.7).

Planet	M_P (M_J)	R_P (R_J)	P (d)	a (AU)	i (°)
Kepler-11 b	0.01353	0.1762	10.30375	0.091	88.5
Kepler-11 c	0.0425	0.28175	13.02502	0.106	89.0
Kepler-11 d	0.01919	0.3068	22.68719	0.159	89.3
Kepler-11 e	0.02643	0.4043	31.9959	0.194	88.8
Kepler-11 f	0.00723	0.2335	46.68876	0.25	89.4
Kepler-11 g	0.95	0.3274	118.37774	0.462	89.8

Source: `http://www.exoplanet.eu`.

Table 4.1: Orbital parameters for the multiple system Kepler-11 (Lissauer et al. 2011). Kepler-11 b and c orbit in a first order mean motion resonance of 5:4. The parent star resembles our Sun, with the exception of its age (8±2 Gyr).

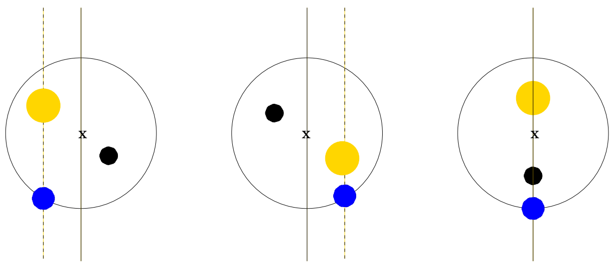

Source: C. von Essen.

Figure 4.6: If a perturbing planet (black circles) happens to be in an inner orbit, the transit timings of the outer planet (blue circles) will be altered (the picture is out of scale). The star is represented with yellow circles.

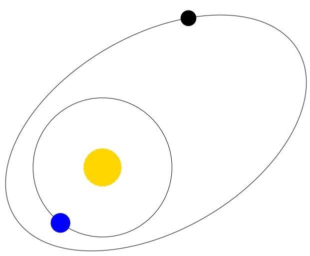

Source: C. von Essen.

Figure 4.7: Interior and transiting planet (blue circle) in a circular orbit; exterior perturber (black circle) in an eccentric orbit.

Since the perturber is in an eccentric orbit, its distance to the star changes with time and it causes a periodic change in the orbital period of the inner binary. The maximum TTV for the inner planet is given by:

$$\delta t_1 \sim \mu_2 e_2 \left(\frac{a_1}{a_2}\right)^3 P_2 \ , \tag{4.14}$$

where r_2 is the distance from the outer planet to the star, and $\mu_2 \sim M_2/M_*$ is the reduced mass of the outer planet.

4.4.3 Planets in mean motion resonances

In this case, Agol et al. (2005) assume a first order resonance, $j + 1 : j$, and one planet less massive than the other ($m_1 << m_2$). The transiting planet is in an interior orbit to the perturbing planet, so $P_2 < P_1$. The two planets will be in conjunction every j orbits of the outer planet and will have the same longitude each time a conjunction occurs. This will increase the eccentricity of the less massive planet and change in consequence the orbital period and semi-major axis. The change in period causes the longitude of the conjunction to change in time, until a shift in 180° has accumulated relative to the initial position. At this point the eccentricity will decrease again. This is called the *libration cycle*. A good fit to the data, obtained by means of numerical simulations, is given by:

$$\begin{aligned} \delta t_2 &\sim \frac{P_2}{4.5j}\frac{m_1}{m_1+m_2} \\ P_{lib} &\sim 0.5 j^{-4/3}\mu_2^{-2/3} P_2 \ , \end{aligned} \tag{4.15}$$

where μ_2 is the reduced mass of the transiting planet given by $M_2/M_{tot} \sim M_2/M_*$. Figure 4.8 shows the transit timing variations for planets in resonant orbits. The system is formed by a planet of mass $M_P = 10^{-3} M_\odot$ in a 12 days orbital period. The perturber's mass is $M_{pert} = 3 \times 10^{-6} M_\odot$

(i.e., Earth-mass). Both orbit around a star of mass $M_* = M_\odot$, in initially circular and coplanar orbits.

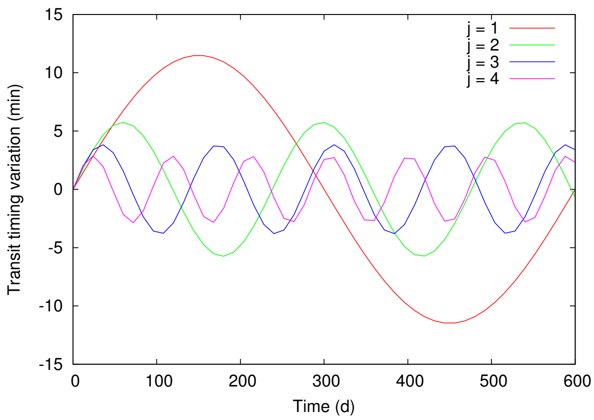

Figure 4.8: Expected transit timing variations for planets in first order mean motion resonances.

4.5 Space-based observations: The Kepler telescope

In March 2009, NASA launched the Kepler space telescope (Borucki et al. 2010; Koch et al. 2010). The main goal of the mission was to detect Earth-sized planets in the habitable zone, orbiting around stars similar to our Sun. The wide field of view, which is fixed around the constellations of Cygnus, Lyra, and Draco, allows simultaneous monitoring of hundred thousands of stars. Kepler photometry is available at either short cadence (~1 minute) for 512 targets, or long cadence (~30 minutes) for 170 000 targets. The differential photometry has an unprecedented precision of 10 - 20 parts per million, needed to detect the signal from an Earth–Sun equivalent transit (Gilliland et al. 2011).

4.5.1 KOI-676: My contribution

KOI-676 (KIC 7447200) was identified as planet host candidate by the Kepler team. The light curves show a modulation which is typically associated to stellar activity. Furthermore, the system is conformed by two planet candidates which are in a very close 13:4 mean motion resonance. The photometric precision and constant monitoring that the Kepler data provides (~500 days, ~90 primary transits for the outer body, ~400 primary transits for the inner body) allowed us to study transit timing variations in the system.

Panagiotis Ioanidis, a colleague of mine at Hamburger Sternwarte, had the leading idea to study the KOI-676 system. I contacted Prof. Eric Agol, who provided us with the N-body code needed to simulate the transit timing variations. Since Panagiotis was a new student, I helped him only initially, involving myself in the basic analysis described in Sections 2 and 3 (data reduction, data analysis, and first TTV analysis). After some time, Prof. Schmitt involved himself more in Panagiotis work, so I stepped back.

Qatar-1: indications for possible transit timing variations

C. von Essen, S. Schröter, E. Agol & J. H. M. M. Schmitt
Astronomy & Astrophysics, Volume 555, Issue 92 (2013)
The original publication is available at: http://adsabs.harvard.edu/abs/2013A%26A...555A..92V

A&A 555, A92 (2013)
DOI: 10.1051/0004-6361/201321407

Astronomy & Astrophysics

Qatar-1: indications for possible transit timing variations⋆

C. von Essen[1], S. Schröter[1], E. Agol[2], and J. H. M. M. Schmitt[1]

[1] Hamburger Sternwarte, University of Hamburg, Gojenbergsweg 112, 21029 Hamburg, Germany
e-mail: cessen@hs.uni-hamburg.de
[2] Dept. of Astronomy, Box 351580, University of Washington, Seattle, WA 98195, USA

Received 5 March 2013 / Accepted 22 May 2013

ABSTRACT

Aims. Variations in the timing of transiting exoplanets provide a powerful tool for detecting additional planets in the system. Thus, the aim of this paper is to discuss the plausibility of transit timing variations (TTVs) on the Qatar-1 system by means of primary transit light curves analysis. Furthermore, we provide an interpretation of the timing variation.

Methods. We observed Qatar-1 between March 2011 and October 2012 using the 1.2 m OLT telescope in Germany and the 0.6 m PTST telescope in Spain. We present 26 primary transits of the hot Jupiter Qatar-1b. In total, our light curves cover a baseline of 18 months.

Results. We report on indications for possible long-term TTVs. Assuming that these TTVs are true, we present two different scenarios that could explain them. Our reported ~190 days TTV signal can be reproduced by either a weak perturber in resonance with Qatar-1b, or by a massive body in the brown dwarf regime. More observations and radial velocity monitoring are required to better constrain the perturber's characteristics. We also refine the ephemeris of Qatar-1b, which we find to be $T_0 = 2456157.42204 \pm 0.0001$ BJD_{TDB} and $P = 1.4200246 \pm 0.0000007$ days, and improve the system orbital parameters.

Key words. methods: data analysis – methods: observational – techniques: photometric – eclipses

1. Introduction

The discovery of Neptune in 1846 was a milestone in astronomy. The position at which the planet was detected by Galle had been predicted – independently – by Le Verrier and Adams, who attributed the observed irregularities of Uranus' orbit to the gravitational attraction of another perturbing body outside Uranus' radius. Thus, Neptune became the first planet to be predicted by celestial mechanics before it was directly observed.

Similar to the case of Neptune, in the realm of exoplanets an additional planet or exomoon can reveal itself by its gravitational influence on the orbital elements of the observed planet. Most notably, for transiting planets a perturber is expected to induce short-term transit timing variations (TTVs; Holman & Murray 2005; Agol et al. 2005); because timing measurements can be carried out quite accurately, the TTV searches are quite sensitive, and it is possible to detect additional objects in the stellar system and to derive their properties with TTVs.

The detection of TTVs in ground-based measurements requires both a sufficiently long baseline and good phase coverage. The search for planets by TTVs has been a major activity in ground-based exoplanet research. So far, TTVs have been claimed in WASP-3b (Maciejewski et al. 2010), WASP-10b (Maciejewski et al. 2011), WASP-5b (Fukui et al. 2011), HAT-P-13 (Pál et al. 2011; Nascimbeni et al. 2011, but see Fulton et al. 2011), and OGLE-111b (Díaz et al. 2008, but see Adams et al. 2010).

In recent years, the search for TTVs in extrasolar planetary systems has entered a new era, marked by the advent of the space-based observatories CoRoT and *Kepler*, which provide photometry of unprecedented accuracy. On one hand, the *Kepler* team has already presented more than 40 TTVs in exoplanetary systems, such as Kepler-9 (Holman et al. 2010), Kepler-11 (Lissauer et al. 2011), Kepler-19 (Ballard et al. 2011), Kepler-18 (Cochran et al. 2011), and Kepler 29, 30, 31 and 32 (Fabrycky et al. 2012). On the other hand, Steffen et al. (2012) searched for planetary companions orbiting hot-Jupiter planet candidates and found that most of the systems show no significant TTV signal. Yet, the *Kepler* satellite observes only a small area of the sky and has a limited lifetime, thus TTV will continue to play a major role also in ground-based studies.

The transiting Jovian planet Qatar-1b was discovered by Alsubai et al. (2011) as the first planet found within The Qatar Exoplanet Survey. Qatar-1A is an old (>4 Gy) K3V star with 0.85 $M_\odot$ and 0.82 $R_\odot$, orbited by a close-in (0.023 AU) planet with a mass of 1.1 M_J and a period of 1.42 d. Qatar-1b has a radius of 1.16 R_J and an inclination angle of 83.47°, implying a nearly grazing transit. Therefore Qatar-1 offers an outstanding opportunity to search for TTVs for several reasons: Its large inclination and close-in orbit yield a high-impact parameter, making the shape and timing of the transit sensitive to variations of the orbital parameters. Its large radius and short orbital period allow for the study of a large number of deep transits over hundreds of epochs.

We have therefore observed transits in Qatar-1b over the past few years, which we describe here. We specifically describe the observational setup in Sect. 2 as well as the data reduction process. We subsequently present the details of our light curve analysis and transit modeling in Sect. 3 and describe our TTV analysis in Sect. 4. We interpret our results in Sect. 5, where we present different dynamical scenarios that were tested to suggest the existence of an additional body in the system. In Sect. 6 we conclude.

⋆ Tables of the transit observations are only available at the CDS via anonymous ftp to cdsarc.u-strasbg.fr (130.79.128.5) or via http://cdsarc.u-strasbg.fr/viz-bin/qcat?J/A+A/555/A92

A&A 555, A92 (2013)

Table 1. Summary of our observations carried out with OLT (top) and PTST (bottom).

Date	Epoch	ET (s)	F	NoP	Airmass	TC
OLT						
2011 March 19	–364	202	R_1	29	1.83 → 1.40	– IBE –
2011 March 26	–359	296	R_1	28	1.45 → 1.19	OIBE –
2011 May 22	–319	173	R_1	48	1.60 → 1.18	OIBEO
2011 May 29	–314	58	R_1	72	1.19 → 1.08	– – BEO
2011 July 5	–288	82	R_1	78	1.13 → 1.03	– – BEO
2011 July 15	–281	136	R_1	86	1.21 → 1.02	– – BEO
2011 August 1st	–269	68	R_1	108	1.12 → 1.02	OIBEO
2011 August 28	–250	80	R_1	42	1.02 → 1.04	– – BEO
2011 October 1st	–226	79	R_1	136	1.12 → 1.02	OIBEO
2012 April 21	–83	141	R_1	97	1.73 → 1.18	OIBEO
2012 April 24	–81	90	R_1	40	1.80 → 1.61	– – BEO
2012 May 1st	–76	70	R_1	177	1.71 → 1.18	OIBEO
2012 June 17	–43	53	R_1	61	1.39 → 1.21	– – – EO
2012 July 1st	–33	76	R_1	112	1.12 → 1.02	OIB – –
2012 August 17	0	50	R_1	425	1.12 → 1.14	OIBEO
2012 September 13	19	64	R_1	124	1.05 → 1.04	OI – – O
2012 September 30	31	59	R_1	100	1.04 → 1.14	– IBEO
2012 October 30	52	52	R_1	275	1.03 → 1.16	OIBEO
PTST						
2012 February 27	–121	90	R_2	109	3.00 → 1.47	OIBEO
2012 May 11	–69	59	R_2	183	2.84 → 1.30	OIBEO
2012 May 28	–57	90	R_2	106	2.00 → 1.18	OIBEO
2012 June 17	–43	40	R_2	168	1.86 → 1.34	– – BEO
2012 July 4	–31	70	R_2	80	1.50 → 1.15	OIBEO
2012 July 14	–24	60	R_2	86	1.42 → 1.22	– – – EO
2012 July 31	–12	60	R_2	133	1.32 → 1.11	OIBEO
2012 August 17	0	40	R_2	182	1.22 → 1.23	OIBEO

Notes. Columns: epoch, exposure time ET, filter configuration F, number of data points NoP, airmass and transit coverage (TC); a description of the transit coding is detailed below. Epochs are counted relative to the best-fitting transit. Transits observed simultaneously with both telescopes are marked in boldface. Observations were obtained in filter configurations R_1 and R_2 denoting the Schuler Johnson-Cousins *R*-band, and the Baader *R*-band, respectively. The letter code to specify the transit coverage during each observation is the following: O: out of transit, before ingress. I: ingress. B: flat bottom. E: egress. O: out of transit, after egress.

2. Observations and data reduction

Our observations comprise 18 transits of Qatar-1 obtained using the 1.2 m Oskar-Lühning telescope (OLT) at Hamburg Observatory, Germany, and 8 transits using the 0.6 m Planet Transit Study Telescope (PTST) at the Mallorca Observatory in Spain.

The OLT data were taken between March 2011 and October 2012 using an Apogee Alta U9000 CCD with a $9' \times 9'$ field of view. Binning was usually 4×4, but the first transit observations were taken in a 2×2 configuration. The binning was increased to reduce individual exposure times. The data were obtained with typical exposure times between 45 and 300 s depending on the night quality, the binning configuration, and the star's altitude. All exposures were obtained using a Johnson-Cousins Schuler *R* filter. Because Qatar-1 is circumpolar at Hamburg's latitude, typical airmass values range from 1 up to 1.9, while the average seeing value is 2.5 arcsec.

The PTST data were taken between May and August 2012 using a Santa Barbara CCD with a $30' \times 30'$ field of view in a 3×3 binning and a Baade *R*-band filter setup. The exposure times range from 50 to 90 s. The observations were obtained with airmass values between 1.1 and 3 and typical seeing values of 2 arcsec. In Table 1 we summarize the main characteristics of our observations obtained at both sites. Combining OLT and PTST data, the observations cover a total of 416 epochs.

Calibration images such as bias and flat fields were obtained on each observing night. We used the IRAF task *ccdproc* for bias subtraction and flat-fielding on the individual data sets, followed by the task *apphot* to carry out aperture photometry on all images including individual photometric errors. We measured fluxes using different apertures centered on the target star and six more stars with a similar brightness as Qatar-1, which are present in both field of views. The apparent brightness of the reference star chosen to produce the differential light curves is very close to Qatar-1. Multiband photometry of the same field of view reveals no significant difference between both stars as a function of photometric color, either suggesting that they are of similar spectral type. This minimizes any atmospheric extinction residuals on the differential light curves, and in addition, the apparent proximity of the two stars (~2 arcmin) minimizes systematic effects related to vignetting, comatic aberration, or CCD temperature gradients, which all increase with increasing distance from the telescope's optical axis (i.e., the center of the chip). We also checked the constancy of the reference star against the other five comparison stars and chose as final aperture the one that minimized the scatter in the resulting light curves. The differential light curves were then produced by dividing the flux of the target star by that of the reference star.

Typical sky brightness values per binned pixel were of about 3500 counts for OLT, and 2000 for PTST. Figure 1 shows the PTST field of view (light background) superposed on the field

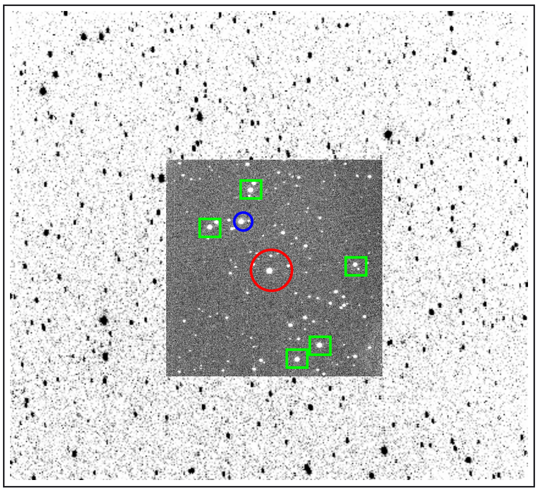

Fig. 1. Oskar-Lühning telescope (dark background) and Planet Transit Search Telescope (light background) field of views. Qatar-1 is indicated with a large red circle centered on the OLT field of view, along with the comparison stars as green squares. The small blue circle upward and to right of Qatar-1 indicates the reference star used to produce the differential photometry.

of view of OLT (dark background). Qatar-1 lies at the center of the field of view, marked with a large red circle. The five comparison stars are indicated with green squares and the reference star, indicated with a small blue circle, is the one used to produce the differential light curves.

After the reduction process, we fitted a straight line to the out-of-transit data points to correct for any residual systematic trend and to normalize the differential light curves. It is worth mentioning that we calculated the timing offsets using both raw and normalized data. We therefore confirm that the normalization process does not produce any shifts in the mid-transits but only more accurate planetary parameters. This might be because the amplitude of any systematic trend present in our light curves was smaller than ~2 mmag.

3. Data analysis

3.1. Data preparation

IRAF provides heliocentric corrections, therefore our time stamps are given as heliocentric Julian dates ($\mathrm{HJD_{UTC}}$) and are converted into barycentric Julian dates ($\mathrm{BJD_{TDB}}$) using the web tool provided by Eastman et al. (2010)[1].

3.2. Fit approach

We fitted the transit data with the transit model developed by Mandel & Agol (2002), making use of their `occultquad` FORTRAN routine[2]. From the transit light curve, we can directly infer the following parameters: the orbital period P, the mid-transit time T_0, the radius ratio $p = R_p/R_s$, the semi-major axis (in stellar radii) a/R_s, and the orbital inclination i. For our fits we assumed a quadratic limb-darkening law with fixed coefficients u_1 and u_2.

[1] http://astroutils.astronomy.ohio-state.edu/time/

[2] http://www.astro.washington.edu/users/agol

Table 2. Best-fit limb-darkening coefficients (LDCs) for OLT and PTST, along with the 1σ errors.

LDCs	OLT	PTST
u_1	0.5860 ± 0.0053	0.6025 ± 0.0051
u_2	0.1170 ± 0.0075	0.1140 ± 0.0073

3.3. Limb-darkening coefficients

Alsubai et al. (2011) presented a spectroscopic characterization of Qatar-1 based on comparing their observed spectrum with synthetic template spectra and suggested that Qatar-1 has an effective temperature T_{eff} of 4861 ± 125 K, a surface gravity $\log g$ of 4.536 ± 0.024, and solar metallicity [Fe/H] of 0.20 ± 0.10. Because our observations with OLT and PTST were obtained using different (non-standard) filter sets, we decided to calculate angle-resolved synthetic spectra from spherical atmosphere models using PHOENIX (Hauschildt & Baron 1999; Witte et al. 2009) for a star with effective temperature $T_{\mathrm{eff}} = 4900$ K, [Fe/H] = 0.20 and $\log g = 4.5$, thereby closely matching the spectroscopic parameters of Qatar-1A. We then convolved each synthetic spectrum with the OLT and PTST filter transmission functions and integrated in the wavelength domain to compute intensities as a function of $\mu = \cos\theta$, where θ is the angle between the line of sight and the radius vector from the center of the star to a reference position on the stellar surface. The thus derived intensities were then fitted with a quadratic limb-darkening prescription, viz.

$$I(\mu)/I(1) = 1 - u_1(1-\mu) - u_2(1-\mu)^2,$$

to obtain the u_1 and u_2 limb-darkening coefficients. As an aside, we note that the best approach to obtain limb-darkening coefficients would be to fit a more sophisticated bi-parametric approximation to the stellar intensities (Claret & Hauschildt 2003) to the PHOENIX intensities, which produces the smallest deviations in the generation of the limb-darkening coefficients, which fits the stellar limb better. However, to introduce such a limb-darkening law in the production of primary transit light curves would be computationally cumbersome. Moreover, Qatar-1 is a nearly grazing system, where changes in limb darkening do not strongly affect the primary transit light curves. We checked that the time that the planet spends in the small-μ regime is very short. Furthermore, at a given time the planet covers a broad range of μ-values. Neglecting these points in determining the limb-darkening coefficients will probably not affect the subsequent parameter determination. To calculate the OLT and PTST limb-darkening coefficients, we fitted a quadratic limb-darkening law to PHOENIX intensities, neglecting the data points between $\mu = 0$ and $\mu = 0.1$. Figure 2 shows the OLT and PTST limb-darkening normalized functions, and Table 2 the fitted limb-darkening coefficients.

3.4. Parameter errors

To determine reliable errors for the fit parameters given the mutual dependence of the model parameters, we explored the parameter space by sampling from the posterior-probability distribution using a Markov-chain Monte-Carlo (MCMC) approach.

A&A 555, A92 (2013)

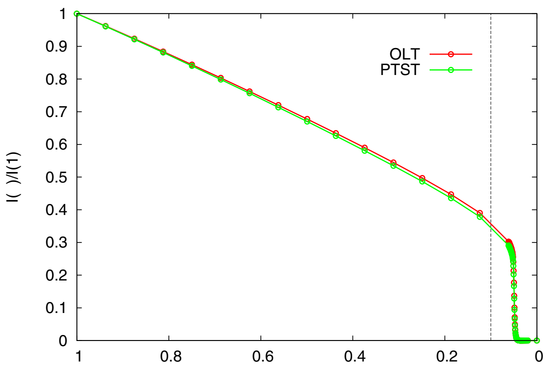

Fig. 2. Qatar-1 normalized intensities considering the OLT and PTST filter transmission functions. Data points on the right of the vertical dashed line were not considered in the fitting procedure.

The near-grazing transit geometry of Qatar-1 introduces a substantial amount of correlation between the system parameters, which can easily render the MCMC sampling process inefficient. To cope with these difficulties we used a modification to the usually employed Metropolis-Hastings sampling algorithm, which is able to adapt to the strong correlation structure. This modified Metropolis-Hastings algorithm is described in the seminal work by Haario et al. (2001) and has become known as the adaptive Metropolis (AM) algorithm. It works like the regular Metropolis-Hastings sampler, but relies on the idea of allowing the proposal distribution to depend on the previous values of the chain.

The regular Metropolis-Hastings algorithm produces chains based on a proposal distribution that may depend on the current state of the chain. The proposal distribution is often chosen to be a multivariate normal distribution with fixed covariance. The main difference between the regular Metropolis sampler and AM is that AM updates the covariance matrix during the sampling, e.g. every 1000 iterations. Because the proposal distribution is thus tuned based on the entire sampling run, AM chains in fact lose the Markov property. Nonetheless, it can be shown that the algorithm retains the correct ergodic properties under very general assumptions, i.e., the covariance matrix stabilizes during the sampling process and AM chains properly simulate the target distribution (Haario et al. 2001; Vihola 2011). Although adaptive MCMC algorithms are a recent development, they have successfully been used by other authors in the astronomical community, for instance by Balan & Lahav (2009), Irwin et al. (2010) and Irwin et al. (2011).

Our MCMC calculations make extensive use of routines of `PyAstronomy`[3], a collection of Python routines providing a convenient interface for fitting and sampling algorithms implemented in the PyMC (Patil et al. 2010) and SciPy (Jones et al. 2001) packages. The AM sampler is implemented in the PyMC package, which is publicly available for download. We refer to the detailed online documentation[4].

We checked that AM does yield correct results for simulated data sets with parameters close to Qatar-1, and found that this approach showed fast convergence and was efficient. To express our lack of more a priori knowledge regarding the Qatar-1 system parameters, we assumed uninformative uniform prior probability distributions for all parameters, but we found that the parameters are well determined, so that the actual choice of the prior is unimportant for our results.

In Fig. 3 we show our 26 obtained light curves, along with the residuals after removing the primary transit feature. Our final relative photometry is available in its entirety in machine-readable form in the electronic version of this paper. First columns contain BJD_{TDB}, second columns normalized flux, and third columns individual errors.

3.5. Correlated noise

Carter & Winn (2009, and references therein) studied how time-correlated noise affects the estimation of the parameter of transiting systems. To quantify whether and to what extent our light curves are affected by red noise, we reproduced part of their analysis as follows: First, we produced residuals from our final fits by subtracting the primary transit model from each light curve. We individually divided each light curve into M bins of equal duration. Since our data are not always equally spaced, we calculated a mean value N of data points per bin. If the data are not affected by red noise, they should follow the expectation of independent random numbers,

$$\sigma_N = \sigma_1 N^{-1/2}[M/(M-1)]^{1/2},$$

where σ_1 is the sample variance of the unbinned data and σ_N is the sample variance (or rms) of the binned data, with the following expression:

$$\sigma_N = \sqrt{\frac{1}{M}\sum_{i=1}^{M}(\langle\hat{\mu}_i\rangle - \hat{\mu}_i)^2},$$

where $\hat{\mu}_i$ is the mean value of the residuals per bin, and $\langle\hat{\mu}_i\rangle$ is the mean value of the means.

If correlated noise is present, then each value σ_N will differ by a factor β_N from their expectation. The parameter β, an estimation of the strength of correlated noise in the data, is found by averaging β_N over a range Δn corresponding to time scales that are judged to be most important. For data sets free of correlated noise, we expect $\beta = 1$. For primary transit observations, Δn is the duration of ingress or egress. For Qatar-1, the time between first and second contact (or equivalently, the time between third and fourth contact) is ~15 min.

In Fig. 4 we show the results of our correlated noise analysis for nine of the longest light curves. Black lines represent the expected behavior in the absence of red noise, and red and green lines represent the variance of the binned data for OLT and PTST, respectively, as a function of bin size. As expected, the larger the bin size, the smaller the rms. For each light curve we calculated β considering $\Delta n = 15$ minutes. For the OLT and PTST primary transits, β lies between $\beta = 0.78$ and $\beta = 1.33$, with $\langle\beta\rangle = 1.038$. Thus, there is no evidence for significant correlated noise in our light curves.

Finally, Pont et al. (2006) suggested to enlarge individual photometric errors by a factor β to account for systematic effects on the light curves. This would increase the parameter errors without changing the parameter estimates. Since our light curves do not present any strong evidence of correlated noise, we did not modify the individually derived errors.

[3] http://www.hs.uni-hamburg.de/DE/Ins/Per/Czesla/PyA/PyA/index.html
[4] http://pymc-devs.github.io/pymc/

C. von Essen et al.: Transit timing variations on Qatar-1

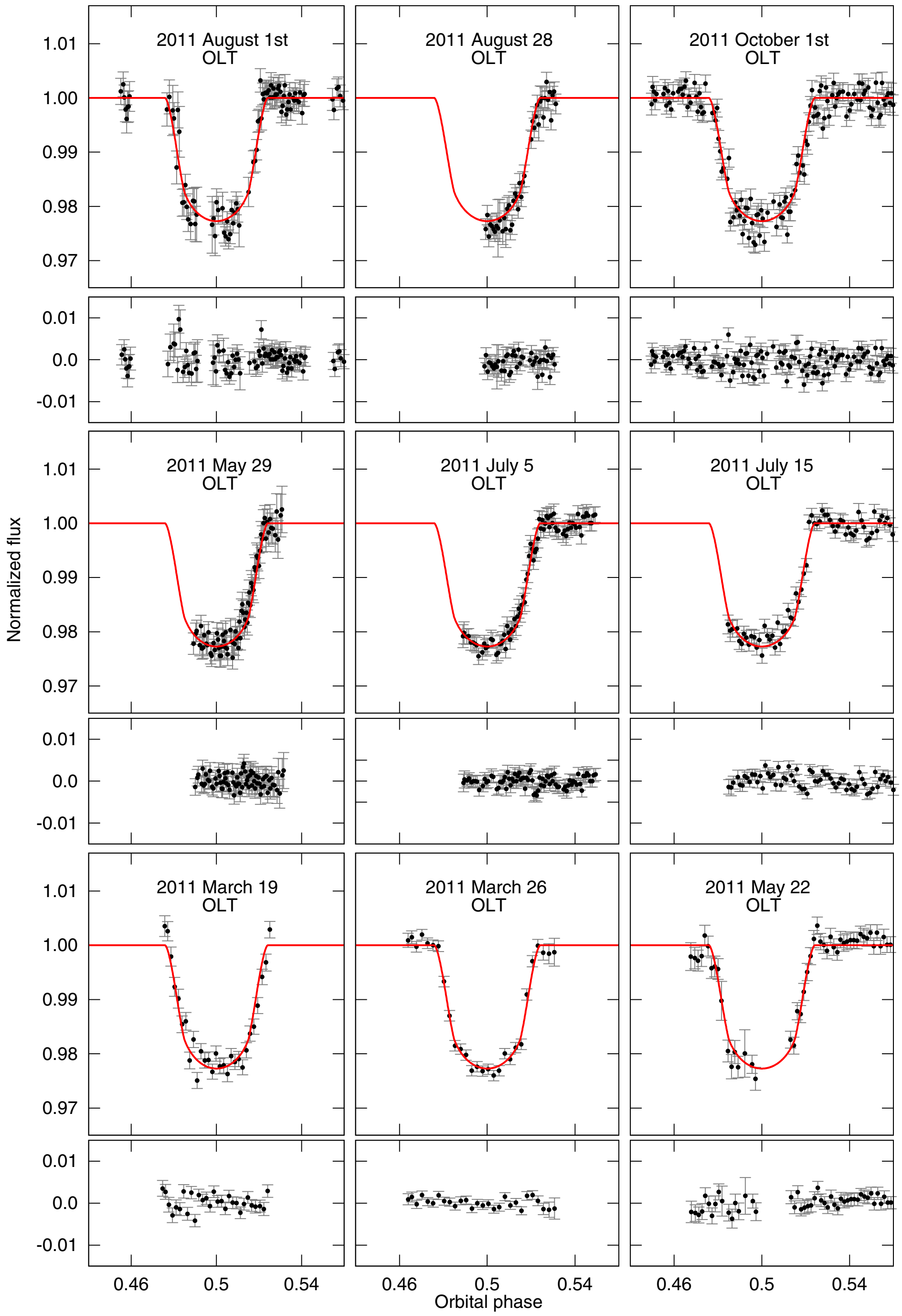

Fig. 3. OLT and PTST light curves (*top panels*). Superposed is the Mandel & Agol (2002) primary transit light-curve model in a continuous line, considering the parameters obtained in Sect. 3.2. As indicated by the dates, the light curves evolve in time *from bottom to top* and *from left to right*. The residuals (*bottom panels*) have been calculated after subtracting the best transit fit parameters.

A&A 555, A92 (2013)

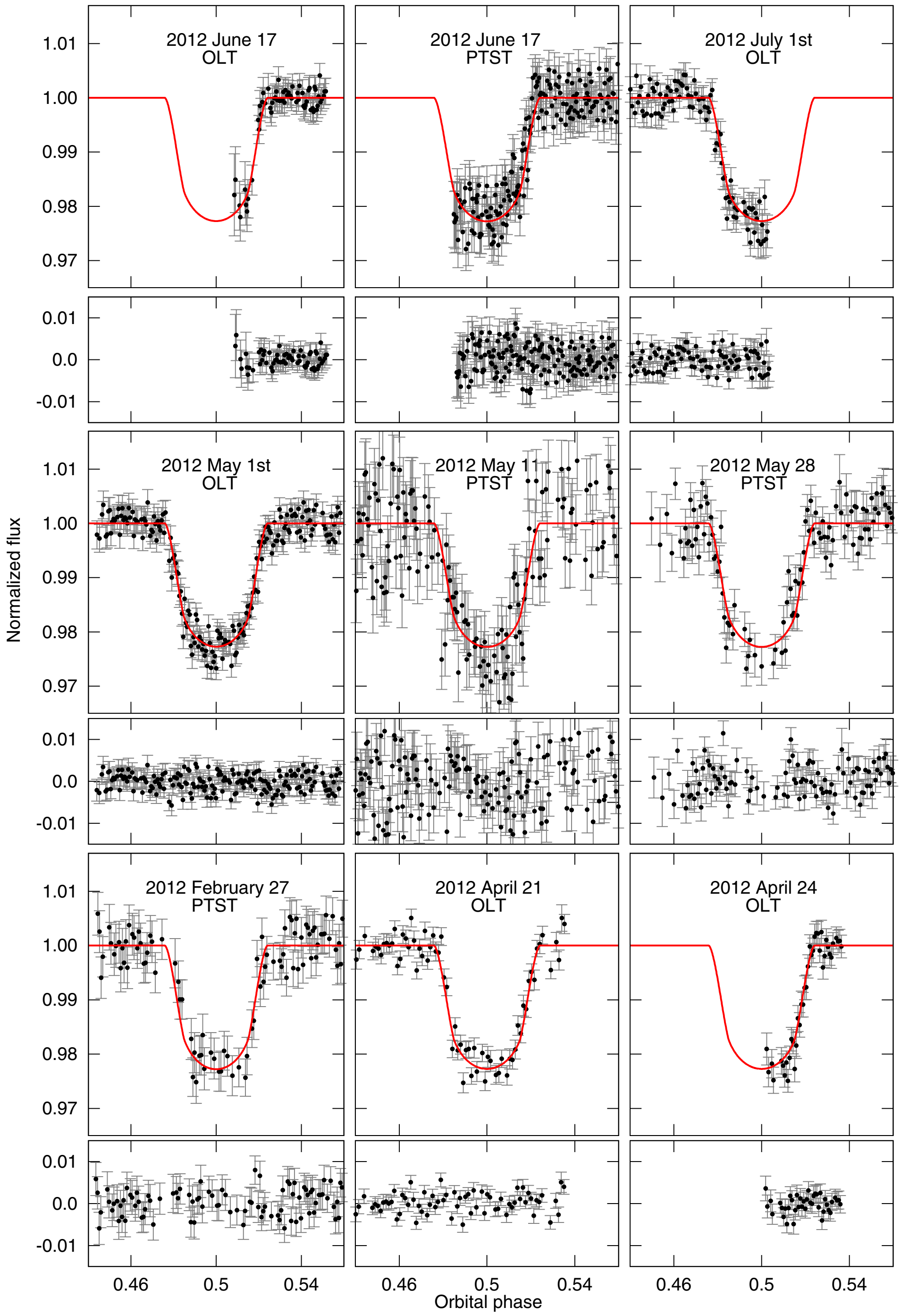

Fig. 3. continued.

C. von Essen et al.: Transit timing variations on Qatar-1

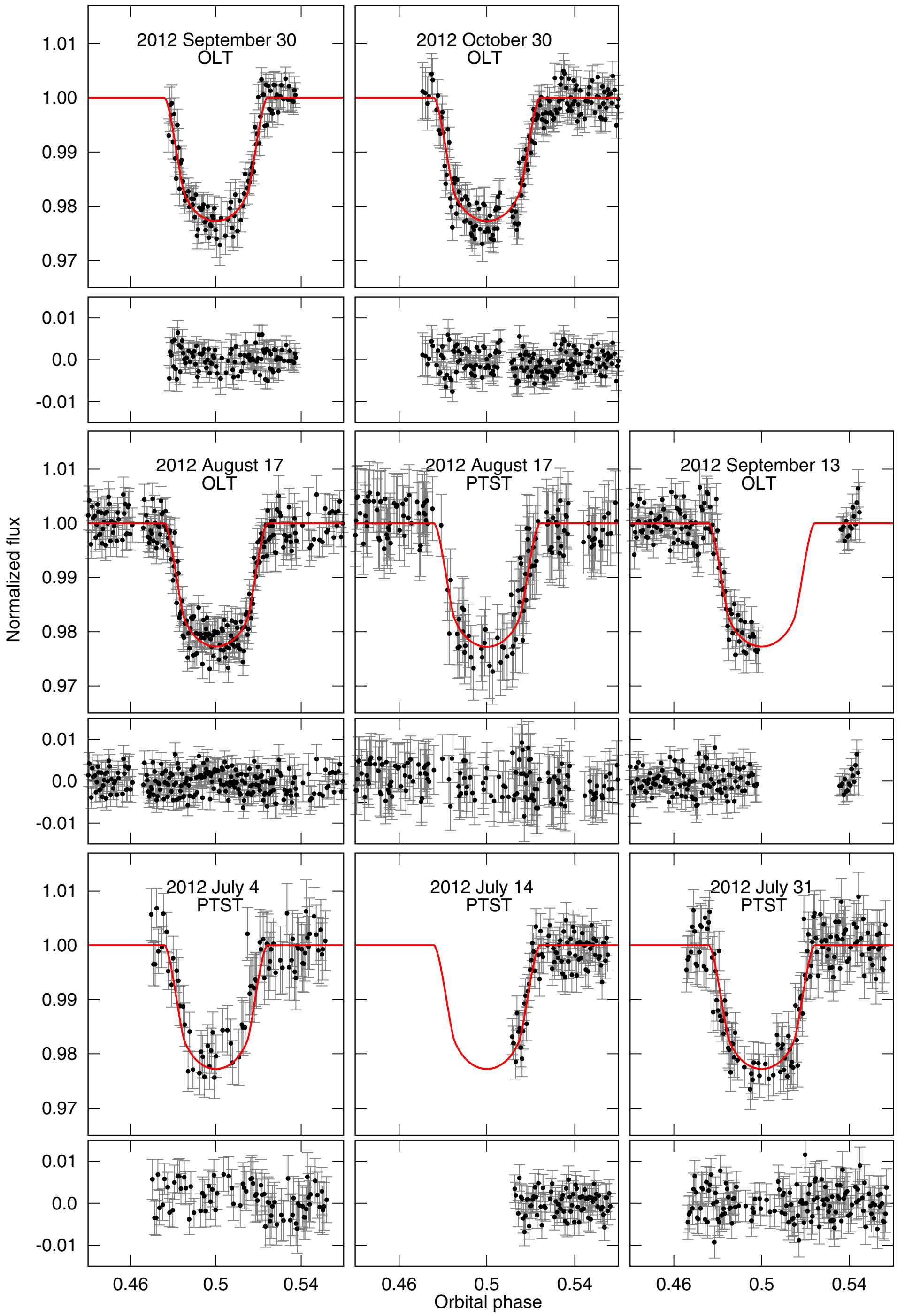

Fig. 3. continued.

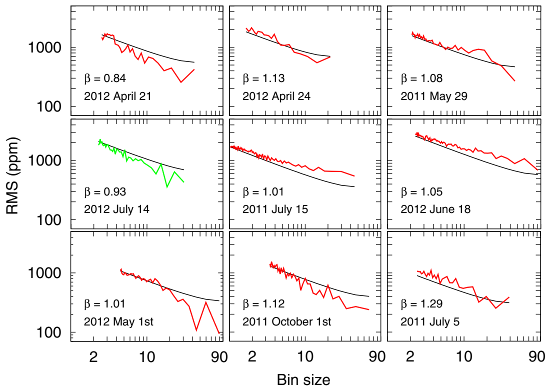

Fig. 4. Qatar-1 rms in parts per million (ppm) of the time-binned residuals as a function of bin size in logarithmic scale. Red and green lines correspond to OLT and PTST data respectively, and black lines show the expected behavior under the presence of uncorrelated noise.

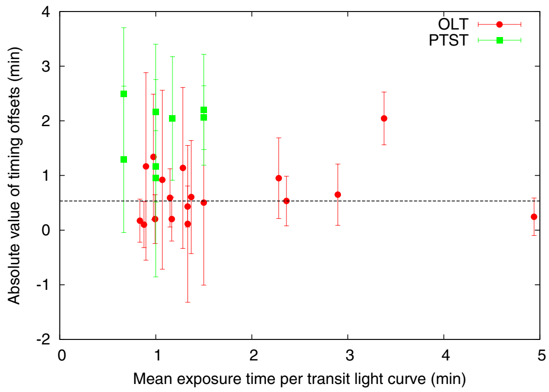

Fig. 6. Timing-residual magnitudes in minutes for OLT (red circles) and PTST (green squares), as a function of mean exposure times. The horizontal dashed line indicates half of the mean exposure time.

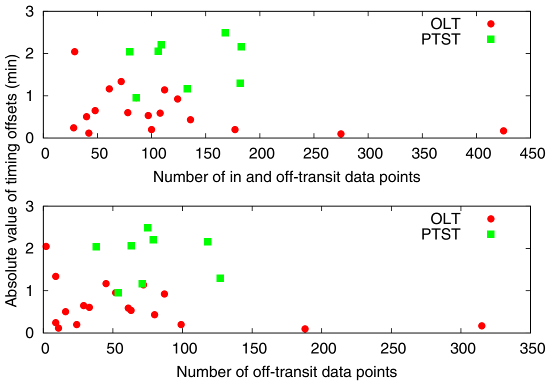

Fig. 5. Timing-residual magnitudes in minutes as a function of in and off-transit data point number (*top*) and off-transit data point number only (*bottom*). The outermost point close to zero is the primary transit, which was selected to be the 0th epoch. Mid-transit errors are not plotted to avoid visual contamination.

3.6. Effects of exposure times and transit coverage

The accuracy in determining of the mid-transit time is affected by the number of data points during transit and the number of off-transit data points, even more so when a normalization is involved.

To study whether the mid-transits are affected by the transit observation duration, we computed the timing residual magnitudes as a function of the number of data points per transit. If any systematic effect dominates the light curves, a larger timing offset for those transits that are sampled the least is expected. We show our results in Fig. 5. Since the light curves are normalized and the mid-transits might be sensitive to normalizations, we also computed the timing-residual magnitudes as a function of the number of off-transit data points. We used the Pearson correlation coefficient r to quantify the correlation of the mid-transit offsets. In both cases this was $r \sim -0.11$ for all data points, and $r \sim 0.05$, which rules out the 0th epoch, which was expected to be zero by construction. We found no significant correlation.

Kipping (2010) studied the effects of finite integration times on the determination of the orbital parameters. He showed that the time difference between the mid-transit moment and the nearest light curve data point might cause a shift in the TTV signal, which is expected to be one half of the rate sampling. To test how significant this effect is over our light curves, we calculated the mean exposure times per observing night, which was about 80 s. Figure 6 shows the mean exposure times per night, versus the magnitude of the timing residuals. Most of the data points lying around the half-mean exposure time (~35 s) were identified to have the most accurate mid-transit timings, with exposure times of about one minute, which makes it unlikely that they are affected by a sampling effect. The Pearson correlation coefficient of $r = -0.15$ again reveals no significant correlation.

3.7. Results

In general terms, the parameters P and T_0 are usually correlated with each other, but are uncorrelated with the remaining transit parameters. Therefore, these parameters can be determined quite accurately without interference of the remaining ones. We used a Nelder-Mead simplex to approach the best-fit solution, which is provided as the starting values of the MCMC sampler. The AM algorithm then samples from the posterior distribution for the parameters to obtain error estimates. After 10^8 iterations we discarded a suitable burn-in (typically 10^6 samples) and determined the combination of parameters resulting in the lowest deviance. We consider the lowest deviance as our global best-fit solution. The errors were derived from the 68% highest probability density or credibility intervals (1σ). Our results are summarized in Table 3. None of our fit parameters are consistent with those reported by Alsubai et al. (2011); a possible explanation for this inconsistency might be that these authors determined the system parameters using only four light curves, two of which were incomplete, obtained in less than two weeks. During the revision of this paper, Covino et al. (2013) presented high-precision radial velocity measurements from which the Rossiter-McLauglin effect was observed. The authors also obtained five new photometric transit light curves, from which the orbital parameters of the system were improved. With respect to the orbital period, one of the most important parameters for determining TTVs,

Table 3. Best-fit (lowest deviance) parameters for our 26 transits of Qatar-1 after 10^8 MCMC samples.

Parameter	Value (1σ errors)	Alsubai et al. (2011)
i (°)	84.52 ± 0.24	$83.47^{+0.40}_{-0.36}$
p (R_p/R_s)	0.1435 ± 0.0008	0.1454 ± 0.0015
a (R_s)	6.42 ± 0.10	$6.1005^{+0.067}_{-0.065}$
P (days)	1.4200246 ± 0.0000004	1.420033 ± 0.000016

Notes. LDCs are fixed at the values reported in Table 2.

Table 4. OLT (top) and PTST (bottom) fitted mid-transits with 1σ errors and the OC data points.

Epoch	T_0 BJD$_{\mathrm{TDB}}$– 2 455 500	O–C (days)
OLT		
–364	140.53449 ± 0.00033	0.00142
–359	147.63337 ± 0.00023	0.00017
–319	204.43373 ± 0.00038	–0.00045
–314	211.53337 ± 0.00079	–0.00093
–288	248.45453 ± 0.00071	–0.00042
–281	258.39446 ± 0.00051	–0.00066
–269	275.43500 ± 0.00037	–0.00041
–250	302.41596 ± 0.00099	0.00007
–226	336.49677 ± 0.00026	0.00030
–83	539.56037 ± 0.00031	0.00037
–81	542.40039 ± 0.00104	0.00035
–76	549.50031 ± 0.00027	0.00014
–43	596.36017 ± 0.00119	–0.00081
–33	610.56044 ± 0.00102	–0.00079
0	657.42192 ± 0.00027	–0.00012
19	684.40315 ± 0.00113	0.00064
31	701.44294 ± 0.00031	0.00014
52	731.26325 ± 0.00029	–0.00007
PTST		
–121	485.60059 ± 0.00070	0.00153
–69	559.43884 ± 0.00086	–0.00150
–57	576.47921 ± 0.00040	–0.00143
–43	596.35925 ± 0.00084	–0.00173
–31	613.39986 ± 0.00078	–0.00142
–24	623.34079 ± 0.00125	–0.00066
–12	640.38093 ± 0.00045	–0.00081
0	657.42114 ± 0.00093	–0.00090

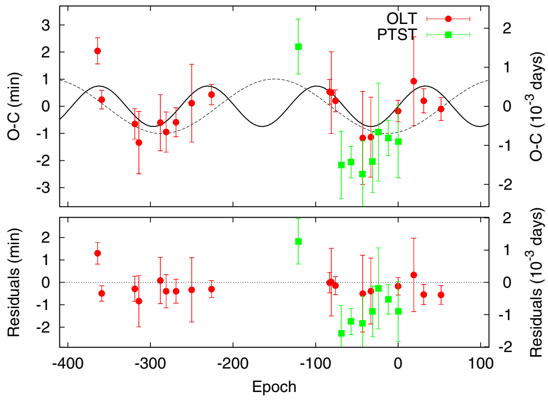

Fig. 7. OC diagram for Qatar-1 in minutes (left axis) and days (right axis) considering the OLT (red circles) and PTST (green squares) data points, along with the timing residuals. Our initial best-fitting model is overplotted with a continuous black line, and the second one with a dashed black line.

our best-fitted orbital period seems to be consistent within errors with the one found by Covino et al. (2013).

To obtain individual mid-transit times $T_{\mathrm{mid},i}$, we considered the best-fit values of p, a, i, u_1, u_2, and P. We specified Gaussian priors on these parameters and refitted each one of the 26 individual transit light curves for the mid-transit time $T_{\mathrm{mid},i}$. Our results are listed in Table 4 together with the derived 1σ errors on these transit times. To compute the timing deviations compared with a constant period we fitted the observed mid-transit times $T_{\mathrm{o},i}$ to the expression

$$T_{\mathrm{o},i} = P \cdot E_i + T_{\mathrm{o}} \,,$$

finding the ephemeris

$$P = 1.4200246 \pm 0.0000004 \text{ days}$$
$$T_0 = 2456157.42204 \pm 0.0001 \text{ BJD}_{\mathrm{TDB}}$$

as best-fitting values. All errors are obtained from the 68.27% confidence level of the marginalized posterior distribution for the parameters. With these parameters we computed the OC-values also listed in Table 4. We used the available simultaneous observations separated two months from each other as a diagnostics of our fitting procedure. Both mid-transits (epochs –43 and 0) are consistent with each other within the errors.

4. Transit timing variation analysis

4.1. OC diagram

In the absence of any timing variations we expect no significant deviations of the derived OC-values from zero. Testing the null hypothesis OC = 0 with a χ^2-test, we found $\chi^2_{\mathrm{red}} = 2.56$ with 24 degrees of freedom. This high value led us to reject the null hypothesis that OC vanishes.

We then applied the Lomb-Scargle periodogram (Lomb 1976; Scargle 1982; Zechmeister & Kürster 2009) to search for any significant periodicity contained in the OC diagram. Figure 7 shows the data points used to perform the periodogram, along with a list in Table 4. The resulting periodogram reveals a first peak at $\nu_{\mathrm{TTV},1} = 0.00759 \pm 0.00075$ cycl P^{-1} (corresponding to a period of 187 ± 17 days) and a second one at about half the frequency $\nu_{\mathrm{TTV},2} = 0.00367 \pm 0.00059$ cycl P^{-1} (corresponding to 386 ± 54 days). For both periodic signals, new ephemeris were refitted using the linear trend and a sinusoidal variation in the form

$$T_{\mathrm{o},i} = P \cdot E_i + T_{\mathrm{o}} + A_{\mathrm{TTV}} \sin(2\pi\nu_{\mathrm{TTV}}[E_i - E_{\mathrm{TTV}}]).$$

For the most significant frequency, the fitted amplitude and phase are $A_{\mathrm{TTV},1} = 0.00052 \pm 0.0002$ days (equivalently, 0.75 ± 0.28 min) and $\phi_{\mathrm{TTV},1} = 0.04 \pm 0.05$. We then recalculated $\chi^2_{\mathrm{red}} = 1.85$ for the first frequency. Using an F-test to check the significance of the fit improvement we obtained a p-value of 0.02, indicating that the sinusoidal trend does indeed provide a better description than the constant at 2.8σ level. We can also compare the models using the Bayesian information criterion, BIC = $\chi^2 + k \ln N$, which penalizes the number k of model parameters given $N = 26$ data points. We obtained BICs of 68.1 and 57.2 for the constant and sinusoidal trend, respectively. Since the BIC is no more than a criterion for model selection

A&A 555, A92 (2013)

Table 5. ETD-fitted instant of minima with 1σ errors and the OC data points.

Epoch	T_0 BJD$_{\rm TDB}$ − 2 455 500	O–C (days)
ETD		
0	18.41096 ± 0.00020	0
93	150.47263 ± 0.00058	–0.00040
119	187.39490 ± 0.00063	0.00128
155	238.51887 ± 0.00062	0.00445
158	242.77532 ± 0.00088	0.00083
189	286.79573 ± 0.00059	0.00055
194	293.89601 ± 0.00041	0.00072
196	296.73493 ± 0.00039	–0.00040
219	329.39461 ± 0.00049	–0.00123
231	346.43651 ± 0.00054	0.00039
238	356.37502 ± 0.00077	–0.00124
246	367.73872 ± 0.00054	0.00227
264	393.29753 ± 0.00051	0.00068
265	394.71796 ± 0.00049	0.00109
329	485.59892 ± 0.00067	0.00062
341	502.63734 ± 0.00044	–0.00122
401	587.84221 ± 0.00053	0.00230
412	603.46031 ± 0.00058	0.00016
419	613.40040 ± 0.00038	0.00009
434	634.70330 ± 0.00038	0.00266
443	647.47797 ± 0.00041	–0.00286
446	651.74233 ± 0.00046	0.00142
450	657.41961 ± 0.00049	–0.0013
455	664.52112 ± 0.00043	0.00001
495	721.32109 ± 0.00073	–0.00090
510	742.62146 ± 0.00048	–0.0008

among a set of models, the method one more time favors the sinusoidal trend.

We finally estimated the false-alarm probability (FAP) of the TTV signal, using a bootstrap resampling method by randomly permuting the mid-transit values (5×10^5 times) along with their individual errors, fixing the observing epochs and calculating the Lomb-Scargle periodogram afterward. We estimated the FAP as the frequency with which the highest power in the scrambled periodogram exceeds the maximal power in the original periodogram. In this fashion we estimated an FAP of 0.05% for our observed TTV signal, consistent with our previous estimates.

To further check whether the addition of the sinusoidal variation provides an explanation for the timing offsets, we made use of the mid-transits of Qatar-1 available in the Exoplanet Transit Database[5] (ETD; Poddaný et al. 2010) to reinforce our results. The ETD data are very heterogeneous, we therefore converted the best 26 mid-transits from HJD$_{\rm UTC}$ to BJD$_{\rm TDB}$. Each ETD primary transits has a data quality indicator ranging from 1 (small scatter and good time-sampling) to 4 (the opposite). For our analysis we only selected the transits with quality flags 1 (5 primary transits) and 2 (21 primary transits). These transits span a total of ~500 epochs. We produced the OC diagram (Table 5) using the following fitted ephemeris:

$$P = 1.4200223 \pm 0.0000004 \text{ days}$$
$$T_0 = 2\,455\,518.410961 \pm 0.0002 \text{ BJD}_{\rm TDB}.$$

The primary transit selected for the 0th epoch is the most accurate one of all available light curves. We produced a periodogram using the resulting timing offsets and found one peak at $\nu_{\rm TTV,ETD} = 0.00784 \pm 0.0011$ cycl P^{-1} (corresponding to a period of 181 ± 22 days) with an amplitude of $A_{\rm TTV,ETD}$ = 0.0009 ± 0.0005 days (equivalently, 1.29 ± 0.72 min) and a phase of $\phi_{\rm TTV,ETD} = 0.02 \pm 0.03$. Within the errors, the frequency, amplitude, and phase are consistent with the ones found using OLT and PTST data. Figure 8 shows two periodograms, the one on top produced using our data, and the one on bottom produced with ETD data.

[5] http://var2.astro.cz/ETD/

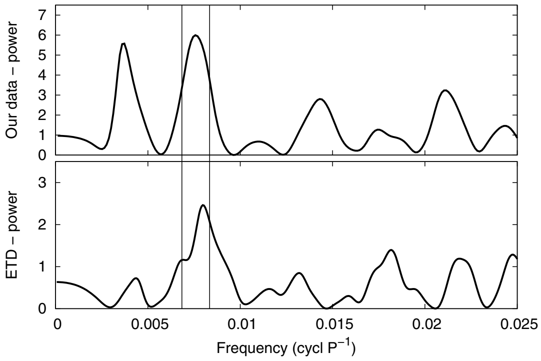

Fig. 8. Zechmeister & Kürster (2009) periodograms generated from the timing residuals of Qatar-1, showing a peak at $\nu_{\rm TTV,1} = 0.00759 \pm 0.00075$ cycl P^{-1} (our data, *top panel*) and $\nu_{\rm TTV,ETD} = 0.0078 \pm 0.0011$ cycl P^{-1} (ETD data, *bottom panel*). Vertical lines indicate the 1σ error on $\nu_{\rm TTV,1}$. The parameters derived from our periodogram are maximum power =6.1, and FAP for the maximum-power peak =0.19%.

4.2. Error analysis

To test the reliability of our error estimates for each mid-transit time and to check the influence of the error magnitude on the estimated peak frequencies, we iteratively constructed new Lomb-Scargle periodograms randomly increasing the individual mid-transit errors mostly by a factor of two.

At each iteration, we first added the absolute value of a random number that was drawn from a normal distribution (μ = 0, σ = 0.0004 days) to each mid-transit error, and calculated the leading frequency afterward. After 5×10^5 of such iterations, we found that the only effect on the error increment is the permutation of the leading frequency from $\nu_{\rm TTV,1}$ to $\nu_{\rm TTV,2}$. This permutation occurred only ~9% of the times.

In Fig. 9 we show the resulting histogram of the calculated leading frequencies. They all fall inside the 1σ errors of $\nu_{\rm TTV,1}$ and $\nu_{\rm TTV,2}$, estimated from our original fits. Thus, the derived mid-transit errors do not significantly affect the outcome in terms of dominating frequencies.

5. Interpretation of the observed transit timing variations

For the purposes of this section we assumed that the reported TTVs are real and explored possible physical scenarios that would explain the observed variations. We considered both the ~190 and ~380 day periods, although the ETD data set is consistent only with the former period. As is well known, a suitably placed third body in the Qatar-1 system can lead to perturbations in the orbit of Qatar-1b, which manifest themselves as TTVs. Since there are no complete analytical solutions to the three-body problem, we made use of a numerical integration scheme.

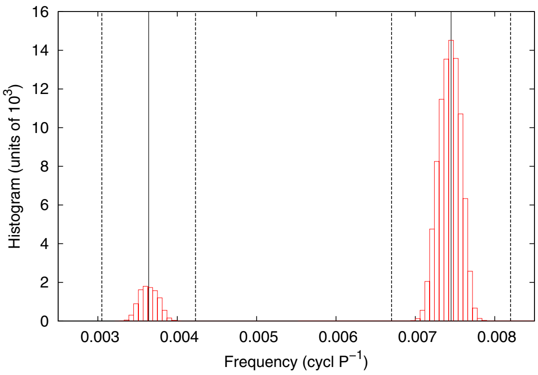

Fig. 9. Histogram of the leading frequencies obtained after incrementing the individual mid-transit errors, in units of 10^3. Vertical continuous lines indicate our best two leading frequencies $\nu_{TTV,1}$ and $\nu_{TTV,2}$, along with 1σ errors (dashed vertical lines).

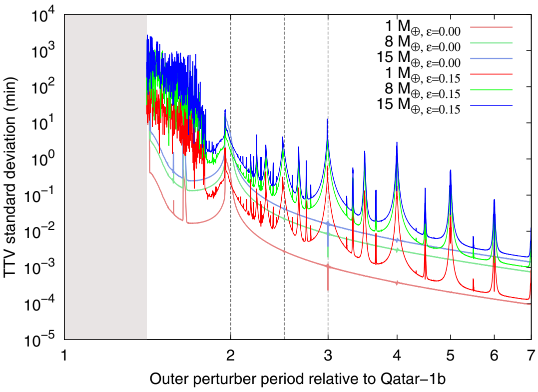

Fig. 10. Simulated TTV standard deviation in minutes of Qatar-1b as a function of the outer perturber period, for two values of eccentricity and three values of perturber masses. The gray area on the left correspond to perturber orbits that would make the Qatar-1b orbit unstable. The mean motion resonances 2:1, 3:1, and 5:2 are indicated with vertical dashed lines.

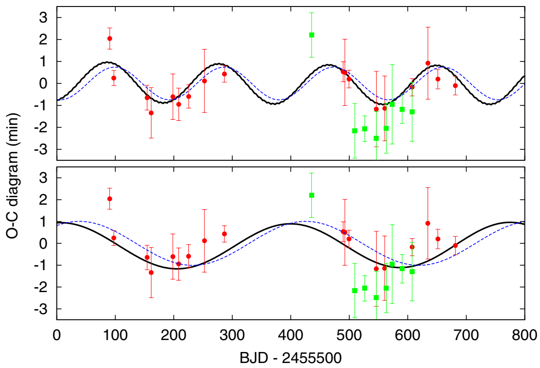

Fig. 11. OC diagram for OLT (red circles) and PTST (green squares) data points plus N-body solutions for two different dynamical scenarios (black lines) and our best initial sinusoidal fit (blue dashed lines) artificially shifted in phase for a better comparison.

Table 6. Three possible solutions for our two main TTV signals for three different dynamical scenarios.

Resonance 5:2, ~190 days	Qatar-1b	Perturber
Mass (M_{Jup})	1.090	0.019
Orbital period (days)	1.4200246	3.550061
Eccentricity	0	0.3
ω (°)	274	21
Ω (°)	235	90
t	0	0
Resonance 2:1, ~190 days	**Qatar-1b**	**Perturber**
Mass (M_{Jup})	1.090	0.005
Orbital period (days)	1.4200246	2.8400492
Eccentricity	0	0.15
ω (°)	190	30
Ω (°)	330	120
t	0	0
Resonance 3:1, ~380 days	**Qatar-1b**	**Perturber**
Mass (M_{Jup})	1.090	0.035
Orbital period (days)	1.4200246	4.2600738
Eccentricity	0	0.135
ω (°)	202	31
Ω (°)	300	90
t	0	0

Notes. From top to bottom, resonances are 5:2, 2:1, and 3:1. ω: longitude of periastron; Ω: longitude of ascending node; t: time of periastron passage.

Because a planetary orbit is determined by a large number of parameters (i.e., the eccentricity, the longitude of the nodes, the orbital inclination, among many others), it is a real challenge to estimate true orbital parameters by fitting TTV models to ground-based mid-transit shifts only. We therefore started with the simplest approach and assumed coplanar orbits using the inclination derived from the light curve fitting, along with the best-fit orbital period, and the transiting planet mass and eccentricity obtained by Alsubai et al. (2011) as fixed. Given trial mass, orbital period, eccentricity, longitude of periastron and ascending node, and the time of periastron passage, the N-body code calculates the time of occurrence of the primary transits taking into account the interaction between the planets. We specifically considered two scenarios, a putative low-mass planet in a resonant orbit relative close to Qatar-1b, and a putative high-mass planet or brown dwarf in an 190-day orbit around Qatar-1.

5.1. Weak perturber in resonance with Qatar-1b

Two planetary bodies in orbital resonance with each other will experience long-term changes in their orbital parameters. On one hand, since only a relative short stretch of data (less than two years) is available, expecting a unique solution is too ambitious. On the other hand, most of the perturber's dynamical setups will translate into negligible TTVs.

Taking into account these difficulties, we calculated the modeled TTV scatter for a two-planetary system, to study in advance which would be the parameter space giving rise to TTVs similar to the scatter of our data. We first considered both bodies in circular orbits and then the perturber in an eccentric orbit. The

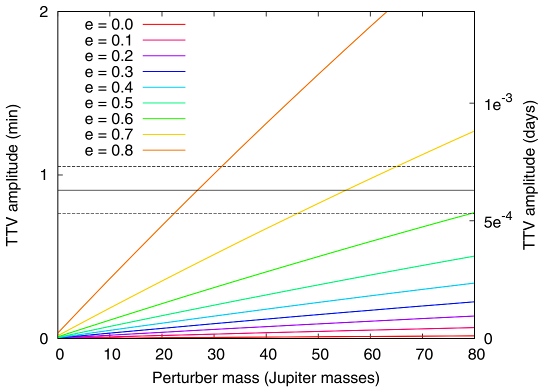

Fig. 12. TTV amplitude as a function of the mass of the perturber for different eccentricity values. The black continuous line shows the best-fitted amplitude to our OC diagram, along with 1σ errors (dashed lines).

mass of the perturber was systematically changed between 1, 8, and 15 $M_\oplus$. Figure 10 shows our results. The vertical dashed lines indicate the 2:1, 3:1, and 5:2 resonances. In these regions, perturbers of the order of several Earth masses would produce TTVs similar to the observed ones.

We thus investigated some possible solutions that would satisfy the first two TTV periods assuming the specific resonant orbits indicated in Fig. 10. As an example we show in Fig. 11 and Table 6 three arbitrary cases; similar solutions can be derived with other choices of resonant orbits. To produce Fig. 11 we ran our N-body simulation with specified initial conditions (cf., Table 6) and compared the results with the observed OC-values and our (original) sinusoidal fit (cf., Fig. 11). As is clear from Fig. 11, all these solutions have χ^2 values similar to our first fitting attempt. Thus, it is futile to produce a proper fitting procedure.

5.2. Massive perturber in a 190-day orbit

As an alternative to a lower-mass perturber in a resonant orbit, we also considered a more massive perturber in a non-resonant 190-day orbit. In this case the TTV amplitude strongly depends on the mass and the eccentricity of the assumed perturber. Again considering the simplest case of coplanar orbits and both longitude of periastron and longitude of the ascending node fixed to zero, we computed the amplitude of the TTV signal as a function of the perturber mass and its orbital eccentricity using our N-body code, and we compared the predicted TTV amplitudes with those observed. Our results are shown in Fig. 12, where we plot the expected TTV amplitude as a function of the perturber mass for various eccentricities in the range between zero and 0.8. For low eccentricity values we require perturber masses of more than 80 Jupiter masses, i.e., we would require a low-mass star. For eccentricities above 0.6 a brown dwarf could explain the observed TTV amplitudes. It is obvious that such an object would lead to RV variations in the host of Qatar-1, which could in principle be observed. Since for a very eccentric orbit the RV variations are concentrated around the periastron passage and since only ten days of RV measurements are available for Qatar-1 so far, any long-term RV variations of Qatar-1 are unknown so far and could confirm or reject the presence of a massive perturber.

6. Conclusions

Our analysis of the mid-timing residuals of Qatar-1 taken during almost two years indicate that the orbital period of the exoplanet is not constant. The observed long-term timing variations are highly significant from a statistical point of view and can be explained by very different physical scenarios. RV monitoring of Qatar-1 will provide an upper limit to the mass of a possible perturber and continued timing observations of Qatar-1 are required to better delineate the solution space for the possible perturber geometries.

Acknowledgements. C. von Essen acknowledges funding by the DFG in the framework of RTG 1351, and P. Hauschildt, S. Witte and H. M. Müller for discussions about the PHOENIX code and limb-darkening effects.

References

Adams, E. R., López-Morales, M., Elliot, J. L., Seager, S., & Osip, D. J. 2010, ApJ, 714, 13
Agol, E., Steffen, J., Sari, R., & Clarkson, W. 2005, MNRAS, 359, 567
Alsubai, K. A., Parley, N. R., Bramich, D. M., et al. 2011, MNRAS, 417, 709
Balan, S. T., & Lahav, O. 2009, MNRAS, 394, 1936
Ballard, S., Fabrycky, D., Fressin, F., et al. 2011, ApJ, 743, 200
Carter, J. A., & Winn, J. N. 2009, ApJ, 704, 51
Claret, A., & Hauschildt, P. H. 2003, A&A, 412, 241
Cochran, W. D., Fabrycky, D. C., Torres, G., et al. 2011, ApJS, 197, 7
Covino, E., Esposito, M., Barbieri, M., et al. 2013, A&A, 554, A28
Díaz, R. F., Rojo, P., Melita, M., et al. 2008, ApJ, 682, L49
Eastman, J., Siverd, R., & Gaudi, B. S. 2010, PASP, 122, 935
Fabrycky, D. C., Ford, E. B., Steffen, J. H., et al. 2012, ApJ, 750, 114
Fukui, A., Narita, N., Tristram, P. J., et al. 2011, PASJ, 63, 287
Fulton, B. J., Shporer, A., Winn, J. N., et al. 2011, AJ, 142, 84
Haario, H., Saksman, E., & Tamminen, J. 2001, Bernoulli, 7, 223
Hauschildt, P. H., & Baron, E. 1999, J. Comput. Appl. Math., 109, 41
Holman, M. J., & Murray, N. W. 2005, Science, 307, 1288
Holman, M. J., Fabrycky, D. C., Ragozzine, D., et al. 2010, Science, 330, 51
Irwin, J., Buchhave, L., Berta, Z. K., et al. 2010, ApJ, 718, 1353
Irwin, J. M., Quinn, S. N., Berta, Z. K., et al. 2011, ApJ, 742, 123
Jones, E., Oliphant, T., Peterson, P., et al. 2001, SciPy: Open source scientific tools for Python, http://www.scipy.org
Kipping, D. M. 2010, MNRAS, 408, 1758
Lissauer, J. J., Fabrycky, D. C., Ford, E. B., et al. 2011, Nature, 470, 53
Lomb, N. R. 1976, Ap&SS, 39, 447
Maciejewski, G., Dimitrov, D., Neuhäuser, R., et al. 2010, MNRAS, 407, 2625
Maciejewski, G., Dimitrov, D., Neuhäuser, R., et al. 2011, MNRAS, 411, 1204
Mandel, K., & Agol, E. 2002, ApJ, 580, L171
Nascimbeni, V., Piotto, G., Bedin, L. R., et al. 2011, A&A, 532, A24
Pál, A., Sárneczky, K., Szabó, G. M., et al. 2011, MNRAS, 413, L43
Patil, A., Huard, D., & Fonnesbeck, C. J. 2010, J. Stat. Software, 35, 1
Poddaný, S., Brát, L., & Pejcha, O. 2010, New Astron., 15, 297
Pont, F., Zucker, S., & Queloz, D. 2006, MNRAS, 373, 231
Scargle, J. D. 1982, ApJ, 263, 835
Steffen, J. H., Ragozzine, D., Fabrycky, D. C., et al. 2012, Proc. Nat. Acad. Sci., 109, 7982
Vihola, M. 2011, Stochastic Processes and their Applications, in press [arXiv:0903.4061]
Witte, S., Helling, C., & Hauschildt, P. H. 2009, A&A, 506, 1367
Zechmeister, M., & Kürster, M. 2009, A&A, 496, 577

Qatar-1: transit timing variation analysis and Hα photometric follow-up campaign

C. von Essen, S. Lalitha, A. Ofir & J. H. M. M. Schmitt
Submitted to MNRAS, September 2013

Mon. Not. R. Astron. Soc. **000**, 1–12 (–) Printed September 19, 2013 (MN LaTeX style file v2.2)

Qatar-1: transit timing variation analysis and Hα photometric follow-up campaign

C. von Essen[1]⋆, S. Lalitha[1], A. Ofir[2] & J.H.M.M. Schmitt[1]
[1]*Hamburger Sternwarte, University of Hamburg, Gojenbergsweg 112, 21029 Hamburg, Germany*
[2]*Institut für Astrophysik, Georg-August-Universität, Friedrich-Hund-Platz 1, 37077, Göttingen, Germany*

Accepted. Received.

ABSTRACT

In 2011, our group started an ongoing primary transit follow-up of the Qatar-1 system. Our main goal was to better constrain the system orbital and physical parameters and to analyze the plausibility of transit timing variations. Qatar-1A is a moderately active star. The modulation caused due to activity can be misinterpreted as timing variation induced by the orbiting exoplanet. Hence, we carried out an Hα photometric follow-up as well. We observed 16 new primary transits of Qatar-1b between May and September, 2013. To this end, we used the 1.2 m OLT telescope in Germany and the 0.6 m PTST telescope in Spain. Combining this follow-up campaign with the one previously published by our group, we collected 42 primary transits within a time baseline of 2 years. After producing a more strict analysis over the primary transit light curves we find no significant transit timing variation signal. Our results are in better agreement with the current planet formation theories and observations, which reveal that no planetary system hosting a hot-Jupiter has been found to be multiple so far.

Key words: planets and satellites: fundamental parameters – stars: activity – stars: low-mass – methods: data analysis – methods: observational – techniques: photometric

1 INTRODUCTION

In the last few years more refined observing techniques and improved instrumentation have revealed that stars can host planetary systems just like our Solar System, which contains a total of eight planets. As of now about ∼25% of the confirmed exoplanetary systems have more than one planet; for example, 55 Cnc (e.g., Fischer et al. 2008; Dawson & Fabrycky 2010), 47 Ursae Majoris (Gregory & Fischer 2010), and very recently GJ 667 (Anglada-Escudé et al. 2013) are multiple systems discovered by the radial velocity (RV) method, Kepler-11 (Lissauer et al. 2011), Kepler-18 (Cochran et al. 2011), and Kepler-20 (Fressin et al. 2012) are some examples detected by the transit method. Obviously the observations of multiple transits with different depths and different periods provide very direct evidence for a planetary systems, while the RV detections of multiple planets have to rely on essentially a (at times controversial) Fourier decomposition of the observed RV signal.

A further advantage of the transit method is based on the fact that once a transiting exoplanet has been detected, variations in the mid-transit times can reveal the presence of further exoplanets; this technique is known as the transit timing variation method (TTV). Nowadays TTVs provide a powerful tool for confirming transiting planets (Steffen et al. 2013) as well as to present new planetary candidates (Ford et al. 2012).

A drawback for both methods are, however, the effects of stellar activity. It is well known that star spots induce a radial velocity signal that can be confused with an exoplanet signature (see e.g., Barnes et al. 2011; Boisse et al. 2011; Hartman et al. 2011), i.e., they show an activity-induced Rossiter-McLaughlin effect. For the transit method the presence of spots can alter the depth and shape of the transit light curve and prevent us from computing accurate physical and orbital parameters (Czesla et al. 2009). For instance, if a spot is located at the stellar limb, then it can interfere with the light curve at ingress or egress causing a perturbation that could be misinterpreted as a timing variation. For example, TTVs with an amplitude of ∼3.5 minutes were reported in the WASP-10 system by Maciejewski et al. (2011). However, two years later Barros et al. (2013) found that the observed transit time variations might be induced by spot occultation features or systematic effects not properly accounted for.

von Essen et al. (2013) (henceforth abbreviated by vE13) recently presented a study of 26 primary transits of the Qatar-1 system, showing indications of TTVs. Transits in Qatar-1 were first reported by Alsubai et al. (2011), who characterized the host star as an old K type star, with 0.85 $M_\odot$ and 0.82 $R_\odot$. The hot-Jupiter, Qatar-1b, with a radius of 1.16 R_J orbits the star each ∼1.42 days with an inclination angle of 83.47°. This geometry implies nearly grazing transits, making the system highly sensitive to TTVs. Al-

⋆ E-mail: cessen@hs.uni-hamburg.de

though Qatar-1 is not particularly bright (V∼12.8, Droege et al. 2006), the combination of a large exoplanetary radius and a short orbital period produces deep transits which are easy to observe even with a small telescope. Although the long-term timing variations reported by vE13 were significant from a statistical point of view, no unique physical scenario for the observed TTV signal could be derived. Thus, to better constrain the characteristics of the possible perturbers and to verify the reported TTV indications, we extended our primary transit follow-up. Meanwhile, Covino et al. (2013) observed the system spectroscopically and reported Qatar-1A to be a moderately active star. Motivated by this, we initiated a photometric follow-up of Qatar-1A in Hα in order to assess the possible impact of stellar activity on the determination of mid-transit times.

The purpose of this paper is to describe these new observations and to reassess the presence of TTVs in Qatar-1. We describe the observational setup and the data reduction processes in Section 2. Afterward, we present in Section 3 the studies carried out over our primary transit light curve analysis. In Section 4 we describe the transit timing variation analysis, while in Section 5 we show the studies produced over the Hα data set. Finally, in Section 6 we write down our conclusions.

2 OBSERVATIONS AND DATA REDUCTION

2.1 New primary transit light curves

Our new observations comprise 7 transits of Qatar-1 obtained using the 1.2 m Oskar-Lühning telescope (OLT) at the Hamburg Observatory, Germany, and 9 transits using the 0.6 m Planet Transit Study Telescope (PTST) at the Observatorio Astronómico de Mallorca, in Spain. [1]

The OLT data were taken between June and August 2013. The typical exposure times ranged between 40 to 60 seconds. All exposures were obtained using a Johnson-Cousins Schuler R filter. Due to seasonal effects and the high latitude at Hamburger Sternwarte's site, the star could always be observed close to culmination and zenith with airmass values ranging from 1 up to 1.2, while the average seeing value was 2 arcsec, considerably smaller than in vE13. The PTST data were taken between May and August 2013. The exposure times ranged from 35 to 60 seconds, while the airmass between 1.1 and 2.3. The average seeing value was 2 arcsec. All exposures were obtained using a Baade R-band filter setup.

In addition to the 26 light curves presented in vE13, we include 16 more. Table 1 summarizes the main characteristics of the new observations obtained at both observing sites. Combining OLT and PTST data from both campaigns, the observations span ∼650 epochs, which are about two years.

Bias and flat fields were obtained in each observing night. To pre-reduce the data we used the IRAF task *ccdproc*, and to produce the photometric light curves we used the task *apphot*. We measured fluxes inside different apertures centered on the target star and seven more stars in the case of OLT's field of view. In the case of PTST, a larger field of view allowed us to measure fluxes in four more additional stars. Following the same criteria as described in vE13, we used always Qatar-1 and the same reference star to produce the differential photometry, while the remaining stars were used to check the reference star for constancy.

[1] We refer the reader to vE13 for a fully description of the instrumental setup.

2.2 Hα follow-up campaign

For the Hα photometric follow-up we carried out new observations using the OLT. We collected 22 nights between July and September 2013, covering all orbital phases of the planet. The data sets, with the exception of one, were obtained under the same binning and filter configurations. To minimize systematic effects, Qatar-1 was located always in the same position of the CCD. Due to the excellent guiding system of the OLT, the centroid of the star was not displaced by more than 2 pixels per night. To ensure a proper photometric follow-up we measured fluxes always for the same reference stars. Furthermore, we estimated the mean seeing (FWHM) per night. To ensure that the same proportion of flux was always collected, we chose the aperture radius as a multiple of the FWHM, which also provides error estimates that are comparable between nights. The final aperture was set to 1×FWHM, which is the one that minimizes the noise in the photometry (Howell 2006).

Since Qatar-1 is faint in Hα, we carried out exposures of ∼200 seconds to ensure a sufficiently high S/N. To improve the photometry we acquired bias, flat fields, and darks every night. We carried out the data reduction using the same IRAF packages previously described. In Figure 1 we show the OLT's 9×9 arcmin field of view. Qatar-1 is labeled with a number "1", while the remaining reference stars with numbers "2" to "8". After producing several differential light curves permuting the reference stars, we found that the combination of the stellar fluxes of the stars labeled with a number "3" (the star that is used to produce the differential light curves for the primary transit data), the number "6", and the number "8", produce light curves with the smallest scatter. Therefore, the differential light curves of Qatar-1 in Hα were produced after dividing the fluxes of star "1" (Qatar-1) and "6". Since any variability observed in Qatar-1 light curve strictly depends on the scatter of the control light curve, the latter was produced checking the constancy of star "6" against the mean flux of stars "3" and "8". However, it is worth mentioning that the observed Hα variability is independent of the selection of the reference stars. Table 2 lists the main characteristics of the observations. After years of acquiring photometric data and experience in the site, we found that the resulting light curves are more precise if the telescope is slightly defocused (see e.g., **?**). Therefore, large seeing values are not the product of atmospheric turbulence but defocused images. The relevant value to be considered as photometric noise source is the variation of the FWHM. Every night, the variation has been smaller than 1 arcsec, which is the key to obtain more stable photometry.

3 ANALYSIS OF PRIMARY TRANSIT DATA

Below we describe the analysis and list the values derived from the new data set as well as from a re-analysis of the vE13 data; we thus obtain an homogeneous study of the data obtained in both campaigns.

3.1 Time stamps

IRAF provides accurate heliocentric corrections. We convert the time stamps from Julian dates to heliocentric Julian dates (HJD_{UTC}) first using the IRAF task *setjd*. These are then converted to barycentric Julian dates (BJD_{TDB}) using the web tool provided by Eastman et al. (2010)[2].

[2] http://astroutils.astronomy.ohio-state.edu/time/

Table 1. Summary of primary transit observations carried out with OLT (top) and PTST (bottom) specifying epoch, exposure time ET, filter configuration F, number of data points NoP, airmass, transit coverage (TC), the scatter of the data σ, β (a parameter that measures correlated noise), and the degree of the polynomial fitted to the off-transit data DEG. Epochs are counted relative to the best-fitting transit. Transits observed simultaneously with both telescopes are marked in boldface. Observations were obtained in filter configurations R_1 and R_2 denoting the Schuler Johnson-Cousins R-band, and the Baader R-band, respectively. The letter code to specify the transit coverage during each observation is the following: O: out of transit, before ingress. I: ingress. B: flat bottom. E: egress. O: out of transit, after egress.

Date	Epoch	ET (s)	F	NoP	Airmass	TC	σ	β	DEG
OLT									
2013 June 4	-50	60	R_1	88	$1.0 \rightarrow 1.0$	- - BEO	0.0039	1.65	0
2013 June 14	-43	60	R_1	157	$1.1 \rightarrow 1.0$	OIBEO	0.0029	1.26	0
2013 July 21	-17	50	R_1	184	$1.1 \rightarrow 1.0$	- IBEO	0.0035	1.44	1
2013 August 14	0	50	R_1	194	$1.0 \rightarrow 1.1$	OIBEO	0.0023	0.82	0
2013 August 24	7	40	R_1	130	$1.0 \rightarrow 1.0$	OI - - -	0.0038	1.39	0
2013 August 27	9	40	R_1	150	$1.0 \rightarrow 1.0$	- - BEO	0.0027	1.52	1
PTST									
2013 May 11	-67	35	R_2	170	$2.3 \rightarrow 1.6$	OIBEO	0.0030	2.37	0
2013 May 18	-62	55	R_2	159	$1.7 \rightarrow 1.2$	OIB - O	0.0031	1.15	1
2013 May 25	-57	60	R_2	154	$1.6 \rightarrow 1.1$	OIBEO	0.0030	1.68	1
2013 July 1	-31	60	R_2	206	$1.4 \rightarrow 1.1$	OIB - -	0.0031	1.81	1
2013 July 8	-26	60	R_2	118	$1.2 \rightarrow 1.1$	OIB - -	0.0033	2.73	1
2013 July 31	-10	40	R_2	123	$1.3 \rightarrow 1.1$	- - - EO	0.0021	1.87	1
2013 August 4	-7	40	R_2	234	$1.1 \rightarrow 1.4$	OIBEO	0.0023	1.33	1
2013 August 14	0	50	R_2	168	$1.3 \rightarrow 1.1$	OIBEO	0.0030	1.54	0
2013 August 21	5	45	R_2	168	$1.3 \rightarrow 1.7$	OIBEO	0.0039	1.58	0
2013 August 27	9	45	R_2	110	$1.3 \rightarrow 1.1$	- - BEO	0.0038	1.36	0

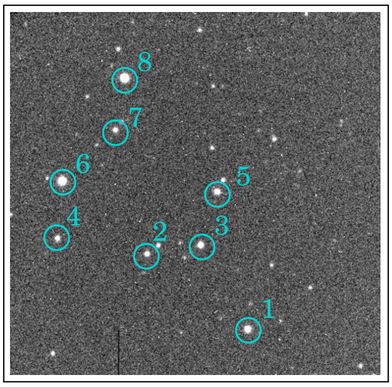

Figure 1. OLT's 9′ × 9′ field of view. Labeled with a 1 is Qatar-1. Although we measured fluxes over 7 more reference stars, the differential photometry was carried out using fluxes from stars 3, 6, and 8. The last two are the brightest stars within the field of view. North is pointing up, while East to the left of the figure.

3.2 Limb-darkening coefficients

The filter sets available in OLT and PTST do not belong to a standard filter system. Therefore, we calculated our own set of limb darkening coefficients in vE13, using the transmission functions of the filters and synthetic PHOENIX spectra (Hauschildt & Baron 1999). The resulting limb-darkening coefficients (LDCs) for a quadratic limb-darkening law are listed in Table 3. As in our previous analysis LDCs will be considered as fixed in every fitting procedure.

3.3 Correlated noise

Carter & Winn (2009) studied the influence of time-correlated noise with respect to the determination of the orbital parameters of transiting systems. A straightforward example implemented over accurate – short-cadence Kepler data of Tres-2, is given in Kippint & Bakos (2011).

Following Carter & Winn (2009) we studied the effects of correlated noise on our light curves. First, we produced residual light curves, subtracting the primary transit model from the data (Mandel & Agol 2002). As orbital parameters we used the values obtained in vE13, listed in this work in the first column of Table 5. Then, we divided each light curve into M bins of equal duration, each bin counting with N number of data points. Since our data is not always equally spaced, N is the mean value of data points per bin. If the data is free of any correlated noise, then the noise structure of the residual light curves should follow the expectation of independent random numbers $\hat{\sigma_N}$,

$$\hat{\sigma_N} = \sigma_1 N^{-1/2} [M/(M-1)]^{1/2} , \quad (1)$$

where σ_1 is the sample variance of the unbinned data and σ_N is the sample variance (or RMS) of the binned data, with the following expression:

$$\sigma_N = \sqrt{\frac{1}{M} \sum_{i=1}^{M} (< \hat{\mu}_i > - \hat{\mu}_i)^2} , \quad (2)$$

where $\hat{\mu}_i$ is the mean value of the residuals per bin, and $< \hat{\mu}_i >$ is the mean value of the means.

In the presence of correlated noise, each σ_N differs by some factor β_N from their expectation $\hat{\sigma_N}$. The factor β, which is listed in the 8^{th} column of Table 1, is obtained after averaging the β_N's obtained over time bins close to the duration of Qatar-1's transit

Table 2. Summary of the photometric Hα follow-up carried out with OLT, specifying date, exposure time ET, number of data points NoP, airmass, the duration of the observation D, and the mean FWHM in arcsec.

Date	ET (s)	NoP	Airmass	D (h)	FWHM (")
2013 July 20	180	28	1.0 → 1.1	1.8	5.2 ± 0.5
2013 July 21	210	16	1.0 → 1.0	0.9	5.4 ± 0.6
2013 July 25	180	20	1.0 → 1.0	1.2	3.7 ± 0.5
2013 July 27	240	40	1.0 → 1.0	3.4	5.1 ± 0.6
2013 August 1[st]	240	44	1.0 → 1.0	4.2	3.8 ± 0.3
2013 August 2	240	47	1.0 → 1.0	3.9	2.4 ± 0.4
2013 August 4	210	43	1.0 → 1.0	4.0	3.8 ± 0.7
2013 August 10	200	22	1.0 → 1.0	1.8	5.1 ± 0.5
2013 August 13	180	34	1.0 → 1.0	3.5	6.2 ± 0.3
2013 August 14	200	33	1.0 → 1.0	2.9	3.3 ± 0.3
2013 August 15	240	8	1.0 → 1.1	0.5	2.9 ± 0.2
2013 August 16	240	12	1.0 → 1.0	1.4	2.9 ± 0.4
2013 August 20	240	14	1.0 → 1.0	1.5	2.8 ± 0.2
2013 August 21	240	8	1.0 → 1.0	0.6	2.1 ± 0.2
2013 August 23	200	63	1.0 → 1.1	4.7	2.5 ± 0.4
2013 August 24	200	24	1.0 → 1.0	1.8	2.2 ± 0.1
2013 August 25	200	61	1.0 → 1.0	4.2	2.5 ± 0.4
2013 August 26	200	24	1.1 → 1.0	2.1	2.4 ± 0.2
2013 August 27	200	42	1.0 → 1.0	2.7	2.3 ± 0.3
2013 August 28	200	31	1.1 → 1.0	2.3	1.8 ± 0.2
2013 August 29	200	19	1.0 → 1.0	1.6	2.2 ± 0.1
2013 August 31	200	17	1.0 → 1.0	1.9	3.5 ± 0.2
2013 September 4	200	55	1.0 → 1.2	4.4	2.4 ± 0.2
2013 September 5	200	31	1.0 → 1.2	2.4	2.5 ± 0.2
2013 September 6	200	53	1.0 → 1.2	3.7	2.2 ± 0.1
2013 September 7	200	30	1.0 → 1.2	2.3	3.0 ± 0.1
2013 September 9	200	21	1.0 → 1.0	1.6	4.4 ± 0.4
2013 September 12	200	28	1.0 → 1.0	2.6	2.7 ± 0.3
2013 September 13	200	19	1.0 → 1.0	1.6	2.1 ± 0.2
2013 September 16	200	12	1.0 → 1.0	1.4	5.0 ± 0.6

Table 3. Best-fit limb-darkening coefficients for OLT and PTST, along with the 1 σ errors.

LDCs	OLT	PTST
u_1	0.5860 ± 0.0053	0.6025 ± 0.0051
u_2	0.1170 ± 0.0075	0.1140 ± 0.0073

ingress (or, equivalently, egress), which is estimated to be 15 minutes for Qatar-1's system. To estimate β, we used as time-bin 0.8, 0.9, 1, 1.1, and 1.2 times the duration of ingress. Finally, as suggested by Pont et al. (2006), to account for systematic effects on the light curves we enlarged the photometric errors by a factor of β.

Generally, for the PTST the β values are up to two times larger than for the OLT. Although the site characteristics (i.e., atmospheric transparency) are expected to be superior in Mallorca compared Hamburg, the PTST has a primary mirror of 0.6 m and does not include an independent guiding system, while OLT has an aperture of 1.2 m, and includes a special CCD to carry out the telescope guiding. This allows a larger area in the sky to find an optimal guiding star and, therefore, a better pointing model. Howell (2009) and **?**, among others, already studied how the photometry improves when a guiding system is used. Additionally, the accuracy on the determination of the orbital parameters strongly depends on the time gap between points (Kipping 2010). Closely related to this last issue, while analyzing TTVs in the WASP-3 system Maciejewski et al. (2010) reported a systematic offset between data collected from different sites. Intriguingly, the fitted mid-transits obtained from light curves with short exposure times were above zero in the O-C diagram, while the ones obtained from light curves with up to 2 times higher exposure times were below zero. Since we are combining observations obtained with different instrumental setups as well, to avoid systematic effects related to time sampling we decided to make the exposure times between sites comparable, lowering in consequence the photometric signal in PTST data. Additionally, PTST photometry is more prone to suffer of scintillation effects (see e.g., Young 1993, their first equation). Taking into account that the exposure times and the elevation of the Hamburger Sternwarte and the Observatorio Astronómico de Mallorca are comparable, the only substantial difference with respect to the magnitude that scintillation will bring into the photometry is the diameter of the primary mirror (dpm). Indeed, the PTST dpm is a factor of two smaller than OLT's. All together, it is expected for PTST light curves to be more prone to correlated noise effects and, therefore, have larger β values.

3.4 Primary transit data normalization

The normalization of the light curves is crucial for the determination of proper transit timing variations. To ensure that the errors related to the out-of-transit data fit propagates into the accuracy of the orbital parameters, the normalization was produced simultaneously with the primary transit model fitting. To determine the degree of the polynomial to fit the OOT data points, we used the Bayesian information criterion (BIC), BIC = χ^2 + k ln N. The BIC penalizes the number k of model parameters given N data points. Using the scatter of the light curves σ_{data} as initial error estimates, rather than the underestimated photometric errors provided by IRAF, we calculated the BIC between a given light curve and a polynomial with degree 0 to 4. The degree that minimized the BIC was taken into account to produce the primary transit fitting. The degree of the optimal polynomial is listed in the last column of Table 1. According to our modeling, in most of the cases a zeroth or first degree is sufficient for transit normalization.

3.5 Fit approach: towards best fit orbital parameters

With the photometric errors of the complete data set at values $\sigma_{data} \times \beta$, we proceed to calculate the orbital parameters of the system. To this effect, we selected only complete and low-scatter light curves from both campaigns. Table 4 lists the most relevant characteristics of the chosen light curves from the vE13 campaign, while in Table 1 complete primary transits are listed in column 7 as OIBEO. In total, we simultaneously fitted 12 primary transit light curves, obtained between October 2011 and August 2013. As primary transit model we used Mandel & Agol (2002)'s developed `occultquad` FORTRAN routine[3]. The parameters that we can infer from the fitting procedure are the orbital period, P, the semi-major axis in stellar radii, a/R_S, the mid-transit time, T_0, and the orbital inclination, i. Furthermore, we assumed a quadratic limb-darkening law with fixed coefficients u_1 and u_2, as listed in Table 3.

To produce the fit, and to obtain reliable error estimates, we used a Nelder-Mead simplex to approach the best-fit solution, which is provided as the starting values of the Marcov-chain Monte Carlo (MCMC) sampler. The adaptive Metropolis algorithm (AM)

[3] `http://www.astro.washington.edu/users/agol`

[t]

Table 4. Most relevant parameters of the primary transits of vE13 calculated in this work and used to determine the global orbital parameters.

Date	σ	β	DEG
OLT			
2011 Oct. 1	0.00225	0.817	1
2012 May 1	0.00217	1.105	0
2012 Oct. 30	0.00285	1.193	0
PTST			
2012 Feb. 27	0.00312	1.069	0
2012 May 28	0.00376	1.167	1
2012 Jul. 31	0.00364	0.908	1

[ht!]

Table 5. Best-fit (lowest deviance) parameters for our 12 transits of Qatar-1 after 5×10^6 MCMC samples. LDCs are fixed at the values reported in Table 3. A constant value of 2456000 has been subtracted to the mid-transit times.

Parameter	von Essen et al. (2013)	This work
i (°)	84.52 ± 0.24	83.91 ± 0.41
p (R_p/R_s)	0.1435 ± 0.0008	0.1459 ± 0.0014
a (R_s)	6.42 ± 0.10	6.15 ± 0.14
P (days)	1.4200246 ± 4×10^{-7}	1.4200236 ± 6×10^{-7}
T_0 (BJD$_{\mathrm{TDB}}$)	157.42204 ± 1×10^{-4}	519.52802 ± 1×10^{-4}

then samples from the posterior distribution for the parameters to produce error estimates (see vE13 for further details on AM). We explored the parameter space by sampling from the posterior-probability distribution using a MCMC approach (for a detailed description on errors, we refer to Section 3.4 of vE13). After 5×10^6 iterations we discarded a suitable burn-in (5×10^5 samples) and determined the combination of parameters resulting in the lowest deviance.

Our MCMC calculations make extensive use of routines of `PyAstronomy`[4], a collection of Python routines providing a convenient interface for fitting and sampling algorithms implemented in the PyMC (Patil et al. 2010) and SciPy (Jones et al. 2001) packages. The AM sampler is implemented in the PyMC package. We refer to the detailed online documentation[5].

We show our results in Table 5. The errors were derived from the 68.27% highest probability density or credibility intervals. For a quick comparison, the left column of the table shows the best fit parameters obtained in vE13. Within the errors, both parameter sets are consistent. Although the global parameters in this work were determined using better light curves than those used by vE13, the error estimates increased, generally, up to two times the ones reported in our previous work. This is the product of a different error treatment, and the simultaneous fitting of the normalization polynomials.

[4] http://www.hs.uni-hamburg.de/DE/Ins/Per/Czesla/PyA/PyA/index.html
[5] http://pymc-devs.github.io/pymc/

3.6 New primary transit light curves

Figure 2a shows the 16 new primary transit light curves, along with the residuals after removing the primary transit feature (Mandel & Agol (2002) primary transit model, in combination with our best-fit orbital parameters listed in the second column of Table 5).

4 TRANSIT TIMING VARIATION ANALYSIS

4.1 The O-C diagram

In order to obtain the individual mid-transit times we use the limb-darkening coefficients and our best fit values a/R_s, p, i, and P. Instead of considering them as fixed (this would incorrectly imply that they are perfectly determined) we specified Gaussian priors on a/R_s, p, i, and P. We fit a primary transit model and a normalization polynomial to the individual primary transit light curves using the degree of the polynomial established by the BIC criteria. Table 6 shows the resulting mid-transit times $T_{0,i}$, together with 1σ errors.

To compute the timing deviations compared with a constant period, we fitted the observed mid-transit times $T_{0,i}$ to a linear trend as a function of the transit epoch E_i:

$$T_{0,i} = P \cdot E_i + T_0 \,, \qquad (3)$$

finding our ephemeris to be as best-fitting values. All errors were obtained from the 68.27% confidence level of the marginalized posterior distribution for the parameters.

Finally, the calculated mid-transit times were obtained using our new ephemeris, as listed in Table 5.

4.2 Timing analysis

Covino et al. (2013) presented a photometric analysis of Qatar-1 using five primary transit light curves; two transits were obtained using the Asiago Faint Object Spectrograph and Camera (AFOSC) at the 1.82 m Copernico telescope in northern Italy between May 2011 and August 2012. Additionally, three more transits were observed between August 2011 and September 2012 using the 1.23 m telescope at the German-Spanish Calar Alto Observatory (CAHA).

Combining Covino et al. (2013) photometric data and our best-fit orbital parameters, we re-determined mid-transit times. Figure 3 shows the resulting O-C diagram. The OLT mid-transit shifts are plotted in red circles, while PTSTs in green squares. Covino et al. (2013)'s data is plotted in blue diamonds. Mid-transit shifts that were obtained after fitting complete primary transit light curves are indicated with black empty points. It is clearly seen that mid-transit residuals are consistent with zero (μ_{O-C} ~-4 sec, σ_{O-C} ~35 sec).

In the absence of any timing variations one expects no significant deviations of the derived O-C-values from zero. For our study we divided the complete data set into three convenient subsamples and tested the null hypothesis (absence of TTVs) with a χ^2-test. Considering TTVs obtained only from complete primary transits yields χ^2_{red} = 1.8 (with 11 degrees of freedom, dof), while the complete data set yields χ^2_{red} = 3.5 (41 dof), the largest χ^2 value is obtained by considering mid-transit times only from incomplete primary transits, χ^2_{red} = 3.9 (30 dof).

Evidently, a more stringent correlated noise analysis of the individual error measurements, in combination with a simultaneous normalization and primary transit model fitting, reveals an O-C diagram that presents large TTVs for incomplete primary transits,

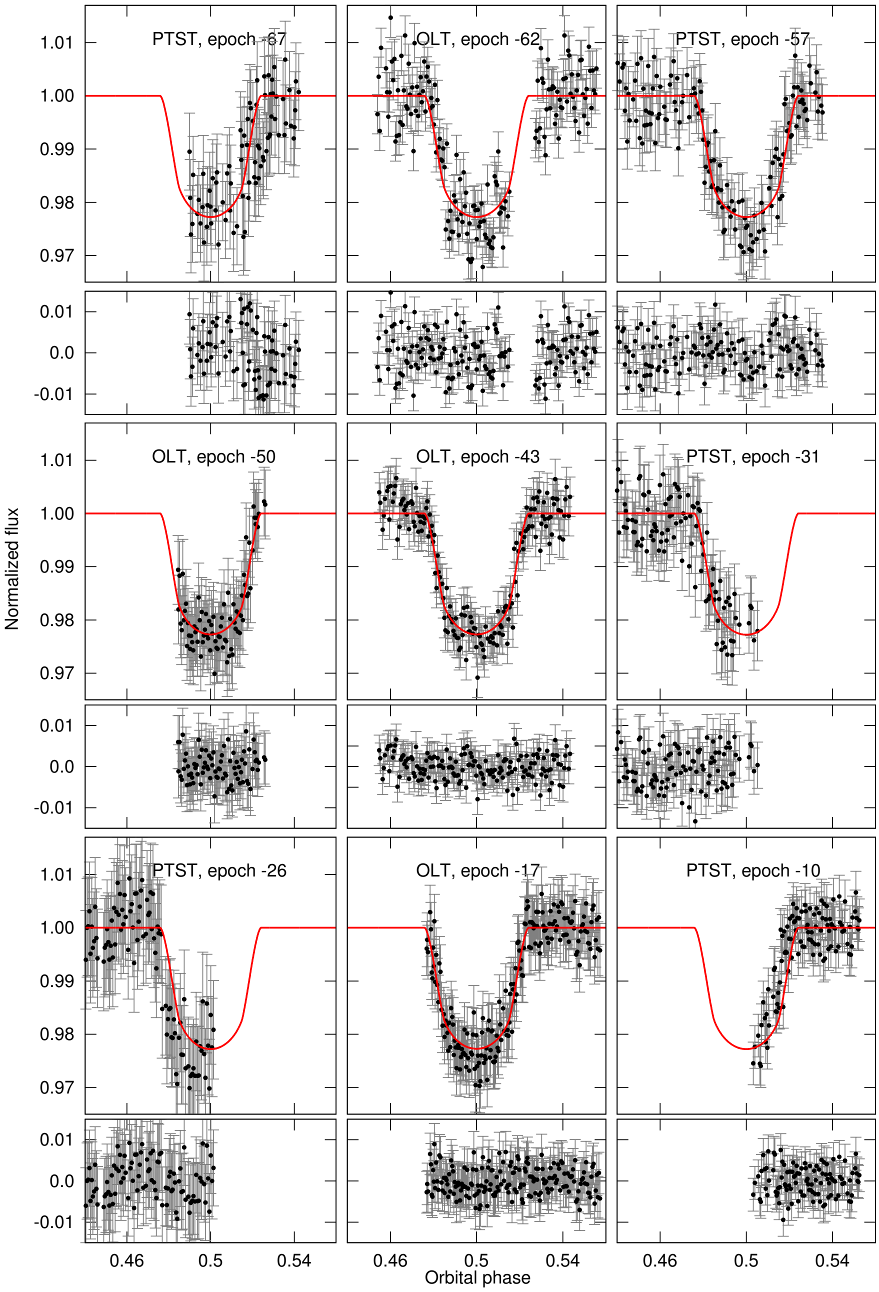

Figure 2a. Top panels show OLT and PTST light curves. In red continuous line is superposed the Mandel & Agol (2002) primary transit light-curve model using the best-fit global parameters listed in Section 3. Time progresses from top to bottom and from left to right. Residuals, calculated after subtracting the primary transit model, are displayed in the bottom panels.

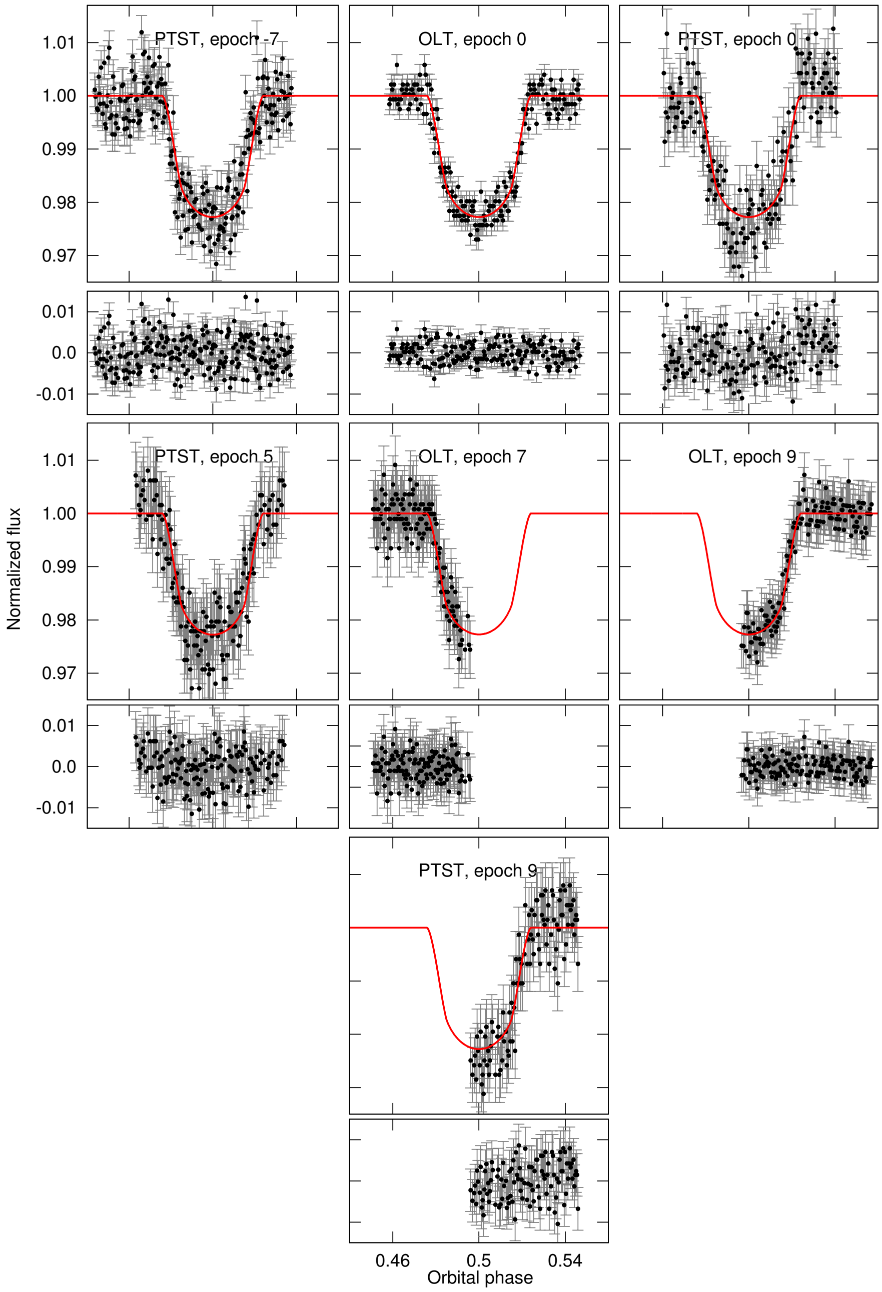

Figure 2b. Same as Figure 2a

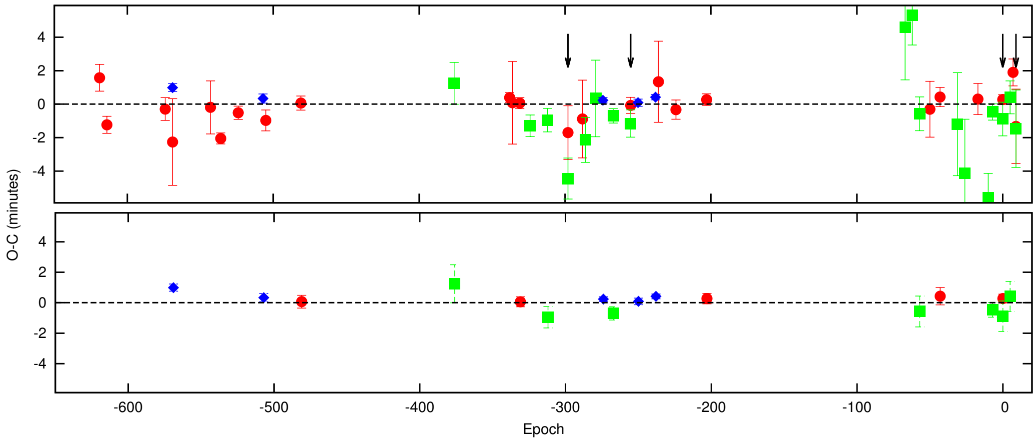

Figure 3. Top: O-C diagram for the complete data set. OLT mid-transit times are shown as red circles, and in green squares for PTST. Data points in blue diamonds correspond to the 5 primary transits obtained by Covino et al. (2013). Arrows indicate the epochs were simultaneous data were acquired. Bottom: O-C diagram but considering mid-transit shifts obtained from complete light curves.

while zero-consistent TTVs for accurate light curves. We therefore suspect that the observed mid transit time shifts are unlikely related to any real transit timing variation, and more probably related to systematic modeling effects.

4.3 Comparison analysis of mid-transit times

In general the values of derived mid-transit depend on two aspects. The first is related to the determination of the ephemeris. It is common practice to assign the zeroth epoch to the primary transit light curve with the best photometric precision and transit coverage. If more data is obtained and, as a consequence, a better light curve is acquired, a change in the zeroth epoch results in a more accurate mid-transit time and a shift in the epoch of the remaining primary transit times. Since the periodogram analysis is independent of phase information, this will not give rise to a change in the periodicity of the TTV signal. Additionally, the value of the orbital period has to be considered. In particular, the best-fit orbital period between vE13 and this work changed. However, both are mutually consistent and extremely accurate. Therefore, the new orbital period cannot be responsible for any significant shifts in the O-C diagram.

The second aspect, clearly, is related to the primary transit observations. Fig. 4 shows the difference of the individually fitted mid-transit times ($\Delta T_{o,C}$) obtained in vE13 and this work, therefore the new data points presented in Fig. 2a are not included. The top panel shows the $\Delta T_{o,C}$ for the complete sample, while the bottom panel considers only those derived from complete primary transit light curves. For the most significant frequency found in the periodogram analysis presented in vE13, the fitted amplitude was reported to be $A_{TTV,1} = 0.00052 \pm 0.0002$ days, roughly one minute. While the scatter present in OLT and PTST data in the bottom panel is smaller than the detected TTV amplitude (dashed horizontal lines), this is not true when all the light curves are considered. Although the difference between new and old mid-transit times remains around – and mostly below – 30 seconds (quite small considering our photometric precision, the enlargement on the individual errors, the change in the out-of-transit data fitting procedure, and the transit coverage), it is significant in comparison with the reported TTV signal. Given the intrinsically small detected TTV amplitude and the observed differences between our first and last analysis, it is expected for the TTV signal to change.

[ht!]

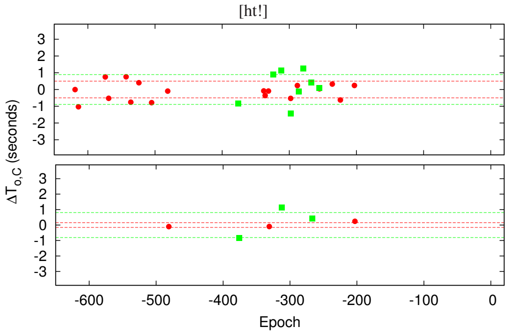

Figure 4. Mid-transit shifts difference, $\Delta t_{o,C}$, obtained subtracting the mid-transit shifts from vE13 to the ones reported in this work. Red circles correspond to OLT light curves, while green squares to PTST's. Top: complete sample. Bottom: $\Delta t_{o,C}$ from complete primary transits only. Horizontal color-coded dashed lines show $\pm 1\sigma$ the scatter of the data points.

Complete primary transits have proven to be almost unaffected to the improvement of the detection technique. This indicates that incomplete light curves are unreliable for TTV analysis.

5 Hα FOLLOW UP OBSERVATIONS

5.1 Analysis of variability by means of photometric data

Chromospheric Hα emission is known to be one of the primary indicators of magnetic activity in low-mass stars (see e.g., Cincunegui et al. 2007, for a characterization of activity indicators

[ht!]

Table 6. OLT (top) and PTST (bottom) fitted mid-transit times with 1 σ errors and the O-C data points in days.

Epoch	T_0 BJD$_{\rm TDB}$ - 2455500	O-C (days)
OLT		
-619	140.53448 ± 0.00055	-0.00109
-614	147.63265 ± 0.00035	0.00085
-574	204.43425 ± 0.00047	0.00020
-569	211.53300 ± 0.00180	0.00156
-543	248.45505 ± 0.00110	0.00013
-536	258.39393 ± 0.00023	0.00142
-524	275.43528 ± 0.00027	0.00035
-505	302.41541 ± 0.00043	0.00067
-481	336.49670 ± 0.00029	-0.00004
-338	539.56031 ± 0.00020	-0.00027
-336	542.40014 ± 0.00171	-0.00005
-331	549.50024 ± 0.00022	-0.00004
-298	596.36347 ± 0.00112	-0.00249
-288	610.56510 ± 0.00172	-0.00388
-255	657.42194 ± 0.00033	0.00005
-236	684.40337 ± 0.00168	-0.00092
-224	701.44250 ± 0.00040	0.00022
-203	731.26341 ± 0.00023	-0.00018
-50	948.52663 ± 0.00115	0.00020
-43	958.46730 ± 0.00039	-0.00029
-17	995.38784 ± 0.00064	-0.00021
0	1019.52822 ± 0.00020	-0.00019
7	1029.46951 ± 0.00055	-0.00131
9	1032.30732 ± 0.00154	0.00092
PTST		
376	485.60000 ± 0.00086	-0.00086
-324	559.43947 ± 0.00044	0.00089
-312	576.47998 ± 0.00048	0.00066
-298	596.35789 ± 0.00084	0.00308
-286	613.39978 ± 0.00093	0.00148
-279	623.34167 ± 0.00159	-0.00023
-267	640.38122 ± 0.00029	0.00048
-255	657.42119 ± 0.00056	0.00079
-67	924.38963 ± 0.00218	-0.00318
-62	931.49025 ± 0.00124	-0.00369
-57	938.58628 ± 0.00070	0.00039
-31	975.50646 ± 0.00213	0.00083
-26	982.60454 ± 0.00224	0.00287
-10	1005.32391 ± 0.00100	0.00388
-7	1009.58754 ± 0.00033	0.00032
0	1019.52741 ± 0.00069	0.00061
5	1026.62843 ± 0.00068	-0.00028
9	1032.30722 ± 0.00160	0.00101

for spectral types from F to M). Therefore, we observed Qatar-1 photometrically using an Hα filter with the main goal to characterize Qatar-1's activity level ans its possible variations. For every observing night obtained with the OLT we calculated the mean and the dispersion of the data and considered them as representative values for the flux and the intra-night scatter. These values are displayed in Figure 5, were differential magnitudes are plotted as a function of time. The graph on top (red circles) shows differential Hα light curve of Qatar-1, on the bottom of the figure we plot (in green, artificially shifted) the control differential light curve (see Section 2.2 for details on the comparison light curve). The scatter of the two overall light curves satisfies $\sigma_{Qatar-1} \sim 3\sigma_{Control}$, indicating that Qatar-1's variability may be inherent; the horizontal dashed lines in Fig. 5 indicates a band of $2\sigma_{Control}$ width around the mean; there are two outliers (shown in black). We are not in a position to say whether they are intrinsic to Qatar-1or instrumental, except for pointing out that such outliers are absent in the control light curve.

We applied a Lomb-Scargle periodogram (**???**) to search for any periodicity in the Qatar-1 Hα light curve, as well as to the control light curve for a sanity check. Figure 6 shows three periodograms. The top one top shows a periodogram obtained from Qatar-1 differential light curve, while the periodogram in the middle corresponds to the control light curve. Although the highest peak in the control light curve is also seen in Qatar-1's periodogram (vertical-dashed blue lines, slightly shifted), the FAP is relative small (0.08%, more than one order of magnitude larger than Qatar-1's FAP). Since this periodicity is present in both light curves and rather insignificantly, it might be the product of systematic effects related to the observations rather than variability caused due to stellar activity. The bottom panel of Fig. 6 shows the window function of the data. We have indicated with vertical-dashed black lines two peaks seen only in the control light curve. These peaks are, consequently, produced by the sampling and are not due to any physically-related periodicity.

For Qatar-1 we thus find a significant peak at $\nu_{Q1} = 0.033 \pm 0.005$ c/d (corresponding to $P_{Q1} = 30 \pm 6$ days). The error for the frequency corresponds to the dispersion σ_{Gauss} of a Gaussian function, which was fitted to the leading peak; the false-alarm probability (FAP) of the maximum power is 0.002%. Covino et al. (2013) showed Qatar-1 to be a slow rotator ($v\sin(i) = 1.7 \pm 0.3$ km/s). Assuming the reported $v\sin(i)$ to be the rotational velocity at the stellar equator and using the stellar radius as estimated by Alsubai et al. (2011) ($R_S = 0.823 \pm 0.025 R_\odot$), the observed $v\sin(i)$ translates into a rotation period of $\sim 25 \pm 5$ days. Thus, within errors both periods seem to be consistent and we therefore interpret ν_{Q1} as the rotation period of the star.

Using the period obtained from the periodogram we fitted a sinusoidal variation to the Qatar-1 data, using the ansatz

$$H_\alpha(t) = \Delta\, mag \cdot \sin(2\pi(t \cdot \nu_{Q1} + \phi)) \,, \tag{4}$$

where $\Delta\, mag$ is the magnitude variation, ϕ the phase, and ν_{Q1} is kept fixed at 0.033 c/d. After fitting the complete data set first, and the data set without the points outside the distribution, we found that changes in the fitted amplitudes are contained within the precision of the data (blue and pink continuous lines, Fig. 5). Therefore, we estimated the photometric Hα variability as $\Delta mag = 0.009 \pm 0.001$. According to Pogson's law (Allen 1973), this corresponds to a flux variation of ~0.8%. In Section 5.3 we show that this variation is possible to be reproduced by small changes in the equivalent width of the Hα line.

5.2 Stellar activity and age

Adopting our estimated rotational period for Qatar-1, $P_{Q1} = 30 \pm 6$ days, we can estimate the gyrochronological age, t_{gyro}, using the relation given by Barnes (2007), Eq. 3. Considering a T_{eff} of 4910 K (Covino et al. 2013), the corresponding color index is (B-V) = 0.9. We obtain an age of $t_{gyro} = 2.7 \pm 1$ Gyr, i.e., Qatar-1 is neither very young nor very old.

5.3 The Hα spectral line in the context of photometric data

In order to obtain spectroscopic information on Qatar-1 we observed took a spectrum using the 1.2m "Hamburg Robotic Tele-

[ht!]

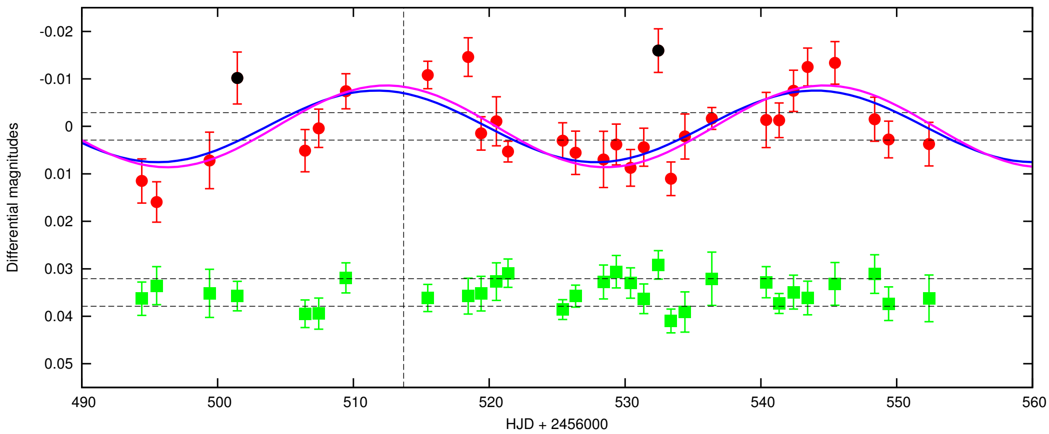

Figure 5. Hα photometric follow-up of Qatar-1. On top and in red circles, the differential light curve for Qatar-1, while on bottom in green squares, the control light curve. Horizontal lines show $\pm 1\sigma$ the scatter of the control light curve. The blue and pink lines show the best-fit sinusoidal to the data. The vertical dashed line shows the position at which we also acquired spectral information on Qatar-1.

[ht!]

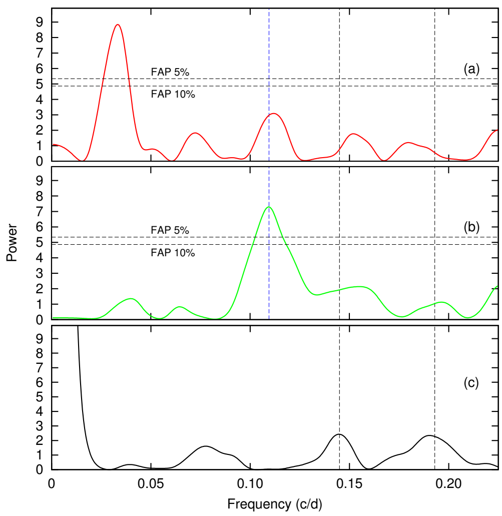

Figure 6. From top to bottom: (a) Lomb-Scargle periodogram of Qatar-1 Hα light curve in red; (b) the control light curve in green; (c) the window function in black. In the three panels vertical black lines show the positions of the two main peaks located in the window function. The blue vertical line shows the position of the most significant peak of the control light curve. The largest peak of the Qatar-1 light curve lies around 0.033 ± 0.005 c/d (~30 days).

[ht!]

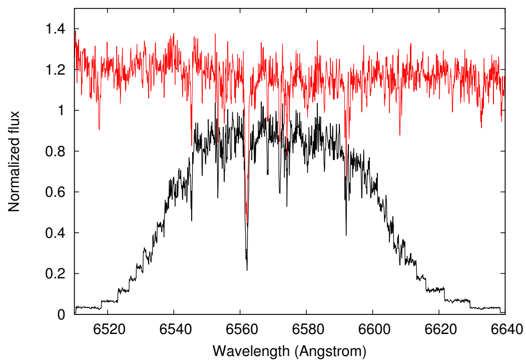

Figure 7. On top and in red continuous line, the HRT Qatar-1 spectra is seen. The black continuous line shows the convolution between the filter transmission function and the spectra. Around 6562 Å lies the Hα line, clearly in absorption.

scope" with its fibre-fed Echelle spectrograph (HRT[6]) located at La Luz Observatory, in Guanajuato, Mexico (Mittag et al. 2011). The spectrum covers the wavelength range between ~380 to ~880 with spectral resolution of about R ~ 20 000. Since Qatar-1 is quite faint we obtained 3 spectra of 30 minute integrations each, which were coadded to minimize the unwanted effects of cosmic rays. Using the pipeline (Mittag et al. 2010), the finally merged spectrum has a SNR of ~ 40, shown in Fig. 7 (in red continuous line) around the Hα line, which is the most prominent absorption feature around 6562 Å. Overplotted in black, we show the convolution between the transmission function of the OLT Hα filter and the HRT spectrum.

To analyze if the measured Hα photometric variation can be reproduced by changes in the equivalent width (EW) of the line only, we carried out the following exercise: We first assumed that the 0.8% variation is effectively a product of stellar activity and caused by Hα EW variations. We then integrated the flux under the

[6] http://www.hs.uni-hamburg.de/DE/Ins/HRT/hrt_main.html

transmission function of the filter and compared that flux with the flux only in the Hα line, where the changes in the equivalent width are measured. We consider that the wings of the Hα line extends ± 2 Å with respect to the line center. By comparing this flux with the flux in the Hα line, the equivalent width should change by as much as 10% in order to produce the observed Hα-filter variations. Such variation can occur for moderately active stars (Herbst & Miller 1989), re-emphasizing that the observed variability might indeed be related to stellar activity.

5.4 The Hα EW in the context of activity

Herbst & Miller (1989) carried out a detailed study on the EW in K and M type stars of different activity levels. In particular they attempted to characterize the activity level of the stars by producing a "EQ main sequence as a function of its color" as a function of the readily observable quantities EW and R-I colors through the empirical relation

$$EW_{H\alpha} = -1.49 + 1.95(R-I) - 0.77(R-I)^2 \,, \qquad (5)$$

which is valid for the range R-I > 0.4. The spectral type of Qatar-1 has been identified as K2V (Alsubai et al. 2011; Covino et al. 2013). The color information reported by Droege et al. (2006) (V = 12.84 ± 0.14, I = 11.71 ± 0.08) is consistent with spectral types K0 to K5. Following the calibration of MK spectral types (Allen 1973), K0 corresponds to R - I = 0.42, K2 to R-I = 0.48, and K5 to R-I = 0.63. Using these values into Eq. 5 yields $EW_{H\alpha} = -0.806$, $EW_{H\alpha} = -0.731$, and $EW_{H\alpha} = -0.567$, respectively. Finally, from our HRT spectrum we calculate the EW of the Hα line as $EW_{H\alpha,HRT} = -0.764 \pm 0.064$. In Fig. 5 the date when the HRT spectrum was acquired is indicated by a dashed vertical line; as is clear from Fig. 5, the spectrum was obtained close to what we believe corresponds to the observed maxima of Hα activity.

In Fig. 8 we show a part of the EW–color index diagram of Herbst & Miller (1989)'s work (their Figure 4), along with our estimated EW of Qatar-1 and the calculated R-I values. The position of Qatar-1 in this EW-R-I diagram is well in the the distribution of the stars reported by Herbst & Miller (1989). Therefore, our analysis seems to support the reported activity of the star reported by Covino et al. (2013).

6 CONCLUSIONS

Based on observations of 42 primary transits obtained from two different observing sites and campaigns, we improved the orbital parameters of the Qatar-1 system. Once we had reliable orbital parameters, we calculated individual mid-transits from the complete data set and, with them, we studied the viability of previously-claimed TTVs in the system. Although in principle the scatter in the O-C diagram seems to be considerable high, we studied separately the mid-transit shifts obtained from complete primary transits and found that they are consistent with no TTV. Therefore, our previously reported indications of transit timing variations are not supported using additional data and longer time coverage.

Furthermore, in an attempt to better characterize the system, we carried out a photometric follow up of the host star in Hα using Hamburger Sternwarte's facilities. We see clear evidences of activity, correlated with what we estimated to be the rotational period of the star. Translating the amplitude of the Hα photometric variation into changes in the equivalent width of the Hα line, we found that they could be caused by a moderately active star, as reported by Covino et al. (2013).

[ht!]

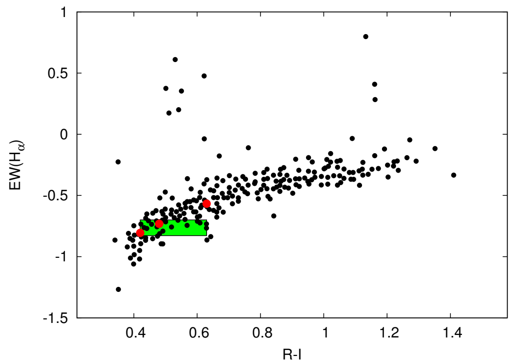

Figure 8. Hα EW, as a function of R-I, obtained from Herbst & Miller (1989) in black points, the values of $EW_{H\alpha}$ obtained using Eq. 5 from the same authors for three different color indexes in red points, and our estimated EW including the errors as a green rectangle.

Although we believe that activity can induce shifts in the O-C diagram, mainly as product of deformations in the light curves caused by stellar spots, the photometric data we have cannot prove such a connection.

ACKNOWLEDGEMENTS

C. von Essen and S. Lalitha acknowledges funding by the DFG in the framework of RTG 1351. A.O. acknowledges financial support from the Deutsche Forschungsgemeinschaft under DFG GRK 1351. The authors acknowledge the HRT team for the spectroscopic observations of Qatar-1 and the subsequent data reduction. C.v.E. recognizes and acknowledges S. Dreizler for his support during the preparation of this work.

References

Allen, C. W. 1973, Astrophysical quantities
Alsubai, K. A., Parley, N. R., Bramich, D. M., et al. 2011, MNRAS, 417, 709
Anglada-Escudé, G., Tuomi, M., Gerlach, E., et al. 2013, A&A, 556, A126
Barnes, J. R., Jeffers, S. V., & Jones, H. R. A. 2011, MNRAS, 412, 1599
Barnes, S. A. 2007, ApJ, 669, 1167
Barros, S. C. C., Bou, G., Gibson, N. P., et al. 2013, MNRAS, 430, 3032
Boisse, I., Bouchy, F., Hobrard, G., et al. 2011, A&A, 528, A4
Carter, J. A. & Winn, J. N. 2009, ApJ, 704, 51
Cincunegui, C., Díaz, R. F., & Mauas, P. J. D. 2007, A&A, 469, 309
Cochran, W. D., Fabrycky, D. C., Torres, G., et al. 2011, ApJS, 197, 7
Covino, E., Esposito, M., Barbieri, M., et al. 2013, ArXiv e-prints
Czesla, S., Huber, K. F., Wolter, U., Schroeter, S., & Schmitt, J. H. M. M. 2009, A&A, 505, 1277

Dawson, R. I. & Fabrycky, D. C. 2010, ApJ, 722, 937
Droege, T. F., Richmond, M. W., Sallman, M. P., & Creager, R. P. 2006, PASP, 118, 1666
Eastman, J., Siverd, R., & Gaudi, B. S. 2010, PASP, 122, 935
Fischer, D. A., Marcy, G. W., Butler, R. P., et al. 2008, ApJ, 675, 790
Ford, E. B., Ragozzine, D., Rowe, J. F., et al. 2012, ApJ, 756, 185
Fressin, F., Torres, G., Rowe, J. F., et al. 2012, Nature, 482, 195
Gregory, P. C. & Fischer, D. A. 2010, MNRAS, 403, 731
Hartman, J. D., Bakos, G. A., Torres, G., et al. 2011, ApJ, 742, 59
Hauschildt, P. H. & Baron, E. 1999, Journal of Computational and Applied Mathematics, 109, 41
Herbst, W. & Miller, J. R. 1989, AJ, 97, 891
Howell, S. B. 2006, Handbook of CCD Astronomy, ed. R. Ellis, J. Huchra, S. Kahn, G. Rieke, & P. B. Stetson
Howell, S. B. 2009, in Bulletin of the American Astronomical Society, Vol. 41, American Astronomical Society Meeting Abstracts 213, 202.02
Jones, E., Oliphant, T., Peterson, P., et al. 2001, SciPy: Open source scientific tools for Python, http://www.scipy.org
Kipping, D. & Bakos, G. 2011, ApJ, 733, 36
Kipping, D. M. 2010, MNRAS, 408, 1758
Lissauer, J. J., Fabrycky, D. C., Ford, E. B., et al. 2011, Nature, 470, 53
Lomb, N. R. 1976, Ap&SS, 39, 447
Maciejewski, G., Dimitrov, D., Neuhauser, R., et al. 2010, MNRAS, 407, 2625
Maciejewski, G., Dimitrov, D., Neuhauser, R., et al. 2011, MNRAS, 411, 1204
Mandel, K. & Agol, E. 2002, ApJ, 580, L171
Mittag, M., Hempelmann, A., Gonzalez-Perez, J. N., & Schmitt, J. H. M. M., 2010, Advances in Astronomy, 2010
Mittag, M., Hempelmann, A., Gonzalez-Perez, J. N., Schmitt, J. H. M. M.& Hall, J. C. 2011, in Astronomical Society of the Pacific Conference Series, Vol. 448, 16th Cambridge Workshop on Cool Stars, Stellar Systems, and the Sun, ed. C. Johns-Krull, M. K. Browning, & A. A. West, 1187
Patil, A., Huard, D., & Fonnesbeck, C. J. 2010, Journal of Statistical Software, 35, 1
Pont, F., Zucker, S., & Queloz, D. 2006, MNRAS, 373, 231
Scargle, J. D. 1982, ApJ, 263, 835
Southworth, J., Hinse, T. C., Jrgensen, U. G., et al. 2009, MNRAS, 396, 1023
Steffen, J. H., Fabrycky, D. C., Agol, E., et al. 2013, MNRAS, 428, 1077
von Essen, C., Schroeter, S., Agol, E., & Schmitt, J. H. M. M. 2013, A&A, 555, A92
Young, A. T. 1993, The Observatory, 113, 41
Zechmeister, M. & Krüster, M. 2009, A&A, 496, 577

This paper has been typeset from a TEX/ LATEX file prepared by the author.

Modeling correlated noise to study transit timing variations I. A description of the source code and first results

C. von Essen & S. Cellone

Submitted to A&A, September 2013

Astronomy & Astrophysics manuscript no. TTVsim
September 23, 2013

Modeling correlated noise to study transit timing variations I. A description of the source code and first results

C. von Essen[1], S. Cellone[2,3,4]

[1]Hamburger Sternwarte, Universität Hamburg, Gojenbergsweg 112, 21029 Hamburg, Germany
[2]Consejo Nacional de Investigaciones Científicas y Técnicas, Av. Rivadavia 1917, C1033AAJ, Ciudad Autónoma de Buenos Aires, Argentina
[3]Facultad de Ciencias Astronómicas y Geofísicas, Universidad Nacional de La Plata, Paseo del Bosque, B1900FWA, La Plata, Argentina
[4]Instituto de Astrofísica de La Plata (CCT-La Plata, CONICET-UNLP), Paseo del Bosque, B1900FWA, La Plata, Argentina

September 2013

ABSTRACT

Aims. The use of inhomogeneous and low-quality transit light curves could be playing a main role against exoplanetary search via transit timing variations. Our goal is to investigate to what extent are ground-based observations reliable to detect additional planets in already known planetary systems.

Methods. To meet this goal, we simulated primary transit observations caused by a real system conformed by a hot Jupiter that is orbiting around a K type star. To resemble real ground-based observations, we attempt to reproduce, by means of physically and empirically motivated relationships, the unwanted effects caused by the Earth atmosphere over the synthetic light curves. Therefore, the synthetic data present different photometric quality and transit coverage. In addition, we introduced a perturbation in the mid-transit times of the hot Jupiter, caused by an Earth-sized planet in a 3:2 mean motion resonance. Analyzing the synthetic light curves produced after certain epochs, we attempt to recover the synthetically added transit timing variation signal by means of primary transit fitting techniques.

Results. We present an extensive description of the structure of the code, along with a discussion and motivation for the considered noise sources. Additionally, we provide a comparison analysis between real and synthetic light curves, to test up to what extent do both data sets present the same degree of distortion. Finally, we present our first analysis on the primary transit light curves towards transit timing variation analysis.

Key words. atmospheric effects – methods: data analysis – techniques: photometric – planets and satellites: fundamental parameters

1. Introduction

Around ~900 exoplanets have been found so far, from which roughly one third transit their host star. Once a planet has been detected via the transit method, variations in its timing can provide a powerful tool to detect further planets with masses even down to one Earth mass (Agol et al. 2005; Holman & Murray 2005).

The advent of highly-accurate space-based observations such as Kepler (Borucki et al. 2010) or CoRoT (Baglin et al. 2006) space missions marked a new era for exoplanet search. For instance, Kepler light curves already revealed clear signatures of transit timing variations (TTVs; see e.g., Holman et al. 2010; Lissauer et al. 2011; Ballard et al. 2011; Steffen et al. 2013). However, these space missions were neither designed to observe the whole sky nor to follow up already known single exoplanetary systems outside their fields of view. At present, this role can only be played by ground-based telescopes located across the globe.

To produce reliable TTV studies, optimal ground-based observations of primary transits would require, to start, a sufficiently long time baseline, good phase coverage, and deep primary transits. However, TTV studies are carried out under less strict conditions. Literature already reveals how misleading can ground-based observations be. For instance, after analyzing archival data along with two consecutive transit observations, Díaz et al. (2008) reported TTVs in OGLE-Tr-111. Later on, Adams et al. (2010b) obtained 6 additional transit light curves. After re-analyzing the complete data set, the authors found no detection of TTVs. Before the Kepler team released the first quarters, Mislis et al. (2010) reported a significant variation in the inclination of Tres-2, one planetary system within Kepler's field of view. Schröter et al. (2012), in turn, re-analyzed all the published observations in addition to the Kepler data. While ground-based observations revealed a declining trend in inclination, Kepler data were consistent with no variation at all (see Schröter et al. 2012, Figure 2). Intriguingly, Tres-2 has one of the largest primary transit depths. Another system that has been systematically observed during primary transit is WASP-3. Using observations obtained by means of small aperture telescopes, Maciejewski et al. (2010) firstly reported the detection of TTVs in the system. Additionally, after collecting more than 3 years of transit observations Eibe et al. (2012) reported probable variations in the transit duration, instead of the claimed TTVs. However, Montalto et al. (2012) studied thirty-eight archival light curves in an "homogeneous way", and found no significant evidence of TTVs in WASP-3 system.

Although the TTV technique is a powerful method to detect exoplanets in multiple systems, the systematic disagreement between authors causes critical readers to disbelieve low-amplitude results. Furthermore, planet formation theories (Fogg & Nelson 2007; Mandell et al. 2007) and highly precise observations

Please give a shorter version with: \authorrunning and/or \titilerunning prior to \maketitle

(Steffen et al. 2012; Steffen & Farr 2013) reveal that hot Jupiters are prone to conform single systems instead of multiple ones. It is natural then to ask ourselves if ground-based observations are precise enough to detect the imprints that a less-massive body would produce in the timings of a hot Jupiter, or if our atmosphere and its effects over photometric data is playing against us. These circumstances motivated us to write a code capable to create realistic synthetic light curves affected by several systematic effects that are commonly present in ground-based observations. The main goal is to study under which conditions can the artificially added TTV signal be retrieved. This first work presents a detailed account of our code, a brief report of our initial results of TTV modeling and the most evident conclusions that we have drawn from it. A more detailed analysis of the simulated data is in preparation.

2. Our code: Generalities

2.1. Starting point: Stellar and planetary properties

To begin with, our code needs the configuration and the properties of the system to be simulated. In the case of the host star, the inputs are the stellar radius R_S, the spectral and subspectral type, the celestial coordinates α and δ in J2000.0, the apparent visual magnitude $m_{V,*}$ and the mass M_S. For the transiting (and more massive) planet the inputs are the orbital parameters needed for the transit model (Mandel & Agol 2002), i.e. the semi major axis a, the orbital period P, the inclination i, the planetary radius R_{Trans} and the mid-transit time T_o, in addition to the planetary mass M_{Trans}. For the perturbing planet the inputs are its mass M_{Pert} and the order of the mean-motion resonance j, since we will consider timing variations caused by an Earth sized planet in an outer orbit inside a first order resonance $j : j+1$ (Section 2.2). We then convert the star and both planet parameters in convenient units for the program. Considering k ~400 epochs (this equates to ~2 years of follow-up observations in the frame of the transiting exoplanet), we calculate the transit timing variation that the perturber exerts on each mid-transit $T_{o,k}$.

Instead of fixing the required parameters arbitrarily, we reproduced a real system: Qatar-1 (Alsubai et al. 2011). It is the first exoplanet discovered by the Alsubai Project exoplanet transit survey. The host has been characterized as an old K type star. A high orbital inclination angle implies a nearly grazing transit, which would make the system highly sensitive to TTVs. As a result of the large exoplanetary radius and the short orbital period of the exoplanet, the transits are deep and easy to observe, even with small aperture telescopes. Table 1 shows the orbital parameters obtained by Alsubai et al. (2011), considered as input values for our code. Our group has been carrying out follow-up observations of the system for more than two years (von Essen et al. 2013). Therefore, part of our analysis will include a comparison test between real and synthetic data.

2.2. Producing the TTV imprint

Agol et al. (2005) derived an order of magnitude of the perturbation that is caused when two planets coexist in a first-order mean-motion resonance. The authors estimated the amplitude δt_{max} and the libration cycle P_{lib} of the timing variations (their Eq. 33 and Eq. 34, respectively) to be:

$$\delta t_{max} \sim \frac{P_{Trans}}{4.5j} \frac{m_{Pert}}{(m_{Pert} + m_{Trans})} \ , \quad (1)$$

Table 1. Input parameters (Qatar-1, Alsubai et al. 2011). The program does not require error estimates. In consequence, they are not listed.

Star	M_S ($M_\odot$)	0.85
	R_S ($R_\odot$)	0.823
	Spectral type	K2
	V (mag)	12.9
	α (^{hs})	20.2251
	δ (°)	65.1619
Planet	T_o (BJD-TDB)	2455518.4102
	P (days)	1.420033
	i (°)	83.47
	a (UA)	0.02343
	R_P (R_J)	1.164
	M_P (M_J)	1.090
Perturber	M_{Pert} (M_J)	0.007
	j	2

$$P_{lib} \sim 0.5 j^{-4/3} \left(\frac{m_{Trans}}{m_{Star}}\right)^{-2/3} P_{Trans} \ . \quad (2)$$

Therefore, the perturbations are added to the unperturbed mid-transit times as follows:

$$T_{o,k} = T_o + k \times P_{Trans} + \delta t_{max} \ \sin\left[2\pi P_{Trans}(k-1)/P_{lib}\right] \ . \quad (3)$$

T_o is the starting epoch given as input parameter in Barycentric Julian Dates ($\mathrm{BJD_{TDB}}$), $k \times P_{Trans}$ are the unperturbed mid-transits for each epoch k, and δt_{max} $\sin\left(2\pi P_{Trans}(k-1)/P_{lib}\right)$ is the perturbation term. Once the TTV signal is added, the program does a main loop over each perturbed epoch $T_{o,k}$.

2.3. The ground-based observatories

For the purposes of our analysis we consider three "virtual observatories". They populate the northern hemisphere and are separated mostly in geographic longitude, in order to ensure an optimal night coverage.

The code requires basic information on the sites and the instrumental setup, such as the mean seeing, the extinction coefficient κ, the geographic coordinates, the available filters and CCDs, and the primary mirror apertures. The values considered within our code are listed in Table 2. Particularly, the Hamburger Sternwarte and the Observatorio Astronómico de Mallorca host the telescopes that were used to perform the photometric follow-up on Qatar-1. In consequence, the observations collected at both sites will play a main role in the testing of our code. Nonetheless, the program is general and the given locations, atmospheric characteristics, and equipment sets can be easily changed to others.

To carry out a TTV analysis, it is of common use to combine light curves that were produced under inhomogeneous instrumental setups and atmospheric conditions (see e.g., Nascimbeni et al. 2013; Maciejewski et al. 2010; Shporer et al. 2009). To investigate if this procedure influences a possible TTV detection, our program chooses the observatory and filter randomly.

2.4. Limb-darkening coefficients

Claret & Hauschildt (2003); Claret (2004), and Claret & Bloemen (2011) have been providing the exoplanet community with the computation of limb-darkening coefficients. Although the authors cover most of (if not all)

Please give a shorter version with: \authorrunning and/or \titilerunning prior to \maketitle

Table 2. Basic description of the observatories considered to produce our synthetic light curves. The first two, Hamburger Sternwarte and Observatorio Astronómico de Mallorca, are in fact real observatories that belong to the University of Hamburg. Their instrumentation and sky quality descriptions are also realistic. Although Mc Donald observatory also exists, the instrumental setup presented here is of our own invention. mag/AM denotes magnitudes per airmass value.

Observatory	Geographic coordinates	Primary mirror (m)	Available filters	CCD	<seeing> (″)	$<\kappa_V>$ (mag/AM)
Hamburger Sternwarte	$\lambda = 53.48°$ $\phi = 10.2414°$	1.2	Johnson-Cousins R,I Sloan i	ALTA U 9000	2.5	0.20
Observatorio Astronómico Mallorca	$\lambda = 39.64°$ $\phi = 2.9509°$	0.6	Johnson-Cousins R,I Sloan r	ST7XM	2.0	0.18
Mc Donald Observatory	$\lambda = 30.67°$ $\phi = -104.021°$	1.5	Sloan r, i, z	STL11000M	1.5	0.14

Table 3. Limb-darkening coefficients for the filters considered in this simulation. They were obtained using synthetic PHOENIX spectra.

Filter	u_1	u_2
Johnson-Cousins *R*	0.5960	0.1147
Johnson-Cousins *I*	0.4669	0.1478
Sloan *r*	0.6180	0.1086
Sloan *i*	0.4863	0.1437
Sloan *z*	0.3812	0.1629

the standard systems, many observations are carried out using non-standard filters. Since it is our intention to make the code as general as possible, we produced the limb-darkening coefficients in our own fashion.

As a first step we produced angle-resolved synthetic spectra using PHOENIX (Hauschildt & Baron 1999; Witte et al. 2009), given the effective temperature, the metallicity, and the surface gravity of the target star. We then convolved the synthetic spectra with each filter transmission function (see Table 2 for available filters) and integrated them afterward in wavelength. We ended up with intensities as a function of $\mu = cos\,\theta$, where θ is the angle between the line of sight and the line from the center of the star to a position of the stellar surface. Intensities were fitted afterward with a quadratic limb-darkening law:

$$I(\mu)/I(1) = 1 - u_1(1-\mu) - u_2(1-\mu)^2\ , \qquad (4)$$

from where the u_1 and u_2 quadratic limb-darkening coefficients were obtained. The final limb-darkening coefficients are listed in Table 3. Once the site, the CCD, and the filter are randomly chosen, the corresponding limb-darkening coefficients are added to the program variables.

2.5. Reference stars

After the site is selected, the program chooses between one up to seven reference stars randomly, which will be later combined to perform the differential photometry. The selection of the reference stars (*rs*) complies one of the following three criteria:

- The *rs* are the same for all the sites along all epochs. Therefore, the program will choose them only once.
- The *rs* are the same, but for each site only. Therefore, three different sets of reference stars will be chosen once.
- The *rs* will be always different. Therefore, the number of *rs*, their angular separation relative to the target star in ($\Delta\alpha$,$\Delta\delta$), and their spectral type, will be selected during each epoch.

The celestial coordinates of the target star are precessed from J2000.0 to $T_{o,k}$. Then the ($\Delta\alpha$,$\Delta\delta$) separations of the *rs*, relative to the target star, are randomly determined. The values that $\Delta\alpha$ and $\Delta\delta$ can take are limited by the telescope's field of view. In a further step, another subroutine assigns the spectral and sub-spectral type, from where the effective temperature T_{eff} is then added to the program variables.

Instead of assigning the spectral type to the *rs* from a flat distribution (i.e., any spectral type has the same probability to be randomly selected), we carried out a more realistic approach. To this end, we used the Henry Draper (HD) catalog (Nesterov et al. 1995; Kharchenko & Roeser 2009). The catalog provides, among others, the spectral types of ~88 000 stars as a function of their apparent magnitude. Since accurate photometric light curves are generally obtained when the brightness difference between target and *rs* is small (see e.g., Howell 2006), the knowledge of the apparent magnitude of the target star would set constraints on the fluxes of convenient *rs*. One adequate limit, considered within our code, is given by $\Delta m = |m_{V,*} - m_{V,ref}| < 0.5$. Therefore, we firstly selected from the catalog the stars within the range of magnitudes ($m_{V,*} - 0.5, m_{V,*} + 0.5$). Then, we counted the number of stars per spectral types O,B,A,F,G,K, and M. The resulting histogram is listed in Table 4. Finally, to assign the spectral types to the reference stars, we used the normalized histogram as probability distribution function. Although the HD catalog is quite extensive, the number of stars is relatively low to produce a further discrimination with respect to the sub-spectral type. Therefore, the subclass is randomly chosen.

Table 4. Stellar number as a function of spectral type for the stars with magnitudes close to $m_{V,*}$ (14 077 out of ~88 000 stars) obtained from the Henry Draper catalog.

Spectral type	Number of stars
O	21
B	511
A	5058
F	2648
G	2542
K	2327
M	970

2.6. Visibility

In a further step, the program verifies whether the mid-transit time $T_{o,k}$ occurs at night. As "night", we consider the time between astronomical twilight. Therefore, we calculate sunrise and sunset times for a Sun at -18° with respect to the selected site's horizon. If the transit occurs during night, we inspect whether the star's altitude at mid transit is higher than 35°. This is rendered to avoid non-linear extinction effects in our synthetic light curves. If, however, $T_{o,k}$ occurs during daylight or during night but with the star under 35° of altitude, then the program skips the rest, increments one epoch, and repeats all the steps again up to this one.

2.7. Duration of the observations

With the mid-transit time taking place at night, and the star above 35°, the program produces a random length for the synthetic transit light curves. As time scale we use the transit duration T_{dur}, which can be calculated from the system's orbital parameters (Haswell 2010):

$$T_{dur} = \frac{P}{\pi} \mathrm{asin}\left(\frac{\sqrt{(R_S + R_P)^2 - a\cos(i)^2}}{a}\right), \tag{5}$$

In order to ensure synthetic light curves as realistic as possible, with the calculated observation length the program randomly selects one among four transit observation scenarios:

- The transit is complete, including also a considerable amount of out of transit (OOT) data before and after transit.
- The transit is partially complete. It includes OOT data before and after transit, but has also data gaps in between.
- The transit is not complete. The mid-transit time is observed but ingress or egress and OOT data before or after transit, respectively, are completely missing.
- The transit is not complete. The mid-transit time is not observed. Only a small fraction of ingress or egress along with some OOT data are produced.

The segment of the transit that is missing and the longitude of the OOT data points are always a random multiple of the transit duration. Particularly, the duration of the OOT data points is smaller than ~ 2-3 hours, since real observations of primary transit events tend to be produced in this fashion.

Subsequently, the program estimates the exposure time, considered as fixed within each epoch. This resembles robotic telescopes, for which the exposure time is estimated a priori in order to reach certain signal-to-noise ratio. The exposure time is estimated considering the telescope's primary mirror size, the altitude of the star at mid-transit, the star visual magnitude, the filter response, the atmospheric mean extinction, the CCD quantum efficiency, the Moon phase, and the desired signal-to-noise ratio.

2.8. Time stamps

Making use of the duration of the observation and the exposure time as time steps, we produce a temporal array in universal time (equivalently, in Julian dates). Using Carter & Winn (2009) web tool[1], we then convert the Julian dates into barycentric Julian dates employing the celestial coordinates of the star in J2000.0, the geographic coordinates of the site, and its elevation.

[1] http://astroutils.astronomy.ohio-state.edu/time/utc2bjd.html

With the time stamps in barycentric Julian dates, we calculate the projected separation between planet and star centers δ_j for each instant BJD_j:

$$\delta_j = \sqrt{1 - \cos(\phi_j)^2 \sin(i)^2}\,\frac{a}{R_S} \tag{6}$$

which requires the previous knowledge of the orbital phase:

$$\phi_j = \frac{2\pi(BJD_j - T_{o,k})}{P} - n_{orb} \tag{7}$$

for a given orbit number n_{orb}.

With δ_j, the planet-to-star ratio $p = R_P/R_S$, and the quadratic limb-darkening coefficients u_1 and u_2 we produce the synthetic star flux-drop during transit using Mandel & Agol (2002) primary transit model.

Once the basic structure of the light curves is complete (i.e., primary transit model as a function of barycentric Julian dates) we add correlated and uncorrelated noise, and save the product at each step.

3. Our code: Correlated noise sources

In general, the variations in the observations that are not associated to intrinsic fluctuations of a stellar source are correlated in time. With respect to ground-based observations, this is caused by transparency variations in the Earth's atmosphere or changes in the altitude of the star along the observations, for instance. Therefore, the natural scatter in the data will not be white but "red" instead. "Red noise" is the manifestation of systematic effects in photometric time series, and is "red"-colored because it manifests itself in the milli-magnitude regime. We believe that this time-dependency is the main cause of misleading results in the TTV analysis. Therefore, the intention of this work is to model correlated noise sources and add them into the light curves, in order to study to which extent are the mid-transit times affected by correlated noise.

3.1. Residual modulation due to first order atmospheric extinction

First order atmospheric extinction, (i.e., extinction independent of stellar color), is airmass dependent. Since differential photometry involves at least two stars at different elevations, a residual modulation due to airmass differences can be detected, increasing when the elevation difference between the target star (sub-index *) and the reference stars (sub-index $1, 2, \cdots, n$) increases as well. For any star, absorption by the atmosphere can be described by Bouguer's law, viz.:

$$m = m_o - \kappa\chi\ , \tag{8}$$

where m_o denotes the stellar magnitude outside the atmosphere, κ the extinction coefficient in magnitudes per airmass (mag/AM), $\chi = sec(z)$ the airmass value during a certain observation, and z the zenith distance of the star. Since light curves are produced only when the altitude of the star at mid-transit time is larger than ~35°, the linear representation of airmass is sufficiently accurate.

To decrease the scatter of the final light curve, it is of common practice to consider as reference star the combination of many others. Hence, considering Bouguer's and Pogson's laws,

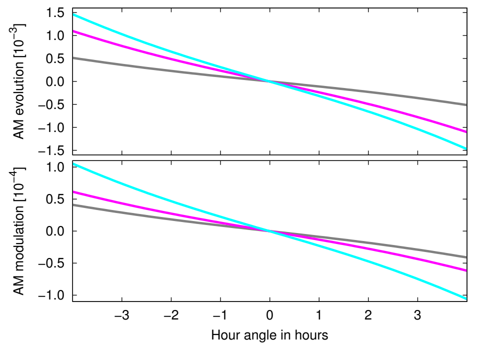

Fig. 1. Top panel: airmass difference between target and reference star, as a function of hour angle, in units of 10^{-3}. Bottom panel: airmass modulation due to airmass differences (Eq. 9), in units of 10^{-4}. The lines correspond to an angular separation of 7 arcmin and κ_{HSO} = 0.2 mag/AM (gray), 15 arcmin and κ_{MCD} = 0.14 mag/AM (pink) and 20 arcmin and κ_{OAM} = 0.18 mag/AM (cyan).

the airmass modulation AM_{mod} that will affect the differential light curve will follow:

$$log(AM_{mod}) = \frac{\kappa}{2.5}\left(\chi_* - \frac{1}{n}\sum_{i=1}^{n}\chi_i\right) , \quad (9)$$

The second term inside the parenthesis accounts for the combined airmass contribution of n reference stars.

The top panel of Figure 1 shows how the airmass difference between target and one particular reference star evolves, as a function of the angular separation between stellar objects (color-coded) and the hour angle t. $t = 0$ denotes the culmination instant of the target star. The bottom panel of the same Figure shows how the airmass modulation AM_{mod} evolves, as the stars move across the sky. Note that the angular separation between stars are constrained by the size of the field of view of each telescope.

To calculate the airmass χ_i for each reference star, we use the previously selected $\Delta\alpha$ and $\Delta\delta$ displacements, relative to the target star. Although the modulation effect is small, it rapidly increases with the angular separation between target and reference stars. Since small telescopes tend to have large field of views (~ 1 deg or larger) we consider this effect relevant and the first atmospheric-correlated noise source. The unaffected transit light curve is deformed by AM_{mod}.

3.2. Color-dependent residual modulation

Extinction is caused by absorption and scattering of light. Water vapor, ozone, and dust, but mostly Rayleigh scattering in the optical, are contributing to it. Color-dependent extinction (or "second-order extinction") appears because the light of a stellar object, on its path through the atmosphere, has a wavelength-dependent absorption. In consequence, if two stars of dissimilar intrinsic color indexes are observed at same altitudes, the absorption will differ.

When the differential photometry technique is performed using stars of different spectral types, a color-dependent residual shows up. Frequently, the spectral information of the stars involved in the differential photometry is completely missing. Therefore, the effect can not be modeled out. To model it in, we followed Broeg et al. (2005) methodology (see their Section 4.2 for a complete analytic description). For each observation instant j, the second order extinction modulation SOE_{Mod} follows:

$$SOE_{Mod} = R(T_*, \chi_{*,j})/(\Pi_{i=1}^{n} R(T_i, \chi_{i,j}))^{1/n} , \quad (10)$$

$R(T_*, \chi_{*,j})$ accounts for the flux change of the target star due to the Earth's atmosphere, while $R(T_i, \chi_{i,j})$ for each one of the reference stars $i, 1, \cdot, n$. The wavelength dependency has been already integrated out. It involves the filter, the quantum efficiency of the CCD, and the black body curves of the target and reference stars. Figure 2 shows how the second order extinction amplitude depends on the spectral type of the chosen reference stars. Considering a target star with T_{eff} = 4900 K (similar to Qatar-1), we estimated the strength of SOE_{Mod} for one given reference star with effective temperatures 3 000, 4 500, 5 000, 8 000, 10 000, and 15 000 K. As the Figure clearly reveals, the effect grows when the difference between spectral types maximizes. Note that the slope of the residual modulation changes from positive to negative, when the effective temperature of the reference star turns from being larger to smaller than the effective temperature of the target star.

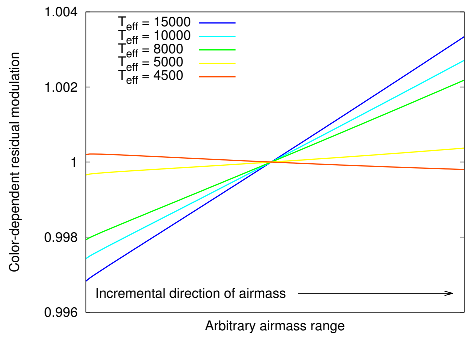

Fig. 2. Color-dependent residual modulation considering different effective temperatures for the reference stars.

3.3. Non-photometric conditions

3.3.1. Irregularities caused by changes in the atmospheric seeing

Although large telescopes are located in the most convenient sites with respect to altitude and photometric conditions, this is not always the case for centimeter–to–meter class telescopes. Small telescopes are located all over the world, where photometric conditions can be far from optimal. Abrupt changes in the atmospheric transparency, the humidity and the ambient temperature, added to cirrus and clouds passing by, can produce unwanted photometric variability. In such sites, atmospheric seeing tends to quickly degrade with airmass.

Aperture photometry involves the measurement of stellar fluxes within a fixed aperture radius. Thus, during any data reduction process the aperture radius can be selected to coincide with, for example, the full-width at half-maximum (FWHM) of the first image. For instance, if the observations are carried out only after culmination, as a product of the degradation of the atmospheric seeing the integrated flux inside the fixed aperture will decrease with time. If changes in the photometric conditions would propagate equally to all the stars within the field of view, the differential photometry technique would be satisfactory to eliminate any unwanted variation. However, real photometry reveals that the point spread function (PSF) of all the stars slightly differ from one another. Therefore, differential light curves will show a residual modulation strongly correlated with airmass. To model this effect, we made use of physically and empirically motivated relationships.

Although atmospheric seeing is a very local measurement that strongly depends on the position of the turbulent atmospheric layers, we started considering seeing as scaling with the airmass to the power of 0.6 (see e.g., Sarazin & Roddier 1990; Gusev & Artamonov 2011). Figure 3 shows the evolution of seeing (equivalently, FWHM) as a function of airmass. The FWHM measurements correspond to Qatar-1. The observations were carried out at Hamburger Sternwarte. The black continuous line indicates a fit to the data of the form $FWHM(\chi) \propto \chi^{0.6}$.

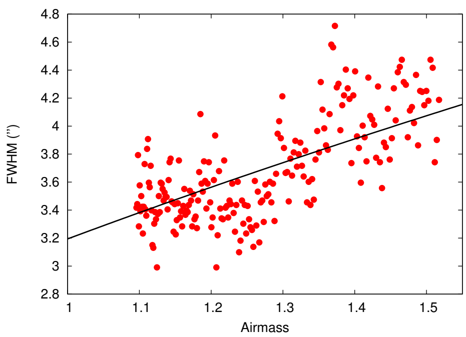

Fig. 3. FWHM evolution as a function of the airmass. FWHM$\propto \chi^{0.6}$ properly reproduces the trend of the observed changes in the FWHM. During the observations the telescope was slightly defocused. Therefore, the values of the FWHM are not a realistic measurement of the characteristic seeing of the site.

Furthermore, the stellar integrated fluxes are estimated as the volume under a three-dimensional normal distribution, $G(\mu, \sigma)$. The FWHM is related to the normal distribution via the standard deviation σ as $FWHM = 2\sqrt{2ln(2)}\sigma$. For a given aperture radius R_{ap} and FWHM, the volume is easily integrable. In polar coordinates, for any given star:

$$\begin{aligned} F_{star} &= \int_0^{2\pi}\int_0^{R_{ap}} G(r,\theta)\; r\; dr\; d\theta \\ &= \int_0^{2\pi}\int_0^{R_{ap}} A\; e^{-r^2/2\sigma^2}\; r\; dr\; d\theta \end{aligned} \tag{11}$$

where A denotes the intensity peak of the normal distribution. For a fixed exposure time, an increase in airmass translates into a decrease in the intensity peak. To shape this out, we studied the intensity peak evolution present in our observations of Qatar-1. Figure 4 shows the evolution of A as a function of airmass, for $i = 9$ stars. From our combined HSO and OAM data we found that a linear relation, in the form:

$$A(\chi)_i = -a_i\chi + b_i\; , a > 0 \tag{12}$$

is sufficient to properly reproduce the observed variation. Furthermore, the relation between the slope and the intercept satisfies:

$$|a_i|/b_i = \mathbb{C} + \epsilon_i \tag{13}$$

for each i star within the field of view, for $\epsilon << 0$, and $\mathbb{C}$ a number close to 0.5. Independently of the intrinsic brightness of the stars, our observations reveal that the ratio $|a_i|/b_i$ stays approximately the same during a given observing run, as reflected in Eq. 13.

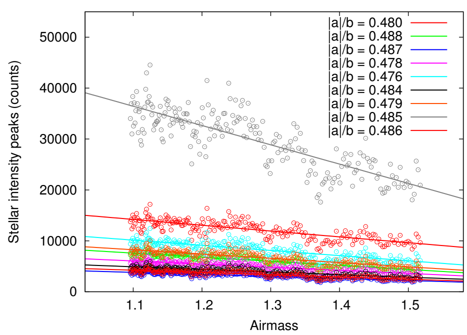

Fig. 4. Intensity peaks of 9 stars within HSO field of view, as a function of airmass (saturation level of HSO CCD lies at 65535 counts). A linear trend, as reported in Eq. 12, is overplotted in continuous line.

With the FWHM and A empirically described as a function of airmass, we re-analyzed our observations to set constraints on the dispersion of both parameters. As an example, the top panel of Figure 5 shows the variation of the FWHM for Qatar-1 with respect to the mean FWHM of the night. In the bottom panel of the Figure we show the relative difference between the FWHM of Qatar-1 and the FWHM of eight reference stars within HSO field of view. We used two times the standard deviation of the data points as an upper limit to assess the dispersion of the FWHM. Equivalently, a similar procedure was repeated for the intensity peaks.

To model the residual modulation in the light curves caused by changes in the photometric conditions, for each epoch the code generates the random number $\mathbb{C}$, close to 0.5. Then, for the target and the $i = 1, \cdot, n$ reference stars, the code produces $n + 1$ ϵ_i and $n + 1$ a_i. With Eq. 13 the intercepts b_i are determined, and by means of Eq. 12 the peak intensities for the $n + 1$ stars are finally obtained. The resultant modulation is given by:

$$FWHM_{mod} = F_*/(\Pi_{i=1}^{n} F_{ref,i})^{1/n} \tag{14}$$

The primary transit light curves are then further modified by the estimated $FWHM_{mod}$.

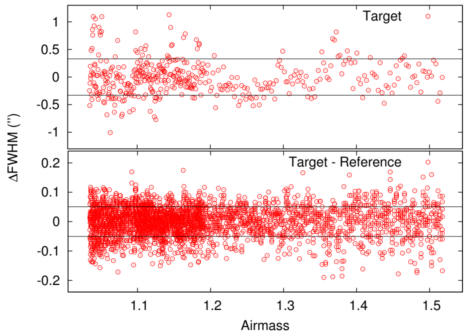

Fig. 5. Changes in the FWHM for Qatar-1 (top) and for eight reference stars (bottom) relative to Qatar-1. Airmass values between 1 and 1.2 are oversampled with respect to the rest, because the star was observed before and after culmination. The standard distribution of both data sets was used to set constraints on the scatter of the simulated FWHM.

3.3.2. Scintillation

Astronomical seeing refers to the blurring of astronomical images caused by the turbulence in the Earth's atmosphere. In addition, the brightness of stars appears to vary due to a process called scintillation. Scintillation is caused by small-scale fluctuations in the density of the air as a result of temperature gradients. Based on Young (1993) approach, we estimate the contribution of scintillation noise to the accuracy of photometric measurements:

$$S = 0.0030\, D^{-2/3}\, \chi^{3/2}\, e^{h_{obs}/h_o}\, \tau^{-1/2}\ , \tag{15}$$

where D is the telescope diameter in meters, h_{obs} is the altitude of the observatory above sea level in km for h_o = 8 km, and τ the exposure time in minutes. In differential light curves scintillation translates directly into the scatter of the data. To include this effect into our light curves, we calculate random Gaussian noise with $\mu = 1$ and σ equal to the given scintillation semi-amplitude. The only changing factor on Young's scintillation expression is the airmass, so the standard deviation will not be constant but will be modulated by the star's altitude, as seen in real light curves, where photometric precision decreases with χ. Consequently, the primary transit synthetic light curves account for scintillation as well.

3.3.3. Clouds and lights

A photometric night is neither defined by the brightness of the sky, nor by its extinction value. Since an increase of the sky brightness can be compensated by longer exposure times, and a low extinction coefficient only means that the sky is fairly transparent, what defines a photometric night is the stability of the sky conditions as the night evolves. Obviously, not all nights are photometric. Cirrus cloud formation (i.e. thin clouds holding ice crystals located at altitudes above 5000 m) are a common phenomenon. They can be easily noticed during the day or during the night under the presence of the Moon, when Moonlight is reflected by the ice crystals inside the clouds. However, cirrus can go unnoticed during dark nights.

When sky conditions are far from optimal, true flux levels of stellar sources cannot be properly measured. They are modulated by the continuous fluctuations dominating the sky conditions. Generally, sky inhomogeneities translate into the data in two forms. In the first case, the scatter of the data are correlated with the night quality. In the second case, when the clouds are inhomogeneous throughout the field of view and change their position rapidly, the light curves show data points clearly outside the normal data distribution. In addition, observatories can be light-polluted. This dramatically reduces the visibility of the stars and enhances, in turn, the effects associated to fluctuations of the night sky.

Due to the random nature of this effect, we approach its modeling by analyzing real HSO and OAM Qatar-1 data. To this end, we considered several observing nights and counted how many points were observed away from the normal distribution. A given photometric point was considered an outlier if it was more than $2{\times}\sigma$ displaced, being σ the natural scatter of the data, estimated from the residual light curves. For the analyzed HSO and OAM light curves of Qatar-1, up to 20% of the data points were outside the data scatter. Therefore, for each synthetic light curve the code randomly selects between 0% up to 20% of synthetic data points to be placed as outliers. To produce the shift, we calculated a "local standard deviation", taking into account only the flux measurements in the vicinity of the randomly selected points, in order to correlate the amplitude of the "jump" with the actual local dispersion of the data. We then randomly increase or decrease the position of the point from one up to two times the local standard deviation.

3.4. Photometric errors

The photometric errors of each stellar source are usually given by a photometric reduction task. When differential photometry is carried out, the errors associated to the differential light curve are obtained propagating the errors of the involved stars. Because error propagation entangles addition, sky modulations due to changing weather conditions do not vanish, as in the case of differential photometry but, instead, are amplified. Additionally, reduction tasks do not account for systematic effects over the photometry. Therefore, the produced photometric errors are underestimated (see e.g., Gopal-Krishna et al. 1995, for IRAF's underestimated errors). It is our intention to reproduce as credible values for the photometric error bars as possible, and also consider the effects that underestimated photometric errors might induce on our light curves and the subsequent study of TTVs. Therefore, to calculate a representative magnitude for the error bars we used 18 observing nights acquired at HSO, and 7 more obtained at OAM. Our photometry was originally produced using the reduction task *apphot* from IRAF (see the task's help for a rigorous description of how the photometric errors are estimated). Since we do not count with real observations of Qatar-1 for MCD, we assumed smaller values for the errors, taking into account that the sky quality is considerably better at MCD than at HSO or OAM. We produced an histogram of the individual photometric errors of Qatar-1. For both HSO and OAM we fitted a Gaussian profile to the histograms (pink and cyan lines in Fig.6, respectively), from where we obtained the mean μ_{error} and the dispersion σ_{error} of the most representative values for the photometric uncertainties. For each data point j we estimated the magnitude of the individual photometric errors ϵ_j using a Gaussian random number generator and (μ_{error},σ_{error}).

Due to continuous changes in the sky conditions the photometric errors also fluctuate. To estimate the frequencies ν_k at

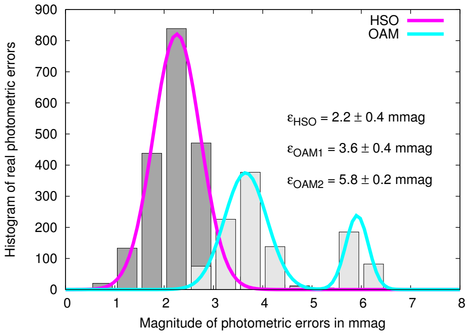

Fig. 6. Most representative error values ϵ for HSO (pink line) and OAM (cyan line) analyzing 18 and 7 primary transit light curves, respectively.

which the sky tends to vary more often, we run a Lomb-Scargle periodogram (Lomb 1976; Scargle 1982; Zechmeister & Kürster 2009) over OAM and HSO data. To this end, we analyzed 25 observing nights produced at HSO spanning two years, and 10 nights produced at OAM covering one year. Once individual periodograms were calculated, we sum them up and use the four main peaks that are more relevant for a transit observation duration (of the order of a couple of hours) to describe the fluctuations of the sky (Figure 7).

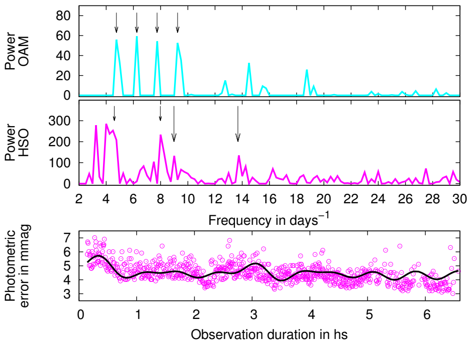

Fig. 7. From top to bottom: most representative sky fluctuations for OAM (cyan line) and HSO (pink line). The bottom plot corresponds to the errors for one observing night at HSO. In black, considering the four main frequencies, μ and σ, we fitted only the phases to the light curve (black line) to show the goodness of our approach.

All together, using the error magnitude ϵ obtained from a normal random distribution, the frequencies ν_k at which the sky tends to vary more often, and a phase value ϕ_k randomly selected between 0 and 1, the final photometric errors $\hat{\epsilon}_j$, for each observation j, are estimated as follows:

$$\hat{\epsilon}_j = \epsilon_j \prod_{k=1}^{m} \sin\left[2\pi(\nu_k\, BJD_j + \phi_k)\right] . \tag{16}$$

3.5. Final light curves

Figure 8 shows how one particular synthetic light curve evolves, when the correlated noise sources are sequentially added. From top to bottom. The last light curve is normalized and the error bars account for correlated noise. These are the light curves that will be used to carry out the TTV analysis.

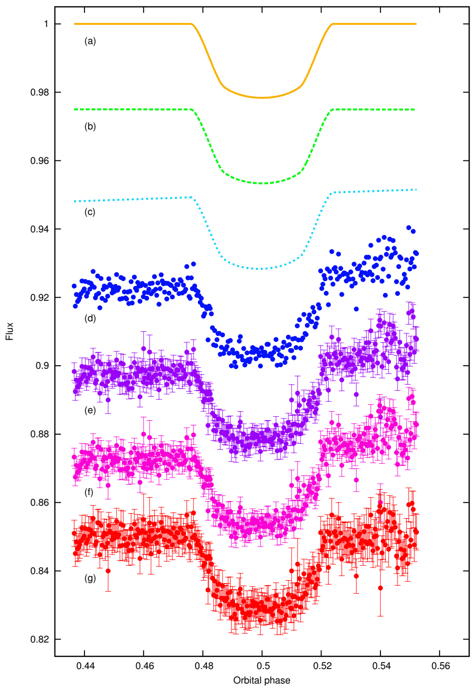

Fig. 8. From top to bottom: (a) Initial light curve (LC). It defines the duration of the observation. The "+" symbol denotes an effect added to the light curve from the previous step; (b) + first order extinction; (c) + second order extinction; (d) + scintillation; (e) + errors + "jumps"; (f) + seeing effects; (g) Normalized LC + correlated noise.

4. Testing our light curves: Real vs. synthetic data

Figure 9 shows real versus synthetic transits of Qatar-1. In both cases, the observations were performed and simulated using Johnson-Cousins R filter and Oskar Lühning Telescope at HSO.

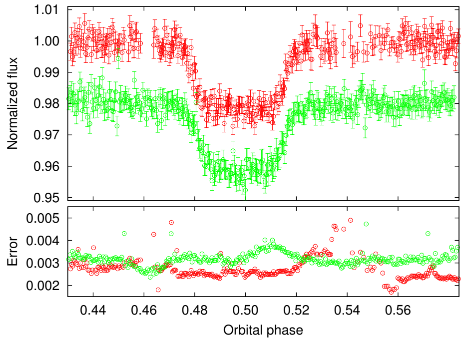

Fig. 9. Real (red) and synthetic (green) light curves of Qatar-1, produced using Oskar Lühning telescope and Johnson-Cousins R filter. Bottom panel shows how error bars change due to non-photometric conditions.

As initial test, both light curves are visually comparable. The most important difference (and advantage) in favor of synthetic light curves is the fact that correlated noise sources are completely known. For real light curves, however, one can only estimate how much are they affected by red noise, but not exactly why and how. In order to properly test the similitude between real and synthetic light curves, a more concise analysis needs to be performed.

4.1. Comparing time-correlated noise structure

Carter & Winn (2009) (and references therein) studied how time-correlated noise affects the estimation of the orbital parameters. To quantify how dominated are our synthetic light curves by red noise, we reproduced their analysis as follows: by subtracting the primary transit model to each light curve, we produced light curve residuals. We then produced M equally-large bins, varying M between 1 and 40 depending on the available data points per transit light curve and calculated N, the mean value of data points per bin. If residuals are not affected by red noise, they should follow the expectation of independent random numbers:

$$\sigma_N = \sigma_1 N^{-1/2}[M/(M-1)]^{1/2} , \tag{17}$$

where σ_1 is the sample variance of the unbinned data and σ_N is the sample variance (or RMS) of the binned data:

$$\sigma_N = \sqrt{\frac{1}{M}\sum_{i=1}^{M}(\mu-\mu_i)^2} , \tag{18}$$

μ_i corresponds to the mean value of the residuals inside each bin, and μ to the mean value of the means μ_i. If correlated noise is present, then each σ_N will differ by a factor β_N from their expectation. By averaging β_N over timescales that are judged to be important for transit observations (ingress or egress duration), the parameter β can be estimated. β accounts for the strength of correlated noise in the data. For Qatar-1, the time between first and second contact (or equivalently, the time between third and fourth contact) is $\Delta n \sim 15$ minutes. To estimate β, we averaged individual β_N's calculated out from bins with sizes 0.8, 0.9, 1.0, 1.1 and 1.2 times Δn.

Figure 10 shows an histogram of β, using the available synthetic light curves produced after 60 runs of our code, considering raw (blue) and normalized (black) data for Johnson–Cousins R filter (see Section 5 for a detailed description about the normalization process). Generally, $\beta = 1$ corresponds to data sets free of correlated noise. A Gaussian distribution is over-plotted on each histogram, after fitting its amplitude A, mean μ and dispersion σ. As expected, the most representative value of β lies around 1.

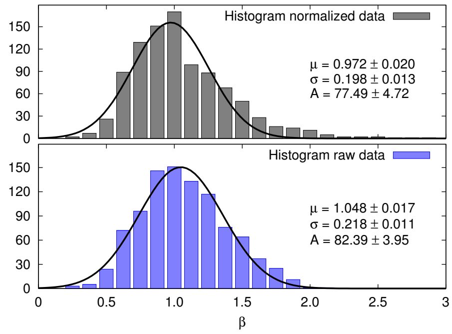

Fig. 10. Histogram of the strength of correlated noise β considering raw (blue) and normalized (black) synthetic light curves.

To test the β-values obtained from our synthetic data, we compared them to β-values obtained from real photometry. For a quick comparison of the noise structure, Figure 11 shows the results of our correlated noise analysis for the longest three nights of Qatar-1 real data on top (red lines), and three randomly chosen synthetic light curves on bottom (green lines). In all cases, black lines show how residuals should behave in absence of red noise. Red and green lines represent the variance of the binned data for HSO real and synthetic light curves, respectively, as a function of the bin size. As expected, the larger the bin size, the smaller the RMS. For some of our available Qatar-1 primary transit light curves we estimated β by averaging β_N over the same 5 bin sizes already stated. Raw data reveals $0.51 < \beta < 1.75$, while normalized data is consistent with $0.51 < \beta < 1.78$. Comparing the histograms against real data, ~90% of our synthetic light curves present the same amount of correlated noise. Considering that the number of synthetic light curves significantly exceeds our observations, the correlated noise structure is indeed comparable.

4.2. Comparing autocorrelation signals

In statistics, autocorrelation occurs when residual error terms from observations of the same variable at different times are correlated. If residuals are dominated by Gaussian white noise, then the normalized autocorrelation of the residuals follows a normal distribution with mean $\mu = 0$ and dispersion $\sigma = 1/\mathrm{N}$. N denotes the number of data points. Ideally, for white noise most of the residual autocorrelation signal should fall within 95% confidence bands around the mean. If the autocorrelation signal of

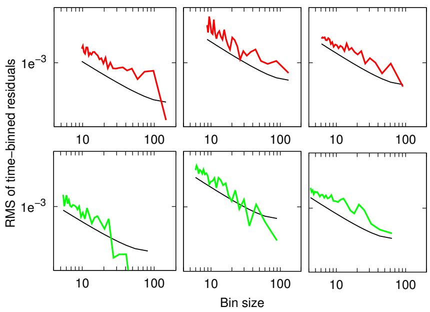

Fig. 11. RMS of time-binned residuals as a function of bin size for real (red and top) and synthetic (green and bottom) light curves, respectively.

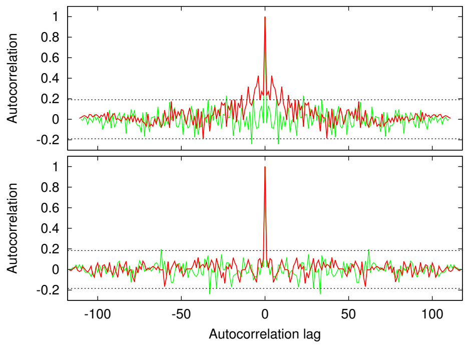

Fig. 12. Autocorrelation function for real residual light curves (red) and simulated white noise (green) as comparison. Top: real data account for correlated noise. Bottom: real data fall inside the 95% confidence band, indicated with black-dashed horizontal lines.

a given data set doesn't behave as mentioned, then the data accounts for correlated noise.

Figure 12 shows an example of the difference in the residual autocorrelation that exists among real photometry of Qatar-1 obtained during two different nights. As a comparison, the autocorrelation for simulated residuals affected only by Gaussian white noise is plotted in green, along with the 95% confidence band indicated in black-dashed lines. The autocorrelation function for two HSO observing nights is plotted in red. On top, the real light curve is affected by correlated noise, since the central part of the autocorrelation function clearly escapes the 95% confidence band. On bottom, correlated noise appears to be negligible.

Furthermore, we compared the autocorrelation structure between real and synthetic data sets (Figure 13). The autocorrelation function was calculated from the residual light curves, obtained after the primary transit model was subtracted. To compare real to synthetic light curves we carried out the following analysis: we first calculated the autocorrelation function of real photometric data, and plotted the largest autocorrelation value $AC_{max,real}$ as a function of the data point number (red filled circles). Since it only takes to validate $AC_{max,real}$ against the 95% confidence band to estimate if the light curves are indeed affected by red noise, we considered sufficient to use $AC_{max,real}$ to compare both sets. As expected, there is a trend that follows smaller $AC_{max,real}$ values for larger N's. Finally, we estimated $\mu_{AC_{max,real}} \pm \sigma_{AC_{max,real}}$ and $\mu_N \pm \sigma_N$.

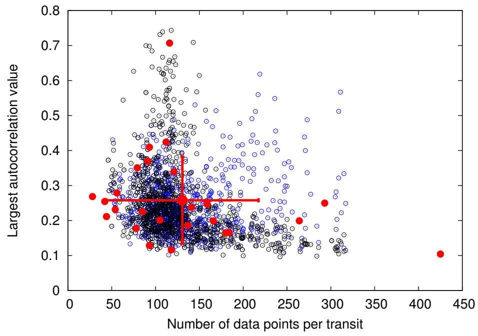

Fig. 13. Largest autocorrelation value for synthetic light curves (blue circles correspond to raw data while black ones to normalized light curves) and 25 real observations carried out with HSO and Johnson-Cousins R filter.

Using the synthetic light curves we repeated the same process for raw (blue) and normalized (black) data. In both cases, ~80% of the data points fall within the $1\sigma_{AC_{max,real}}$, plotted in Fig. 13 with red error bars. Taking into account that we count with substantially more synthetic than real data, the remaining 20% can be neglected. Therefore, real and synthetic data seem to present similar correlated noise structure.

5. Recovering the TTV signal: General aspects

Once the synthetic light curves are generated (usually between 50 to 70 each run), recovering the TTV signal is the next step to follow. Before transit fitting starts, we visually inspect the generated light curves, removing those presenting extremely poor transit coverage, scatter that might be comparable to the transit depth, or are extremely affected by correlated noise. The number of deleted light curves clusters around 7 per run. A common procedure on handling light curves is the normalization. Regularly, a low order polynomial is fitted to the OOT data points, which has no physical implications but only mathematical ones. The complete light curve is then divided by it. The normalization of the synthetic data is carried out considering one of the following criteria:

- If more than 10 data points were produced before transit start and more than 10 after transit end, a second order polynomial is fitted to the OOT data points.
- If the transit is incomplete and more than 20 OOT data points before (or after) transit were produced, a first order polynomial is fitted to the OOT data points.
- If none of both previous conditions are satisfied (i.e., the number of OOT data points is too low) then the light curve is left untouched.

Once the light curves are normalized, we produce a synthetic O-C diagram to study if the TTV signal can be retrieved. To this end, we proceed as follows:

– To obtain good estimates for the system parameters, the light curves must account for OOT data before and after primary transit. Therefore, we first choose the best ones within the sample. Usually, the number of selected light curves are ~15, divided among the 5 filters and the 3 observatories that the code considers (Sect. 2.3). It is worth to mention that an incorrect selection of transit light curves (i.e., by considering primary transits with large scatter, incomplete, or strongly affected by atmospheric effects) leads to *very* inaccurate orbital parameters.
– From the latter sub-sample, we choose the best light curve with respect to data scatter and sampling rate. It will be considered as the 0^{th} epoch.
– We then proceed to fit the selected data by sampling from the posterior probability distribution using a Markov-chain Monte Carlo (MCMC) approach. To this end, we use the transit model developed by Mandel & Agol (2002)[1]. From the transit light curve we can directly infer the following parameters: the orbital period, P, the mid-transit time, T_o, the planet to star radius ratio, $p = R_p/R_s$, the semi-major axis in stellar radii, a/R_s, the orbital inclination, i, and the limb-darkening law. For our fits we assume a quadratic limb-darkening prescription with fixed coefficients u_1 and u_2 (Table 3).
– After 5×10^5 iterations we discard a suitable burn-in (typically 10^5 samples) and determine the combination of parameters resulting in the lowest deviance (henceforth, global parameters). We consider the lowest deviance as our global best-fit solution. The errors for the global parameters are derived from the 68 % highest probability density or credibility intervals (1 σ).
– To consider the existing information in the further determination of the individual mid-transit times, we specify Gaussian priors on a/R_s, i, p, T_o, and P. Then, we fit each synthetic light curve to obtain the best-fit mid-transit times $T_{o,k}$. As individual error measurements, we consider the MCMC errors at 1σ level.
– To produce the synthetic O–C diagram, "Calculated" mid-transits are an integer multiple of the global orbital period, counting from the 0^{th} epoch. "Observed" mid-transits are the ones individually fitted in the previous step.

Figure 14 shows five synthetic light curves previously normalized, one for each available filter. The data quality and also even their duration vary considerably. Light curves of this kind, combined all together, will be the ones used to perform the TTV analysis. In addition, Figure 15 shows one of the many synthetic O-C diagrams, obtained from the previously described procedure. One curious aspect is how the seasonal effect can be observed, noticed in the lack of data points around epochs -120 and 100.

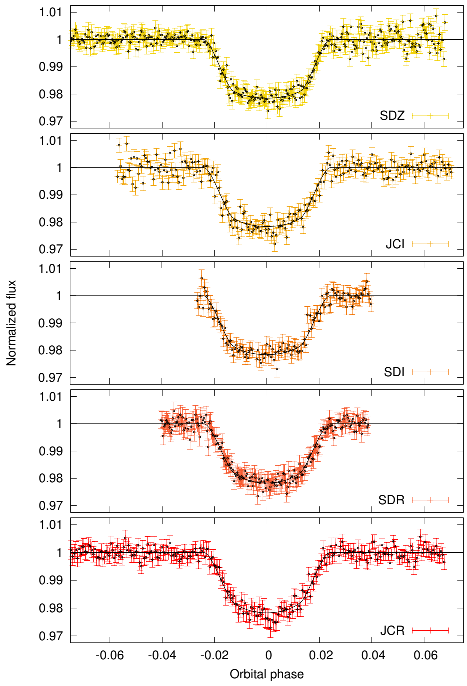

Fig. 14. Sample of synthetic light curves. In continuous line, Mandel & Agol (2002) primary transit model for each limb darkening coefficient set.

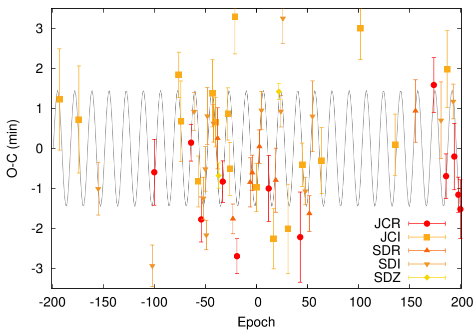

Fig. 15. Synthetic O-C diagram. The mid-transit shifts are color-coded according to the randomly selected filter. The timing variation added by the code to each mid-transit time is plotted with gray continuous line. Clearly, some points scatter outside the true TTV signal.

6. Recovering the TTV signal: First results

6.1. Determination of the global parameters

The determination of the individual mid-transit times strongly depends on the accuracy of the orbital parameters. Therefore, we characterized their accuracy considering as error estimates

[1] http://www.astro.washington.edu/users/agol

the ones produced by the code (mainly underestimated), and new ones accounting for correlated noise.

To this end, we first fitted Mandel & Agol (2002)'s primary transit model to each synthetic light curve. We then subtracted the fitted model, from where residual synthetic data were obtained. We used the residuals to calculate the scatter of each light curve, σ_{LC}, and the β-value to account for correlated noise (see Section 4.1). Instead of using only the errors that the code provides, we used the scatter of the data σ_{LC} enlarged by β as well. Therefore, each run was conformed by two sets: identical times and fluxes, but different error estimates (henceforth "no red" for underestimated errors and "red" for errors that account for correlated noise).

After fitting the synthetic data as described in Section 5, we show in Figure 16 our results. Blue circles and 1σ errors correspond to the global parameters obtained by means of "no red" synthetic data. Black squares and 1σ errors account for correlated noise ("red"). The initial orbital parameters used by the code to produce the synthetic data have been subtracted from the best-fit solutions. In consequence, the resulting parameters are clustering around zero (red diamond). Although the black data points are not all consistent with the input parameters, they scatter closer to the expected values. In other words, individual photometric errors that account for correlated noise yield better estimates for the orbital parameters. The sub-plot from the upper-left part of Fig. 16 shows the already known correlation between the semi-major axis and the orbital inclination via the impact parameter $b = a\cos(i)$. Surprisingly, the resulting combination of semi-major axis and inclination overestimate the impact parameter in most of the cases. This might be product of the normalization process. Comparing both sets of solutions, $\sigma_{a,nored}/\sigma_{a,red} = 1.5$, $\sigma_{i,nored}/\sigma_{i,red} = 1.7$, $\sigma_{p,nored}/\sigma_{p,red} = 1.9$, and $\sigma_{P,nored}/\sigma_{P,red} = 1.6$. Our results reveal that a proper treatment of the individual photometric errors yields a significantly better solution for each orbital parameter.

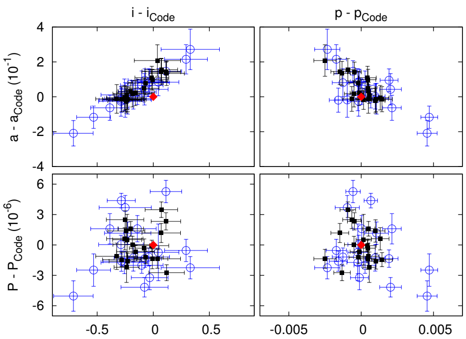

Fig. 16. Global parameters obtained from "not red" (blue open circles) and "red" (black filled squares) synthetic data. The best-fit values have been shifted to the ones used by the code as input.

6.2. Observed offset in the O-C diagram

To estimate how much are the mid-transit times affected by the transit duration, we randomly selected 20 synthetic O-C diagrams, from where we computed the timing residuals (the absolute value of the difference between the observed timing offset and the mid-transit shift produced by the code) as a function of transit coverage, number of OOT data points, and number of data points during primary transit. For the latter, Figure 17 shows our results, when "no red" and "red" sets are considered (blue and black data points, respectively). To quantify the correlation of the mid-transit offsets we used the Pearson correlation coefficient r:

$$r_{xy} = \frac{\sum_{i=1}^{n} (x_i - \mu_x)(y_i - \mu_i)}{[\sum_{i=1}^{n} (x_i - \mu_x)^2 \sum_{i=1}^{n} (y_i - \mu_y)^2]^{1/2}} , \qquad (19)$$

for x number of data points during primary transit and y the timing residuals. $r_{nored} = -0.35$ and $r_{red} = -0.27$ confirm that the correlation, which is observable even by visual inspection, truly exists. Similar results were obtained analyzing the timing residuals against OOT data points and transit coverage. Thus, we caution the use of incomplete light curves or poorly sampled primary transits to carry out TTV studies.

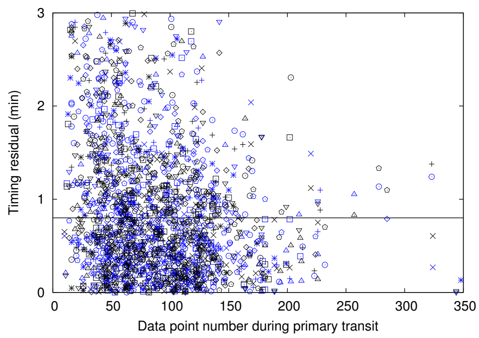

Fig. 17. Timing residuals as a function of the number of data point number during primary transit. Blue points: "no red" data sets. Black points: "red" data sets. The horizontal black line indicates the mean value of the residual offsets (below one minute). The plot has been produced from the analysis of 20 synthetic O-C diagrams.

6.3. Scatter in the O-C diagram: How much do systematics contribute?

When a periodogram analysis of the O-C diagram reveals no significant peak (i.e., there is no cyclic transit time variation observed) it is of common practice to use the scatter in the O-C diagram to place upper limits on the mass and orbital separation of a hypothetical perturbing planet (see e.g., Adams et al. 2010a, 2011). To this end, different dynamical scenarios are considered and analyzed (for example, an inner perturber, an outer perturber, or two bodies in mean-motion resonances, Agol et al. 2005). In each dynamical configuration, the semi-major axis and the orbital eccentricity vary within a range of possible values. At each step, the scatter of the theoretical O-C diagram is computed, and compared to the scatter that is observed. This procedure is repeated considering different masses for the perturbing body.

As seen in Section 6.2, poor primary transit coverage can yield to a considerably large timing offset that is completely independent of any TTV. Therefore, to understand whether unaccounted correlated noise sources lead to under- or over-estimations of the characteristics of the perturbing body, we followed the just mentioned approach. To this end, we compared the scatter of the synthetic O-C diagram to the first order mean-motion resonance scenario.

First, we computed the observed standard deviation of each synthetic O-C diagram:

$$\sigma_{OC,synth} = \left[\frac{1}{N_{OC}-1} \sum_{k=1}^{N_{OC}} [T_{o,k} - (T_o + P n_{orb,k})]^2 \right]^{1/2} \quad (20)$$

where N_{OC} is the number of light curves that the code generated in a given run, minus the ones that were deleted after visual inspection (Section 5). $n_{orb,k}$ corresponds to the orbit number with respect to the zeroth epoch, and T_o and P are the best-fit mid-transit time for the zeroth epoch and the orbital period, respectively.

If two planets coexist in mean motion resonance, as pointed in Section 2.2 the perturbation term $PT(k)$ added to the unperturbed mid-transit times, for a given k epoch, has the following expression:

$$PT(k) = \delta t_{max} \sin[2\pi P_{Trans}(k-1)/P_{lib}] \ . \quad (21)$$

From Eq. 21 we can compute the theoretically expected scatter:

$$\begin{aligned} \sigma_{model} &= <(PT(k))^2>^{1/2} \\ &= <(\delta t_{max} \sin[2\pi P_{Trans}(k-1)/P_{lib}])^2>^{1/2} \\ &= (\frac{<\delta t_{max}^2>}{2})^{1/2} \\ &= \frac{\delta t_{max}}{\sqrt{2}} \ . \end{aligned} \quad (22)$$

Therefore, to estimate the perturber's mass by comparing the observed scatter, $\sigma_{OC,synth}$, to the theoretical one, σ_{model}, we require information about the orbital period and the mass of the transiting planet (which is normally known from transit and RV modeling), in addition to the order of the resonance. The only parameter that will vary, while comparing σ_{model} to $\sigma_{OC,synth}$, is the mass of the perturber.

Every run yields slightly different orbital parameters (Section 6.1). Therefore, to be able to compare the results obtained at each run we considered the orbital period and the planetary mass used by the code as input parameters, and relatively large errors for the mentioned parameters (0.1% and 10%, respectively). Kipping (2010) studied the effects of finite integration times on the determination of the orbital parameters. If we consider the error on the mid-transit times that large exposure times produce, we will be able to define a lower limit on the amplitude of the TTV that we can really detect. Since we are considering only the case of first order mean-motion resonances produced by an Earth-sized planet, $j \geq 3$ would yield TTV amplitudes too small to be detected for exposure times of the order of one minute. Furthermore, the model has been claimed to be inaccurate for $j = 1$ (Agol et al. 2005). Therefore, it would not be inappropriate to restrict the resonance order to $j = 2$ in principle, if our aim is to be consistent with the data that we count with.

Figure 18 shows the resulting synthetic O-C standard deviation in black circles when "red" (y-axis) and "no red" (x-axis) data sets are plotted against each other (see Section 6.1 for the definition of "red" and "no red"). In vertical and horizontal continuous lines we plotted the scatter obtained from Eq. 22, when 1 (red), 1.5 (pink), 2 (blue), 2.5 (cyan), and 3 (green) times the input perturber mass $m_{Pert} = 0.007\ M_J$ are considered. Propagating the errors of P and m_{Trans} allowed us to produce an error estimate for σ_{model}. The latter is plotted only horizontally with dashed lines following the mentioned color-coding, to avoid visual contamination.

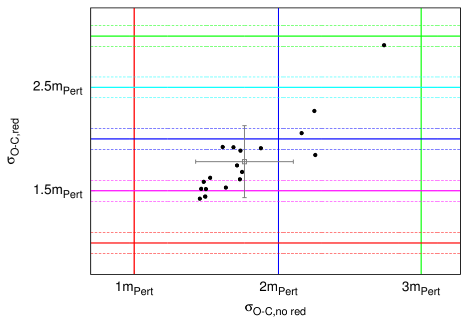

Fig. 18. Synthetic O-C scatter for "red" and "no red" data sets for 20 runs of the code.

After comparing the predicted to the observed scatter, we found two main results: first, the scatter of the synthetic O-C diagram, associated to "red" and "no red" data sets, yield equivalent planetary masses. Second and most important, the planetary masses obtained from the scatter of the synthetic O-C diagrams are over-estimated in *all* the cases, by a factor of two or more. Therefore, we caution to use poor ground-based observations to determine realistic upper limits for the perturber.

6.4. Periodogram analysis

In both continuous and discrete cases, Fourier theory explains how any function can be represented or approximated by sums of simple trigonometric *and periodic* functions. Given any time series, it is possible to find sines and cosines with different periodicity, phases and amplitudes that, when added together, can reproduce the time series back again.

Regarding TTV studies, once an O–C diagram is produced, the first natural step is to look for any kind of periodicity associated to the effects that a perturbing planet might cause on the timings of a transiting exoplanet. However, correlated noise sources affecting mid-transit timings can disguise true signals. To test how much do systematic effects translate into an O-C diagram, we run our code 10 more times, producing synthetic light curves *not* affected by transit timing variations, but affected by every systematic source instead.

We then run a periodogram over each O-C diagram, searching for any leading period that could fake a planetary perturber signal. Considering the 10 runs, for "no red" data we found that five O-C diagrams showed peaks with FAP < 20%, while for "red" data we found only one. Figure 19 shows the O-C diagrams for "no red" (blue) and "red" (black) synthetic data. Looking more carefully into the light curves that generated the mid-transit shifts indicated with rectangles, we can generally pinpoint the following cases:

1) The light curves are incomplete. Second order extinction effects are negligible. Then, both data sets have comparable mid-transit shifts.
2) The light curves are incomplete. Only OOT data points are available after egress or before ingress. Normalization is not recommendable when the light curve does not present OOT data before *and* after transit.
3) The light curve is complete, and strongly affected by second order extinction. It is safe to proceed with the normalization only in this cases.

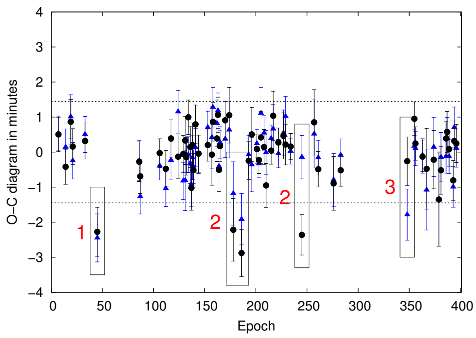

Fig. 19. O-C diagram for non-existent TTV signal. "no red" data points (blue triangles) and "red" ones (black circles) are inconsistent with zero. Dashed lines indicate the TTV maximum amplitude that a 0.007 M_J perturber would exert over the transiting exoplanet.

Figure 20 shows the Lomb-Scargle periodogram, considering as input the synthetic O-C diagram showed in Figure 19 (blue triangles). The upper limit of the periodogram is determined by the Nyquist frequency. The top Figure shows a clear and unrealistic peak, with a false alarm probability (FAP) around 8%. After removing only 4 points out of 63 indicated in Fig 19 with rectangles, we run the periodogram again. The bottom panel of the Figure shows the new periodogram. No significant periodic signal is observed. Therefore, the selection of the light curves and its posterior reduction has to be taken seriously. The addition of inadequate light curves might lead to a non-existent signal.

7. Summary and conclusions

Our main goal is to study whether ground-based observations are reliable to carry out TTV studies. To this end, we simulated primary transit observations caused by a hot Jupiter. Furthermore, we artificially added a perturbation in the mid-transit times of the synthetic light curves, caused by and Earth-sized planet in a 3:2 mean motion resonance. The synthetic data accounts with what we believe are the most significant sources of light curve deformations: airmass, atmospheric extinction, and chaotic variability in the sky conditions during observations. We then tested the quality of our light curves, comparing their noise characteristics to the ones present in real data.

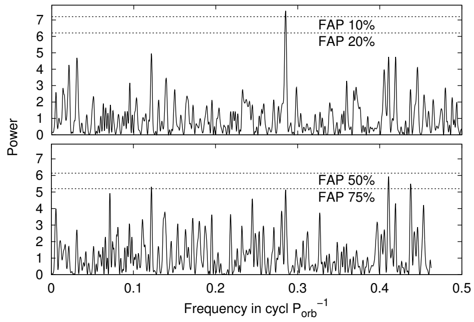

Fig. 20. Lomb-Scargle periodogram for a non-existent TTV signal. Top: the considered data points show a significant peak at $P_{TTV} \sim 3.3 P_{orb}$. Bottom: ruling out the mid-transits indicated by rectangles in Figure 19, the signal has vanished.

As expected, our first results disfavors the use of incomplete light curves. The scatter present in the O-C diagram is sometimes used to set constraints in the characteristics of the perturbing body. After reproducing this approach, our study reveals that it is more likely that a systematic effect, not really accounted for, is causing the scatter in the O-C diagram. This, in consequence, produced upper limits for the perturbing body mass that was a factor of 2 or more overestimated.

In a future publication we will present more in detail the effects of the normalization process over the light curves, when is appropriate to fit the limb-darkening coefficients as well, and how accurately are the mid-transit times determined, as a function of the data scatter and the transit coverage.

8. Acknowledgments

C. von Essen acknowledges funding by the DFG in the framework of RTG 1351, and E. Suarez, A. Ofir, and P. Ioannidis for fruitful discussions.

References

Adams, E. R., López-Morales, M., Elliot, J. L., Seager, S., & Osip, D. J. 2010a, ApJ, 714, 13
Adams, E. R., López-Morales, M., Elliot, J. L., Seager, S., & Osip, D. J. 2010b, ApJ, 721, 1829
Adams, E. R., López-Morales, M., Elliot, J. L., Seager, S., & Osip, D. J. 2011, ApJ, 728, 125
Agol, E., Steffen, J., Sari, R., & Clarkson, W. 2005, MNRAS, 359, 567
Alsubai, K. A., Parley, N. R., Bramich, D. M., et al. 2011, MNRAS, 417, 709
Baglin, A., Auvergne, M., Boisnard, L., et al. 2006, in COSPAR Meeting, Vol. 36, 36th COSPAR Scientific Assembly, 3749
Ballard, S., Fabrycky, D., Fressin, F., et al. 2011, ApJ, 743, 200
Borucki, W. J., Koch, D., Basri, G., et al. 2010, Science, 327, 977
Broeg, C., Fernández, M., & Neuhäuser, R. 2005, Astronomische Nachrichten, 326, 134
Carter, J. A. & Winn, J. N. 2009, ApJ, 704, 51
Claret, A. 2004, A&A, 428, 1001
Claret, A. & Bloemen, S. 2011, A&A, 529, A75+
Claret, A. & Hauschildt, P. H. 2003, A&A, 412, 241

Please give a shorter version with: \authorrunning and/or \titilerunning prior to \maketitle

Díaz, R. F., Rojo, P., Melita, M., et al. 2008, ApJ, 682, L49
Eibe, M. T., Cuesta, L., Ullán, A., Pérez-Verde, A., & Navas, J. 2012, MNRAS, 423, 1381
Fogg, M. J. & Nelson, R. P. 2007, A&A, 461, 1195
Gopal-Krishna, Sagar, R., & Wiita, P. J. 1995, MNRAS, 274, 701
Gusev, A. S. & Artamonov, B. P. 2011, ArXiv e-prints
Haswell, C. A. 2010, Transiting Exoplanets
Hauschildt, P. H. & Baron, E. 1999, Journal of Computational and Applied Mathematics, 109, 41
Holman, M. J., Fabrycky, D. C., Ragozzine, D., et al. 2010, Science, 330, 51
Holman, M. J. & Murray, N. W. 2005, Science, 307, 1288
Howell, S. B. 2006, Handbook of CCD Astronomy, ed. R. Ellis, J. Huchra, S. Kahn, G. Rieke, & P. B. Stetson
Kharchenko, N. V. & Roeser, S. 2009, VizieR Online Data Catalog, 1280, 0
Kipping, D. M. 2010, MNRAS, 408, 1758
Lissauer, J. J., Fabrycky, D. C., Ford, E. B., et al. 2011, Nature, 470, 53
Lomb, N. R. 1976, Ap&SS, 39, 447
Maciejewski, G., Dimitrov, D., Neuhäuser, R., et al. 2010, MNRAS, 407, 2625
Mandel, K. & Agol, E. 2002, ApJ, 580, L171
Mandell, A. M., Raymond, S. N., & Sigurdsson, S. 2007, ApJ, 660, 823
Mislis, D., Schröter, S., Schmitt, J. H. M. M., Cordes, O., & Reif, K. 2010, A&A, 510, A107
Montalto, M., Gregorio, J., Boué, G., et al. 2012, MNRAS, 427, 2757
Nascimbeni, V., Cunial, A., Murabito, S., et al. 2013, A&A, 549, A30
Nesterov, V. V., Kuzmin, A. V., Ashimbaeva, N. T., et al. 1995, A&AS, 110, 367
Sarazin, M. & Roddier, F. 1990, A&A, 227, 294
Scargle, J. D. 1982, ApJ, 263, 835
Schröter, S., Schmitt, J. H. M. M., & Müller, H. M. 2012, A&A, 539, A97
Shporer, A., Mazeh, T., Pont, F., et al. 2009, ApJ, 694, 1559
Steffen, J. H., Fabrycky, D. C., Agol, E., et al. 2013, MNRAS, 428, 1077
Steffen, J. H. & Farr, W. M. 2013, ApJ, 774, L12
Steffen, J. H., Ragozzine, D., Fabrycky, D. C., et al. 2012, Proceedings of the National Academy of Science, 109, 7982
von Essen, C., Schröter, S., Agol, E., & Schmitt, J. H. M. M. 2013, A&A, 555, A92
Witte, S., Helling, C., & Hauschildt, P. H. 2009, A&A, 506, 1367
Young, A. T. 1993, The Observatory, 113, 41
Zechmeister, M. & Kürster, M. 2009, A&A, 496, 577

KOI-676: An active star with at least two planets.

P. Ioannidis, J.H.M.M. Schmitt, Ch. Avdellidou, C. von Essen and E. Agol
Submitted to A&A, September 2013.

Astronomy & Astrophysics manuscript no. koi676small
September 16, 2013

KOI-676: An active star with at least two planets.

P. Ioannidis [1], J.H.M.M. Schmitt [1], Ch. Avdellidou [2], C. von Essen [1] and E. Agol [3]

[1]Hamburger Sternwarte, Universität Hamburg, Gojenbergsweg 112, 21029 Hamburg, Germany
[2] Centre for Astrophysics and Planetary Science, School of Physical Sciences (SEPnet), The University of Kent, Canterbury, CT2 7NH, UK
[3] Dept. of Astronomy, Box 351580, University of Washington, Seattle, WA 98195
e-mail: `pioannidis@hs.uni-hamburg.de`

Received ...; accepted ...

ABSTRACT

We report the detection and characterization of two short period, Neptune-sized planets around the active host star KOI-676. The host star's parameters derived from those planets are (a) mutually inconsistent, and (b) do not conform to the expected host star parameters. We furthermore report the detection of transit timing variations (TTV) in the O-C diagrams for both planets. We explore various scenarios explaining and resolving those discrepancies. A simple scenario consistent with all data appears to be one attributing substantial eccentricities to the inner short-period planets and interpreting the TTV as due to the action of a further, somewhat longer-period planet. To substantiate our suggestions we present the results of N-body simulations to model the TTV and check the stability of the KOI-676 system.

Key words. stars: planetary systems - stars: individual: KIC 7447200 - methods: transit timing variations - methods: data analysis

1. Introduction

Since the launch of the *Kepler* Mission in 2009 a large number of planetary candidates has been found using the the transit method in the high precision *Kepler* light curves. Specifically, in 1790 hosts stars 2321 planetary candidates have been reported, from which about one third are actually hosted in multiple systems (Batalha et al. 2012). The majority of these *Kepler* planetary candidates are expected to be real planets (Lissauer et al. 2012) and therefore the stars present an excellent opportunity for a more detailed study and characterization through the method of Transit Timing Variations (TTV). Ever since the first proposals of the method by Agol et al. (2005) and Holman & Murray (2005) TTV have been widely used to search for smaller, otherwise undetectable planets in systems containing already confirmed planets. In multiple systems this method can be applied in order to confirm the physical validity of the system along with a rough estimate of the components' mass, which can otherwise be obtained only through radial velocity data. For the *Kepler* candidates the *Kepler* team has carried out and reported this kind of analysis for 41 extrasolar planet systems (for the last announcement of the series see Steffen et al. (2013)).

In this paper we present our in-depth analysis and results for a particular system, KOI-676 (= KIC 7447200), which was previously identified and listed as a planet host candidate in the catalog by Borucki et al. (2011). The specific characteristics of KOI-676 which enticed us to perform a detailed study of this candidate system were the high activity of its host star coupled with the fact that the system harbors two transiting planets, which we validate using spectral and TTV analysis as well as through stability tests.

The plan of our paper is as follows: In the first section we describe the methods used to determine the stellar and planetary properties. In the second section we discuss various scenarios to explain the detected discrepancies in the orbital elements of the planets. Furthermore we describe the results of our TTV analysis for both planets, and finally, we summarize with what we believe is the most probable scenario.

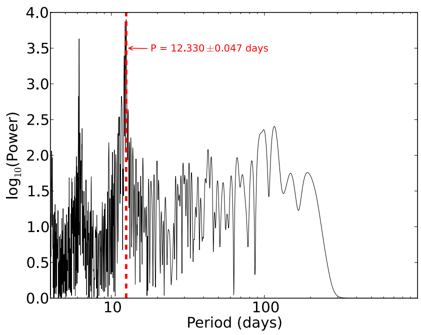

Fig. 1: The Lomb-Scargle Periodogram for the raw lightcurve as logarithmic power (on y axis) vs. period. A polynomial fit was applied to remove systematics related to the rotation of the telescope.

2. Data analysis

2.1. Stellar activity

The *Kepler* data of KOI-676 were obtained from the STDADS archive and contain the data recorded in the quarters Q1 to Q12. In order to achieve better temporal coverage we used

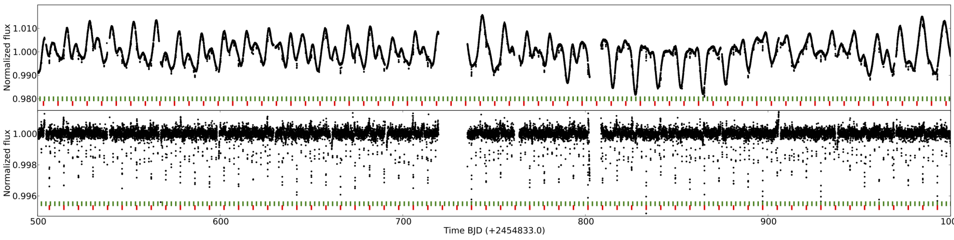

Fig. 2: A fraction of the KOI 676 lightcurve. Top: Part of the raw lightcurve demonstrating the activity of KOI 676. Bottom: The transits of planet a (green) and b (red) for that particular time, with the stellar activity removed by using the kepflatten routine of the Pyke package for pyraf.

both long and short cadence data. We decided to use the SAP data for our analysis in order to avoid any artefacts introduced by the use of SAP_PDC data, given the obvious complexity of the KOI-676 lightcurve (cf., see Figure2). Clearly, the host star of the KOI-676 system is of particular interest by itself.

To give an impression of the activity of KOI-676 a part of the overall *Kepler* lightcurve of KOI-676 covering 500 days is shown in Fig.2. Peak to peak variations on the order of 2% can easily be identified on time scales of a few days, and in addition, variations on longer time scales are also visible. In order to assess the dominant time scales of variability we computed a Lomb-Scargle periodogram over the full available data set, which we show in Fig. 1. Two peaks are clearly observable in the resulting periodogram. We interpret the most significant peak at 12.33 ± 0.15 days as the rotation period of the star, while the second, smaller peak at 6.15 ± 0.047 days is interpreted as an alias from the 12.33 day rotation period. We further note that both peaks are quite broad, with significant power residing at frequencies near the peak frequency.

2.2. Data Preparation

For our transit and TTV analysis we must remove all effects of stellar activity as much as possible. In order to rectify the *Kepler* lightcurve of KOI-676 we proceed as follows: For each transit of each planet we select some part of the lightcurve centered at the estimated mid-transit time, including data points before and after ingress and egress, respectively (see Fig.3, upper left). The obvious transit points are then removed (Fig.3, upper right) and a second order polynomial fit is applied to the remaining data points (see Fig.3 lower left). Finally, all selected data points including those obtained during transit are divided by the result of the polynomial fit (see Fig.3 lower right) and we obtain a rectified light curve, normalized to unity for the data prior to the first and after the fourth contact. In this fashion we prepare the transit data for both planets for an application of our transit model fit; we consider only transits by one planet and exclude any simultaneous transits from our analysis.

KOI-676	
KIC-ID	7447200
T_{eff}	4300 K
logg	4.55
$R_\star$	0.69 $R_\odot$
$M_\star$	0.63 $M_\odot$
linear LD	0.7181
quadratic LD	0.0443

Table 1: Stellar parameters of KOI-676 taken from Batalha et al. (2012). The limb-darkening coefficients where calculated for those values from Claret et al. (2012) for those parameters.

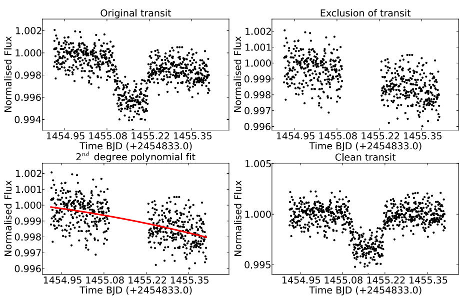

Fig. 3: Demonstration of stellar activity removal procedure; see text for details.

2.3. Model fitting

The effects of the host star's stellar activity are clearly visible also in the transit light curves, which are twofold: (see 2):

Planet	b	c
Period (d)	7.9725 ± 0.0014	2.4532 ± 0.0007
T_0 (LC)	131.7200 ± 0.0002	134.0952 ± 0.0002
$R_{pl}/R_\star$	0.0635 ± 0.0006	0.0498 ± 0.0004
$a/R_\star$	11.566 ± 0.323	4.429 ± 0.077
i	85.73 ± 0.16	77.86 ± 0.26
b	0.861 ± 0.065	0.931 ± 0.038
transits	97 lc / 51 sc	431 lc / 243 sc

Table 2: MCMC analysis transit model fit results and their "1 σ" errors.

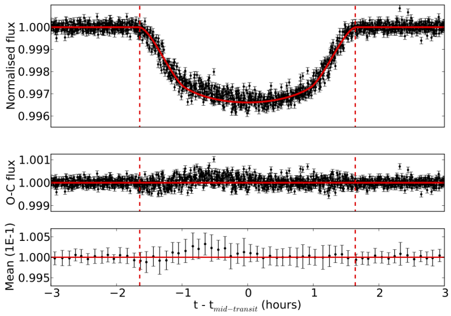

Fig. 4: The folded lightcurve of planet b, using the total number of transits and the best fit model. The lower diagram shows the model residuals binned. The transit profile is affected by spots during and after ingress.

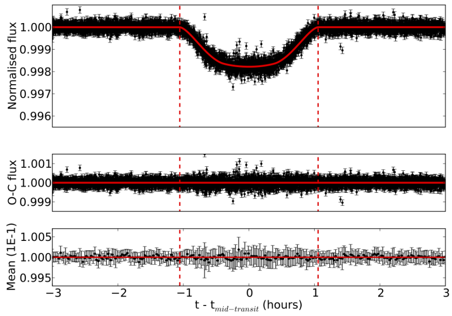

Fig. 5: The folded lightcurve of planet c, using the total number of transits and the best fit model. The affection of spots in this case is less obvious than in case of planet b.

Star spots occulted by the planet on the one hand lead to bumps in the light curve as shown by Wolter et al. (2009), while star spots on the unocculted face of the star on the other hand lead to variable transit depths. Thus, both effects increase the dispersion of the transit data and the incorrect normalization leads to incorrect stellar and planetary parameters. In order to minimize the effects of stellar activity we therefore decided to use transits, following the following two rules:

1. We select those transits occurring close to maximum flux in the activity modulations, which corresponds to smaller spot coverage of the stellar surface
2. We model each transit separately, isolated the transit data and measure the χ^2-test statistics. Only the transits with acceptable fits are selected.,

Thus, for the transit model fit of the inner planet 89 transits were used, while for the outer planet a total of 10; we rejected 154 transits by the inner planet and 41 transits by the outer planet for this analysis. To determine the best fit model we used the analytical transit light curve model by Mandel & Agol (2002) and Markov-Chain Monte-Carlo sampling[1] for the computation of the fit parameters and their errors. In this process we used the limb darkening coefficients for the model as calculated by integrating the values of the Claret catalog (Claret et al. 2012) for the parent star's nominal parameters T_{eff}, $logg$ and $[Fe/H]$ listed in Table 1 .

2.4. Fit results

In Figs.4 and 5 we show the full sample of the derived mean normalized *Kepler* transit light curves and our best fit model (red line; upper panel), the fit residuals for all data points (middle panel) and the mean values of the individual residuals as well as for blocks of twenty adjacent phase points (lower panel). The physical parameters derived from our transit analysis are listed in Tab. 2; note that the inner, shorter period planet is smaller than the outer planet.

[1] http://www.hs.uni-hamburg.de/DE/Ins/Per/Czesla/PyA/PyA

3. Transit Timing Variations

3.1. Timing variation analysis

After completion of the transit model fit procedure and the determination of the global parameters for each planet, we recalculated the mid-transit times for all transits of each planet, i.e., also those that had been rejected for the best model fit. To that end we reapplied the MCMC fitting algorithm for every transit separately, keeping all model parameters fixed except for the individual mid-transit times $t_{MT,i}$ $i = 1, N$. From the observed mid-transit times $t_{MT,i}$, their errors σ_i and the integer transit epochs N_i we derived a mean period P and time reference T_0, by minimizing the expression

$$\chi^2 = \sum_{i=1}^{N} \frac{(t_{MT,i} - t_{calc,i})^2}{\sigma_i^2} = \sum_{i=1}^{N} \frac{(t_{MT,i} - P\,N_i - T_o)^2}{\sigma_i^2} \Rightarrow \qquad (1)$$
$$\chi^2 = \sum_{i=1}^{N} \left(\frac{OC_i}{\sigma_i^2}\right)^2$$

with respect to P and T_0; the thus resulting O-C diagrams for planets b and c are shown in Fig 5.

3.2. TTV results

While in the O-C diagram of planet b (Fig. 6) some modulation is visible, no clear variation is apparent for planet c. In order to assess to what extent TTV might be caused by stellar activity, as for example the observed anomaly in the ingress of the transit of planet b (Fig. 4), we calculated the transit times using two different approaches, additional the one described in 3.1:

- We recalculated the transit times using the method described in 3.1, but by excluding the affected areas of the transit phase.
- We used the analysis described by (Carter & Winn 2009) in order to remove the spot anomalies, considering them as red noise.

The results in both cases where almost identical, thus we decided to use for our analysis the transit times which were produced with the simplest method (paragraph 3.1). In addition we searched for correlations between the timing variations vs. the transit depth and duration, but in any case no correlations were found.

In order to quantify the significance of the observed O-C variations, we carried a χ^2-analysis on the null hypothesis that there are no timing variations, on the long and short cadence data separately and on the joined long and short cadence data. We also carried out the same analysis by averaging the measured O-C values over ten consecutive epochs; the respective χ^2-values and the derived significance levels are listed in Tab. 3.

An inspection of Tab. 3 shows that the unbinned long cadence data show no evidence for any non-zero O-C values, while the short cadence data do; binning does greatly increase the significance of the non-zero O-C values.

Since the values of the χ^2-test statistics sensitively depend on the measurement errors σ_i, we carefully checked the errors of the derived mid-transit times by using two independent methods and convinced ourselves of the internal consistency of our error determination. In addition we checked that the derived χ^2-values are not produced by a few individual outliers. As a result we are confident that the observed TTV are statistically significant.

4. Discussion

4.1. Examination of stellar properties

In order to better determine the stellar parameters of KOI-676, a high resolution spectrum was acquired, using the CAFE instrument on the 2.2 m telescope of the Calar Alto Observatory in Spain. For our analysis we also used two spectra of KOI-676, taken from the CFOP[2] web page. We specifically inspected the spectra for a second set of lines indicating the existence of a close unresolved companion but found none. For the same purpose we also examined the pixel area around the star using the Kepler target fits frames, but found again no evidence of any variable star in the vicinity of the central star that could create a contaminating signal.

To measure the color index B-V, we observed KOI-676 together with with two standard stars (HD 14827 and HD 195919), using the 1.2 m Oskar-Lühning-Telescope (OLT) from Hamburg Observatory and found B-V$_{KOI-676}$ = 1.131 ± 0.064, consistent with the color derived from CFOP (1.088 ± 0.037) and other sources; thus the spectral type of KOI-676 is in the late K range.

We then proceeded to estimate the stars age using the gyrochronology expression 2 derived by Barnes (2007)

$$log(t_{gyro}) = \frac{1}{n}\{log(P) - log(\alpha) - [\beta \cdot log(B-V-0.4)]\}, \quad (2)$$

where t is in Myr, B-V is the measured color, P (in days) is the rotational period, $n = 0.5189$, $\alpha = 0.7725 \pm 0.011$ and $\beta = 0.601 \pm 0.024$. By using 2 with P = 12.33 days and the B-V = 1.131, we estimate an age of 350 ± 50 Myrs for KOI-676; this estimate appears reasonable given its high degree of activity.

4.2. Mean stellar density

When a planet is transiting in front of its parent star, we have the opportunity to accurately derive the ratio between the stellar radius $R_\star$ and the orbital semimajor axis a (cf., Table 2). Combining this information with Kepler's third law, we can compute an expression for the mean density ρ_{mean} of the host star through

$$\rho_{mean} = \frac{3\pi}{G}\frac{a^3}{R_\star^3\, P^2}, \quad (3)$$

with G denoting the gravitational constant in addition to the terms containing only observed quantities. Carrying out this computation using the observed parameters for planets b and c (cf., Table 2) we obtain densities of $\varrho_{\star b} = 0.46 \pm 0.038\ g/cm^3$ and $\varrho_{\star c} = 0.27 \pm 0.004\ g/cm^3$, respectively for the host. On the other hand, based on the nominal stellar parameters of the host star we expect a mean density of $\varrho_o \approx 2.6\ g/cm^3$. Thus the mean host star densities derived from planets b and c are, first, inconsistent with each other, and second, differ by almost an order of magnitude from the expected host star density. Since we firmly believe in Kepler's third law, there must be a physical explanation for both discrepancies.

4.2.1. Ellipticity of planetary orbits

So far our analysis has implicitly assumed circular orbits for both planets. For elliptical orbits the orbital speed and hence the transit duration change during the orbit and therefore there is no unique relation between transit duration and stellar and planetary dimensions. Assuming that the orbital velocity is constant during the actual transit, Tingley & Sackett (2005) relate the transit

[2] https://cfop.ipac.caltech.edu

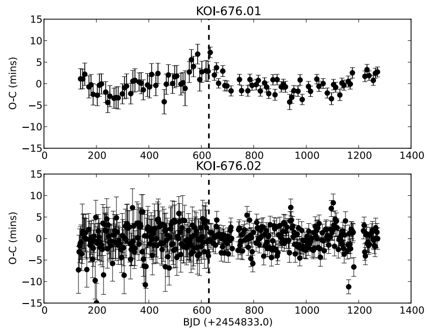

Fig. 6: The O-C diagrams of planet b (upper panel) and c (lower panel), along with the best fit models. The dashed line discriminates the long from the short cadence data.

	Long Cad.	Short Cad.	L & S Mix
b	111.55 (0.77) [96]	138.72 (>0.99) [50]	185.2 (>0.99)
c	430.56 (0.47) [430]	347.49 (>0.99) [242]	447.9 (0.71)
b_{bin}	51.87 (>0.99) [10]	76.08 (>0.99) [5]	67.9 (>0.99)
c_{bin}	61.16 (0.88) [43]	63.5 (>0.99) [24]	47.52 (0.67)

Table 3: χ^2 results with their P-values for the long cadence alone (left column) vs the short cadence alone (middle column) and the combined long and short cadence data (right column) for unbinned and binned data. In the square brackets are listed the degrees of freedom.

duration D_{ell} to the period P and the impact parameter b of a transit through the expression

$$D_{ell} = \frac{\sqrt{(1-e^2)}}{1+e \cdot cos(\phi_t)} \frac{P}{\pi} \frac{\sqrt{(R_\star + R_{pl})^2 - b^2)}}{a}, \tag{4}$$

where ϕ_t denotes the true anomaly at the mid-transit while $R_\star$, R_{pl} and a, denote stellar and planetary radii and semi-major axis respectively. Consequently, the transit duration D_{ell} of an elliptical orbit scales with the transit duration D_{circ} of a circular orbit (for the same system geometry and the same period) through

$$D_{ell} = \frac{\sqrt{(1-e^2)}}{1+e \cdot cos(\phi_t)} \times D_{circ} = g(e, cos(\phi_t)) \times D_{circ}. \tag{5}$$

It is straightforward to convince oneself that the derived sizes for star and planet scale with the scaling function $g(e, cos(\phi_t))$ introduced in Eq.5. Since the mean stellar density scales with $R_\star^3$, we find

$$\varrho_{\star,ell} = \varrho_{circ} \cdot \left(\frac{\sqrt{1-e^2}}{1+e \cdot cos\phi_t} \right)^{-3} \tag{6}$$

and hence the discrepant stellar densities can be explained by introducing suitable eccentricities and true transit anomalies. By solving 6 for different values of e and ϕ_t it is thus possible to to constrain the range of permissible eccentricities as well as values for ϕ_t, for which the derived stellar density becomes equal to the density expected for the spectral type of the star for both planets; the corresponding curves are shown in Fig. 7, where we plot for each planet the combination of e and ϕ_t resulting in a nominal stellar density of 2.7 $g\ cm^{-3}$. Fig. 7 shows that eccentricities of 0.4 (for planet b) and 0.5 (for planet c) are required to produce the expected stellar densities.

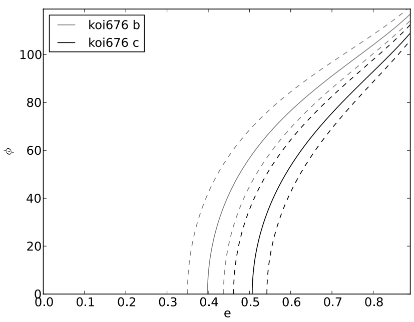

Fig. 7: A contour plot, presenting the possible values of eccentricities versus the angle ϕ. For a circular system the density value should be equal to $\varrho_o \backsimeq 2.6\ g/cm^3$, as it can be calculated for the given $R_\star$ and $M_\star$. The derived from the $a/R_\star$ values of $\varrho_\star$ for the planets KOI-676 b (gray line) and KOI-676 c (white line) can be explained for eccentricities $\gtrsim 0.4$ and $\gtrsim 0.51$ respectively, depending on the true anomaly of the planet during the mid-transit. The dashed lines represent the unsertenty limits.

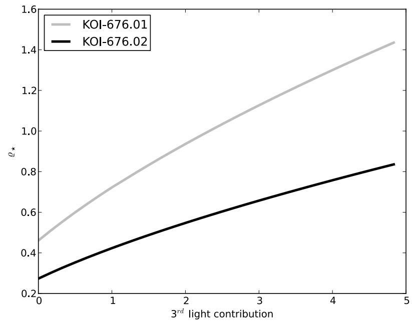

.

Fig. 8: Derived stellar density versus assumed third light contribution F_3

4.2.2. Second (third) light scenario

Despite the fact that neither the optical spectrum nor the centroid analysis of the *Kepler* data have shown any evidence for a companion or blend, it might still be possible that some object in the background or foreground with flux F_3 contributes to the system flux in a way that the observed total flux F_{obs} is given by

$$F_{obs} = F^\star + F_3 \tag{7}$$

where $F^\star$ is the desired planet host's flux, which has to be used for the transit modeling. If the third light contribution F_3 is substantial, the true transit depth would be underestimated and a larger stellar radius for the KOI-676 host star would result, leading to a reduction of the derived mean stellar density. Assuming that the limb darkening coefficients are identical and equal to the values presented in Table 1 for all system sources, we calculate the influence of the third light source on the derived stellar density (Fig.8). We specifically consider the following non-linear system of equations, which relates the observed time between the first and forth contact, T_{14}, the time between the second and third contact, T_{23} and the observed (relative) transit depth at mid-transit d_{obs} to the stellar and planetary radii (each scaled by the semi-major axis) $\tilde{R}_\star$ and $\tilde{R}_p$ and to i the inclination of the orbit normal with respect to the line of sight:

$$sin^2 i\, cos^2 \left(\frac{\pi}{P} T_{14} \right) = 1 - (\tilde{R}_\star + \tilde{R}_p)^2 \tag{8}$$

$$sin^2 i\, cos^2 \left(\frac{\pi}{P} T_{23} \right) = 1 - (\tilde{R}_\star - \tilde{R}_p)^2 \tag{9}$$

and

$$d_{obs} = \frac{(1-c_1-c_2) + (c_1 + 2c_2)\, \mu_c - c_2 \mu_c^2}{1 - \frac{c_1}{3} - \frac{c_2}{6}} \left(\frac{\tilde{R}_\star}{\tilde{R}_p} \right)^2 \tag{10}$$

Here c_1 and $c_2$denote the quadratic limb darkening coefficients and μ_c denotes the expression

$$\mu_c = \sqrt{1 - \frac{cos^2 i}{\tilde{R}_\star^2}}. \tag{11}$$

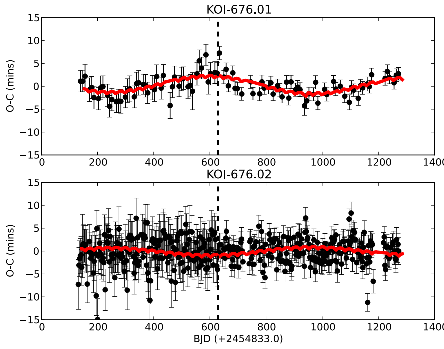

Fig. 9: TTV expected for two planets with eccentric orbits

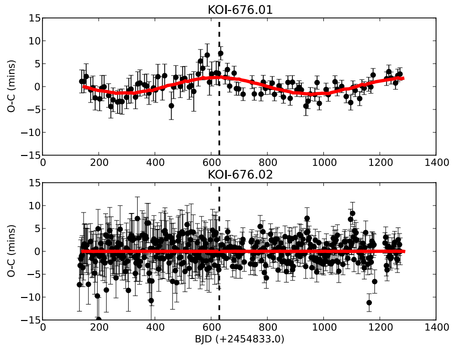

Fig. 10: TTV expected for three planets with non-eccentric orbits

The true transit depth d_{true} is then given by the relationship

$$d_{true} = d_{obs} - \frac{F_3}{F^\star}(1 - d_{obs}), \tag{12}$$

where d_{obs} denotes the observed transit depth. Assuming some third light light contribution $F_3/F^\star$ we can use the observed values of d_{obs}, T_{14} and T_{23} given the observed periods P for both planets and compute $\tilde{R}_\star$ and hence $\varrho_\star$ as a function of $F^\star + F_3$; the results are shown in Fig.8, where we plot the derived stellar densities for both planets. As is clear from Fig.8, the third light contribution would have to be substantial, say two thirds or more of the total system flux, in order to derive values of $\varrho_{\star c}$ as expected for stars on the main sequence in the relevant spectral range. Furthermore, the two planets still yield discrepant densities of their host, so one would have to introduce yet another host for the second planet, which appears at least a little contrived. We thus conclude that the introduction of a third light source does not lead to a satisfactory solution of inconsistency in the derived stellar parameters.

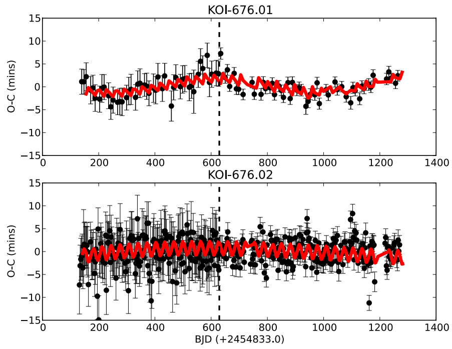

Fig. 11: TTV expected for three planets with eccentric orbits

4.2.3. Inflated star

An other possible scenario explaining the *Kepler* observations of KOI-676 would be the assumption that the host is not on the main sequence, but rather evolved and in fact a giant or sub-giant. Such stars are usually not active, however, there are some classes of evolved stars which are quite active, for example, variables of the FK Com type. Those stars are highly active G-K type sub-giant stars with surface gravities log(g) of ~ 3.5. They show strong photometric rotational modulations caused by a photosphere covered with inhomogeneously distributed spots. An other important characteristic of these objects is their rapid rotation. Generally the $v\ sini$ derived from their spectra is between ~ 50 and 150 $km \cdot s^{-1}$ (Berdyugina 2005). In the case of KOI-676 $v\,sini$ is ~ 4 $km \cdot s^{-1}$, and thus we believe that a FK-com scenario does not provide a suitable explanation for the observed density discrepancy.

4.3. KOI-676 TTV

As described in sec. 3, TTV are detected in both planets. In order to further examine the properties of these variations we searched for any periodicities in the O-C data by constructing a Lomb-Scargle periodogram on every set. For the outer and larger planet, the Lomb-Scargle periodogram shows a leading period of about 690 days, which is apparent in the modulation of the O-C curve in Fig.6, while for the inner and smaller planet the periodicity results remain ambiguous, most probably due to the large scatter in its O-C diagram.

What would be a physical scenario consistent with these O-C diagrams ? We first note that the orbital period ratio of the system is close to a 13/4, if we consider that the errors in periods in Table 2 are also affected by the TTV. This ratio is not close to any, low order, mean motion resonance so the amplitude of any TTV is expected to be relatively small for both planets (Agol

	2 ecc Planets	3 non ecc Planets	3 ecc Planets
b	116.22 [86]	112.4 [81]	117.59 [81]
c	489.57 [420]	447.9 [415]	443.9 [415]

Table 4: χ^2 results of the model for 2 eccentric planets hypothesis, 3 non eccentric planets and 3 eccentric planets. In the square brackets are listed the degrees of freedom.

et al. 2005). To verify this and to model the TTV we use the N-body code as presented in the same paper. The N-body code requires the planetary masses which are unknown; in order to roughly estimate the planetary masses, we use a general mass vs. radius law as described by Lissauer et al. (2011) in the form

$$M_p = R_p^{2.06} \tag{13}$$

For our TTV simulations we first considered only the two transiting planets. Assuming non-eccentric orbits resulted in TTV of less than a minute, which is quite far from the observed variations for both planets. As discussed in detail by Lithwick et al. (2012), the TTV amplitude can also be affected by eccentricity. Implementation of eccentric orbits for both planets, KOI-676 b and KOI-676 c, improved the fit substantially; the modeled TTV together with the data are shown in Fig.9, the fit results in terms of fit quality measured through χ^2 are given in Table 4.

Clearly, also the TTV analysis supports a scenario of two planets with rather eccentric orbits similar to our discussion in 4.2.1. However, in order to produce the observed TTV the system configuration must be such that the true anomaly, of both planets at the time of transit, ϕ_t, should exceed 40°, while also the difference in true anomaly $\Delta\phi_t$ should be $\sim$ 60°, However, this configuration appears impossible due to the physical constraints in Fig.7. Furthermore, our stability tests, (which performed with the **swift_rmvs3** algorithm (Levison & Duncan 1994), show that this configuration is unstable on time scales in excess of $\sim$ 1 Myear.

We therefore conclude that a scenario with only two planets with eccentric orbits is unlikely and introduce a third, hypothetical planet KOI-676.03 in order to stabilize the system. In that case the clear shape of the TTV variations of KOI-676 b should be caused by this outer more massive planet. We consider both eccentric and non-eccentric for KOI-676 b and KOI-676 c. In order to determine period, mass and eccentricity for KOI-676.03, we tested various possible system configurations.

While a unique solution for the longitude of the ascending node Ω and argument of periapsis ω cannot be derived, the period of such a hypothetical third planet as calculated from our simulations should be P $\simeq$ 63 days, in a parameter space between 25 to 300 days. The mass and eccentricity of this hypothetical planet are in the range $\sim$ 0.1-0.6 M_J and e $\simeq$ 0.1-0.3 for both cases; in Fig.10 and again Table 4 (for the case with zero eccentricity) and in Fig.11 and Table 4 (for the eccentric case) we show that such a scenario provides results consistent with the available *Kepler* data. As is clear from Fig.10 and Fig.11 as well as Table 4, the difference between the non-eccentric and eccentric case is marginal at best, while (statistically) preferable over a two planets scenario. The eccentricities of the planets KOI-676 b and KOI-676 c give an additional high frequency TTV signal, which might better explain the higher dispersion of the TTV in KOI-676 c. In that case the model also suggests ϕ_t values around zero with $\Delta\phi < 30$ °, which are in line with Fig.7. Also the system's stability exceeds 10^7 years.

In the case of non eccentric orbits the system would reach fatal instability once masses above 5 M_J are chosen. For eccentric orbits the upper limit for the masses of the system becomes smaller. While this fact suggests a planetary nature of the system components, it also introduces an additional factor of concern about the long term stability of the system. We do point out that this third stabilizing planet does produce a radial velocity signal in the system. For our nominal case we plot in Fig. 13 the expected RV signal in a synthetic radial velocity diagram, which shows peak-to-peak variations in excess of 60 m/sec; clearly such RV variations ought to be detectable despite the high activity level of the host star.

The approximately 4:13 period ratio in addition to the high eccentricities would possibly need a resonant configuration to preserve the stability of the system. This makes us speculate that the system may have reached a tidal fixed point, a state in which the outer planet causes the inner two to precess together Batygin et al. (2009) & Mardling (2010).

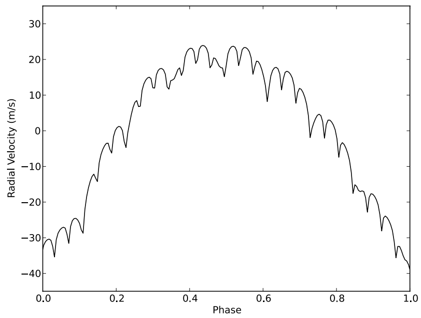

Fig. 13: The predicted, synthetic, radial velocity diagram for the system KOI-676 for P_{03} = 63 days, M_{03} = 0.4 M_j, e_{03} = 0.23 and i_{03} = 60°.

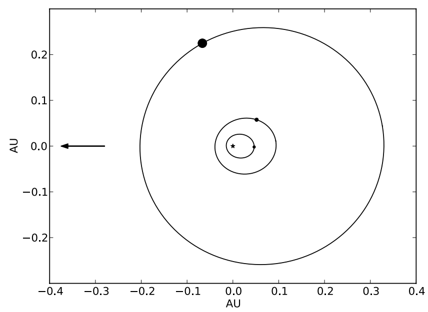

Fig. 12: The suggested system configuration. The earth is at the direction of the arrow.

5. Summary

We report the detection and characterization of two transiting Neptune-sized planets, KOI-676 b and KOI-676 c with periods of 7.9723 days and 2.4532 days respectively around a presumably quite young and active K-type dwarf. These objects were first listed as planetary candidates by the *Kepler* team. We show that the transits of both planets are affected by spots. From the observed transit parameters and in particular from the observed value of $a/R_\star$ it is possible to calculate the mean density of the host star using the Kepler's 3^{rd} law. Interestingly, the two planets yield discrepant mean host star densities, which in addition are inconsistent with the densities expected for a K-type dwarf. Having explored various scenarios we conclude that the assumption of quite eccentric orbits for both planets provides the currently most probable scenario.

In addition, both planets also show transit timing variations. Using N-body simulations we constructed possible system configurations consistent with the *Kepler* data. While it is possible to explain the observed TTV with a two planet scenario, such a scenario requires a very special geometrical configuration and is unstable on time scales of 10^6 years. As a result we believe that there exists a third planet, KOI-676.03, with a mass between $\sim$ 0.3-0.6 M_J in a slightly eccentric ($e \simeq 0.15$) orbit with period $\sim$ 63 days, which stabilizes the whole KOI676 planetary system.

Larger planet masses for KOI-676.03 are unlikely since they lead to great increase of the expected TTV signal on planet b, yet this stabilizing hypothetical planet should produce a clearly detectable RV signal. We therefore suggest RV monitoring of KOI-676, which is likely to provide a substantially increased insight into the KOI-676 planetary system.

6. Acknowledgments

PI and co-author C. von Essen acknowledge funding through the DFG grant RTG 1351/2 "Extrasolar planets and their host stars". The results of this publication are based on data collected by the NASA's *Kepler* satellite. We would like to thank the director and the Calar Alto Observatory staff for the approval and execution of a DDT proposal. Finally we acknowledge the exceptional work by the CFOP team which was essential for this publication.

References

Agol, E., Steffen, J., Sari, R., & Clarkson, W. 2005, MNRAS, 359, 567
Barnes, S. A. 2007, ApJ, 669, 1167
Batalha, N. M., Rowe, J. F., Bryson, S. T., et al. 2012, ArXiv e-prints
Batygin, K., Bodenheimer, P., & Laughlin, G. 2009, ApJ, 704, L49
Berdyugina, S. V. 2005, Living Reviews in Solar Physics, 2, 8
Borucki, W. J., Koch, D. G., Basri, G., et al. 2011, ApJ, 736, 19
Carter, J. A. & Winn, J. N. 2009, ApJ, 704, 51
Claret, A., Hauschildt, P. H., & Witte, S. 2012, VizieR Online Data Catalog, 354, 69014
Holman, M. J. & Murray, N. W. 2005, Science, 307, 1288
Levison, H. F. & Duncan, M. J. 1994, Icarus, 108, 18
Lissauer, J. J., Marcy, G. W., Rowe, J. F., et al. 2012, ApJ, 750, 112
Lissauer, J. J., Ragozzine, D., Fabrycky, D. C., et al. 2011, ApJS, 197, 8
Lithwick, Y., Xie, J., & Wu, Y. 2012, ApJ, 761, 122
Mandel, K. & Agol, E. 2002, ApJ, 580, L171
Mardling, R. A. 2010, MNRAS, 407, 1048
Steffen, J. H., Fabrycky, D. C., Agol, E., et al. 2013, MNRAS, 428, 1077
Tingley, B. & Sackett, P. D. 2005, ApJ, 627, 1011
Wolter, U., Schmitt, J. H. M. M., Huber, K. F., et al. 2009, A&A, 504, 561

Chapter 5

Exoplanet oblateness

During the first evolutionary stages towards stellar formation, the stellar disk contracts to conform a star. At the poles, the gravity acts to increase the contraction. At the equator, in turn, gravitational effects are reduced by centrifugal forces. As a product of rotation the star does not look spherical but oblate, and shows an equatorial bulge whose size mainly depends on its rotation rate. (Rozelot & Neiner 2011). Planets also rotate and, therefore, are not exempt of centrifugal effects.

Oblateness is defined as

$$f = \frac{R_e - R_p}{R_e} \tag{5.1}$$

where R_e and R_p are the equatorial and polar radius of the celestial body under study, respectively. The Solar System has gas giant planets (and even rocky ones, like our own Earth) that present some level of oblateness. As a representative example, Figure 5.1 shows the measured planetary oblateness for six of the eight Solar System planets. The plot clearly reveals the expected anti-correlation between rotation rate and oblateness (see, e.g., Collins 1963; van Belle et al. 2001). Table 5.1 shows some of the most relevant parameters (Armitage 2010), from where the f was estimated.

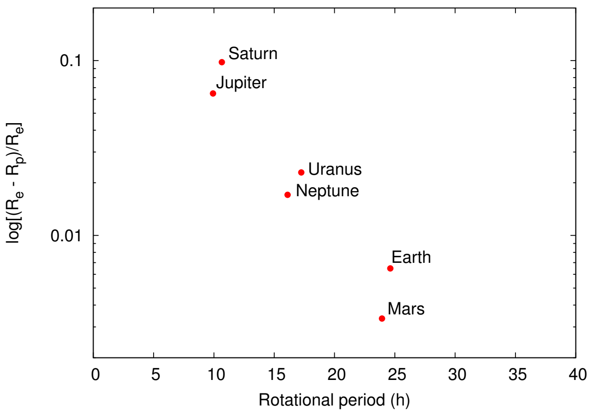

Figure 5.1: Measured oblateness for some of our Solar System planets as a function of their rotational period. The missing ones (Mercury and Venus, such as Pluto) are consistent with $f = 0$.

5.1 Exoplanets and rotation

Equivalently to the planets in the Solar System, the differences between equatorial and polar radius for exoplanets are also expected to be some hundreds of kilometers. It is understandable, then, that such small differences are extremely difficult to detect when such large distances are involved. Nonetheless, enormous efforts to characterize the exoplanet oblateness is being carried out (see, e.g., Seager & Hui 2002; Barnes & Fortney 2003; Carter & Winn 2010*b*; de Wit et al. 2012). The main reason is that measurements on rotation rate and obliquity (the angle between a planet's equatorial plane and its orbital plane) are mandatory to understand how planets formed and how did they tidally evolve (Barnes 2010). Models then have to consider if the planet is perturbed from sphericity mainly due to stellar tides, or due to high rotation.

If a planet is far enough from its parent star, as in the case of Jupiter and the Sun, it is expected that the rotation rate and the produced obliquity depend only on the planet formation and evolution. Thus, a measurement of the planetary oblateness would constrain the planetary rotational period (Seager & Hui 2002).

However, if a planet is synchronously rotating with the host star (like is expected to occur in hot Jupiters), then its rotation will be generally too slow and the oblateness will be, therefore, too

Table 5.1: Main planetary parameters for our Solar System largest planets. MP: minor planet.

Planet	Mass ($M_\oplus$)	Equatorial radius (km)	Oblateness $(R_e - R_p)/R_e$	Rotation	axis tilt (°)
Mercury	0.0553	2 439.7	0.000	58.785 d	~0
Venus	0.815	6 051.8	0.000	243.686 d	177.36
Earth	1.000	6 371.0	0.00335	23.9345 h	23.45
Mars	0.107	3 396.2	0.00648	24.6229 h	25.19
Jupiter	317.83	71 492	0.06487	9.9250 h	3.13
Saturn	95.159	60 268	0.09796	10.656 h	26.73
Uranus	14.536	25 559	0.02293	17.24 h	97.77
Neptune	17.147	24 764	0.01708	16.11 h	28.32
Pluto (MP)	0.0021	1 153	0.000	6.405 d	122.53

insignificant to be detected (Guillot 2004). If f is anyways detected and the age of the system is known, it would be then straight forward to constrain the planet's tidal dissipative factor Q, a parameter that determines the dynamical evolution of planetary bodies (Castillo-Rogez 2010).

Knowing Q, the time for the tidal spin-down of the planet (e.g., Hubbard 1984; Guillot et al. 1996) can be estimated

$$\tau \sim Q\left(\frac{R_P^3}{GM_P}\right)\omega_P\left(\frac{M_P}{M_*}\right)^2\left(\frac{a}{R_P}\right)^6 , \qquad (5.2)$$

where a is the semi-major axis, R_P and M_P are the planetary radius and mass, respectively, M_* is the stellar mass, ω_P the planet's primordial rotation rate, and G the universal gravitational constant. As an example, considering Jupiter values of $Q \sim 10^5$ and $\omega_P \sim 1.7\times10^{-4}s^{-1}$, $\tau \sim 2\times10^6$ years.

The Darwin-Radau relation (*Book Review: Solar system dynamics / Cambridge U Press, 2000* 2000) is an approximate equation that relates the moment of inertia factor C/MR_{eq}^2 where C is the planet's moment of inertia around the rotational axis, M is the mass of the object, and R_{eq} the equatorial radius

$$\mathbb{C} \equiv \frac{C}{MR_{eq}} = \frac{2}{3}\left[1 - \frac{2}{5}\left(\frac{5}{2}\frac{q}{f} - 1\right)^{1/2}\right] , \qquad (5.3)$$

For gas giant planets, $\mathbb{C}$ ~0.25 (Hubbard 1984). q denotes the ratio of the centripetal acceleration at the equator to the gravitational acceleration,

$$q = \frac{\Omega^2 R_{eq}^3}{GM_P} . \qquad (5.4)$$

Combining Eq. 5.3 and Eq. 5.4, we obtain a relation for the rotational rate, ω, as a function of the oblateness, f:

$$\Omega = \sqrt{\frac{fGM_P}{R_{eq}^3}\left[\frac{5}{2}\left(1 - \frac{3}{2}\mathbb{C}\right)^2 + \frac{2}{5}\right]} . \qquad (5.5)$$

If we assume that the exoplanets are in synchronous rotation, and $\mathbb{C} = 0.25$, we can re-arrange Eq. 5.5 to solve for oblateness f and estimate oblateness values for known hot Jupiters:

$$f = \frac{\Omega^2 R_{eq}^3}{GM_P}\left[\frac{5}{2}\left(1 - \frac{3}{2}\mathbb{C}\right)^2 + \frac{2}{5}\right]^{-1} . \qquad (5.6)$$

Figure 5.2 shows the obtained oblateness for ~300 transiting hot Jupiters. The Figure clearly reveals not only the already mentioned anti–correlation, but also that most of the exoplanets show oblateness levels that would be very challenging to detect. Although Kepler photometric precision ($\sim 10^{-5}$) is sufficient to detect such changes, only Carter & Winn (2010*a*) and de Wit et al. (2012) could find hints of oblateness in HD 189733, based on Spitzer Space Telescope photometry of secondary transits.

5.2 Geometric model for planetary transits

Mandel & Agol (2002) presented exact analytic formula for the eclipse of a star by a planet. They assumed the planet to behave as an uniform opaque

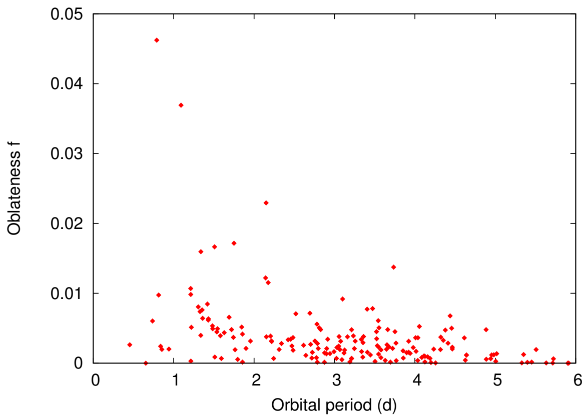

Figure 5.2: Exoplanet oblateness as a function of orbital period for known transiting systems, assuming synchronous rotation and $\mathbb{C}$ = 0.25. Source: www.exoplanet.eu

sphere, from where they obtained a first model of the flux drop during primary transit. To implement exoplanet oblateness as a further parameter of Mandel & Agol (2002)'s primary transit model, as a first step I reproduced their obtained model (Eq. 5.7).

Later on, I added the exoplanet oblateness, represented by the α parameter, under certain conditions that allowed me to produce an analytical model, and some further considerations:

- $p = \frac{R_p}{R_s}$: planet to star radius ratio.
- $z = \frac{d}{R_s}$: projected distance between centers, normalized to the stellar radius, being d the projected distance between stellar and planetary centers.
- $0 < \alpha < 1$, constant of flattener.
- $i = 90°$.
- The total surface of the elliptic planet is considered *the same* as in the circular case.
  Circular case: $A_c = \pi R_p^2$
  Elliptical case: $A_e = \pi \hat{R}_p^2 \alpha$
  $\therefore A_c = A_e \Rightarrow \pi R_p^2 = \pi \hat{R}_p^2 \alpha \Rightarrow R_p^2 = \hat{R}_p^2 \alpha$.

Considering an ellipsoid with semi–axes a, b and c, such as $a = c \neq b$, $a > b$, projecting this 3-dimensional figure in the visual direction results into a 2-dimensional ellipse, with semi–major axis considered as $a = R_p$, semi–minor axis $b = \alpha R_p$, and the ellipse's projected surface given by $A_e = \pi ab = \pi \alpha R_p^2$.

For a source with constant superficial brightness and an elliptical planet, the analytical function that describes the flux drop at primary transit is described by Equation 5.8.

The differences between Eq. 5.7 and Eq. 5.8 are only observable during ingress and egress, and are measurable with respect of the primary transit duration. The differences are of the order of the photometric precision of Kepler light curves and therefore, in principle observable.

$$\lambda^e(p,z) = \begin{cases} 0, & 1+p<z \\ \frac{1}{\pi}\left[p^2\kappa_0 + \kappa_1 - \sqrt{\frac{4z^2-(1+z^2-p^2)^2}{4}}\right], & \mid 1-p \mid< z \leq 1+p \\ p^2, & z \leq 1-p \\ 1, & z \leq p-1 \end{cases} \tag{5.7}$$

$$\begin{cases} \kappa_1 = \cos^{-1}[(1-p^2+z^2)/2z] \\ \kappa_0 = \cos^{-1}[(p^2+z^2-1)/2pz] \\ F^e(p,z) = 1-\lambda^e(p,z) \end{cases}$$

Primary transit model for an uniform source obtained by Mandel & Agol (2002).

$$\lambda^e(p,z) = \begin{cases} 0, & 1+p<z \\ \frac{1}{\pi}\{u_1 - zu_o\sqrt{1-(zu_o)^2} + \alpha p^2 u_2 - \alpha z^2[1-u_o]\sqrt{\frac{p^2}{z^2}-(1-u_o)^2}\} & \mid 1-p \mid< z \leq 1+p \\ p^2\alpha, & z \leq 1-p \\ 1, & z \leq p-1 \end{cases}$$

$$\begin{cases} u_o = [\alpha^2 - \sqrt{\frac{p^2}{z^2}\alpha^2(\alpha^2-1) + \frac{1}{z^2}(1+\alpha^2(z^2-1))}]\frac{1}{(\alpha^2-1)} \\ u_1 = acos(zu_o) \\ u_2 = acos(\frac{z}{p}(1-u_o)) \\ F^e(p,z) = 1-\lambda^e(p,z) \end{cases} \tag{5.8}$$

Analytical primary transit light curve obtained after considering the oblateness as additional parameter.

Light Curves of Planetary Transits: How About Ellipticity?

C. von Essen, K. F. Huber & J. H. M. M. Schmitt
Proceedings IAU Symposium No. 282, 2011
The original publication is available at http://adsabs.harvard.edu/abs/2012IAUS..282..133V

From Interacting Binaries to Exoplanets: Essential Modeling Tools
Proceedings IAU Symposium No. 282, 2011
Mercedes T. Richards & Ivan Hubeny, eds.

doi:10.1017/S1743921311027189

Light Curves of Planetary Transits: How About Ellipticity?

Carolina von Essen, Klaus F. Huber and Jürgen H. M. M. Schmitt

Hamburger Sternwarte, University of Hamburg,
(21029) Hamburg, Germany
email: cessen@hs.uni-hamburg.de

Abstract. The observation of transit light curves has become a key technique in the study of exoplanets, since modeling the resulting transit photometry yields a wealth of information on the planetary systems. Considering that the limited accuracy of ground-based photometry does directly translate into uncertainties in the derived model parameters, simplified spherical planet models were appropriate in the past. With the advent of space-based instrumentation capable of providing photometry of unprecedented accuracy, however, a need for more realistic models has arisen.

Keywords. exoplanets, light curves, modelling, oblateness

1. Motivation

The gas giants in our Solar System are not spherical but oblate. Oblateness, f, is defined as $f = (R_{eq} - R_{pol})/R_{eq}$, where R_{eq} corresponds to the equatorial radius and R_{pol} to the polar radius. Oblateness values for our Solar System gas giants are shown in Table 1.

A relation between oblateness and observables quantities can be obtained by taking into account the Darwin-Radau relation. Defining the parameter $\zeta = \frac{\text{mom. of inertia}}{M\ R_{eq}^2} = \frac{2}{3}\left[1 - \frac{2}{5}\left(\frac{5}{2}\frac{q}{f} - 1\right)^{\frac{1}{2}}\right]$, where the parameter $q = \frac{\Omega^2\ R_{eq}^3}{G\ M_{Pl}}$ is the ratio between the centripetal and gravitational acceleration, defined by Barnes and Fortney (2003), we obtain the following expression for the oblateness: $f = \frac{4\pi^2 R^3}{G\ M\ P^2}\left[\frac{5}{2}\left(1 - \frac{3}{2}\ \zeta\right)^2 + \frac{2}{5}\right]^{-1}$. Assuming $\zeta \sim 0.25$ (in analogy to gas giants in the Solar System) and tidal locking, we calculated f for different exoplanets (see Table 2).

2. Analytical model: comparing oblate and spherical planets

We assume that the planet shape can be modelled as a rotational ellipsoid and the star as a sphere, and the projections are an ellipse and a circle, respectively. In the case $i = 90°$, the symmetry of the problem allows an analytical model for the flux drop during primary transit. The difference between the models (Fig. 1) can be resolved for instance by the Kepler Telescope, given a good model for limb darkening.

Table 1. Oblateness values for the giant planets in our Solar System.

Planet Name	R_{eq}	R_{pol}	f	Planet Name	R_{eq}	R_{pol}	f
Jupiter	71492 km	66854 km	0.0648	Uranus	25559 km	24973 km	0.0229
Saturn	60268 km	54364 km	0.0979	Neptune	24764 km	24341 km	0.0171

Table 2. Oblateness values for short period exoplanets.

System	P [d]	$<\rho>$ (cgs)	f	System	P [d]	$<\rho>$ (cgs)	f
HD 149026	$\sim$ 2.875	$\sim$ 1.17	0.00152	WASP - 15	$\sim$ 3.752	$\sim$ 0.247	0.00422
HD 189733	$\sim$ 2.218	$\sim$ 0.91	0.00328	CoRoT - 1	$\sim$ 1.508	$\sim$ 0.38	0.017
HD 209458	$\sim$ 3.524	$\sim$ 0.38	0.00365	WASP - 19	$\sim$ 0.788	$\sim$ 0.486	0.048

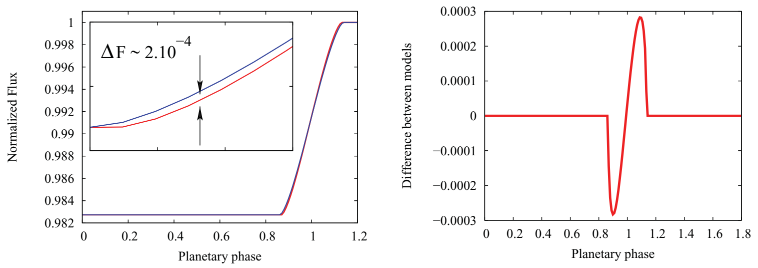

Figure 1. Left: Difference between the two analytical models, considering oblate and spherical planets. Right: Oblateness effects are important only during ingress and egress.

3. Numerical model: Comparison to Kepler data

A realistic model must include an arbitrary inclination and limb darkening, and it has to be compared to real data. We find that models with vanishing and large oblateness fit the data equally well, albeit with different fit parameters. However, one has to take into account that oblateness and inclination are degenerate; an ideal method would be the determination of oblateness and inclination independently. A possible way to minimize the degeneration effects is to take into account the mass - radius relationship for the host-star, such as $R = 1.24\ M^{0.67}$ (for M > 1.3 $M_\odot$). Fig. 2 shows that the inferred mass of the host star depends on the adopted planetary oblateness. Since KIC 9941662 is of spectral type A3, one clearly favors a low oblateness.

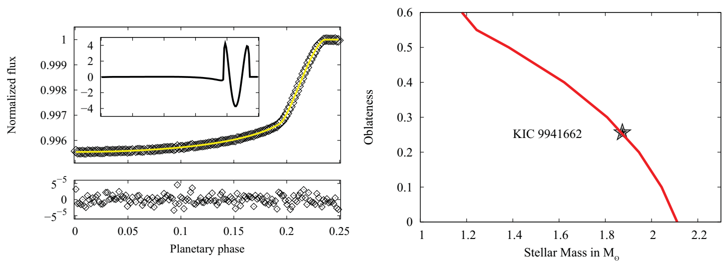

Figure 2. Left: Kepler light curve of KIC 9941662 and fit considering f = 0.5 for χ^2 minimization. Small box: Difference between two models (f = 0 and f = 0.5), multiplied by 10^6. Right: Host-star mass-oblateness relationship for the case of KIC 9941662. ST $\sim$ A3, $T_{eff} \sim$ 8800 K.

References

Mandel, K. & Agol, E. 2002, *ApJ*, 580, 171
Barnes, J. W. & Fortney, J. J. 2003, *ApJ*, 588, 545
Carter, J. A. & Winn, J. N. 2010, *ApJ*, 716, 850

Chapter 6

CoRoT-2: The chromospheric Rossiter-McLaughlin effect

In the following chapter I present a publication on CoRoT-2 system (Czesla et al. 2012), published in Astronomy & Astrophysics. The publication focuses on the –first-time detected– chromospheric Rossiter-McLaughlin effect.

6.1 The transiting system CoRoT-2

CoRoT (Convection Rotation and planetary Transits) is a space mission first launched in 2006, and lead by the French Space Agency (Baglin et al. 2006). CoRoT's main objectives are to search for extrasolar planets with short orbital periods, and to perform asteroseismological measurements on solar-like stars. It is the first space-based telescope dedicated to detect transiting exoplanets. After a continuous monitoring of ~12 000 stars, due to malfunctions CoRoT has been decommissioned. The original plan was to maintain it operational until 2015.

Along the dozens of already confirmed CoRoT exoplanets, the second exoplanet ever found by CoRoT space mission is CoRoT-2b, a transiting planet around an active G star (Alonso et al. 2008). CoRoT-2A is one of the most active planetary hosts known to date. Its magnetic activity is clearly revealed in the optically-observed flux modulation (Figure 6.1). The CoRoT-2 system has been sequentially studied. The latest and most straightforward studies were carried out by Czesla et al. (2009), Huber et al. (2009), and Huber et al. (2010), using light-curve inversion techniques to recover the surface of CoRoT-2A. The exoplanet, CoRoT-2b orbits its host star each ~1.74 days and is reported to be unusually inflated (Alonso et al. (2008) and Bouchy et al. (2008)). Table 6.1 list the system's main characteristics.

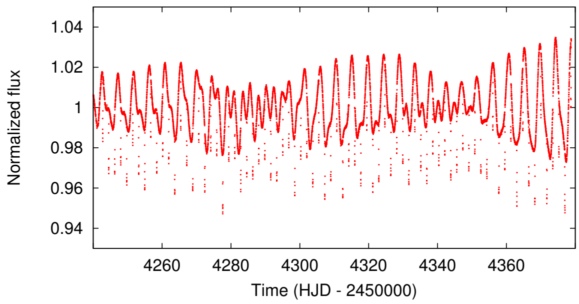

Figure 6.1: CoRoT's normalized flux of CoRoT-2A, with a time bin of 1000 seconds. The main feature is the spot modulation on the stellar surface, along with the 78 primary transits.

6.2 The Rossiter-McLaughlin effect

Generally, stars spin. Unless the rotational axis is pointing directly towards the observer, the stellar rotation will cause some parts of the star's disc to move towards the observer, while other parts will move away. As a product, the lines will be broadened (along with thermal and turbulent broadening), as some of the light will be redshifted while other light will be blueshifted.

During a primary transit, the planet hides different parts of the stellar surface. Therefore, the corresponding velocity components are missing from the spectral lines. As a product, the line profile of the star is affected, and a radial velocity shift can be measured. This is called the "Rossiter-McLaughlin

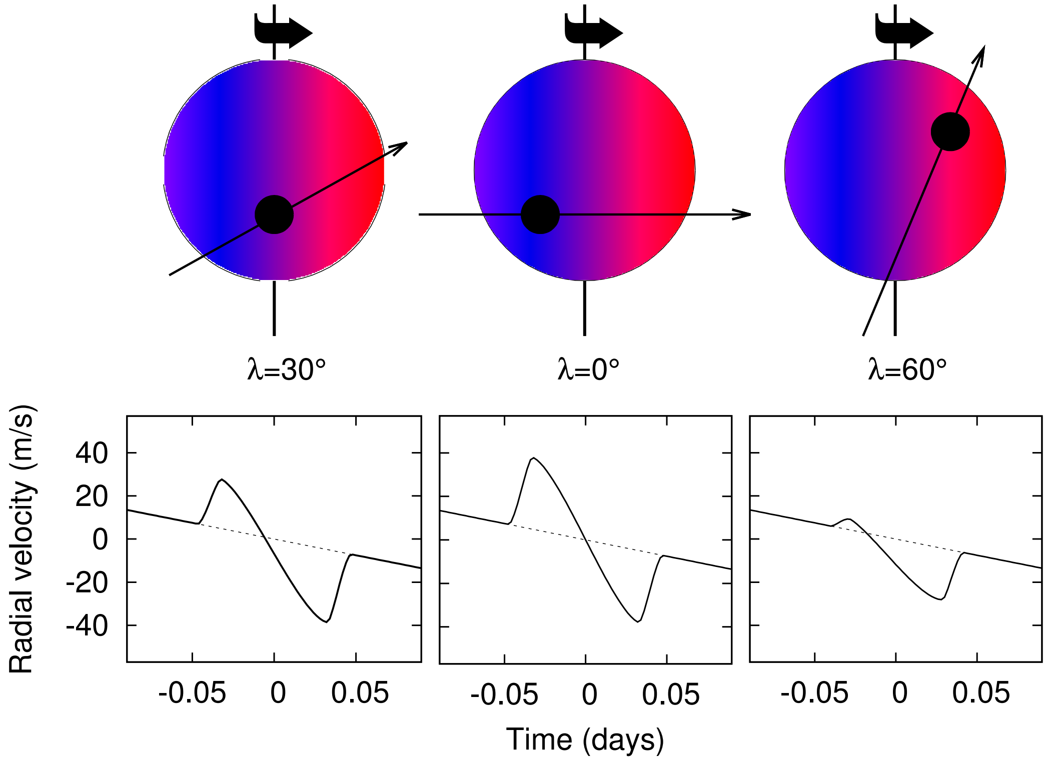

Source: C. von Essen.

Figure 6.2: Three simulations of the RM effect produced by differing the spin-orbit alignment λ. The solid lines are calculated considering a linear limb-darkening law, and semi-major axis, a, orbital inclination, i, orbital period, Per, and planet-to-star radius ratio, R_P/R_S, coincident with the ones listed in Table 6.1. The dashed line accounts for the radial velocity variation of the star due to the reflex orbital motion.

Effect" (RM), which can be used to characterize exoplanetary systems.

The first RM effect was observed by Queloz et al. (2000) and Bundy & Marcy (2000) during primary transits of HD 209458b (Charbonneau et al. 2000). Since then, it has been observed in several systems (Narita et al. (2007), Narita et al. (2009), Triaud et al. (2009), and Jenkins et al. (2010), among many others).

The most important observable that can be determined by means of a high signal-to-noise ratio RM effect is the trajectory of the planet relative to the projected stellar rotation axis, λ, most commonly named "projected spin-orbit angle". Figure 6.2 shows a picture of three trajectories of transiting exoplanets with same impact parameters and different λ's. As it is clearly seen, the shape of the radial velocity wave is completely λ-dependent.

The "spin-orbit angle", ϕ, between the stellar spin and the orbital angular momentum vectors is important to constrain the evolutionary history of a planet. Generally, however, we have no information about ϕ, and we can only empirically constrain λ. Planet formation theories predict an unperturbed alignment between the planetary orbit and the rotational axis of the star (Ward & Hahn 2003), when migration via tidal interactions between the exoplanet and the disc are taking place. On the contrary, when planet-planet interactions or collisions between planetesimals are involved, a more prominent misalignment is expected. The understanding of the planet formation and migration is, thus, one of the leading motivations to study the RM effect.

6.3 CoRoT-2: My contribution

The publication focus on the detection of the first chromospheric Rossiter-McLaughlin effect

CoRoT-2A	
V (mag)	12.6
M_S ($M_\odot$)	0.97 ± 0.06
R_S ($R_\odot$)	0.902 ± 0.018
v sin (i) (km/s)	11.85 ± 0.50
T_{eff} (K)	5652 ± 120
CoRoT-2b	
M_P (M_J)	3.31 ± 0.16
R_P (R_J)	1.465 ± 0.029
ρ_P (g/cm^3)	1.31 ± 0.04
T_{eq} (K)	1537 ± 35
a (R_S)	6.70 ± 0.03
i (°)	87.84 ± 0.10
R_P/R_S	0.1667 ± 0.0006
Per (days)	1.7429964 ± 0.0000017

Table 6.1: CoRoT-2 stellar and planetary parameters obtained from Alonso et al. (2008) and Bouchy et al. (2008).

observed in the Ca II H and K emission-line cores. The observations were carried out using high-resolution UVES spectra, obtained during primary transit of the CoRoT-2 system. Simultaneous photometric observations were also performed.

The join analysis reveals a chromospheric transit duration 15% longer than its visual counterpart. A comparison between models favors an increase in the size of the stellar chromosphere, rather than a reduction in the planetary size.

My contribution to the present publication was to carry out the data reduction of the photometric primary transit, and to determine the orbital parameters of the system by means of light-curve fitting mechanisms (Section 3.2.1 an 3.2.3).

The extended chromosphere of CoRoT-2A: Discovery and analysis of the chromospheric Rossiter-McLaughlin effect

S. Czesla, S. Schröter, U. Wolter, C. von Essen, K. F. Huber, J. H. M. M. Schmitt, D. E. Reichart & J. P. Moore
Astronomy & Astrophysics, Volume 539, Issue 150 (2012)
The original publication is available at: http://adsabs.harvard.edu/abs/2012A%26A...539A.150C

A&A 539, A150 (2012)
DOI: 10.1051/0004-6361/201118042

Astronomy & Astrophysics

The extended chromosphere of CoRoT-2A*

Discovery and analysis of the chromospheric Rossiter-McLaughlin effect

S. Czesla[1], S. Schröter[1], U. Wolter[1], C. von Essen[1], K. F. Huber[1], J. H. M. M. Schmitt[1], D. E. Reichart[2], and J. P. Moore[2]

[1] Hamburger Sternwarte, Universität Hamburg, Gojenbergsweg 112, 21029 Hamburg, Germany
e-mail: stefan.czesla@hs.uni-hamburg.de
[2] Department of Physics and Astronomy, University of North Carolina, Chapel Hill, CB 3255, Phillips Hall, Chapel Hill, NC 27599-3255, USA

Received 7 September 2011 / Accepted 16 January 2012

ABSTRACT

The young G7V dwarf CoRoT-2A is transited by a hot Jupiter and among the most active planet host-stars known to date. We report on the first detection of a chromospheric Rossiter-McLaughlin effect observed in the Ca H and K emission-line cores. In Ca H and K, the transit lasts 15% longer than that observed in visual photometry, indicating that chromospheric emission extends 100 000 km beyond the photosphere. Our analysis is based on a time series of high-resolution UVES spectra obtained during a planetary transit and simultaneously obtained photometry observed with one of the PROMPT telescopes. The chromospheric Rossiter-McLaughlin effect provides a new tool to spatially resolve the chromospheres of active planet host-stars.

Key words. stars: individual: CoRoT-2A – planetary systems – stars: late-type

1. Introduction

The G7V dwarf CoRoT-2A is one of the most active planet host-stars known to date. Every 1.74 d, the star is transited by the unusually inflated hot Jupiter CoRoT-2b (Alonso et al. 2008; Bouchy et al. 2008). CoRoT-2A is young (100–300 Ma) and has basically solar metallicity (Schröter et al. 2011). It shows a high level of magnetic activity as diagnosed from the amplitude of its photometric variation, strong chromospheric emission lines, and coronal X-ray emission (Alonso et al. 2008; Knutson et al. 2010; Schröter et al. 2011). Furthermore, Schröter et al. (2011) provided strong evidence that CoRoT-2A's optical neighbor, 2MASS J19270636+0122577, is a true physical companion of spectral type K9, as earlier hypothesized by Alonso et al. (2008), making CoRoT-2 a wide binary system with at least one planet.

The CoRoT-2 system has been subject to a multitude of photometric and spectroscopic studies. To name but a few: Alonso et al. (2008) reported the discovery of CoRoT-2b and first radial velocity (RV) measurements, later refined by Bouchy et al. (2008); Gillon et al. (2010) studied the secondary transit observed with Spitzer's IRAC instrument and Snellen et al. (2010) analyzed the secondary transit as observed by CoRoT; Lanza et al. (2009), Czesla et al. (2009), and Huber et al. (2009, 2010) used light-curve inversion techniques to recover CoRoT-2A's surface; finally, Ammler-von Eiff et al. (2009) and Schröter et al. (2011) investigated the spectral properties, activity, and X-ray emission of the system.

During a transit, the planet occults different parts of the rotating stellar surface, which leads to the Rossiter-McLaughlin effect (RME). The occultation introduces asymmetries into the rotationally broadened line profile, which result in an apparent radial velocity (RV) shift of the stellar spectrum. The RME, first observed in eclipsing binary stars (Schlesinger 1910; Rossiter 1924; McLaughlin 1924), has become a standard tool to analyze the geometry of exoplanetary systems (e.g., Fabrycky & Winn 2009). Analytical models of this effect, based on the first moment of spectral lines, have been presented by Ohta et al. (2005) and Giménez (2006) and are commonly applied to modeling, although they may not exactly reproduce the results obtained by cross-correlation techniques (e.g., Triaud et al. 2009; Hirano et al. 2010).

The RME has widely been used to measure the projected rotation velocity of planet host-stars and the alignment of their rotation axis relative to the planetary orbit (e.g., Bouchy et al. 2008). Snellen (2004) and Dreizler et al. (2009) proposed the use of the RME to probe the planetary atmosphere by analyzing the differences between measurements in various spectral lines showing potentially large absorption due to the planet's exosphere. In contrast to narrow-band photometry, the differential RME measurement does not rely on accurate photometric calibration (Snellen 2004).

The applicability of the RME is not limited to the study of the planetary orbit and atmosphere, but can be extended to the study of the *stellar* atmosphere. By confining the RME measurement to spectral lines originating in individual layers of the stellar atmosphere, the properties of these layers can be separately analyzed. In this paper, we demonstrate the feasibility of this approach for the stellar chromosphere. While the apparent surface brightness of the photosphere decreases toward the limb, the optically thin chromosphere and corona show limb-brightening (Wolter & Schmitt 2005). Narrow-band transit light-curves of limb-brightened emission lines are expected to display characteristic profiles (Assef et al. 2009; Schlawin et al. 2010), which

* Based on observations obtained with UVES at the ESO VLT Kueyen telescope (program ID 385.D-0426).

A&A 539, A150 (2012)

also applies to the RME derived from chromospheric emission lines. Therefore, the RME observed in chromospheric emission lines allows us to probe the spatial structure of the chromosphere, including both the chromospheric center-to-limb variation and inhomogeneities due to active regions. These measurements can be used to study the chromospheres of active planet host-stars and examine whether faculae dominate over spots on the surfaces of young, active stars, as found by Radick et al. (1998).

In this paper, we present time-resolved transit spectroscopy of CoRoT-2A obtained with the UVES spectrograph and simultaneous photometry obtained with the "Panchromatic Robotic Optical Monitoring and Polarimetry Telescopes" (PROMPT, Reichart et al. 2005). We refine the wavelength calibration of the spectra and discuss the RME observed in photospheric lines. In Sect. 3.3, we report the first detection of the prolonged RME in the chromospheric emission-line cores of Ca H and K, before closing with a discussion of our findings.

2. Observation

We acquired 24 high-resolution spectra of CoRoT-2A using the UVES spectrograph (Dekker et al. 2000) mounted at the VLT Kueyen. The observations were obtained on June 7, 2010, under program-ID 385.D-0426(A) and cover a full planetary transit of CoRoT-2b, including one hour before and two hours after the actual transit; the spectra have individual exposure times of 800 s.

The UVES spectrograph was set up in *dichroic 2* mode with a slit width of 0.7 arcsec. For the selected setup, UVES provides a wavelength coverage of 3800−9000 Å with gaps at 5000−5700 Å and 7500−7680 Å at a resolving power of about 60 000. Owing to the worsening seeing conditions during the second half of the night, we inserted the image slicer into the light path to reduce light losses during exposures Nos. 12–24. To reduce the UVES echelle data, we applied the REDUCE package developed by Piskunov & Valenti (2002); for a more detailed discussion of the data and the reduction, we refer the reader to Schröter et al. (2011).

The transit observed with UVES was simultaneously followed by one of the six 0.41 m Ritchey-Chrétien telescopes belonging to the PROMPT observatory (Reichart et al. 2005) located at the "Cerro Tololo Inter-American Observatory" (CTIO) in Chile. The telescope is equipped with an "Apogee Alta U47" detector with a $1k \times 1k$ pixel array with a gain of 4.91 electrons/ADU and a read-out noise of 10 electrons.

A total of 528 science frames were taken with a fixed exposure time of 30 s. No filter was used in the observations. We calibrated all science frames using a master bias, but refrained from applying a sky-flat correction, because the sky-flat exposures showed a strong illumination gradient from the center to the periphery, possibly caused by the projected shadow of the shutter. The following reduction was carried out using standard routines from the IRAF *daophot* package for image processing.

3. Analysis

We present an analysis of the temporal evolution of the observed spectra including a detailed presentation of the wavelength calibration, which is crucial to our analysis. All line profile and model fits as well as the Markov-chain Monte Carlo (MCMC) calculations make extensive use of routines of our

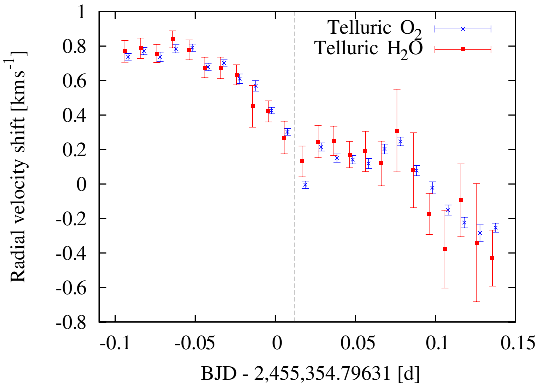

Fig. 1. Time-dependent drift of the UVES wavelength calibration determined from 64 isolated H_2O (red) and O_2 (blue) telluric absorption lines (small temporal displacement for clarity). The dashed line indicates the insertion of the image slicer.

PyAstronomy[1] collection of Python packages, which provide a convenient interface to fitting and sampling algorithms implemented in the PyMC (Patil et al. 2010) and SciPy (Jones et al. 2001) packages.

3.1. Refining the wavelength calibration using telluric standards

Our wavelength calibration was obtained using Th-Ar lamp spectra. Since those spectra are not taken simultaneously with the science spectra, they cannot account for instrumental wavelength drifts produced, for example, by environmental effects. To obtain a more accurate, time-dependent wavelength calibration, we exploited telluric absorption lines. The power of this technique has already been demonstrated, for instance, by Snellen (2004), who used atmospheric H_2O lines in a UVES spectrum to show that a precision of ~5–10 m s^{-1} can be attained, and by Figueira et al. (2010), who found that the accuracy obtained by using atmospheric features can compete with that reached with gas-cell methods on timescales of days.

To obtain an absolute wavelength calibration, we determined the wavelengths of the strong atmospheric lines of H_2O and O_2. Telluric absorption lines of H_2O are present around 6500 Å and in the 6900−7400 Å region, while those pertaining to O_2 populate the regions 6200−6300, 6800−6950, and 7650−7700 Å.

We selected the 64 strongest, isolated telluric lines (27 H_2O, 37 O_2) and fitted them with Gaussians. The best-fit wavelengths were then compared with the spectral atlas of telluric absorption lines provided by the "high-resolution transmission molecular absorption database" (HITRAN[2]; Rothman et al. 2009). The sample standard deviation between observed and nominal wavelengths was used as an error estimate. Errors were determined for H_2O and O_2 separately and found to be larger for the H_2O lines, which predominantly populate the wavelength band beyond 7000 Å, where the signal-to-noise (S/N) ratio decreases.

In Fig. 1, we show the thus obtained apparent RV shift of the 24 spectra. Clearly, the difference between nominal and

[1] http://www.hs.uni-hamburg.de/DE/Ins/Per/Czesla/PyA/PyA/index.html
[2] http://www.cfa.harvard.edu/hitran

observed wavelength of the telluric lines follows a systematic, time-dependent trend. The blue shift corresponds to a drifting of approximately 1 km s^{-1} in five hours. The drift is neither linear nor monotonic, but shows a humpy behavior. Most notably, there is a sudden jump of 0.2 km s^{-1} after the 12th observation. We find no wavelength-dependence of the trend in the 6200−7700 Å range covered by telluric lines.

This telluric drift may be caused by instrumental and atmospheric effects. As an evolving velocity field in the atmosphere gives rise to a Doppler shift, it induces a wavelength-proportional line shift. To check whether this is the case, we determined the apparent shift of telluric lines in seven echelle orders. Our analysis suggests that the drift of telluric lines does not show the characteristics of a Doppler shift, but is dominated by a displacement of the spectrum on the detector (about 0.1 CCD pixels at 6700 Å).

The telluric line drift may be the result of a changing dispersion relation caused by a variation in the ambient conditions. The ambient pressure and temperature reported in the FITS headers, indeed, follow a pattern reminiscent of the telluric line drift. Figure 2 shows both quantities as a function of time. Ambient pressure and temperature are both strongly correlated with the telluric drift pattern yielding Pearson correlation coefficients of 0.92 and 0.80, corresponding to shifts of 1.38 km s^{-1}/hPa and 1.12 km s^{-1}/°C. According to the ESO UVES User Manual (Kaufer et al. 2011) and the ESO Quality Control Group (2005), variations in temperature yield shifts of typically 0.35 pixels/°C (0.5 km s^{-1}/°C) in dispersion direction and changes in the ambient pressure cause typical shifts of 0.05 pixels/hPa (0.1 km s^{-1}/hPa). Given the environmental conditions during the night (see Fig. 2), temperature variations dominate the instrumental drift.

Although the observed drift in our spectra is larger than that inferred from the UVES manual, we identify the ambient conditions as the likely dominating cause of the apparent drift. This conclusion is in line with the results of Reiners (2009), who analyze similar differential velocity drifts.

3.2. *Photospheric Rossiter-McLaughlin effect and optical photometry*

Below, we present a joint analysis of the photospheric Rossiter-McLaughlin effect derived from the UVES spectra and simultaneously obtained optical photometry.

3.2.1. Analysis of PROMT data

The photometry was obtained using PROMPT. To reduce these data, we carried out the usual CCD data reduction steps. We identified USNO-B1.0-0913-0447626 as the most well-suited comparison star and obtained the differential light curve for CoRoT-2A along with several control light-curves using other comparison stars. To obtain the light curves, we extracted the photons from circular apertures centered on the individual stars. The local sky level was measured within an annulus surrounding the aperture. In the case of CoRoT-2A, the aperture also comprised its bona-fide physical companion, 2MASS J19270636+0122577. The resulting light curve was normalized using a linear fit to the out-of-transit points and is shown in the lower panel of Fig. 4.

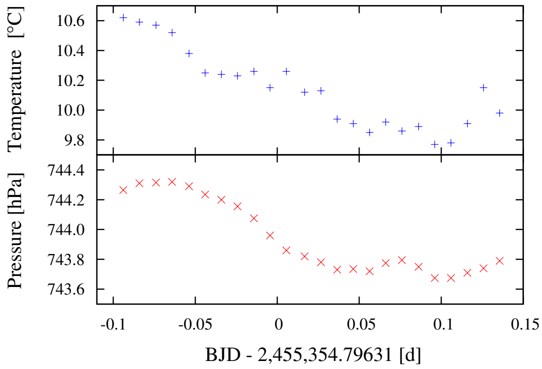

Fig. 2. Time dependence of ambient pressure and temperature during the UVES observations.

3.2.2. Measurement of the photospheric Rossiter-McLaughlin effect

We determined the radial-velocity shift of the stellar spectrum obtained with UVES by cross-correlating it with a synthetic template of CoRoT-2A according to the prescription by Zucker (2003). The template was calculated with the SPECTRUM stellar synthesis code (Gray & Corbally 1994) and is based on Kurucz model atmospheres (Kurucz 1993). The stellar parameters were adopted from Schröter et al. (2011).

Before cross-correlating them, the observed spectra were continuum-normalized. To define the continuum, we manually specified an appropriate number of supporting points for a piecewise linear fit, chosen by comparing the spectra with the template. We then calculated the cross-correlation function for different parts of the spectrum that show no contamination by telluric absorption lines. While the blue parts of the spectra are most convenient from that point of view, they completely lack telluric lines that could be used to correct for the systematic instrumental drift described in Sect. 3.1. We, therefore, computed the cross-correlation in the 5700−7500 Å range and subsequently subtracted the instrumental drift inferred from the telluric lines. The result is shown in Fig. 3 along with a quadratic fit to the out-of-transit points used in the modeling.

3.2.3. Joint modeling of photometry and Rossiter-McLaughlin effect

In our modeling, we apply the analytical RME curves presented by Ohta et al. (2005) and the transit model developed by Pál (2008). In addition to the RME model, we take into account the orbital reflex motion of the host star using a sinusoidal curve. In our approach, we neglect the slightly non-zero ($e = 0.0143^{+0.0077}_{-0.0076}$) eccentricity determined by Gillon et al. (2010), whose influence on our model is small.

The transit model has the following parameters: the orbital period, P, the mid-transit time, T_0, the radius ratio, r_p/R_s, the semi-major axis in stellar radii, a/R_s, the orbital inclination, i, the linear stellar limb-darkening coefficient, ϵ, and the contribution of third light, L_3, given as a fraction of the host-star's luminosity.

The RME model of Ohta et al. (2005) encompasses, apart from the third light contribution, all parameters used in the transit model. In addition, it includes the sky-projected stellar

A&A 539, A150 (2012)

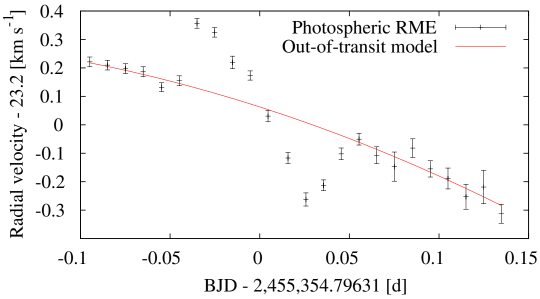

Fig. 3. The photospheric Rossiter-McLaughlin effect observed with UVES and a quadratic out-of-transit model.

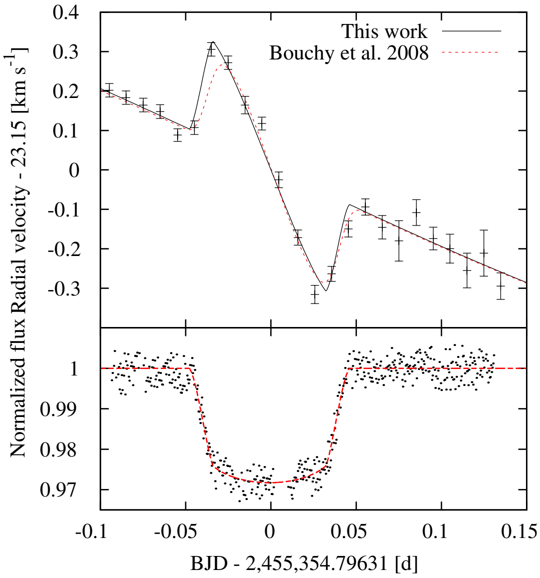

Fig. 4. *Upper panel*: photospheric Rossiter-McLaughlin effect of CoRoT-2A determined in the 5700–7500 Å band, our most likely model (solid), and the model given by Bouchy et al. (2008) (dashed). *Lower panel*: transit simultaneously observed with PROMPT and most likely model from our joint transit+RME fit.

rotational velocity, $v\sin(I_s)$, and the sky-projected angle between stellar spin axis and planetary orbit normal, λ. Furthermore, we characterize the stellar reflex motion using a sine with RV semi-amplitude, K, and an RV zero point, V_0. In the computation of the RV curve, we used an "overbinned" model to account for the finite (800 s) integration time per spectrum. In particular, each observed bin was divided into 15 model bins, which were finally averaged and compared to the observation.

In an active star such as CoRoT-2A, stellar activity could affect the measured RV curve (Albrecht et al. 2011; Bouchy et al. 2008). Additionally, systematic effects due to the observed instrumental drift may still be present. To account for RV shifts not caused by the stellar reflex motion and the RME itself, we fitted the out-of-transit points of our RV measurement using a quadratic model (see Fig. 3) and subtracted the quadratic term (4.08 km d^{-2}). The resulting RV curve is shown in the top panel of Fig. 4 and was used in the modeling.

The parameters in question had already been measured in previous works. To take the existing information into account in our modeling, we specified Gaussian priors based on previous results for the parameters: $v\sin(I_s)$, λ, K, V_0, r_p/R_s, L_3, a, and i. For the radius ratio, r_p/R_s, we used the difference between the values derived by Alonso et al. (2008) and Czesla et al. (2009) as the width of the prior. For all other parameters, except for the eccentricity, which was neglected, we used uniform priors covering the full physically reasonable space. The information on parameters and priors is summarized in Table 1.

We proceeded by sampling from the posterior probability distribution using a Markov-chain Monte Carlo (MCMC) approach. In Fig. 4, we show the most likely model given the data and the prior information. The expectation values for the parameters and 95% credibility intervals derived from the posterior are given in Table 1. We note that the prior information has a noticeable influence on the posterior, especially that on the stellar rotation velocity, $v\sin(I_s)$. If we neglect this prior information by using a broad uniform prior, the posterior yields $v\sin(I_s) = 12.9$ (11.9, 13.9) km s^{-1}, increasing the amplitude of the RME model.

Our analysis shows that CoRoT-2A's companion, 2MASS J19270636+0122577, provides 5.2% of the total flux in the PROMPT band, which is comparable to the number of 5.6% derived by Alonso et al. (2008) in the CoRoT band. The observed transit center, T_0, shows a slight displacement of −76.7 s if compared to the ephemerides given by Alonso et al. (2008).

Table 1. Priors and sampling results.

Quantity[a]	Prior	Source[c]
	Prior information	
$v\sin(I_s)$ [km s^{-1}]	11.46 ± 0.37	B08
λ [°]	7.1 ± 5	B08
K [km s^{-1}]	0.563 ± 0.014	A08
i [°]	87.84 ± 0.1	A08
p	0.1667 ± 0.0053	A08/C09
L_3 [%]	5.6 ± 1	A08
a [R_s]	6.7 ± 0.03	A08
ϵ, T_0, V_0	uniform	
e	0 (fixed)	
	Posterior	
Quantity	Value and 95% HPD[b]	
$v\sin(I_s)$ [km s^{-1}]	11.95 (11.4, 12.53)	
λ [°]	−1 (−7.7, 6)	
K [km s^{-1}]	0.564 (0.541, 0.587)	
i [°]	87.84 (87.67, 88)	
p	0.1639 (0.1621, 0.1656)	
L_3 [%]	5.2 (3.2, 7.1)	
a [R_s]	6.73 (6.69, 6.76)	
ϵ	0.33 (0.28, 0.37)	
T_0 [s]	−76.7 (−88.2, −65.3)	
V_0 [m/s]	63.3 (52.9, 72.6)	

Notes. [a] We use the nomenclature of Ohta et al. (2005); in addition, K is the radial velocity semi-amplitude, V_0 the RV offset, and L_3 the third light contribution. [b] In parentheses, the 95% HPD credibility intervals are given. [c] A08 = Alonso et al. (2008), B08 = Bouchy et al. (2008), C09 = Czesla et al. (2009).

The numbers are, however, compatible considering that the 1σ uncertainty in the Alonso et al. ephemerides amounts to 95 s at the given epoch, which covers our value. Using the reference point, $T_{0,\mathrm{A}}$, given by Alonso et al. and our transit center, T_0, we can slightly improve the estimate of the planet's orbital period using the equation

$$P_\mathrm{o} = \frac{(2\,455\,354.796\,312\,\mathrm{d} - 76.7\,\mathrm{s}) - T_{0,\mathrm{A}}}{641} = 1.742\,995\,02 \pm 0.000\,001\ \mathrm{d}. \quad (1)$$

We caution that large starspots may affect the transit timing, but as our period estimate lies within the error given by Alonso et al. (2008), their effect is unlikely to be larger than the observed offset of −77 s. Whether the small deviation is due to starspots, cannot be decided on the basis of the data at hand.

In the upper panel of Fig. 4, we show our data points (see also Table A.1), our best-fit RME model, and the model derived by Bouchy et al. (2008) (their "combined MCMC fit" shifted to our RV offset); in Table 1, we list the associated parameter values and the 95% highest probability density (HPD) credibility intervals derived using MCMC sampling.

The RME observed with UVES shows a slightly larger amplitude than reported by Bouchy et al. (2008), which causes the larger $v\sin(I_\mathrm{s})$ value derived from our data. While the derived linear limb-darkening coefficient, ϵ, of 0.3 appears to be low compared to the number of 0.66 reported by Claret (2004) for a star like CoRoT-2A in the r' band, it is in better agreement with the number of 0.41 ± 0.03 given by Alonso et al. (2008), neglecting their small (0.06) quadratic term.

Although the amplitude of the RV shift produced by the orbital motion of the planet, K, cannot be reliably determined given that our data cover only about 10% of the orbital period, we find our number of 564 (541, 587) m s^{-1} to be in good agreement with the value of 563 ± 14 m s^{-1} derived by Alonso et al. (2008) using the full orbit.

CoRoT-2A is an active star, which had a substantial spot coverage during the half-year long CoRoT observation (Alonso et al. 2008; Czesla et al. 2009; Huber et al. 2010). It is likely that spots were also present during the transit under consideration. Parameter uncertainties imposed by stellar activity on the order of a few percent have been found for CoRoT-2A, e.g., by Czesla et al. (2009), and we expect to find a similar effect in our current measurements.

Our photometry suggests that the planet-to-star radius ratio is about 2% smaller than observed by Alonso et al. (2008). Such a decrease may be caused by a corresponding decrease in the total spot coverage of the star, which would make the planet appear smaller. A smaller planet could also account for the larger model value of the stellar rotation velocity, which would then counterbalance the less pronounced RME effect produced by a smaller planet. Alternatively, the spot coverage on the eclipsed section of the star may be larger, thus, making the transit appear less deep (Czesla et al. 2009). We refrain from pointing out individual spot-crossing events in our photometry, because the data do not allow a unique identification.

Strong stellar activity as observed on CoRoT-2A can mask the true values of the physical parameters, leading to differences between individual measurements. To quantify this activity scatter, a larger sample of measurements, allowing a statistical analysis, would be needed.

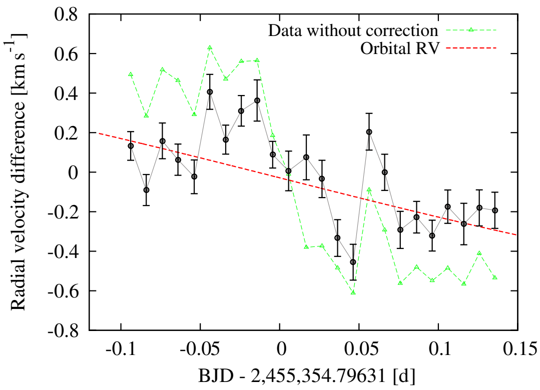

Fig. 5. Chromospheric Rossiter-McLaughlin effect: radial velocity shift of the Ca H and K lines. Circular data points: RV corrected for telluric drift; triangles: uncorrected RV shift; and dashed line: orbital radial velocity model.

3.3. The chromospheric Rossiter-McLaughlin effect

As the planet eclipses the chromosphere during the transit, the RME should also be observable in chromospheric emission lines. Among the chromospheric features in CoRoT-2A's spectrum, we find that only the cores of the Ca H and K lines are usable for our analysis. These lines are both strong enough and sufficiently uncontaminated by photospheric emission. A detailed analysis of the chromospheric features in Hα, Hβ, the Na I lines, or the Ca infrared triplet is impeded by a comparably large photospheric background, which is small in the Ca H and K emission-line cores (see Fig. 7, or Fig. 4 in Schröter et al. 2011).

In the red, we used the telluric lines as standards to improve our wavelength calibration (cf., Sect. 3.1). Because this procedure remains impossible in the blue owing to the lack of appropriate telluric lines, we adopted another approach to obtain a correction for the instrumental drift: We derived the photospheric RME in the blue part of the spectrum using a synthetic spectrum and a line list obtained from VALD (Piskunov et al. 1995) to determine the wavelength of 38 unblended stellar absorption lines between 3800 and 4300 Å. Our previously calculated red RME model was then subtracted and the residual signal was attributed to the drift. While we used the thus derived correction to model the chromospheric RME, we emphasize that the detection of the effect is independent of this correction.

To estimate the apparent RV shift of the Ca H and K line cores, we determined their barycenters using small 0.5 Å-wide segments centered around the cores' nominal positions (cf., Fig. 7). As both should be similarly affected, we averaged the results yielding a mean RV shift in the Ca H and K emission line cores.

In an alternative approach, we approximated the Ca H and K emission-line cores with Gaussians and used MCMC sampling to explore the posterior probability distribution. The measurement errors were assumed to obey a normal distribution and were derived by comparing the observed spectrum to an appropriate synthetic template. Both the barycenter and the Gaussian fit approach yielded comparable results. The resulting RV shifts are listed in Table A.1, and the outcome of the MCMC analysis is shown in Fig. 5, which shows an RV curve with a signature strongly reminiscent of the photospheric RME; the errors

A&A 539, A150 (2012)

correspond to 68% credibility intervals. We found that the center of the Gaussian is not correlated with any other parameter and concluded that the estimate is insensitive to the shape of the emission-line core.

To check the significance of the detection, we tested the null hypothesis that the RV variation in the Ca H and K cores is described by the orbital motion of the planet alone. Applying χ^2 statistics, the null hypothesis can be rejected with a p-value of 10^{-10}, indicating that our data include an additional contribution to the RV variation, which we attribute to the chromospheric RME.

To exclude the possibility that we merely detected the RME present in the residual photospheric flux underneath the Ca H and K emission-line cores, we used simulated spectra. First, we obtained a synthetic spectrum of the Ca H and K line region without emission-line cores, shifted it according to the observed photospheric RME, and applied noise to simulate the observation. We then used the same barycenter method applied to the UVES spectra and found that no RV shift can be detected that can be distinguished from noise. This is a consequence of the broad Ca H and K line wings. Second, we added the emission-line cores. Our simulations show that both the RV signal resulting from the barycenter method and the Gaussian fit to the cores are dominated by the shift in the cores and virtually unaffected by the underlying photospheric flux. We, therefore, conclude that the observed additional RV shift is not a relic of the photospheric RME, but is, indeed, related to the chromospheric emission.

3.3.1. Interpreting the radial velocity signature

The similarity of the chromospheric RV signature (see Fig. 5) and the photospheric RME suggests that the surface of CoRoT-2A is covered by active regions – at least the fraction eclipsed by the planet. The chromospheric and photospheric RME can, however, be described by the same model with different parameter values accounting for the physical conditions in the chromosphere and the photosphere. In particular, the wavelength-dependent center-to-limb variation and a, potentially, wavelength-dependent radius ratio must be taken into account (Vidal-Madjar et al. 2003; Dreizler et al. 2009).

In a first attempt to model the chromospheric RME, we considered only the RV offset, V_0^c, and the center-to-limb variation, i.e., the limb-darkening coefficient, ϵ, as free parameters. The remaining model parameters remained fixed at the photospheric values given in Table 1. We, again, imposed uniform priors on all parameters and used MCMC sampling to explore the posterior probability distribution. The optimal solution found after 10^6 iterations is shown in Fig. 6. The fit describes the data qualitatively, but, formally, the quality remains poor with a χ^2-value of 76.3 for 22 degrees of freedom.

In a second fitting attempt, we allowed for an extended chromosphere, i.e., a larger radius of the star, by introducing a scaling factor. Using a uniform prior for the scaling, we repeated the MCMC sampling and found that the data are reproduced best if the chromospheric radius is a factor of 1.16 (1.1, 1.23) larger than the photospheric radius, $R_{\rm ph}$. Formally, the fit is improved yielding a χ^2-value of 58.8 with 21 degrees of freedom for the lowest deviance solution.

Clearly, the 95% highest probability density (HPD) interval favors a larger chromospheric radius (see Table 2). To solidify

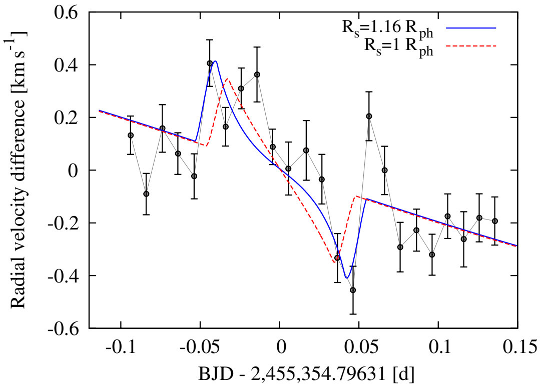

Fig. 6. Chromospheric Rossiter-McLaughlin effect: data points (filled black circles), best-fit model with radii fixed at *photospheric* values (dashed red), and best-fit model with free stellar radius (solid blue).

Table 2. Results of the modeling of the chromospheric Rossiter-McLaughlin effect.

Quantity	Value[a]	95 % HPD
ϵ	−0.4	[−16.5, 1.0[b]]
V_0^c [km s^{-1}]	21.953	[21.918, 21.987]
ϵ	−4.4	[−20.0[b] , −0.6]
V_0^c [km s^{-1}]	21.957	[21.922, 21.992]
R_s [$R_{\rm photo}$]	1.16	[1.10, 1.23]

Notes. [a] We report the value pertaining to the lowest deviance solution after 10^6 iterations. [b] This limit of the credibility interval is determined by the finite range of our uniform prior.

the significance of the result, we used an F-test to compare the vying models. We calculated the estimator

$$\hat{F} = \frac{(\chi_a^2 - \chi_b^2)/(\nu_a - \nu_b)}{\chi_b^2/\nu_b} \quad (2)$$

and compared its value to an F-distribution with $\nu_a - \nu_b$ and ν_b degrees of freedom (e.g., Rawlings et al. 1998). We found that the improvement is significant at the 98% confidence level.

In an alternative approach, we used the method described by Newton & Raftery (1994, see their Sect. 7, Eq. (13)) to estimate the marginal likelihood using the harmonic mean computed from the posterior sample generated by the Markov chain. Given the marginal likelihoods, we computed the Bayes factor, B, and obtained $\log_{10}(B) = 3.5$. In the scale introduced by Jeffreys (see, e.g., Kass & Raftery 1995, and references), this yields "decisive" evidence in favor of the model that proposes a larger chromospheric radius for CoRoT-2A. We conclude that this model provides a significantly better description of the data.

We note that a model in which the planetary radius is enlarged to account for the prolonged transit is not supported by our data. To explain the longer transit, the planetary radius would have to be larger by about a factor of two, which would drastically increase the amplitude of the RME as a whole and is inconsistent with the data.

Taking the stellar radius into account, the relative enlargement of 16% can be converted into an absolute "chromospheric" scale of 100 000 km. For the Sun, Beck & Rezaei (2011) observed Ca H and K emission up to 5000 km above the solar limb. The largest solar prominences such as the "Grand Daddy Prominence" reach projected heights of 112 000 km as measured in Hα emission (Pettit 1946). Reverting to the solar analog, we speculate that CoRoT-2A is covered with structures reminiscent of the Grand Daddy Prominence in size. Whether these structures are stable cannot be decided on the basis of the data, although, in our measurement, the chromospheric RME appears to be symmetric, which indicates the presence of extended structures on both sides of the star. We interpret this as evidence of a stable configuration or at least a high filling factor of active regions creating large chromospheric structures.

We found that ϵ, which parametrizes the chromospheric center-to-limb variation, appears to be negative. This indicates that the chromosphere is limb-brightened. At some point, the limb-brightened RME model effectively becomes a "ring model", which is relatively indifferent to further changes in ϵ. As our data do not rule out this region, the exact level of chromospheric limb-brightening cannot currently be determined.

As shown in Fig. 6, some data points are incompatible with either RME model. This may be due to the following reasons: statistics and systematics, chromospheric inhomogeneities, and intrinsic variability.

During the transit, the RME curve could be affected by plage-crossing events. We checked that features with RV amplitudes of $\approx$150 m s^{-1} can be reproduced assuming a plage region with a size similar to that of the planetary disk and twice the photospheric brightness (cf., Sect. 3.3.2). Additionally, the chromospheric emission may show intrinsic variability unrelated to the transit. However, we argue that neither intrinsic variability nor systematics due to the wavelength calibration are likely to mimic the prolonged transit signature observed in Ca H and K. Nevertheless, such an effect cannot ultimately be excluded.

3.3.2. Distribution of chromospheric and photospheric emission

The detection of the RME in the Ca H and K lines shows that a significant fraction of the chromospheric emission regions must be eclipsed during the entire transit. Any differences in the distribution of chromospheric and photospheric surface brightnesses should be reflected by a variable equivalent width (EW) of the Ca H and K emission-line cores during the transit, because chromospheric emission would be measured relative to the photospheric continuum. To obtain an estimate of the EW, we summed the signal in 1.4 Å wide bands centered on the Ca H and K emission-line cores (see Fig. 7) and compared it to the signal obtained in the two photospheric bands in the regions 3981–3996 Å and 3861–3909 Å. The choice of these bands is arbitrary, but we verified that our results depend only weakly on this choice. The resulting ratio, R, is a measure of the quantity

$$R(t) = \frac{\langle b_{\mathrm{vis}}(\lambda_{\mathrm{Ca}})\rangle(t)}{\langle b_{\mathrm{vis}}(\lambda_{\mathrm{Ph}})\rangle(t)}, \tag{3}$$

where $\langle b_{\mathrm{vis}}(\lambda_{\mathrm{Ca,Ph}})\rangle$ is the mean surface brightnesses of the visible fraction of the star in Ca H and K and the photosphere.

Figure 8 shows the outcome. No variation in the observed EW is detectable within the limits of our uncertainties. The ratio of Ca H and K signal to the continuum signal in the aforementioned bands amounts to $R = (2.31 \pm 0.028) \times 10^{-2}$. The given error corresponds to the sample standard deviation. It does not differ for in- and out-of-transit points and is attributed to a combination of measurement errors and intrinsic variability.

If the photospheric and chromospheric emission were equally distributed on the visible surface of CoRoT-2A, the EW

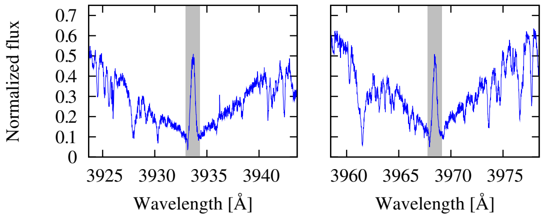

Fig. 7. CoRoT-2A's Ca H and K lines. Gray intervals indicate the bands used to measure the flux in the emission-line cores (see text for details).

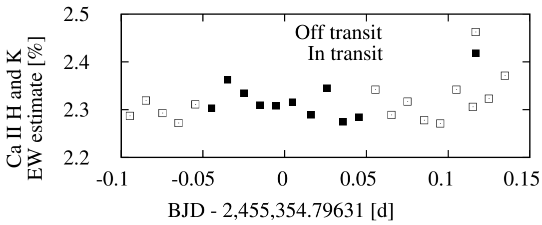

Fig. 8. Ratio of integrated fluxes in both the Ca H and K emission-line cores (see Fig. 7) to those in the comparison bands (see text).

of the Ca H and K cores and, therefore, R would remain constant during transit, because the occultation has the same effect on both photospheric and chromospheric emission. A change in R indicates a deviation from the equal distribution on the currently occulted section of the stellar disk. If, for example, an active region is occulted, more chromospheric than photospheric emission should be blocked, leading to a decrease in R.

In the following, we quantify the relation between surface brightness distribution and R. The brightness, $B(\lambda)$, of the entire stellar disk at any wavelength, λ, can be written as

$$B(\lambda) = f\langle b_{\mathrm{occ}}(\lambda)\rangle + F\langle b_{\mathrm{vis}}(\lambda)\rangle \tag{4}$$

where f is the occulted area of the stellar disk and F the visible area. For the special case of $\langle b_{\mathrm{occ}}\rangle = \langle b_{\mathrm{vis}}\rangle = b_0$, we obviously obtain $B = (f + F)b_0$. Starting from exactly this situation, we introduce a bright chromospheric plage region with a local surface brightness, $\langle b'_{\mathrm{occ}}(\lambda_{\mathrm{Ca}})\rangle$, which is a factor of α higher than the mean surface brightness. Hence, we write $\langle b'_{\mathrm{occ}}(\lambda_{\mathrm{Ca}})\rangle = \alpha b_0(\lambda_{\mathrm{Ca}})$.

The conservation of total brightness demands that a local increase in the surface brightness across the eclipsed section of the star must be balanced by an adjustment of the mean brightness of the visible fraction, $\langle b_{\mathrm{vis}}(\lambda_{\mathrm{Ca}})\rangle$, which we parametrize by β so that $\langle b'_{\mathrm{vis}}(\lambda_{\mathrm{Ca}})\rangle = \beta b_0$.

Assuming that the photospheric surface brightness remains unaffected, the ratio R is proportional to β (see Eq. (3)). Starting from $B = f\alpha b_0 + F\beta b_0$, we obtain the relation

$$\beta = 1 + \frac{f}{F}(1 - \alpha). \tag{5}$$

In the case of CoRoT-2A, the factor f/F amounts to $\approx$0.03. Thus, if a plage region with a local Ca H and K surface brightness that is a factor of $\alpha = 15$ higher than the mean brightness were eclipsed, the observed EW would be a factor of 2 lower. The relative stability of R, which varies by only about 3%, suggests that the surface brightness of the Ca H and K emission does not strongly deviate from that of the photosphere. According to our result, the photospheric and chromospheric surface brightnesses are the same to within a factor of about 2.

An analysis of the chromospheric emission in the Ca infrared triplet, which is visible as a substantial filling-in of the line cores, yielded compatible but less conclusive results due to the much larger photospheric contribution.

3.4. Searching for planetary Na I absorption

During a primary eclipse, stellar light passes through the planetary atmosphere, potentially giving rise to planetary absorption features. These features have, indeed, been detected in several systems using the Hubble Space Telescope and more recently ground-based data (e.g., Charbonneau et al. 2002; Redfield et al. 2008). According to Seager & Sasselov (2000), the most prominent planetary absorption features in the optical should be caused by neutral sodium.

To search for planetary sodium absorption features in our spectra, we combined them to yield in- and out-of-transit templates with a S/N ratio of 90 and 110 around Na , respectively. As discussed by Schröter et al. (2011), the sodium doublet is affected by strong blue-shifted interstellar absorption. Additionally, the line core is contaminated by residual sky emission. In the course of our observations, the strength of the sky contribution increased monotonically following the airmass. We found that a correction for the sky emission is problematic, because the sky spectrum shifts in wavelength relative to the stellar spectrum producing spurious absorption in the in-transit template. The quality of our combined template spectra does not allow us to subtract a heuristic model of the sky emission without introducing additional residuals. Therefore, we found it impossible to deduce a reasonable upper limit to the planetary sodium absorption.

4. Discussion and conclusion

We have presented our analysis of 24 high-resolution UVES spectra of CoRoT-2A and simultaneously obtained photometry, observed during a planetary transit. We have reported on the – to the best of our knowledge – first detection of a prolonged RME in the chromospheric Ca H and K emission-line cores. Furthermore, we have presented a joint analysis of the photospheric RME and the transit photometry.

During our analysis, we found that the wavelength calibration of UVES undergoes a substantial drift, which we corrected using telluric standards. While the modeling of the RME depends on the details of this correction, neither the detection of the photospheric nor the chromospheric RME does.

Our modeling yielded an improved estimate of the orbital period of the planet and shows that our data favor an RME amplitude slightly larger than that reported by Bouchy et al. (2008) using HARPS and SOPHIE data. This results in a larger estimate of the projected rotational velocity, $v \sin(I_s)$, of the star. This difference potentially reflects a change in the total stellar spot coverage between the observations. As Alonso et al. (2008), we derived a weak limb-darkening relative to the theoretical numbers given by Claret (2004). We speculate that a larger contribution from plage regions and, therefore, the observed activity, may be responsible for this. While the planet clearly passes across the stellar disk, our search for planetary absorption features in sodium remained inconclusive, owing to the lack of signal and contaminating sky emission.

The presence of the chromospheric RME indicated that chromospheric emission was eclipsed during every phase of the visual transit – and beyond. We present evidence that the transit observed in Ca H and K lasts about 15% longer than its visual counterpart. Our modeling shows that the data are most closely reproduced by increasing the size of the stellar chromosphere. In contrast, boosting the planetary radius by a factor of two, as would be needed to explain the longer transit, is incompatible with the data. The observed chromospheric scale of 100 000 km is compatible with large solar structures such as the "Grand Daddy Prominence". Our observations indicate that such structures could cover a substantial fraction of the surface of CoRoT-2A and other very active stars.

The analysis of the chromospheric RME favors chromospheric limb-brightening. However, in a subsequent analysis of the EW of the Ca H and K emission-line cores, we found no differences between the surface brightness distributions of chromospheric and photospheric emission to within the uncertainties of our data.

Besides the scale height of the chromosphere, the analysis of the chromospheric RME allows to explore the structure of the stellar chromosphere covered by the planetary disk, i.e., the center-to-limb variation and inhomogeneities due to active regions. Indeed, the asymmetry of the chromospheric RME curve (see Fig. 6; $0 < \text{time} < 0.05$ d) may be a consequence of inhomogeneities in the chromospheric surface-brightness distribution. However, the sparse phase coverage, the uncertainties imposed by the instrumental RV drift, and the likely presence of intrinsic variability do not allow to safely attribute these variations to surface features. Nonetheless, both points could be addressed by dedicated observations with today's instrumentation. In particular, what is needed to verify our results is higher temporal resolution, spectra of equivalent or higher S/N, and improved RV stability – hence, a brighter target.

To increase the amount of chromospheric signal, future observations could include other emission-line cores in the UV region such as the Mg H and K lines at ≈2800 Å, which are not covered by the present data. As for Ca H and K, these lines have weak photospheric contributions, but are, unfortunately, impossible to observe from the ground.

As an alternative to the chromospheric RME, the chromospheric center-to-limb variation and inhomogeneities could also be studied using narrow-band transit-photometry centered on chromospheric emission lines (Assef et al. 2009; Schlawin et al. 2010). In contrast to the RME, however, this method relies on a precise photometric calibration (Snellen 2004), which is difficult to achieve especially in ground-based observations.

Our analysis demonstrates the power of the Rossiter-McLaughlin effect for the exploration of the stellar atmosphere and clearly underlines the need for dedicated observations.

Acknowledgements. We thank the anonymous referee for thoughtful comments. This work makes use of observational data obtained with UVES at the ESO Very Large Telescope, Paranal, Chile. S.C., C.v.E., and K.F.H. are supported in the framework of the DFG-funded Research Training Group "Extrasolar Planets and their Host Stars" (DFG 1351/1). and U.W. acknowledge support from the DLR under grant 50OR0105. S.S. acknowledges support from the DLR under grant 50OR0703. PROMPT observations were made possible by the Robert Martin Ayers Science Fund.

Appendix A: Details of observations and data analysis

Table A.1. Details of data and data analysis.

No.	HJD $-2\,400\,000$ d	IS[a]	Airmass	Seeing [″]	Pressure [hPa]	Temp. [°C]	T[b]	RV [km s^{-1}]	ΔRV Ca [km s^{-1}]
1	55 354.701526	n	1.377	0.94	744.27	10.62	n	23.424 ± 0.017	0.16 ± 0.07
2	55 354.711337	n	1.319	1.07	744.31	10.59	n	23.412 ± 0.017	−0.06 ± 0.08
3	55 354.721503	n	1.270	0.89	744.32	10.57	n	23.400 ± 0.017	0.19 ± 0.09
4	55 354.731315	n	1.231	1.08	744.32	10.52	n	23.389 ± 0.017	0.09 ± 0.08
5	55 354.741612	n	1.196	0.95	744.29	10.38	n	23.335 ± 0.016	0.01 ± 0.09
6	55 354.751424	n	1.170	1.03	744.25	10.26	y	23.357 ± 0.017	0.44 ± 0.09
7	55 354.761459	n	1.149	1.07	744.19	10.24	y	23.559 ± 0.017	0.20 ± 0.07
8	55 354.771271	n	1.133	1.12	744.16	10.23	y	23.528 ± 0.017	0.34 ± 0.08
9	55 354.781191	n	1.122	1.36	744.08	10.26	y	23.422 ± 0.022	0.41 ± 0.10
10	55 354.791007	n	1.115	1.31	743.96	10.20	y	23.376 ± 0.016	0.12 ± 0.07
11	55 354.801043	n	1.113	1.15	743.89	10.26	y	23.233 ± 0.020	0.03 ± 0.10
12	55 354.812237	y	1.116	1.45	743.80	10.12	y	23.086 ± 0.019	0.08 ± 0.11
13	55 354.822116	y	1.124	1.29	743.78	10.13	y	22.940 ± 0.023	−0.04 ± 0.09
14	55 354.831931	y	1.135	0.98	743.73	9.91	y	22.990 ± 0.019	−0.32 ± 0.09
15	55 354.841743	y	1.152	0.98	743.74	9.91	y	23.100 ± 0.020	−0.44 ± 0.09
16	55 354.851776	y	1.174	0.95	743.70	9.85	n	23.152 ± 0.021	0.23 ± 0.09
17	55 354.861589	y	1.201	0.92	743.78	9.92	n	23.096 ± 0.030	0.03 ± 0.09
18	55 354.871404	y	1.235	0.83	743.80	9.86	n	23.056 ± 0.051	−0.26 ± 0.09
19	55 354.881691	y	1.277	0.85	743.75	9.89	n	23.121 ± 0.033	−0.20 ± 0.08
20	55 354.891506	y	1.326	0.83	743.68	9.77	n	23.048 ± 0.029	−0.29 ± 0.08
21	55 354.901320	y	1.385	0.71	743.68	9.78	n	23.014 ± 0.037	−0.15 ± 0.09
22	55 354.911400	y	1.456	0.73	743.71	9.91	n	22.950 ± 0.044	−0.23 ± 0.11
23	55 354.921213	y	1.539	0.86	743.74	10.15	n	22.984 ± 0.058	−0.15 ± 0.09
24	55 354.931026	y	1.640	1.18	743.79	9.98	n	22.890 ± 0.034	−0.16 ± 0.09

Notes. [(a)] Was the Image Slicer (IS) used? (Yes/No). [(b)] Was the observation obtained during transit? (Yes/No).

References

Albrecht, S., Winn, J. N., Johnson, J. A., et al. 2011, ApJ, 738, 50
Alonso, R., Auvergne, M., Baglin, A., et al. 2008, A&A, 482, L21
Ammler-von Eiff, M., Santos, N. C., Sousa, S. G., et al. 2009, A&A, 507, 523
Assef, R. J., Gaudi, B. S., & Stanek, K. Z. 2009, ApJ, 701, 1616
Beck, C. A. R., & Rezaei, R. 2011, A&A, 531, A173
Bouchy, F., Queloz, D., Deleuil, M., et al. 2008, A&A, 482, L25
Charbonneau, D., Brown, T. M., Noyes, R. W., & Gilliland, R. L. 2002, ApJ, 568, 377
Claret, A. 2004, A&A, 428, 1001
Czesla, S., Huber, K. F., Wolter, U., Schröter, S., & Schmitt, J. H. M. M. 2009, A&A, 505, 1277
Dekker, H., D'Odorico, S., Kaufer, A., Delabre, B., & Kotzlowski, H. 2000, in SPIE Conf. Ser. 4008, ed. M. Iye, & A. F. Moorwood, 534
Dreizler, S., Reiners, A., Homeier, D., & Noll, M. 2009, A&A, 499, 615
ESO Quality Control Group 2005, UVES – general pipeline information, http://www.eso.org/observing/dfo/quality/UVES/pipeline/
Fabrycky, D. C., & Winn, J. N. 2009, ApJ, 696, 1230
Figueira, P., Pepe, F., Lovis, C., & Mayor, M. 2010, A&A, 515, A106
Gillon, M., Lanotte, A. A., Barman, T., et al. 2010, A&A, 511, A3
Giménez, A. 2006, ApJ, 650, 408
Gray, R. O., & Corbally, C. J. 1994, AJ, 107, 742
Hirano, T., Suto, Y., Taruya, A., et al. 2010, ApJ, 709, 458
Huber, K. F., Czesla, S., Wolter, U., & Schmitt, J. H. M. M. 2009, A&A, 508, 901
Huber, K. F., Czesla, S., Wolter, U., & Schmitt, J. H. M. M. 2010, A&A, 514, A39
Jones, E., Oliphant, T., Peterson, P., et al. 2001, SciPy: Open source scientific tools for Python, http://www.scipy.org
Kass, R. E., & Raftery, A. E. 1995, J. Am. Stat. Assoc., 90, 773
Kaufer, A., Dumas, C., & Monaco, L. 2011, UV-Visual Echelle Spectrograph User manual, VLT-MAN-ESO-13200-1825, Issue 88.2
Knutson, H. A., Howard, A. W., & Isaacson, H. 2010, ApJ, 720, 1569
Kurucz, R. L. 1993, SYNTHE spectrum synthesis programs and line data (Cambridge, MA: Smithsonian Astrophysical Observatory)
Lanza, A. F., Pagano, I., Leto, G., et al. 2009, A&A, 493, 193
McLaughlin, D. B. 1924, ApJ, 60, 22
Newton, M. A., & Raftery, A. E. 1994, J. R. Statist. Soc. B, 56, 3
Ohta, Y., Taruya, A., & Suto, Y. 2005, ApJ, 622, 1118
Pál, A. 2008, MNRAS, 390, 281
Patil, A., Huard, D., & Fonnesbeck, C. J. 2010, J. Stat. Soft., 35, 1
Pettit, E. 1946, PASP, 58, 310
Piskunov, N. E., & Valenti, J. A. 2002, A&A, 385, 1095
Piskunov, N. E., Kupka, F., Ryabchikova, T. A., Weiss, W. W., & Jeffery, C. S. 1995, A&AS, 112, 525
Radick, R. R., Lockwood, G. W., Skiff, B. A., & Baliunas, S. L. 1998, ApJS, 118, 239
Rawlings, J. O., Pantula, S. G., & Dickey, D. A. 1998, Applied regression analysis, 2nd edn., Springer texts in statistics (New York, NY: Springer)
Redfield, S., Endl, M., Cochran, W. D., & Koesterke, L. 2008, ApJ, 673, L87
Reichart, D., Nysewander, M., Moran, J., et al. 2005, Nuovo Cimento C Geophysics Space Physics C, 28, 767
Reiners, A. 2009, A&A, 498, 853
Rossiter, R. A. 1924, ApJ, 60, 15
Rothman, L. S., Gordon, I. E., Barbe, A., et al. 2009, J. Quant. Spec. Radiat. Transf., 110, 533
Schlawin, E., Agol, E., Walkowicz, L. M., Covey, K., & Lloyd, J. P. 2010, ApJ, 722, L75
Schlesinger, F. 1910, Publications of the Allegheny Observatory of the University of Pittsburgh, 1, 123
Schröter, S., Czesla, S., Wolter, U., et al. 2011, A&A, 532, A3
Seager, S., & Sasselov, D. D. 2000, ApJ, 537, 916
Snellen, I. A. G. 2004, MNRAS, 353, L1
Snellen, I. A. G., de Mooij, E. J. W., & Burrows, A. 2010, A&A, 513, A76
Triaud, A. H. M. J., Queloz, D., Bouchy, F., et al. 2009, A&A, 506, 377
Vidal-Madjar, A., Lecavelier des Etangs, A., Désert, J., et al. 2003, Nature, 422, 143
Wolter, U., & Schmitt, J. H. M. M. 2005, A&A, 435, L21
Zucker, S. 2003, MNRAS, 342, 1291

Part III

Summary and conclusions

Chapter 7

Closing thoughts

7.1 Summary and conclusions

In this thesis, we carried out the characterization of transiting exoplanets and their host stars. The studies focused on four transiting systems: WASP-33 (a δ Scuti star), Qatar-1 (a metal-rich K dwarf star), and CoRoT-2 and KOI-676 (two active planet-hosting stars). To study the physical and orbital properties of the mentioned systems, we carried out different observational techniques, making use of ground-based photometry, polarimetry, and spectroscopy, as well as space-based data provided by the Kepler space telescope. We further characterized some aspects of transiting systems by means of simulated data.

WASP-33: The δ Scuti star and the hot Jupiter

After two years of carrying out a photometric follow-up, we collected and analyzed an extensive set of data of WASP-33, as never produced before. The collected photometry consists of in- and out-of-transit data, and provides complete phase coverage. With it, we studied the pulsation spectrum of the host, and the primary transits of the exoplanet. Not only our data set is the only one that comprises dedicated out-of-transit photometric coverage to study the stellar pulsations in detail, but additionally multi-color and simultaneous observations to study the nature of the modes.

Our analysis revealed eight significant frequencies. Some of them seem to be consistent with previous reports. With the frequencies, amplitudes, and phases we construct a pulsation model which we use to correct the primary transit light curves, re-determining afterward the orbital parameters by means of pulsation-clean data. Our final orbital parameters are consistent with those reported by other authors. Interestingly, the derived parameter values are hardly affected by taking into account the pulsations in the modeling. However, the errors decrease. One possible explanation could be that the amplitudes of WASP-33 pulsations, at least in the high frequency range where our studies focus, are found to be small in nature.

Our extensive primary transit observations, obtained in different filter bands, allowed us to notice a decrease in the planet-to-star radius ratio with wavelength, also observed by other authors. Simultaneous multi-band photometry of primary transits of WASP-33 will help to better constrain this dependency.

Considering that our work has been produced using fully ground-based observations, we were able to provide an extensive study of the pulsation spectrum of this unique δ Scuti planet-hosting star. This, in turn, has helped to better comprehend how much do the pulsations affect the determination of the system parameters.

WASP-33: Measuring polarized light by the exoplanet atmosphere

The close-in orbit of WASP-33b, in combination with the high apparent brightness of its host star, make the system an ideal target to measure stellar polarized light by the exoplanet atmosphere. We observed the system during two campaigns, using the 2.2 m telescope and the "Calar Alto Faint Object Spectrograph" instrument in Calar Alto, Spain. In this thesis we present a method that aims to reach, in a short time, the signal-to-noise that is required to detect the mentioned polarized light.

Since the polarization signal produced by the exoplanet atmosphere is extremely small, a major work needs to be invested in the characterization of the instrumental polarization and its stability. Therefore, in addition to WASP-33 we observed polarized and unpolarized standard stars. In this thesis we presented fist results with respect to the instrumental polarization, and a full description of the observing technique.

Qatar-1: ground-based observations and transit timing variation studies

During our first follow-up campaign of the Qatar-1 transiting system, our analysis of the mid-timing residuals revealed an inconstant orbital period. We found the observed long-term timing variations to be significant from a statistical point of view, but we failed to explain the observed variations by an unique orbital configuration.

In order to determine stronger constraints on the possible perturber characteristics, we continued our photometric follow-up and extended the primary transit sample up to 42, spread along two years. Based on the complete sample, we re-calculated the individual mid-transits and studied, one more time, the viability of the previously-claimed TTVs. Although we found a considerably large scatter in the O-C diagram, we studied separately the mid-transit shifts obtained from complete primary transits and found that they are consistent with no TTV. Therefore, our previously reported indications of transit timing variations are not supported using additional data and longer time coverage.

Furthermore, since the star was claimed to be moderately active, we carried out a photometric follow-up of the star in Hα using Hamburger Sternwarte's facilities. After a careful and homogeneous data reduction we observed clear evidences of activity, correlated with what we estimated to be the rotational period of the star (~30 days). Using the rotational period, by means of gyrochronologic studies we estimated the age of the star to be ~2.7 Gyr. Although we believe that activity can induce shifts in the observed mid-transit times (mainly as product of deformations in the light curves caused by stellar spots), the photometric data we have cannot prove such a connection.

Transit timing variations: testing ground-based observations by means of primary transit modeling

Although Qatar-1 first observing campaign revealed a transit timing variation signal, a further study relying on better quality observations could not reproduce the firstly found signal. Surprisingly, this sort of disagreement happened before. The literature reveals how misleading can ground-based observations be, when several authors observe the same system and drop out completely different TTVs results.

To study whether the discrepancies are just the product of extremely bad luck, or (a little less naively) the product of systematic effects that are not properly considered, we simulated primary transit observations that resemble real ground-based observations. To this end, we modeled the unwanted effects caused by the Earth atmosphere over the synthetic light curves, mostly related to airmass and extinction. After testing the quality of our synthetic data against real observations, we produced the regular steps towards transit timing variation studies. In this thesis we presented a full description of the code that produces the synthetic data. Additionally, we have identified the main sources of misleading TTVs, and the basic characteristics that the light curves need to fulfill, in order to avoid erroneous results.

Exoplanet oblateness

All our solar system planets, with the exception of Mercury, are some how oblate. Since the primary transit shape is a consequence of the relative shapes between the exoplanet and the host star, aggravated by limb-darkening effects, it is straight forward to attempt to model the flux drop at primary transit adding as parameter the exoplanet oblateness. Although the observed difference between a spherical and oblate exoplanet would be very challenging to detect by means of ground-based observations, the advent of space-based instrumentation capable of producing photometry of unprecedented accuracy provided the necessary data to make the attempt.

We produced an initial model following the exact same steps that were carried out by other authors, but considering the projected area of the spheroid into the direction of the observer instead of the projection of a sphere. Although Kepler space telescope data provides the photometric precision required to determine the observed difference due to oblateness, this parameter and inclination are degenerate. An ideal method would be the determination of oblateness and inclination independently.

CoRoT-2 and KOI-676: two very active stars hosting exoplanets

After observing CoRoT-2 photometrically and spectroscopically in simultaneous, we reported the first detection of a prolonged Rossiter-McLaughlin effect in the chromospheric Ca II H and K line cores. Nonetheless, our results are close to the noise limit and require further confirmation.

KOI-676 was first listed as planetary system candidate. After producing a deep study over the primary transit data we could report the detection and characterization of two transiting Neptune-sized planets, KOI-676b and KOI-676c. We showed that the transits of both planets are affected by spots, and calculated the mean densities of both planets. In addition, both planets also showed transit timing variations. Using N-body simulations we constructed possible system configurations consistent with the Kepler data, and found that the best dynamical scenario is represented by the two Neptunes and a third perturbing planet in a slightly eccentric orbit.

7.2 Future work

Is it possible to estimate the orbital parameters of an exoplanetary system when the latter does not transit the star? Polarimetric measurements of stellar light polarized by an exoplanet atmosphere is slowly becoming an answer to that question. Polarimetry is a highly versatile tool that allows to study the geometry of many astrophysical processes. When applied to extrasolar planets, it provides the unique opportunity to determine the orbital inclination and, thus, the true mass of exoplanets. This has been remained, so far, impossible for non–transiting planets. As of now, only a single polarimetric detection of an exoplanet has been published. This method has not been popular amongst the exoplanetary science field, because the polarized signal is of the order of 0.01-0.1%, extremely challenging to detect, even by current instruments and telescopes. Hence, to increase the signal-to-noise ratio collecting in an efficient way photons from the source of interest, I developed a novel observing technique and applied it in Calar Alto Observatory (cf. the detailed method is described in Chapter 3).

My test target, WASP-33b, is the only known exoplanet orbiting a pulsating star. The hot Jupiter WASP-33b orbits its δ Scuti host star with a period of $\sim$1.22 days. We successfully carried out two observing campaigns at Calar Alto. Our main goal was to establish polarimetry as a viable alternative to primary transit analysis. The observed data is completely reduced. Furthermore, we characterized the instrumental polarization. As a next step, I plan to estimate the Stokes parameters for WASP-33, in order to fit the phase–dependent polarization model to the data. Therefore, I will be able to compare the orbital parameters of the system obtained by the transiting method with that of the polarimetric method. The results from this study will provide an input into the study of exoplanetary atmospheres, since the polarized signal carries the information of its composition.

Further, I have photometrically identified eight pulsation frequencies of WASP-33A. In our work, we attempted to identify the pulsation modes by means of a multi-color photometric data. However, the collected photometry was not sensitive enough to establish the modes of oscillation properly. Later on, by the end of this year I plan to carry out a spectroscopic follow-up of the system, with the main goal to properly determine the oscillation modes. This study will provide an insight into the interiors of WASP-33A.

In the case of transiting planets, an accurate determination of the orbital parameters depends on the stellar physical parameters. Values such as the transit depth are scaled down to the star's size. A "standard" approach in the determination of such stellar parameters use evolutionary models. These models provide the mass and the radius of stars using mainly their effective temperature and metallicity. I successfully proposed to follow up moderate active G and K planet host-stars to study the constancy of such fundamental stellar parameters, to better understand how reliable can be the planetary-derived ones. In particular, I plan to use the observed HRT spectra to search for variations in the T_{eff} and the [Fe/H], correlated with the rotational period of the host star.

These observations will divulge new characteristics to better understand the extra-solar planets and their host stars.

List of Figures

List of Tables

Bibliography

Aerts, C. (1996), 'Mode identification of pulsating stars from line-profile variations with the moment method: a more accurate discriminant.', *A&A* **314**, 115–122.

Aerts, C., Christensen-Dalsgaard, J. & Kurtz, D. W. (2010), *Asteroseismology*.

Agol, E., Steffen, J., Sari, R. & Clarkson, W. (2005), 'On detecting terrestrial planets with timing of giant planet transits', *MNRAS* **359**, 567–579.

Alonso, R., Auvergne, M., Baglin, A., Ollivier, M., Moutou, C., Rouan, D., Deeg, H. J., Aigrain, S., Almenara, J. M., Barbieri, M., Barge, P., Benz, W., Bordé, P., Bouchy, F., de La Reza, R., Deleuil, M., Dvorak, R., Erikson, A., Fridlund, M., Gillon, M., Gondoin, P., Guillot, T., Hatzes, A., Hébrard, G., Kabath, P., Jorda, L., Lammer, H., Léger, A., Llebaria, A., Loeillet, B., Magain, P., Mayor, M., Mazeh, T., Pätzold, M., Pepe, F., Pont, F., Queloz, D., Rauer, H., Shporer, A., Schneider, J., Stecklum, B., Udry, S. & Wuchterl, G. (2008), 'Transiting exoplanets from the CoRoT space mission. II. CoRoT-Exo-2b: a transiting planet around an active G star', *A&A* **482**, L21–L24.

Anderson, R. I., Mowlavi, N. & Eyer, L. (2013), The Galactic Cepheid period-luminosity relation revisited using bona fide cluster Cepheids, *in* R. de Grijs, ed., 'IAU Symposium', Vol. 289 of *IAU Symposium*, pp. 153–156.

Armitage, P. J. (2010), *Astrophysics of Planet Formation*.

Baba, N. & Murakami, N. (2003), 'A Method to Image Extrasolar Planets with Polarized Light', *PASP* **115**, 1363–1366.

Baglin, A., Auvergne, M., Boisnard, L., Lam-Trong, T., Barge, P., Catala, C., Deleuil, M., Michel, E. & Weiss, W. (2006), CoRoT: a high precision photometer for stellar ecolution and exoplanet finding, *in* '36th COSPAR Scientific Assembly', Vol. 36 of *COSPAR Meeting*, p. 3749.

Balona, L. A. & Evers, E. A. (1999), 'Mode identification and asteroseismology of delta Scuti stars', *MNRAS* **302**, 349–361.

Barnes, J. W. & Fortney, J. J. (2003), 'Measuring the Oblateness and Rotation of Transiting Extrasolar Giant Planets', *ApJ* **588**, 545–556.

Barnes, R. (2010), *Formation and Evolution of Exoplanets*.

Behr, A. (1959), 'Beobachtungen zur Wellenlängenabhängigkeit der interstellaren Polarisation', *Veroeffentlichungen der Universitaets-Sternwarte zu Goettingen* **7**, 175–180.

Belkacem, K., Samadi, R., Goupil, M.-J. & Dupret, M.-A. (2008), 'Stochastic excitation of non-radial modes. I. High-angular-degree p modes', *A&A* **478**, 163–174.

Benedict, G. F. & McArthur, B. E. (2012), The HST/FGS Cepheid Period-Luminosity Calibration and Subsequent Uses, *in* 'American Astronomical Society Meeting Abstracts #220', Vol. 220 of *American Astronomical Society Meeting Abstracts*, p. 518.04.

Berdyugina, S. V., Berdyugin, A. V., Fluri, D. M. & Piirola, V. (2008), 'First Detection of Polarized Scattered Light from an Exoplanetary Atmosphere', *ApJ* **673**, L83–L86.

Berdyugina, S. V., Berdyugin, A. V., Fluri, D. M. & Piirola, V. (2011), 'Polarized Reflected Light from the Exoplanet HD189733b: First

Multicolor Observations and Confirmation of Detection', *ApJ* **728**, L6.
Book Review: Solar system dynamics / Cambridge U Press, 2000

Book Review: Solar system dynamics / Cambridge U Press, 2000 *(2000)*, Irish Astronomical Journal **27**, *234*.

Borucki, W. J., Koch, D., Basri, G., Batalha, N., Brown, T., Caldwell, D., Caldwell, J., Christensen-Dalsgaard, J., Cochran, W. D., DeVore, E., Dunham, E. W., Dupree, A. K., Gautier, T. N., Geary, J. C., Gilliland, R., Gould, A., Howell, S. B., Jenkins, J. M., Kondo, Y., Latham, D. W., Marcy, G. W., Meibom, S., Kjeldsen, H., Lissauer, J. J., Monet, D. G., Morrison, D., Sasselov, D., Tarter, J., Boss, A., Brownlee, D., Owen, T., Buzasi, D., Charbonneau, D., Doyle, L., Fortney, J., Ford, E. B., Holman, M. J., Seager, S., Steffen, J. H., Welsh, W. F., Rowe, J., Anderson, H., Buchhave, L., Ciardi, D., Walkowicz, L., Sherry, W., Horch, E., Isaacson, H., Everett, M. E., Fischer, D., Torres, G., Johnson, J. A., Endl, M., MacQueen, P., Bryson, S. T., Dotson, J., Haas, M., Kolodziejczak, J., Van Cleve, J., Chandrasekaran, H., Twicken, J. D., Quintana, E. V., Clarke, B. D., Allen, C., Li, J., Wu, H., Tenenbaum, P., Verner, E., Bruhweiler, F., Barnes, J. & Prsa, A. (2010), 'Kepler Planet-Detection Mission: Introduction and First Results', Science **327**, *977–.*

Bouchy, F., Queloz, D., Deleuil, M., Loeillet, B., Hatzes, A. P., Aigrain, S., Alonso, R., Auvergne, M., Baglin, A., Barge, P., Benz, W., Bordé, P., Deeg, H. J., de La Reza, R., Dvorak, R., Erikson, A., Fridlund, M., Gondoin, P., Guillot, T., Hébrard, G., Jorda, L., Lammer, H., Léger, A., Llebaria, A., Magain, P., Mayor, M., Moutou, C., Ollivier, M., Pätzold, M., Pepe, F., Pont, F., Rauer, H., Rouan, D., Schneider, J., Triaud, A. H. M. J., Udry, S. & Wuchterl, G. (2008), 'Transiting exoplanets from the CoRoT space mission. III. The spectroscopic transit of CoRoT-Exo-2b with SOPHIE and HARPS', A&A **482**, *L25–L28.*

Breger, M., Lenz, P., Antoci, V., Guggenberger, E., Shobbrook, R. R., Handler, G., Ngwato, B., Rodler, F., Rodriguez, E., López de Coca, P., Rolland, A. & Costa, V. (2005), 'Detection of 75+ pulsation frequencies in the δ Scuti star FG Virginis', A&A **435**, *955–965.*

Browning, M. K., Brun, A. S. & Toomre, J. (2004), 'Simulations of Core Convection in Rotating A-Type Stars: Differential Rotation and Overshooting', ApJ **601**, *512–529.*

Bundy, K. A. & Marcy, G. W. (2000), 'A Search for Transit Effects in Spectra of 51 Pegasi and HD 209458', PASP **112**, *1421–1425.*

*Carter, J. A. & Winn, J. N. (2010*a*), 'Empirical Constraints on the Oblateness of an Exoplanet',* ApJ **709**, *1219–1229.*

*Carter, J. A. & Winn, J. N. (2010*b*), 'The Detectability of Transit Depth Variations Due to Exoplanetary Oblateness and Spin Precession',* ApJ **716**, *850–856.*

Castillo-Rogez, J. (2010), History of the Dissipation Factor Used in Planetary Tides Modeling, in *'AAS/Division for Planetary Sciences Meeting Abstracts #42', Vol. 42 of* Bulletin of the American Astronomical Society, *p. 959.*

Chandrasekhar, S. (1946), 'On the Radiative Equilibrium of a Stellar Atmosphere. X.', ApJ **103**, *351.*

Charbonneau, D., Brown, T. M., Latham, D. W. & Mayor, M. (2000), 'Detection of Planetary Transits Across a Sun-like Star', ApJ **529**, *L45–L48.*

Christian, D. J., Pollacco, D. L., Skillen, I., Street, R. A., Keenan, F. P., Clarkson, W. I., Collier Cameron, A., Kane, S. R., Lister, T. A., West, R. G., Enoch, B., Evans, A., Fitzsimmons, A., Haswell, C. A., Hellier, C., Hodgkin, S. T., Horne, K., Irwin, J., Norton, A. J., Osborne, J., Ryans, R., Wheatley, P. J. & Wilson, D. M. (2006), 'The SuperWASP wide-field exoplanetary transit survey: candidates from fields 23 h < RA < 3 h', MNRAS **372**, *1117–1128.*

Codina-Landaberry, S. & Magalhaes, A. M. (1976), 'On the polarizing interstellar dust', A&A **49**, *407–413.*

Collier Cameron, A., Guenther, E., Smalley, B., McDonald, I., Hebb, L., Andersen, J., Augusteijn, T., Barros, S. C. C., Brown, D. J. A., Cochran, W. D., Endl, M., Fossey, S. J., Hartmann, M., Maxted, P. F. L., Pollacco, D., Skillen, I., Telting, J., Waldmann, I. P. & West, R. G. (2010), 'Line-profile tomography of exoplanet transits - II. A gas-giant planet transiting a rapidly rotating A5 star', MNRAS **407***, 507–514.*

Collins, II, G. W. (1963), 'Continuum Emission from a Rapidly Rotating Stellar Atmosphere.', ApJ **138***, 1134.*

Cowling, T. G. (1941), 'The non-radial oscillations of polytropic stars', MNRAS **101***, 367.*

Coyne, G. V. & Pellicori, S. F. (1970), 'Wavelength Dependence of Polarization. XX. The Integrated Disk of the Moon', AJ **75***, 54.*

Coyne, G. V., Gehrels, T. & Serkowski, K. (1974), 'Wavelength dependence of polarization. XXVI. The wavelength of maximum polarization as a characteristic parameter of interstellar grains.', AJ **79***, 581–589.*

Czesla, S., Huber, K. F., Wolter, U., Schröter, S. & Schmitt, J. H. M. M. (2009), 'How stellar activity affects the size estimates of extrasolar planets', A&A **505***, 1277–1282.*

Czesla, S., Schröter, S., Wolter, U., von Essen, C., Huber, K. F., Schmitt, J. H. M. M., Reichart, D. E. & Moore, J. P. (2012), 'The extended chromosphere of CoRoT-2A. Discovery and analysis of the chromospheric Rossiter-McLaughlin effect', A&A **539***, A150.*

*De Ridder, J., Aerts, C., Dupret, M.-A. & Neuforge, C. (2002*a*), Do Temperature Variations at the Surface of a Hot Non-Radial Pulsator Change Significantly the Line-Profile Variations?,* in *C. Aerts, T. R. Bedding & J. Christensen-Dalsgaard, eds, 'IAU Colloq. 185: Radial and Nonradial Pulsationsn as Probes of Stellar Physics', Vol. 259 of* Astronomical Society of the Pacific Conference Series*, p. 218.*

*De Ridder, J., Dupret, M.-A., Neuforge, C. & Aerts, C. (2002*b*), 'Influence of non-adiabatic temperature variations on line profile variations of slowly rotating beta Cephei stars and SPBs. II. Simulations of line profile time series',* A&A **385***, 572–584.*

De Ridder, J., Telting, J. H., Balona, L. A., Handler, G., Briquet, M., Daszyńska-Daszkiewicz, J., Lefever, K., Korn, A. J., Heiter, U. & Aerts, C. (2004), 'Asteroseismology of the β Cephei star ν Eridani - III. Extended frequency analysis and mode identification', MNRAS **351***, 324–332.*

de Wit, J., Gillon, M., Demory, B.-O. & Seager, S. (2012), 'Towards consistent mapping of distant worlds: secondary-eclipse scanning of the exoplanet HD 189733b', A&A **548***, A128.*

Dollfus, A. & Auriere, M. (1974), 'Optical polarimetry of planet Mercury', Soviet Ast. **23***, 465–482.*

Dollfus, A. & Coffeen, D. L. (1970), 'Polarization of Venus I Disk Observations', A&A **8***, 251.*

Dollfus, A., Deschamps, M. & Ksanfomaliti, L. V. (1983), 'The surface texture of the Martian soil from the Soviet spacecraft Mars-5 photopolarimeters', A&A **123***, 225–237.*

Dupret, M.-A., De Ridder, J., De Cat, P., Aerts, C., Scuflaire, R., Noels, A. & Thoul, A. (2003), 'A photometric mode identification method, including an improved non-adiabatic treatment of the atmosphere', A&A **398***, 677–685.*

Feigelson, E. D., Carkner, L. & Wilking, B. A. (1998), 'Circularly Polarized Radio Emission from an X-Ray Protostar', ApJ **494***, L215.*

Fendt, C., Beck, R. & Neininger, N. (1998), 'Spiral pattern in the optical polarization of NGC 6946', A&A **335***, 123–133.*

Garrido, R., Garcia-Lobo, E. & Rodriguez, E. (1990), 'Modal discrimination of pulsating stars by using Stromgren photometry', A&A **234***, 262–268.*

Gehrels, T. (1960), 'The wavelength dependance of polarization. II. Interstellar polarization.', AJ **65***, 470–473.*

Gilliland, R. L., Chaplin, W. J., Dunham, E. W., Argabright, V. S., Borucki, W. J., Basri, G., Bryson, S. T., Buzasi, D. L., Caldwell, D. A., Elsworth, Y. P., Jenkins, J. M., Koch, D. G., Kolodziejczak, J., Miglio, A., van Cleve, J., Walkowicz, L. M. & Welsh, W. F. (2011), 'Kepler Mission Stellar and Instrument Noise Properties', ApJS **197**, *6.*

Guillot, T. (2004), Atmospheric Circulation of Hot Jupiters (Invited Review), in *A. Penny, ed., 'Planetary Systems in the Universe', Vol. 202 of* IAU Symposium*, p. 261.*

Guillot, T., Burrows, A., Hubbard, W. B., Lunine, J. I. & Saumon, D. (1996), 'Giant Planets at Small Orbital Distances', ApJ **459**, *L35.*

Hall, J. S. (1949), 'Observations of the Polarized Light from Stars', Science **109**, *166–167.*

Handler, G. (2013), Asteroseismology*, p. 207.*

Handler, G., Weiss, W. W., Shobbrook, R. R., Paunzen, E., Hempel, A., Anguma, S. K., Kalebwe, P. C., Kilkenny, D., Martinez, P., Moalusi, M. B., Garrido, R. & Medupe, R. (2006), 'The rapidly oscillating Ap star HD 99563 and its distorted dipole pulsation mode', MNRAS **366**, *257–266.*

Herrero, E., Morales, J. C., Ribas, I. & Naves, R. (2011), 'WASP-33: the first δ Scuti exoplanet host star', A&A **526**, *L10.*

Heynderickx, D., Waelkens, C. & Smeyers, P. (1994), 'A photometric study of β Cephei stars. II. Determination of the degrees L of pulsation modes', A&AS **105**, *447–480.*

*Hiltner, W. A. (1949*a*), 'On the Presence of Polarization in the Continuous Radiation of Stars. II.',* ApJ **109**, *471.*

*Hiltner, W. A. (1949*b*), 'Polarization of Light from Distant Stars by Interstellar Medium',* Science **109**, *165.*

Holman, M. J. & Murray, N. W. (2005), 'The Use of Transit Timing to Detect Terrestrial-Mass Extrasolar Planets', Science **307**, *1288–1291.*

Hubbard, W. B. (1984), 'Book-Review - Planetary Interiors', S&T **68**, *529.*

Huber, K. F., Czesla, S., Wolter, U. & Schmitt, J. H. M. M. (2009), 'A planetary eclipse map of CoRoT-2a. Comprehensive lightcurve modeling combining rotational-modulation and transits', A&A **508**, *901–907.*

Huber, K. F., Czesla, S., Wolter, U. & Schmitt, J. H. M. M. (2010), 'Planetary eclipse mapping of CoRoT-2a. Evolution, differential rotation, and spot migration', A&A **514**, *A39.*

Jenkins, J. M., Borucki, W. J., Koch, D. G., Marcy, G. W., Cochran, W. D., Welsh, W. F., Basri, G., Batalha, N. M., Buchhave, L. A., Brown, T. M., Caldwell, D. A., Dunham, E. W., Endl, M., Fischer, D. A., Gautier, III, T. N., Geary, J. C., Gilliland, R. L., Howell, S. B., Isaacson, H., Johnson, J. A., Latham, D. W., Lissauer, J. J., Monet, D. G., Rowe, J. F., Sasselov, D. D., Howard, A. W., MacQueen, P., Orosz, J. A., Chandrasekaran, H., Twicken, J. D., Bryson, S. T., Quintana, E. V., Clarke, B. D., Li, J., Allen, C., Tenenbaum, P., Wu, H., Meibom, S., Klaus, T. C., Middour, C. K., Cote, M. T., McCauliff, S., Girouard, F. R., Gunter, J. P., Wohler, B., Hall, J. R., Ibrahim, K., Kamal Uddin, A., Wu, M. S., Bhavsar, P. A., Van Cleve, J., Pletcher, D. L., Dotson, J. L. & Haas, M. R. (2010), 'Discovery and Rossiter-Mclaughlin Effect of Exoplanet Kepler-8b', ApJ **724**, *1108–1119.*

Jones, B. W., Sleep, P. N. & Underwood, D. R. (2006), 'Which exoplanetary systems could harbour habitable planets?', International Journal of Astrobiology **5**, *251–259.*

Koch, D. G., Borucki, W. J., Basri, G., Batalha, N. M., Brown, T. M., Caldwell, D., Christensen-Dalsgaard, J., Cochran, W. D., DeVore, E., Dunham, E. W., Gautier, III, T. N., Geary, J. C., Gilliland, R. L., Gould, A., Jenkins, J., Kondo, Y., Latham, D. W., Lissauer, J. J., Marcy, G., Monet, D., Sasselov, D., Boss, A., Brownlee, D., Caldwell, J., Dupree, A. K., Howell, S. B., Kjeldsen, H., Meibom, S., Morrison, D., Owen, T., Reitsema, H., Tarter, J., Bryson, S. T., Dotson, J. L., Gazis, P., Haas, M. R., Kolodziejczak, J., Rowe, J. F., Van Cleve, J. E., Allen, C., Chandrasekaran, H., Clarke, B. D., Li, J., Quintana, E. V., Tenenbaum, P., Twicken, J. D. & Wu, H. (2010), 'Kepler Mission Design, Realized

Photometric Performance, and Early Science', ApJ **713**, *L79–L86*.

Kosovichev, A. G., Schou, J., Scherrer, P. H., Goode, P. H., Dziembowski, W. A., Rhodes, Jr., E. J. & SOI Structure Inversion Team (1998), Spherical and aspherical structure of the sun: First year of SOHO/MDI observations, in *F.-L. Deubner, J. Christensen-Dalsgaard & D. Kurtz, eds, 'New Eyes to See Inside the Sun and Stars', Vol. 185 of* IAU Symposium*, p. 157*.

Kovács, G., Kovács, T., Hartman, J. D., Bakos, G. Á., Bieryla, A., Latham, D., Noyes, R. W., Regály, Z. & Esquerdo, G. A. (2013), 'Comprehensive time series analysis of the transiting extrasolar planet WASP-33b', A&A **553**, *A44*.

Kurtz, D. W., Martinez, P., Tripe, P. & Hanbury, A. G. (1997), 'The oblique dipole pulsation mode of the rapidly oscillating AP star HD80316', MNRAS **289**, *645–650*.

Kurtz, D. W., Sullivan, D. J., Martinez, P. & Tripe, P. (1994), 'The Pure Dipole Pulsation Mode of the Rapidly Oscillating Ap-Star Alpha-Circini - Determination of the Rotation Period and Evidence for Frequency Variability', MNRAS **270**, *674*.

Landi Degl'Innocenti, E. & Landolfi, M., eds (2004), Polarization in Spectral Lines*, Vol. 307 of* Astrophysics and Space Science Library.

Larson, T. P. & Schou, J. (2008), 'Improvements in global mode analysis', Journal of Physics Conference Series **118***(1), 012083*.

Leavitt, H. S. & Pickering, E. C. (1912), 'Periods of 25 Variable Stars in the Small Magellanic Cloud.', Harvard College Observatory Circular **173**, *1–3*.

Lenz, P. & Breger, M. (2005), 'Period04 User Guide', Communications in Asteroseismology **146**, *53–136*.

Lissauer, J. J., Fabrycky, D. C., Ford, E. B., Borucki, W. J., Fressin, F., Marcy, G. W., Orosz, J. A., Rowe, J. F., Torres, G., Welsh, W. F., Batalha, N. M., Bryson, S. T., Buchhave, L. A., Caldwell, D. A., Carter, J. A., Charbonneau, D., Christiansen, J. L., Cochran, W. D., Desert, J.-M., Dunham, E. W., Fanelli, M. N., Fortney, J. J., Gautier, III, T. N., Geary, J. C., Gilliland, R. L., Haas, M. R., Hall, J. R., Holman, M. J., Koch, D. G., Latham, D. W., Lopez, E., McCauliff, S., Miller, N., Morehead, R. C., Quintana, E. V., Ragozzine, D., Sasselov, D., Short, D. R. & Steffen, J. H. (2011), 'A closely packed system of low-mass, low-density planets transiting Kepler-11', Nature **470**, *53–58*.

Lucas, P. W., Hough, J. H., Bailey, J. A., Tamura, M., Hirst, E. & Harrison, D. (2009), 'Planetpol polarimetry of the exoplanet systems 55Cnc and τBoo', MNRAS **393**, *229–244*.

Mandel, K. & Agol, E. (2002), 'Analytic Light Curves for Planetary Transit Searches', ApJ **580**, *L171–L175*.

Martin, P. G., Clayton, G. C. & Wolff, M. J. (1999), 'Ultraviolet Interstellar Linear Polarization. V. Analysis of the Final Data Set', ApJ **510**, *905–914*.

Mathewson, D. S. & Ford, V. L. (1970), 'Polarization Observations of 1800 Stars', MmRAS **74**, *139*.

Mathias, P., Gillet, D., Aerts, C. & Breitfellner, M. G. (1997), 'A spectroscopic study of the delta Scuti star rho Puppis', A&A **327**, *1077–1086*.

Matthews, J. M., Kuschnig, R., Guenther, D. B., Walker, G. A. H., Moffat, A. F. J., Rucinski, S. M., Sasselov, D. & Weiss, W. W. (2004), 'No stellar p-mode oscillations in space-based photometry of Procyon', Nature **430**, *51–53*.

Narita, N., Enya, K., Sato, B., Ohta, Y., Winn, J. N., Suto, Y., Taruya, A., Turner, E. L., Aoki, W., Yoshii, M., Yamada, T. & Tamura, Y. (2007), 'Measurement of the Rossiter-Laughlin Effect in the Transiting Exoplanetary System TrES-1', PASJ **59**, *763–770*.

Narita, N., Hirano, T., Sato, B., Winn, J. N., Suto, Y., Turner, E. L., Aoki, W., Tamura, M. & Yamada, T. (2009), 'Improved Measurement of the Rossiter-McLaughlin Effect in the Exoplanetary System HD 17156', PASJ **61**, *991–*.

Nesvorný, D. & Morbidelli, A. (2008), 'Mass and Orbit Determination from Transit Timing Variations of Exoplanets', ApJ **688***, 636–646.*

Newton, I. (1999), The Principia : mathematical principles of natural philosophy.

Ngeow, C.-C., Kanbur, S. M., Bellinger, E. P., Marconi, M., Musella, I., Cignoni, M. & Lin, Y.-H. (2012), 'Period-luminosity relations for Cepheid variables: from mid-infrared to multi-phase', Ap&SS **341***, 105–113.*

Öhman, Y. (1946), 'On the Possibility of Tracing Polarization Effects in the Rotational Profiles of Early-Type Stars.', ApJ **104***, 460.*

Patat, F. & Romaniello, M. (2006), 'Error Analysis for Dual-Beam Optical Linear Polarimetry', PASP **118***, 146–161.*

Patat, F. & Taubenberger, S. (2011), 'Characterisation of the CAFOS linear spectropolarimeter', A&A **529***, A57.*

Pollacco, D. L., Skillen, I., Collier Cameron, A., Christian, D. J., Hellier, C., Irwin, J., Lister, T. A., Street, R. A., West, R. G., Anderson, D. R., Clarkson, W. I., Deeg, H., Enoch, B., Evans, A., Fitzsimmons, A., Haswell, C. A., Hodgkin, S., Horne, K., Kane, S. R., Keenan, F. P., Maxted, P. F. L., Norton, A. J., Osborne, J., Parley, N. R., Ryans, R. S. I., Smalley, B., Wheatley, P. J. & Wilson, D. M. (2006), 'The WASP Project and the SuperWASP Cameras', PASP **118***, 1407–1418.*

Queloz, D., Eggenberger, A., Mayor, M., Perrier, C., Beuzit, J. L., Naef, D., Sivan, J. P. & Udry, S. (2000), 'Detection of a spectroscopic transit by the planet orbiting the star HD209458', A&A **359***, L13–L17.*

Quirrenbach, A., Amado, P. J., Mandel, H., Caballero, J. A., Mundt, R., Ribas, I., Reiners, A., Abril, M., Aceituno, J., Afonso, C., Barrado Y Navascues, D., Bean, J. L., Béjar, V. J. S., Becerril, S., Böhm, A., Cárdenas, M. C., Claret, A., Colomé, J., Costillo, L. P., Dreizler, S., Fernández, M., Francisco, X., Galadí, D., Garrido, R., González Hernández, J. I., Guàrdia, J., Guenther, E. W., Gutiérrez-Soto, F., Joergens, V., Hatzes, A. P., Helmling, J., Henning, T., Herrero, E., Kürster, M., Laun, W., Lenzen, R., Mall, U., Martin, E. L., Martín-Ruiz, S., Mirabet, E., Montes, D., Morales, J. C., Morales Muñoz, R., Moya, A., Naranjo, V., Rabaza, O., Ramón, A., Rebolo, R., Reffert, S., Rodler, F., Rodríguez, E., Rodríguez Trinidad, A., Rohloff, R. R., Sánchez Carrasco, M. A., Schmidt, C., Seifert, W., Setiawan, J., Solano, E., Stahl, O., Storz, C., Suárez, J. C., Thiele, U., Wagner, K., Wiedemann, G., Zapatero Osorio, M. R., Del Burgo, C., Sánchez-Blanco, E. & Xu, W. (2010), CARMENES: Calar Alto high-resolution search for M dwarfs with exo-earths with a near-infrared Echelle spectrograph, in *'Society of Photo-Optical Instrumentation Engineers (SPIE) Conference Series', Vol. 7735 of* Society of Photo-Optical Instrumentation Engineers (SPIE) Conference Series.

Rozelot, J.-P. & Neiner, C. (2011), The Pulsations of the Sun and the Stars.

Russell, H. N. (1916), 'On the Albedo of the Planets and Their Satellites', ApJ **43***, 173.*

Scherrer, P. H., Bogart, R. S., Bush, R. I., Hoeksema, J. T., Kosovichev, A. G., Schou, J., Rosenberg, W., Springer, L., Tarbell, T. D., Title, A., Wolfson, C. J., Zayer, I. & MDI Engineering Team (1995), 'The Solar Oscillations Investigation - Michelson Doppler Imager', Sol. Phys. **162***, 129–188.*

Schmidt, G. D., Elston, R. & Lupie, O. L. (1992), 'The Hubble Space Telescope Northern-Hemisphere grid of stellar polarimetric standards', AJ **104***, 1563–1567.*

Seager, S. & Hui, L. (2002), 'Constraining the Rotation Rate of Transiting Extrasolar Planets by Oblateness Measurements', ApJ **574***, 1004–1010.*

Seager, S., Whitney, B. A. & Sasselov, D. D. (2000), 'Photometric Light Curves and Polarization of Close-in Extrasolar Giant Planets', ApJ **540***, 504–520.*

Serkowski, K. (1973), Interstellar Polarization (review), in *J. M. Greenberg & H. C. van de Hulst, eds, 'Interstellar Dust and Related Topics', Vol. 52 of* IAU Symposium*, p. 145.*

Serkowski, K., Mathewson, D. S. & Ford, V. L. (1975), 'Wavelength dependence of interstellar polarization and ratio of total to selective extinction', ApJ **196**, *261–290.*

Shakhovskoi, N. M. (1965), 'Polarization in Variable Stars. II. Eclipsing Binaries', Soviet Ast. **8**, *833.*

Smith, A. M. S., Anderson, D. R., Skillen, I., Collier Cameron, A. & Smalley, B. (2011), 'Thermal emission from WASP-33b, the hottest known planet', MNRAS **416**, *2096–2101.*

Smith, P. H. & Tomasko, M. G. (1984), 'Photometry and polarimetry of Jupiter at large phase angles. II - Polarimetry of the south tropical zone, south equatorial belt, and the polar regions from the Pioneer 10 and 11 missions', A&A **58**, *35–73.*

Stam, D. M., Hovenier, J. W. & Waters, L. B. F. M. (2004), 'Using polarimetry to detect and characterize Jupiter-like extrasolar planets', A&A **428**, *663–672.*

Stamford, P. A. & Watson, R. D. (1981), 'Baade-Wesselink and related techniques for mode discrimination in nonradial stellar pulsations', Ap&SS **77**, *131–158.*

Stenflo, J. O., Baur, T. G. & Elmore, D. F. (1980), 'Resonance-line polarization. IV - Observations of non-magnetic line polarization and its center-to-limb variations', A&A **84**, *60–67.*

Stenflo, J. O., Gandorfer, A. & Keller, C. U. (2000), 'Center-to-limb variation of the enigmatic Na bt I D_1 and D_2 polarization profiles', A&A **355**, *781–788.*

Tomasko, M. G. & Smith, P. H. (1982), 'Photometry and polarimetry of Titan - Pioneer 11 observations and their implications for aerosol properties', A&A **51**, *65–95.*

Tomasko, M. G., West, R. A., Orton, G. S. & Teifel, V. G. (1984), Clouds and aerosols in Saturn's atmosphere, *pp. 150–194.*

Triaud, A. H. M. J., Queloz, D., Bouchy, F., Moutou, C., Collier Cameron, A., Claret, A., Barge, P., Benz, W., Deleuil, M., Guillot, T., Hébrard, G., Lecavelier Des Étangs, A., Lovis, C., Mayor, M., Pepe, F. & Udry, S. (2009), 'The Rossiter-McLaughlin effect of CoRoT-3b and HD 189733b', A&A **506**, *377–384.*

van Belle, G. T., Ciardi, D. R., Thompson, R. R., Akeson, R. L. & Lada, E. A. (2001), 'Altair's Oblateness and Rotation Velocity from Long-Baseline Interferometry', ApJ **559**, *1155–1164.*

Villforth, C., Nilsson, K., Østensen, R., Heidt, J., Niemi, S.-M. & Pforr, J. (2009), 'Intranight polarization variability in radio-loud and radio-quiet AGN', MNRAS **397**, *1893–1908.*

Ward, W. R. & Hahn, J. M. (2003), 'Spiral Bending Waves Launched at a Vertical Secular Resonance', AJ **125**, *3389–3397.*

Whittet, D. C. B., Martin, P. G., Hough, J. H., Rouse, M. F., Bailey, J. A. & Axon, D. J. (1992), 'Systematic variations in the wavelength dependence of interstellar linear polarization', ApJ **386**, *562–577.*

Wiktorowicz, S. J. (2009), 'Nondetection of Polarized, Scattered Light from the HD 189733b Hot Jupiter', ApJ **696**, *1116–1124.*

Wilking, B. A., Lebofsky, M. J. & Rieke, G. H. (1982), 'The wavelength dependence of interstellar linear polarization - Stars with extreme values of lambda/max/', AJ **87**, *695–697.*

Wilking, B. A., Lebofsky, M. J., Kemp, J. C., Martin, P. G. & Rieke, G. H. (1980), 'The wavelength dependence of interstellar linear polarization', ApJ **235**, *905–910.*

Wolstencroft, R. D. & Breon, F.-M. (2005), Polarization of Planet Earth and Model Earth-like Planets, in *A. Adamson, C. Aspin, C. Davis & T. Fujiyoshi, eds, 'Astronomical Polarimetry: Current Status and Future Directions', Vol. 343 of* Astronomical Society of the Pacific Conference Series, *p. 211.*

Zima, W. (2006), 'A new method for the spectroscopic identification of stellar non-radial pulsation modes. I. The method and numerical tests', A&A **455**, *227–234.*

Acknowledgments

Will be written in the “fancy” version only.